Modelling the Response of Evolutive Granular Media to Blast Loadings: Cemented Tailings Backfill

Submitted by

Gongda Lu

Under the supervision of

Dr. Mamadou Fall

Thesis submitted
in partial fulfillment of the requirements
for the Doctorate in Philosophy degree in Civil Engineering

Department of Civil Engineering
Faculty of Engineering
University of Ottawa

July 2017

Abstract

Cemented tailings backfill (CTB), an evolutive granular medium, is utilized extensively in underground mines as a sustainable solution to tailings disposal and for ground control. To achieve full ore recovery, the backfill mass is often exposed to mine blasts during the extraction of ore pillars. Nevertheless, limitations in knowledge regarding the dynamic response of CTB and the lack of design standards to ensure backfill stability during blasting have caused numerous failure incidents of backfill systems. Therefore, the proposition to utilize reliable tools for a rational characterization of CTB behaviour under mine blasts has become imperative. However, current studies conducted to evaluate blast response of mine backfills are based on empirical equations and simple constitutive models, and the evolutive nature of CTB due to multiphysics processes occurring in the material has not yet been considered. Therefore, in this PhD study, a series of fundamental multiphysics models are developed to assess the blast response of CTB with ongoing cementation. Specifically, a novel coupled chemo-viscoplastic cap model is developed to characterize the rate-dependence, irrecoverable compaction, and nonlinear hydrostatic behaviour of CTB under blast loading. The evolution in the dynamic response of CTB due to binder hydration is incorporated in the model and quantified with a binder hydration model. Moreover, the performance of CTB is not only affected by the hydration of binders (chemical, C), but is also significantly influenced by the thermal (T), hydraulic (H), and mechanical (M) factors it is subjected to during its service life. Therefore, a new multiphysics-viscoplastic cap model is then developed to characterize the blast response of CTB under the impact of complex THMC processes of its curing stage. Furthermore, as a granular medium, the early-age CTB with no or negligible cementation is also subjected to the risk of blast-induced liquefaction. Thus, a new total-stress viscoplastic cap model is developed to account for the impedance of pore water and capture excess pore pressure development in early-age backfills during blast loading. The developed multiphysics models are validated against a series of experiments on both laboratory and field scales, and the effectiveness and predictive ability of the models are verified by good agreement between the simulated and measured results. Then, the validated models are applied to practical engineering issues pertaining

to field backfilling operations. These include simulation of the blast wave propagation in field CTB structures and the blast-induced liquefaction susceptibility of early-age fill mass, as well as blast-induced stress redistribution in early-age fill mass. The different dynamic responses of CTB to varied backfilling conditions and design strategies are then scrutinized and analyzed. Thus, the research performed in this PhD study can provide useful tools and technical insight for a better understanding of the blast response of CTB as well as optimal design of CTB systems in such dynamic condition.

Acknowledgement

I would like to express my sincere gratitude to my advisor, Dr. Mamadou Fall for his enduring support, guidance, and encouragement throughout the completion of this study. I truly appreciate the opportunity he provided for me to be inspired by his wisdom, passion and perseverance in doing research at the University of Ottawa.

My sincere appreciation is extended to Dr. Sai Vanapalli at the University of Ottawa for his constructive advices and encouragement on my research work. I would also like to thank my colleague, Dr. Liang Cui, for his generous and kind advice on my study. I also want to thank my other colleagues and fellow graduate students for their support, kindness and persistent friendships during the past years.

The China Scholarship Council is gratefully acknowledged for making the completion of this research possible.

Last, but not least, I wish to deeply thank my parents, my brother and his family for their unconditional support for me to pursue my study, and this work could not have been possible without their unceasing love and encouragement throughout the entire four years.

Table of Contents

List of Figures

List of Tables

Chapter 1.
Introduction

1.1 Background

Historically, ground control in mining has been realized by leaving up to 30% of ore reserves as remnant pillars. However, its limited mechanical performance, along with concerns over the depletion of mineral resources and the adverse environmental impact of ground disposal of mine waste (waste rock and tailings), led to the development of cemented backfill technology in Canada in the 1950s (Nnadi, 1990).

Three main types of cemented backfills are now used in the underground disposal of mine wastes, namely the rockfill, hydraulic backfill, and paste backfill; the latter two types are also termed tailings backfill. Although it does not have a long history compared to its alternatives, cemented tailings backfill (CTB) has been used extensively around the world in mining operations to fill mined-out subsurface voids (stopes) for future mining sequences (Fall and Benzaazoua, 2005; Emad et al., 2015).

CTB represents an evolutive granular material, and it is a mixture of dewatered mine tailings (man-made soils) produced by mineral extraction, binder additives (such as cement, fly ash, and slag), and water. With tailings particles building its matrix or skeleton, the binder additives are included to meet the mechanical stability requirements of backfilling, and the water content is adjusted to reach the desired consistency to transport the backfill to underground mine openings or stopes. Its broad application in the mining industry today can be attributed to the following three main kinds of benefits (Nnadi, 1990; Fall et al., 2005; Klein and Simon, 2006; Atlascopco, 2007; Bussière, 2007; Ghirian and Fall, 2013, 2014):

a) Environmental benefits. Mine backfill can return up to 60% of the waste material to the underground voids, which might otherwise cause severe environmental and geotechnical problems, such as acid mine drainage or tailing dam failures, if disposed on ground surface.

b) Stability benefits. It can act as a passive support system for the surrounding rock walls and pillars, and control subsidence at ground surface, thereby providing a safe subsurface environment for mine workers.

c) Economic benefits. It has led to more mechanized mining techniques, and can also facilitate more selective mining and better ore recovery by allowing the extraction of remnant ore pillars between stopes, thus increasing both mine life span and total return on investment.

1.2 Problem statement

Development and production blasts are routinely used in contemporary mining operations, including mining with backfill. In deep mining methods, such as sublevel open stoping, vertical crater retreat, and cut and fill, the ore slices are gradually blasted and cleaned out, before the mined-out stope is backfilled and retained by containment structures (barricades) at the drawpoint (Atlascopco, 2007). To achieve full ore extraction, these backfill masses are then exposed to blast loadings during the mining of adjacent ore pillars (Helinski et al., 2007; 2010; Emad, 2013).

Thus, in addition to gravity, CTB in the field is also often subjected to blast loading with high pressure and high frequency. Moreover, it may also be exposed to intensive dynamic loads due to fault-slips and rock bursts in regions with high in-situ stress, as mining continues to reach increasingly deeper beneath the earth surface (Kaiser et al. 1995; Sainoki et al., 2016).

Under the circumstances, mature backfill structures may lose integrity or even fail when exposed to dynamic loads, thus incapacitating their performance to support the surrounding rock mass as mechanical elements, and also cause ore dilution (Emad, 2013). On the other hand, the early-age backfill behaves in an undrained manner and exhibits no or weak cementation (Fahey et al., 2009), and it is subjected to the risk of liquefaction in such dynamic loading conditions. The liquefied backfill mass may breach its retaining structures and flow into the adjacent mine stope, thus causing significant casualties and loss of production (Le Roux, 2004).

Therefore, to maintain its functionality as well as its environmental, mechanical and economic benefits, an ideal backfill design should accommodate both static loading due to gravity and dynamic loading due to vibration. However, the current design practice only requires backfill strength to be stable in standing as an unsupported element based on its own weight

(Emad et al., 2014). In fact, most research studies on CTB have commonly been performed under quasi-static conditions, while very few efforts have focused on its dynamic response.

Meanwhile, the challenge for understanding the response of CTB under those dynamic loads becomes more complex, as it is constantly evolving due to the hydration of the binders it contains and its interplay with the environment. Specifically, once placed in the field, the evolution of CTB starts and it is not only a function of the hydration of binders (chemical, C), but also of the thermal (T), hydraulic (H), and mechanical (M) factors of curing processes as well as their mutual interactions (Ghirian and Fall, 2013, 2014).

Therefore, it is of paramount importance to investigate the response of CTB under dynamic loading conditions, and the influence of THMC processes taking place in CTB need to be rationally considered. To date, there have not been any studies conducted that address the blast response of CTB under the influence of multiphysics processes. While the lack of understanding of its dynamic behaviour and rational design procedures has led to conservative design or overdesign (Witteman, 2013), the limitation has also contributed to a number of failure incidents of backfill systems in underground mining (Yumlu and Guresci, 2007; Helinski et al., 2010; Witteman, 2013; Emad et al., 2014).

1.3 Objectives

In consideration of the aforementioned insufficiency in understanding of the blast response of CTB under the influence of multiphysics processes, the main objectives of this PhD study are:

1. To provide a review of the existing models used to describe the behaviour of granular media subjected to blast loadings.

2. To develop novel multiphysics models for the assessment and prediction of the response of tailings backfill to blast loads. This objective includes the following sub-objectives:

2-1 the development of a novel chemo-mechanical model for the assessment and prediction of the behaviour of hydrating tailings backfill under blast loadings;

2-2 the development of a new THMC-mechanical model for the assessment and prediction of the blast response of hydrating tailings backfill by further incorporating all multiphysics factors of its curing process;

2-3 the development of a new hydro-mechanical model for the assessment and prediction of the blast-induced liquefaction of early-age tailings backfill.

3. To numerically investigate the geotechnical responses of field tailings backfill structures to blast loadings. This objective includes the following sub-objectives:

3-1 the simulation of blast wave propagation in field tailings backfill structures;

3-2 the simulation of blast-induced liquefaction susceptibility of field tailings backfill mass at early age;

3-3 the simulation of blast-induced stress redistribution in field tailings backfill mass at early age.

4. To provide technical information and tools that contribute to a better understanding of the behaviour of tailings backfill structures subjected to blast loadings.

1.4 Research approaches and methods

1.4.1 Research approaches

The research approaches adopted in the study are schematically illustrated by the flowchart in Figure 1.1. Due to the complex coupled THMC processes that affect material evolution, the development of multiphysics models to assess the blast response of CTB will be carried out in four steps.

First, a comprehensive literature review on existing models of granular media for blast loading will be presented. By providing a critical review on the advantages and limitations of different available solutions, an appropriate mathematical model to capture the response of CTB under blast loading will be developed.

Second, given the dominance of the effect of binder hydration on material evolution, a new model that couples the influence of binder hydration (chemical, C) on the blast response of CTB will be developed.

Subsequently, as the CTB properties and thus its dynamic response are also affected by thermal (T), hydraulic (H), mechanical (M) factors of its curing process in addition to binder hydration (C), these coupled multiphysics processes will be supplemented. Thus, a new model that can capture the blast response of hydrating CTB during complex THMC curing processes will be proposed. Note that the effect of the THMC processes is insignificant during blast loading because of the short duration of such an impact.

Finally, to assess the blast-induced liquefaction of early-age CTB, a new total-stress model will be developed to characterize its hydro-mechanical behaviour and pore pressure response under blast loading. The correlation between the three fundamental models for blast response of CTB to be developed in the study is illustrated in Figure 1.2.

After the developed multiphysics models are validated against experimental data, they will be applied to practical engineering issues pertaining to field backfilling operations. These include simulation of blast wave propagation in field CTB structures, blast-induced liquefaction susceptibility of early-age fill mass, and blast-induced stress redistribution in early-age fill mass. Investigation and analysis of these practical problems can provide valuable insight and contribute to a better understanding of the behaviour of field tailings backfill structures subjected to blast loadings, thereby facilitate more rational design of backfill systems.

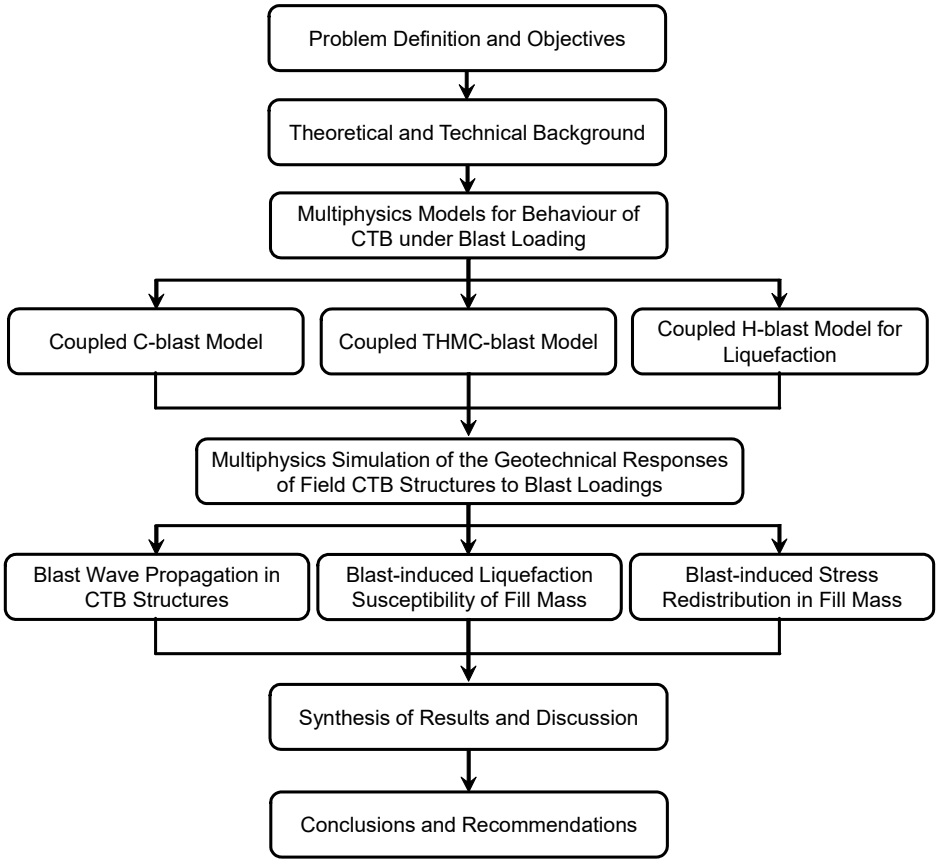

Figure 1.1 Flowchart of the thesis

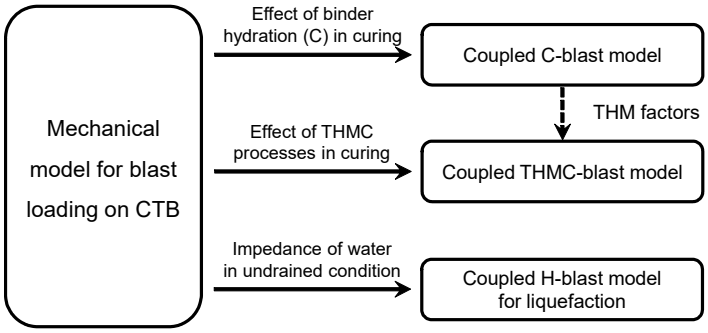

Figure 1.2 Correlation between fundamental models developed in the study

1.4.2 Numerical tool used

The finite element code COMSOL Multiphysics is adopted in this study to develop fundamental models and conduct simulations of the blast response of CTB that is undergoing multiphysics processes in its curing stage. COMSOL Multiphysics is a general-purpose software platform that solves coupled physical problems, through the use of partial differential equations (PDEs); it can perform various types of analyses, including stationary and time-dependent, linear and nonlinear, eigen-frequency, and modal analyses (COMSOL, 2009). The software allows for the straightforward implementation of user-defined constitutive laws, such as variable material properties and stress–strain relations; it can also accommodate large deformations by the multiple coordinate systems incorporated. Detailed technical information and data on COMSOL Multiphysics are available in COMSOL (2009). There is no existing model in COMSOL Multiphysics for simulating the blast response or THMC processes of materials. Therefore, in this study, the constitutive relations that characterize the evolutive behaviours of CTB will be implemented in COMSOL Multiphysics, along with the establishment of conservation equations for each physical field, in order to reproduce the THMC processes of the material in its curing stage. Meanwhile, constitutive models for the blast response of CTB will also be developed and implemented in COMSOL Multiphysics. THMC processes and the blast response of CTB will be coupled by transferring global field variables in the software.

1.5 Thesis organization

The tasks and organization of the thesis are illustrated in Figure 1.3 below.

Chapter 1 provides a general introduction to the PhD study. The problem statements, objectives, and research approaches adopted in this study are presented.

Chapter 2 presents background information on CTB and its stability issues associated with blast loading. The fundamentals of blast wave propagation in porous media are also provided, and the multiphysics processes affecting the evolution of CTB are summarized.

Chapter 3 provides a comprehensive literature review on available models of granular media for blast loading, and can aid in framing the appropriate model choice to capture the blast response of CTB by comparing their advantages and limitations. This chapter also demonstrates that the fundamental models proposed for the blast response of CTB in this thesis are novel.

Chapter 4 elucidates the development of fundamental multiphysics models used to describe the behaviour of CTB under blast loading, which comprises three technical papers. First, a new model that integrates the effect of the process of cement hydration on the blast response of CTB is developed in Section 4.2. Then, in Section 4.3, a novel model that couples the influence of THMC processes of CTB during the curing stage on its blast response is proposed. Subsequently, in Section 4.4, a new total-stress model for characterizing the blast-induced liquefaction of early-age CTB is developed.

Chapter 5 focuses on practical engineering applications of the developed fundamental multiphysics models to clarify and assess the field behaviour of CTB under blast loading in mining operations. This chapter consists of three technical papers, which include simulation of blast wave propagation in field CTB structures, the blast-induced liquefaction susceptibility of early-age fill mass, and blast-induced stress redistribution in early-age fill mass.

In Chapter 6, the results obtained in the study are synthesized to provide insights into the issue of CTB response to blast loading and implications for the optimal design strategies for CTB.

Chapter 7 presents the main conclusions and recommendations for future research.

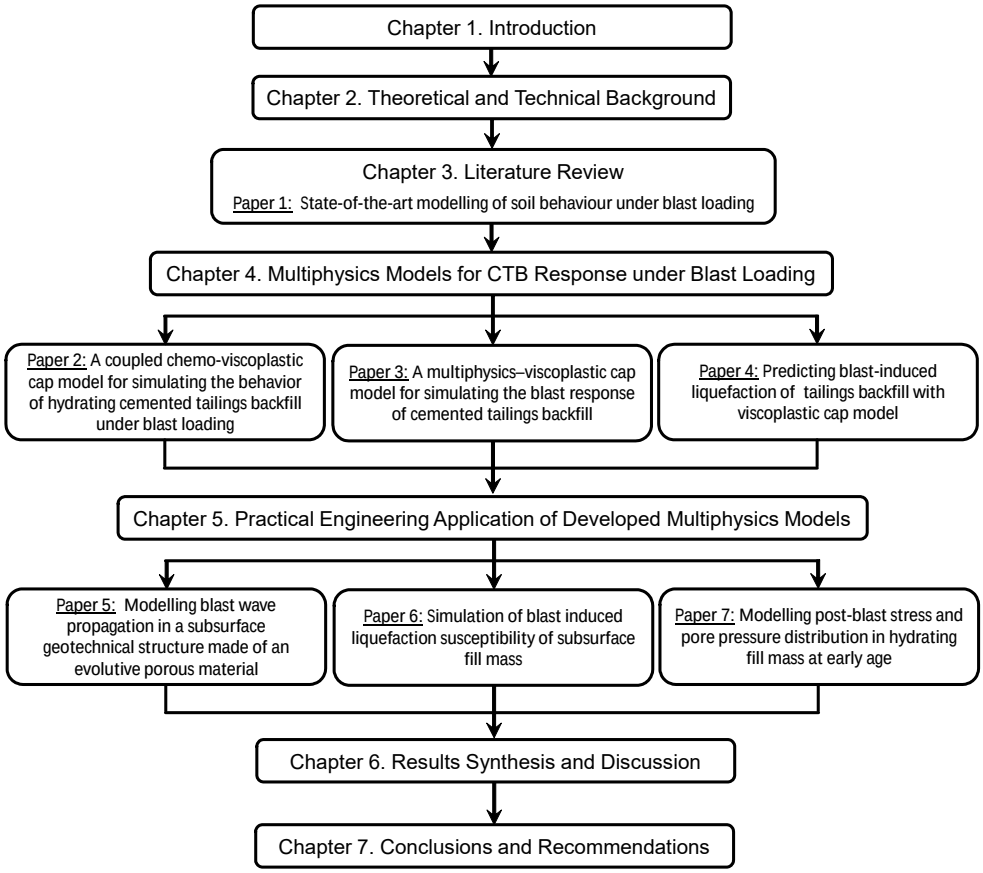

Figure 1.3 Tasks and organization of the thesis

1.6 Novelty of the study

Given the current absence of research that assesses the blast response of CTB under the influence of multiphysics processes, the novelty of this PhD study can be elucidated as follows.

The literature review presented in Paper 1 is a comprehensive summary of the existing mathematical models that characterize the blast response of granular media at the time of writing.

The coupled chemo–viscoplastic cap model developed in Paper 2 is the first tool to capture the blast response of hydrating cementitious materials that exhibit time-evolutive properties on account of the effect of binder hydration.

By introducing the influence of coupled thermal, hydraulic, and mechanical factors—in addition to that of binder hydration—the multiphysics–viscoplastic cap model developed in Paper 3 represents the first model that can evaluate the blast response of hydrating cementitious

materials while fully considering the effect of the multiphysics processes during the curing period.

In Paper 4, a new total-stress viscoplastic cap model is proposed. It represents a novel approach to simulating the liquefaction of granular media induced by explosive loadings.

Paper 5 is the first analysis of blast wave propagation in cementitious materials that undergo multiphysics processes due to binder hydration, and of their interactions with the curing environment.

The liquefaction susceptibility analysis in Paper 6 is the first investigation of the liquefaction potential of early-age tailings backfill mass associated with mine blasting in practical engineering conditions.

The last paper, Paper 7, is the first examination of stress redistribution in field hydrating backfill mass, as caused by mine blast operations; it poses significant implications for the design of retaining structures for field backfills.

1.7 References

Al-Qasimi EMA, Charlie WA, Woeller DJ. Canadian liquefaction experiment (CANLEX): Blast-induced ground motion and pore pressure experiments. Geotechnical Testing Journal 2005, 28(1): 1-13.

Aref L. A study of the geotechnical characteristics and liquefaction potential of paste backfill. PhD Thesis, University of McGill, Montreal, Canada, 1998.

Atlas Copco. Mining Methods in Underground Mining. Second Edition. 2007.

Bussière B. Colloquium 2004: Hydrogeotechnical properties of hard rock tailings from metal mines and emerging geoenvironmental disposal approaches. Canadian Geotechnical Journal 2007; 44(9):1019–1052.

COMSOL Multiphysics User's Guide, Version 3.5a, COMSOL AB, Stockholm, Sweden, 2009.

Emad MZ. Dynamic Performance of cemented rockfill under blast-induced vibrations. PhD Thesis. McGill University, Montreal, Canada, 2013.

Emad MZ, Mitri H, Kelly C. Effect of blast–induced vibrations on fill failure in vertical block mining with delayed backfill. Canadian Geotechnical Journal 2014; 51:975–983.

Emad MZ, Mitri H, Kelly C. State-of-the-art review of backfill practices for sublevel stoping system. International Journal of Mining, Reclamation and Environment 2015; 29(5): 544–556.

Fahey M, Helinski M, Fourie A. Some aspects of the mechanics of arching in backfilled stopes. Can Geotech J 2009;46(11):1322–36.

Fall M, Belem T, Samb S, Benzaazoua M. Experimental characterization of the stress–strain behaviour of cemented paste backfill in compression. Journal of Material Science 2007; 42(11):3914–3922.

Fall M, Benzaazoua M, Ouellet S. Experimental characterization of the influence of tailings fineness and density on the quality of cemented paste backfill. Mineral Engineering 2005; 18(1):41–44.
Fall M, Célestin JC, Pokharel M, Touré M. A contribution to understanding the effects of curing temperature on the mechanical properties of mine cemented tailings backfill. Engineering Geology 2010;114:397–413.
Fall M, Samb SS. Effect of high temperature on strength and microstructural properties of cemented paste backfill. Fire Safety Journal 2009; 44(4):642–651.
Ferdosi B, James M, Aubertin M. Numerical simulations of the seismic and post-seismic behaviour of tailings. Canadian Geotechnical Journal 2015; 52: 1-8.
Ghirian A, Fall M. Coupled thermo–hydro–mechanical–chemical behaviour of cemented paste backfill in column experiments. Part I: Physical, hydraulic and thermal processes and characteristics. Engineering Geology 2013; 164:195–207.
Ghirian A, Fall M. Coupled thermo–hydro–mechanical–chemical behaviour of cemented paste backfill in column experiments. Part II : Mechanical, chemical and microstructural processes and characteristics. Engineering Geology 2014; 170:11–23.
Grujicic M, Pandurangan B, Cheeseman BA, Roy WN, Skaggs, RR, Gupta, R. Parameterization of the porous–material model for sand with various degrees of water saturation. Soil Dynamics and Earthquake Engineering 2008; 28:20–35.
Helinski M, Fahey M, Fourie A. Numerical modeling of cemented mine backfill deposition. Journal of Geotechnical and Geoenvironmental Engineering 2007; 133(10): 1308–1319.
Helinski M, Fahey M, Fourie A. Coupled two-dimensional finite element modelling of mine backfilling with cemented tailings. Canadian Geotechnical Journal 2010; 47: 1187–1200.
Huang S, Xia K, Qiao L. Dynamic tests of cemented paste backfill: effects of strain rate, curing time, and cement content on compressive strength. Journal of Material Science 2011; 46(15):5165–5170.
Kaiser, P.K., McCreath, D.R., and Tannant, D.D. 1995. Rockburst Support. In: Rockburst Research Handbook, Vol. 2. CAMIRO Mining Division.
Kesimal A, Yilmaz E, Ercikdi B, Alp I, Deveci H. Effect of properties of tailings and binder on the short– and long–term strength and stability of cemented paste backfill. Materials Letters 2005; 59(28):3703–3709.
Klein K, Simon D. Effect of specimen composition on the strength development in cemented paste backfill. Canadian Geotechnical Journal 2006; 43:310–324.
Le Roux K. In situ properties and liquefaction potential of cemented paste backfill. PhD Thesis. University of Toronto, Toronto, Canada, 2004.
Mohanty, B, Yang, R, LeBlanc, M, and Kelly, C. Dilution control and vibration studies at an underground mine. Proceedings of the Annual Conference on Explosives and Blasting Technique, International Society of Explosives Engineers, CONF 21//V2, pages 20, 1995.
Nnadi GN. Dynamic behaviour of cemented mine backfill. PhD Thesis. Queen's University, Kingston, Canada, 1990.
Saebimoghaddam A. Liquefaction of early age cemented paste backfill. PhD Thesis. University of Toronto, Toronto, Canada, 2009.
Sainoki A, Mitri H. Dynamic modelling of fault slip induced by stress waves due to stope production blasts. Rock Mechanics and Rock Engineering 2016; 49:165–181.

Shahsavari M, Moghaddam R, Grabinsky M. Liquefaction screening assessment for as-placed cemented paste backfill. 67th Canadian Geotechnical Conference, Regina, SK, Canada, 2014.

van Gool BS. Effects of blasting on the stability of paste fill stopes at Cannington Mine. PhD Thesis. James Cook University, Townville, Australia, 2007.

Witteman ML. Unsaturated flow in hydrating porous media: application to cemented paste backfill. Master Thesis. Carleton University, Ottawa, Canada, 2013.

Yumlu M, Guresci M. Paste backfill bulkhead monitoring–a case study from Inmet's Cayeli mine, Turkey. In Proceedings of the 9th International Symposium in Mining with Backfill, Montréal, Quebec, 2007.

Chapter 2.
Theoretical and Technical Background

2.1 Introduction

Underground mining activities can result in enormous subsurface voids (stopes) as well as large amounts of mine waste on the ground surface. The unsupported, mined-out cavities could result in a stability issue with the surrounding rock mass, while the disposal of mine waste on the earth's surface might give rise to problems, such as acid mine drainage or the failure of waste retaining structures (Klein and Simon, 2006; Bussière, 2007; Rankine and Sivakugan, 2007; Ghirian and Fall, 2013). In past decades, returning mine wastes to subsurface voids emerged as an alternative solution to resolving the adverse impacts associated with underground mining. Cemented tailings backfill (CTB) is one of the most popular backfilling strategies, and it has been used extensively around the world due to the superior environmental, mechanical, and economic benefits it provides, as discussed in Chapter 1. However, the stability of the backfill systems is strongly affected by the blasting procedures as routines in contemporary mining.

To better understand how CTB behaves under blast loading, a review of the theoretical and technical background is provided in this chapter. Specifically, background information of typical mining methods that involve backfilling as well as current CTB technology is briefly presented in Sections 2.2 and 2.3. Subsequently, the stability issues of backfill systems associated with mine blasting are discussed in Section 2.4. Then, as CTB represents a typical kind of porous medium, the fundamentals of blast wave propagation in these media are provided in Section 2.5. Finally, since the blast response of CTB is constantly changing due to its evolution under the influence of multiphysics factors in its curing process, a brief summary of these THMC processes occurring in the material is presented in Section 2.6.

2.2 Typical methods of mining with backfill

1) Sublevel open stoping

This mining method generally involves a large stope size, especially in the vertical dimension, to promote mining efficiency. Therefore, sublevel open stoping is more feasible for orebodies with steep dip and regular boundaries as well as stable host rock. The orebody is divided into separated stopes, and pillars are set between stopes to support the roof and hanging wall. The ore slices are blasted in a panel retreating away from working end of the drift in a left-to-right manner. The successive blasts will use the open space from previous blasts to expand into (Hustrulid, 1982). Then, the blasted ore of primary stopes is recovered at drawpoints constructed at the bottom of large open stopes, and subsequently the cavities are backfilled by uncemented waste rock, sand or tailings. To enable the extraction of the remaining ore pillars of secondary stopes, cemented tailings backfill can be used if the practice is economically justified (Atlascopco, 2007). The layout of sublevel open stoping is shown in Figure 2.1.

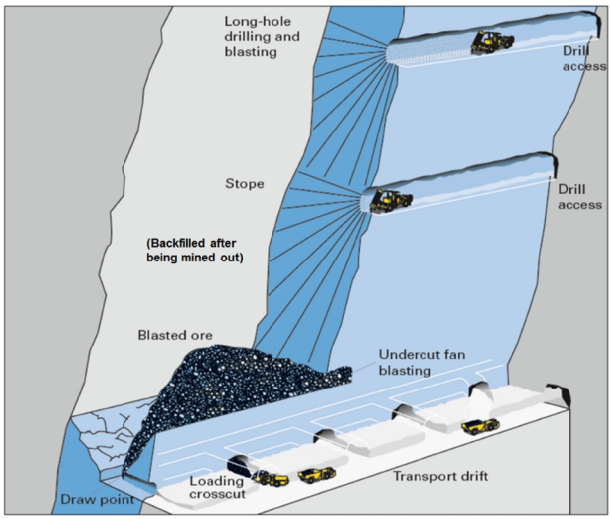

Figure 2.1 Layout of sublevel open stoping (Adopted from Atlascopco, 2007)

2) Vertical crater retreat

The prerequisites of ore deposits for this mining method is similar to sublevel open stoping, but vertical crater retreat differs in that the concentrated charges are detonated to excavate the horizontal ore slices from the bottom to the top of the stope upwards. After the blasted ore accumulated drawpoints is removed, each stope is then backfilled with cemented backfill to allow for the extraction of adjacent ore pillars (Hustrulid, 1982; Atlascopco, 2007). The layout of the vertical crater retreat is shown in Figure 2.2.

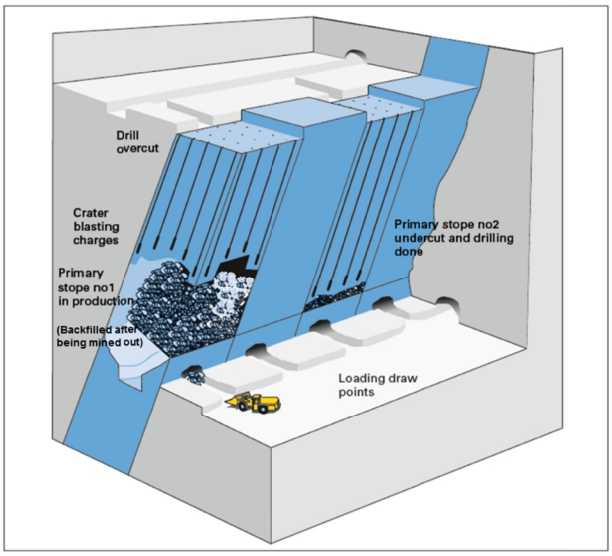

Figure 2.2 Layout of vertical crater retreat (Adopted from Atlascopco, 2007)

3) Cut and fill mining

Cut and fill mining is an ideal method for steeply dipping ore deposits in weak host rock, and it also excavates the orebody in horizontal slices from the bottom upwards. After the blasted ore is cleaned out, backfills are placed in the stope. The fill mass can serve both to support the surrounding walls, and as the platform for mining personnel and equipment to extract the adjacent ore slices. Therefore, this method allows more selective mining than its alternatives as high grade ore can be mined separately while low grade one is left behind in the stope, thus it is preferred for orebodies with irregular geometry and scattered mineralization (Atlascopco, 2007). The layout of cut and fill mining is shown in Figure 2.3.

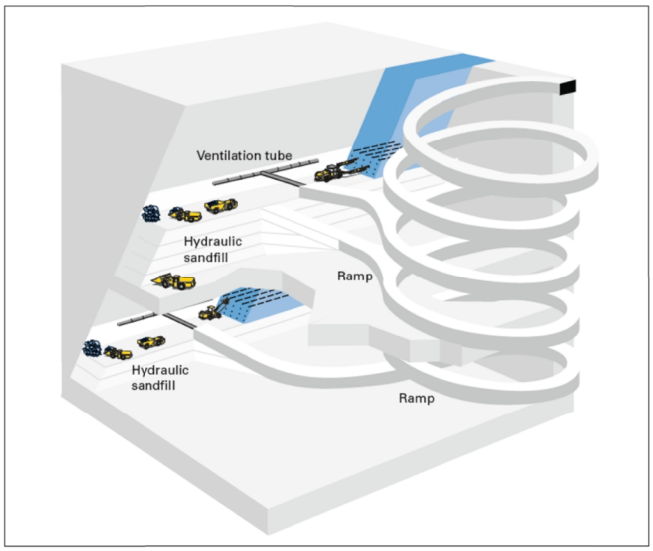

Figure 2.3 Layout of cut and fill mining (Adopted from Atlascopco, 2007)

2.3 Cemented tailings backfill

Mine tailings produced by mineral processing constitute the granular aggregates of cemented tailings backfill (CTB). Then, binders are added to improve the strength of CTB to meet design criteria. As cement consumption can account for up to 80% of backfill costs and 20% of total expenditure for mine operations (Grice, 1998), low cement contents of 3% to 7% are commonly employed, and blast furnace slag and fly ash are often used as alternative binding agents in preparing CTB to reduce cement consumption. After adding a sufficient amount of water, CTB behaves as homogenous slurry, and it is delivered by gravity or pump through pipe networks to a deposition point and is discharged into mined-out stopes from the top. Permeable retaining structures called barricades or bulkheads are constructed in the access drives (drawpoints) at the bottom of the stope to resist the horizontal stress imposed by the fill mass. A typical backfilled stope is illustrated in Figure 2.4.

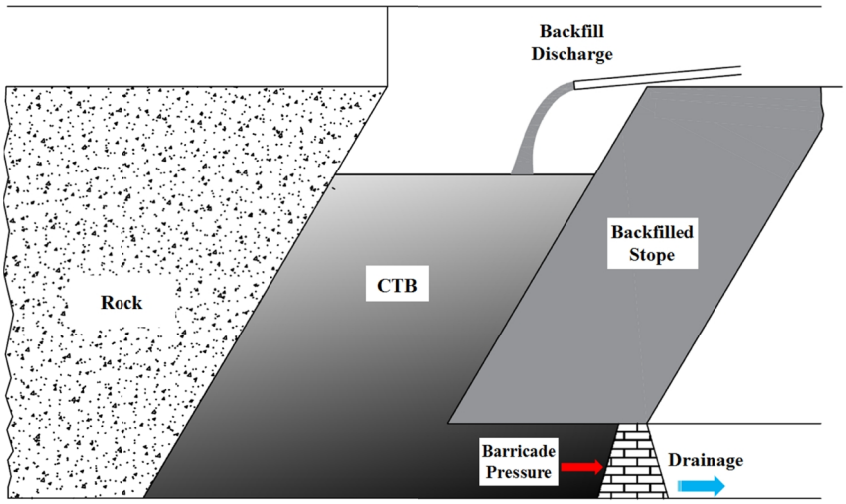

Figure 2.4 Schematic diagram of mining with backfill (Modified after Cui, 2017)

The design of CTB systems depends on two main factors as a trade-off between efficiency and safety. Firstly, backfilling process should be as quick as possible without compromising the containment barricade. Secondly, the backfill should develop sufficient strength to become self-supporting and facilitate removal of adjacent rock, which requires a turn-around time (downtime) that allows curing between successive stope development (ore blasting and collection) and backfilling cycles (Thompson et al., 2012; Witteman, 2013). Therefore, various design strategies for backfilling are used in mine operations to achieve the balance between stability of CTB systems and mining productivity.

There are two main types of cemented tailings backfill, namely, cemented paste backfill (CPB) and cemented hydraulic backfill (CHB), and they differ from each other primarily in the gradation and fraction of tailings aggregates. CPB is prepared in plants by dewatered full-stream (unclassified) mine tailings, and the solid content in CPB typically ranges between 75% and 85% by weight, while CHB is composed of classified tailings with less fine particles and its solid content lies between 60% and 70%. Generally, CPB would exhibit better mechanical and operational performance compared to CHB. Therefore, CPB is more popular in open stoping mining with higher and greater exposures, while CHB requires longer turn-around cycles and is more practiced for cut and fill mining (Hassani and Archibald, 1998).

Despite its various benefits, the lack of understanding of CTB behaviour has led to conservative design of backfill systems, including unnecessarily high binder content, long turn-around time and large barricade resistance (Witteman, 2013). Moreover, current design criteria

and analytical approaches to CTB and the retaining structures are based on stress equilibrium in quasi-static conditions, while the influence of dynamic loading has not been considered.

2.4 Stability issues of CTB under mine blasts

Development and production blasts are routinely used in contemporary mining operations, including mining with backfill. Development blasts refer to blasts required to access orebodies and transport the minerals after excavation, and production blasts denote blasts applied in mining the ore body (van Gool, 2007). During the extraction of remnant ore pillars separated by backfilled stopes, the backfill structures are gradually exposed and subjected to production blasts. However, the current backfill design only considers minimal compressive strength for the backfill to be stable and standing as an unsupported element on its own weight (Emad et al., 2014). As a result, a number of backfill structure failures caused by blasting have been reported to date, and most of these failures exhibited a wedge shape initiating at the top of the exposed backfill face (Emad, 2013).

Furthermore, the backfill is often prepared with excessive water to enable its transportation to mined-out cavities, and it is then retained by barricades constructed at the bottom of the stope. Therefore, when it is at early age, backfill could exhibit no or weak cementation and is subjected to the risk of liquefaction caused by dynamic loads from mine blasting. When liquefaction happens, the full hydrostatic pressure of the backfill mass exerting on the barricade may breach the retaining structure and flow into the adjacent mine stope (Le Roux, 2004; Saebimoghaddam, 2010). However, current analyses of backfill stress acting on the retaining structures are limited to quasi-static conditions, while the influence of dynamic loading has been ignored (e.g. Mitchell, et al., 1975; Li and Aubertin, 2009). Due to the insufficient understanding of the material behaviour under dynamic loading, addition of a minimum of 1.5% –2% binders in the backfill or developing an unconfined compressive strength of 100 kPa has been adopted as a rule of thumb to eliminate liquefaction (Le Roux, 2004; Atlascopco, 2007). While this approach of empirical nature would lead to overdesign for some backfill systems, it could still possibly be optimistic as the occurrence of liquefaction also depends on the intensity of dynamic loading. This limitation of the lack of rational design and assessment procedures is believed to have contributed to the failures of numerous retaining structures reported in mines (Yumlu and Guresci, 2007; Helinski et al., 2010).

The failures of backfill or retaining structures could lead to significant casualties and ore dilution. Therefore, to ensure mine safety and profitability, knowledge of backfill response under mine blast conditions is urgently required and the design criteria for backfilling, which depend only on quasi-static conditions, should be improved to account for the effect of dynamic loadings.

2.5 Fundamentals of blast wave propagation in porous media

The propagation of blast waves in geomaterials has always been a focus in civil, defense, and mining engineering (e.g. Ivanov, 1967; Dowding and Hryciw, 1986; Wang et al. 2004; Emad et al., 2014). When an explosive is detonated in a blast hole, the chemical reaction generates a gas at an extremely high temperature that exerts pressure on the blast hole walls, and pushes the walls outwards. The explosion sends stress waves through the media, and they expand cylindrically from the blast hole (Henrych, 1979). Fundamental information about these stress waves will be provided in this section.

2.5.1 Characterization of blast-induced waves

Stress or deformation waves represent the basis for evaluating explosion processes taking place in explosives and the surrounding media. In a continuum of solids, the characteristics of an elastic wave are defined in terms of its velocity, which is function of the shear modulus (G), bulk modulus (K), and density (ρ) of the material. The velocities of the elastic compressive wave (c_p) and shear wave (c_s) are expressed as:

$$c_p = \sqrt{\frac{K + \frac{4}{3}G}{r}} \qquad c_s = \sqrt{\frac{G}{r}} \tag{2.1}$$

Blast waves are significantly more difficult to evaluate than elastic waves due primarily to their high amplitude of pressure, which can result in nonlinear volumetric deformation. For a blast shock, its front is a discontinuous jump with a shock velocity U. The initial states of a solid element with velocity u, material density ρ, internal energy E, and pressure P would suddenly change from a non-shock condition to a shock condition with such a discontinuous jump across

the shock front, as depicted in Figure 2.5 below. As a result, there are five unknowns that must be solved by five equations in order to evaluate the wave propagation process (Lee, 2006).

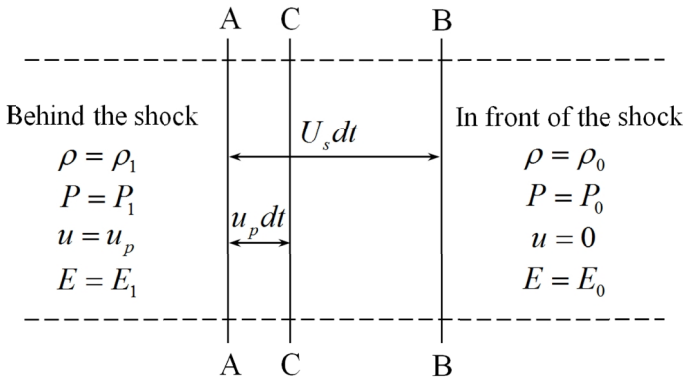

Figure 2.5 Details of plane shock wave propagating in a solid (From Zukas, 2004)

The first three equations are formulated by the conservation of mass, momentum, and energy, respectively (Cooper, 1996; Zukas, 2004):

$$\begin{aligned} & r_0 U_s = r_1 (U_s - u_p) \quad \text{or} \quad V_1 U_s = V_0 (U_s - u_p) \\ & P_1 - P_0 = r_0 U_s u_p \\ & P_1 u_p = \frac{1}{2} r_0 U_s u_p^2 + r_0 U_s \left(E_1 - E_0 \right) \end{aligned} \tag{2.2}$$

where r_0, P_0, V_0 are the density, pressure, and volume of an element in the initial condition (before the shock arrives), r_1, P_1, V_1 corresponds to properties behind the shock front (after the passage of the shock wave), and U_s and u_p are the velocities of the pressure pulse and the material.

Eliminating U_s and u_p in the conservation of energy results in the equation known in the literature as the Rankine-Hugoniot (jump) relation:

$$E_1 - E_0 = \frac{1}{2}\left(\frac{1}{r_0} - \frac{1}{r_1} \right)\left(P_1 + P_0 \right) = \frac{1}{2}\left(V_0 - V_1 \right)\left(P_1 + P_0 \right) \tag{2.3}$$

The fourth equation required to solve the problem of shock wave propagation is an empirical relationship known as the Hugoniot. The Hugoniot is the experimentally determined curve relating to any two state variables, such as shock velocity, pressure, particle velocity, or the specific volume of the material, and common combinations are *U-u*, *P-V*, and *P-u* curves.

These relations form the basis of an equation of state (EOS), which quantifies the material behaviour for a given set of initial conditions (Zukas, 2004).

The fifth or final equation required to evaluate the wave propagation can be defined by applying case-specific constraints to the shock problem, such as boundary conditions, constitutive laws, and thermodynamic conditions.

2.5.2 Classification of waves by type of stress

Stress waves can be distinguished between normal (pressure) and tangential (shear) waves. The former cause a change in the mass element volume, thus they are also called longitudinal waves or P-waves, while the latter cause a change in shape and thus are also called distortion wave or S-waves. In addition to the body waves discussed above, waves can also propagate along the interface of two media, namely surface waves. In geological media, the surface can be the interface of individual layers, such as rock and soil, or that free surface between the earth and air. According to Charlie et al. (1996), the longitudinal wave dominates in the vicinity of an explosion for a buried charge, and this type of compressive wave with high pressure will be the focus of this study. The different types of stress waves generated by a buried explosion are illustrated in Figure 2.6.

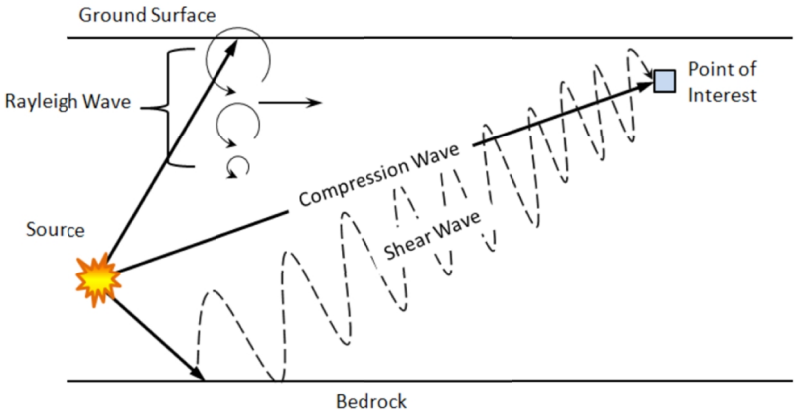

Figure 2.6 General wave paths from an explosion (From Eller, 2010)

2.5.3 Classification of waves by the magnitude of stress

When a contained explosive charge is detonated, the rapid release of energy from the buried explosives produces a compression wave radiating away from the explosion source, and it

produces intense radial compression in the surrounding medium. The compressional stress wave carries most of the energy (Charlie et al., 1996), and its propagation in porous media is briefly presented in this section.

The types of waves propagating in a material depend on the relationship between material strength and the magnitude of the load. The relationship has the general form shown in Figure 2.7(a) for liquids, gases, or water-bearing soil, and in Figure 2.7(b) for solids.

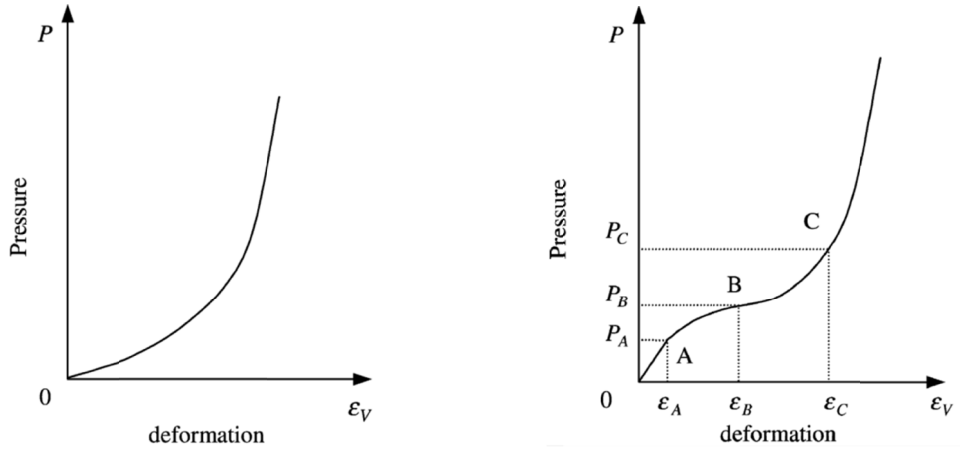

(a) Relationship for liquids, gases, etc. (b) Relationship for solids

Figure 2.7 Relationship between pressure and volume deformation (Adopted from Henrych, 1979)

As can be observed in Figure 2.7(a) for fluid-like materials, the slope of pressure increases with deformation, thus stress waves with higher pressures can propagate faster than lower-pressure waves (Henrych, 1979).

In Figure 2.7(b) for solids, the deformation changes linearly when the pressure exists in the range of $0<P<P_A$, which is referred to as the elastic range. The velocity of a wave propagating within this range is constant and equal to the velocity of sound. Within the window of $P_A < P < P_B$, large displacements of particles occur in the medium. The material is gradually compressed and ceases to transfer shear stresses, and it starts to behave as a liquid. At point B, the shear bonds in the material are completely lost, the particles of the original medium are rearranged, and it changes into a material that sustains only hydrostatic pressure. In this region, the slope of pressure decreases with a rise in pressure, thus the higher pressure will propagate at a lower speed than stress waves with lower amplitudes. This range is known as the plastic range. At

pressure within the range of $P_B < P < P_C$, the medium will behave as a liquid with no transfer of shear stress, and the derivative of pressure increases with deformation. However, the wave velocity in this range is lower than that in the elastic range, and higher pressure is associated with faster propagation than lower-pressure waves. Therefore, the stress waves that fall within this range are termed unstable (subsonic) shock waves. Finally, in the range of pressures higher than P_C, the medium also behaves like a liquid with no transfer of shear stress, and the slope of pressure increases with deformation. Under this condition, higher pressures can propagate faster than the sound and stress waves with lower amplitudes, thus it is called the range of stable (supersonic) shock waves (Henrych, 1979). The stable shock wave prevails in the close vicinity of a detonation. With an increase in distance to the charge, the maximum pressure of the blast wave decreases, and it gradually attenuates into an unstable shock wave, a plastic wave, and finally, into an elastic wave.

2.6 Multiphysics processes and their influences on CTB

The performance of cemented tailings backfill is significantly influenced by complex coupled multiphysics, including thermal (T), hydraulic (H), mechanical (M), and chemical (C) processes of the curing condition (Ghirian and Fall, 2013, 2014). As a result, the quasi-static mechanical behaviour and blast response of CTB are strongly affected by these multiphysics factors (Ghirian and Fall, 2014; Huang et al., 2011; Suazo et al., 2016). To better understand the evolutive behaviour of CTB under blast loading, the influence of THMC processes on CTB and their mutual coupling effects in the curing process are presented in this section (Figure 2.8).

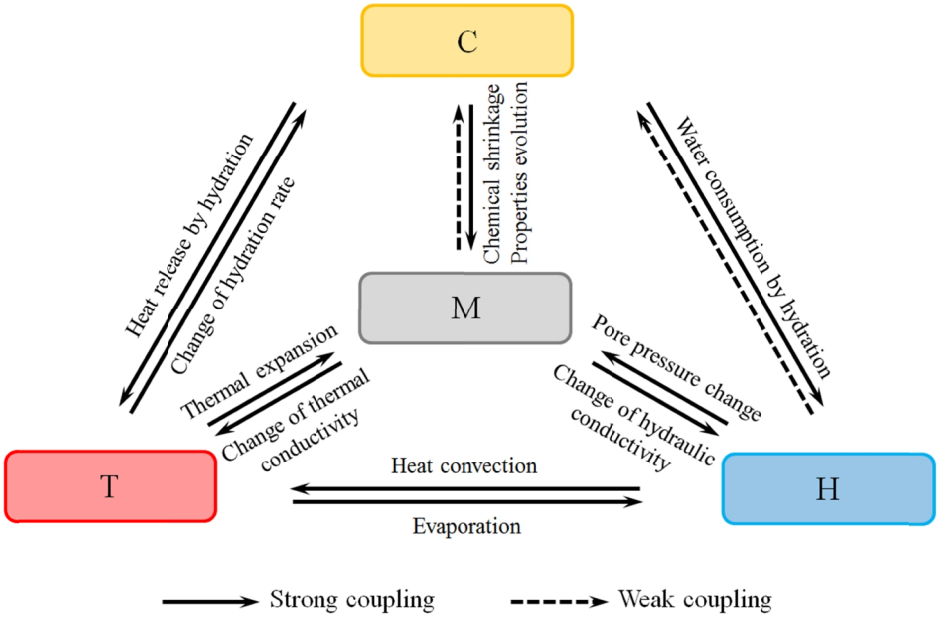

Figure 2.8 Coupled THMC processes in CTB

2.6.1 Chemical process

The chemical process is the main factor that affects the evolution of CTB. When cement interacts with water, the hydration of cement contained in CTB initiates. The progression of the chemical reaction influences CTB properties and behaviour as well as other physics in different mechanisms:

(1) The effect of C on T. The heat released by exothermic binder hydration will affect the temperature distribution in the CTB structure, whose effect on CTB will be elucidated in Section 2.6.3 (Schindler, 2004; Schindler and Folliard, 2005);

(2) The effect of C on H. The binder hydration process consumes interstitial water and generates hydration products which precipitate and refine the flow conducting channels of the porous material. The process will not only reduce the degree of saturation and modify the permeability of CTB, but also induce the development of matric suction (Ghirian and Fall, 2013);

(3) The effect of C on M. The hydration of cement generates three main types of hydration products, namely calcium silicate hydrate (C-S-H), calcium hydroxide (CH), and calcium sulphoaluminate (known as ettringite). The hydration products generated by chemical reactions precipitate and refine the capillary pore space between tailings particles. This would then lead to significant microstructural evolution and consequently contribute to increases in the stiffness and

strength of CTB (Ghirian and Fall, 2013, 2014). However, the mixing water or tailings used in CTB plants may also contain sulfur. The presence of sulfate would strongly inhibit the hydration process at early age, and could also deteriorate CTB at advanced age due to the generation of highly expansive products (Benzaazoua and Belem 2000; Fall and Benzaazoua, 2005). In addition, since the volume of the hydration products is less than the combined volume of the reacted cement and water, binder hydration will result in mechanical deformation through chemical shrinkage (Cui and Fall, 2015).

2.6.2 Hydraulic process

The main hydraulic processes affecting the performance of CTB comprise self-desiccation, surface evaporation, and water seepage within the material, via surrounding or adjacent rocks, as well as due to drainage through barricades (Helinski et al., 2010; Abdul-Hussain and Fall, 2011; Ghirian and Fall, 2013). The hydraulic processes can affect other physics in CTB through the following mechanisms:

(1) The effect of H on T. The migration of pore fluids will cause variations in the temperature distribution in CTB by convection, and also by changes in thermal conductivity due to varied levels of saturation;

(2) The effect of H on M. The loss of water can result in the development of matric suction within the backfill mass, which will influence the effective stress distribution, and thus in turn modify the mechanical performance of CTB;

(3) The effect of H on C. The unhydrated binder can be coated with precipitated hydration products. This will inhibit water from diffusing inward to reach the unhydrated binder cores, thus consequently decreasing the hydration rate (Cui and Fall, 2015).

2.6.3 Thermal process

The main source of heat in CTB systems is the heat generated by binder hydration. Its temperature distribution is also affected by the heat convection due to fluid migration as well as thermal exchange with surrounding rock through conduction. The variation in the temperature within a CTB structure can also have tremendous effects on other physics as follows:

(1) The effect of T on H. The increased temperature will promote the loss of water in CTB through surface evaporation (Ghirian and Fall, 2013). Besides, the variation of temperature will also modify the fluid flow fields due to the sensitivity of fluid properties to temperature (e.g. dynamic viscosity).

(2) The effect of T on M. The temperature change in CTB can also lead to mechanical deformations through thermal expansion (Cui and Fall, 2015).

(3) The effect of T on C. The rate of hydration is temperature-dependent, and the increase in temperature is generally associated with a faster hydration rate (Schindler, 2004; Schindler and Folliard, 2005).

2.6.4 Mechanical process

Field CTB is subjected to self-weight, confining pressure from the surrounding rock mass, and thermal stress, etc. Thus, CTB could experience deformation through elastoplastic strain, thermal expansion, and chemical shrinkage in the quasi-static curing process. The strength of CTB can also be improved by a higher curing pressure due to the resulting denser material structure (Roy et al., 1972). The mechanical processes also affect other physics predominately through variations in porosity due to resultant volumetric deformation:

(1) The effect of M on T. According to Côté and Konrad (2005), the thermal conductivity of porous media is influenced by the porosity, thus the heat transfer in CTB is dependent on the mechanical processes.

(2) The effect of M on H. As the hydraulic conductivity of porous media is a measure of its space available for fluid flow (i.e. porosity), the fluid migration in CTB is also affected by the volumetric deformation.

(3) The effect of M on C. A large curing pressure can increase the accessibility of cement grains to the water required for hydration, thus increasing the rate of hydration (Zhou and Beaudoin, 2003; Lin and Meyer, 2009; Ghirian and Fall, 2015). However, this effect is generally not considered due to the relatively low stress levels in CTB structures.

As can be concluded, the performance of CTB, including the mechanical performance of the primary concern in practice, is evolving in a highly coupled manner due to the changing THMC conditions in the curing process. Furthermore, the mechanical performance of CTB is also strongly influenced by its recipe as the initial condition of the material. To be more specific,

the initial amount of water with respect to the binder in CTB (water-to-cement ratio, *w/c*) has a significant impact on its mechanical performance, and a lower *w/c* ratio is associated with higher CTB strength and faster strength gain (Boumiz et al., 1996; Bentz et al., 2009). In addition, the increase in the dosage of the binder for preparing CTB would lead to the generation of more hydration products, and its mechanical performance would be improved (Zelic et al., 2004).

Therefore, these multiphysics processes occurring in the service life of CTB and its initial conditions should be sufficiently considered in order to rationally characterize its quasi-static behaviour as well as dynamic response.

2.7 Conclusions

Theoretical and technical background information on tailings backfill technology in underground mining is summarized in this chapter. The literature review also reveals that, despite the fact that blasting is routinely utilized in mining operations, the current studies and design criteria have not considered the influence of blast loading on the stability of CTB and its retaining structures. In addition, the performance of CTB is constantly evolving due to multiphysics factors in the curing process. Therefore, to reliably evaluate its dynamic behaviour, multiphysics modelling of the blast response of CTB is conducted in this PhD research.

2.8 References

Abdul–Hussain N, Fall M. Thermo–hydro–mechanical behaviour of sodium silicate–cemented paste tailings in column experiments. Tunnelling and Underground Space Technology 2012; 29:85–93.

Atlas Copco. Mining methods in underground mining. Second edition. 2007.

Benzaazoua M, Belem T. Optimization of sulfurous paste backfill mixtures for increased long-term strength and durability. Waste Treatment and Environmental Impact in the Mining Industry 2000; 1(1): 343–352.

Bentz DP, Peltz MA, Winpigler J. Early-age properties of cement-based materials. II: Influence of water-to-cement ratio. Journal of Materials in Civil Engineering 2009; 21: 512-517.

Boumiz A, Vernet C, Tenoudji FC. Mechanical properties of cement pastes and mortars at early ages evolution with time and degree of hydration." Advanced Cement Based Materials 1996; 3: 94–106.

Bussière B. Colloquium 2004: hydrogeotechnical properties of hard rock tailings from metal mines and emerging geoenvironmental disposal approaches. Canadian Geotechnical Journal 2007; 44(9):1019–1052.

Charlie WA, Veyera GE, and Durnford DS, et al. Porewater pressure increases in soil and rock from underground chemical and nuclear explosions. Engineering Geology 1996; 43(4): 225-236.

Cooper PW . Explosives engineering. Wiley Inc., New York, N.Y., USA. 1996.

Côté J, Konrad JM. A generalized thermal conductivity model for soils and construction materials. Canadian Geotechnical Journal 2005; 42: 443–458.

Cui L. Multiphysics modeling and simulation of the behaviour of cemented tailings backfill. Ph.D. Thesis. University of Ottawa, Ottawa, Canada, 2017.

Cui L, Fall M. A coupled thermo–hydro-mechanical–chemical model for underground cemented tailings backfill. Tunnelling and Underground Space Technology 2015; 50:396–414.

Doherty JP, Hasan A, Suazo GH, Fourie A. Investigation of some controllable factors that impact the stress state in cemented paste backfill. Canadian Geotechnical Journal 2015;12:1–12.

Dowding CH, Hryciw RD. A laboratory study of blast densification of saturated sand. Journal of Geotechnical Engineering 1986; 112(2):187-99.

Eller JM. Predicting pore pressure response in in-situ liquefaction studies using controlled blasting. PhD thesis. Oregon State University, Corvallis, USA, 2010.

Emad MZ. Dynamic performance of femented rockfill under blast-Induced vibrations. Ph.D. Thesis. McGill University, Montreal, Canada, 2013.

Emad MZ, Mitri H, Kelly C. Effect of blast–induced vibrations on fill failure in vertical block mining with delayed backfill. Canadian Geotechnical Journal 2014; 51,975–983.

Fall M, Benzaazoua M. Modeling the effect of sulphate on strength development of paste backfill and binder mixture optimization. Cement and Concrete Research 2005; 35(2): 301–314.

Ghirian A, Fall M. Coupled thermo–hydro–mechanical–chemical behaviour of cemented paste backfill in column experiments. Part I: Physical, hydraulic and thermal processes and characteristics. Engineering Geology 2013; 164:195–207.

Ghirian A, Fall M. Coupled thermo–hydro–mechanical–chemical behaviour of cemented paste backfill in column experiments. Part II : Mechanical, chemical and microstructural processes and characteristics. Engineering Geology 2014; 170:11–23.

Ghirian A, Fall M. Coupled behaviour of cemented paste backfill at early ages. Geotechnical Geological Engineering 2015; 33:1141–1166.

Grice T. Underground mining with backfill. Proceedings of the 2nd Annual Summit-Mine Tailings Disposal Systems Australian 1998, 234-239.

Hassani F, Archibald J. Mine Backfill. Canadian Institute of Mining, Metallurgy, and Petroleum: Montreal, 1998.

Helinski M, Fahey M, Fourie A. Coupled two-dimensional finite element modelling of mine backfilling with cemented tailings. Canadian Geotechnical Journal 2010; 47: 1187–1200.

Henrych J. The dynamics of explosion and its use. Elsevier, New York, USA, 1979.

Huang S, Xia K, Qiao L. Dynamic tests of cemented paste backfill: effects of strain rate, curing time, and cement content on compressive strength. Journal of Material Science 2011; 46(15):5165–5170.

Hustrulid WA. Underground Mining Methods Handbook. Society of Mining Engineers: New York, 1982.

Ivanov PL. Compaction of noncohesive soils by explosions. US Department of the Interior, Bureau of Reclamation and Natrual Science Foundation, Washington, DC, 1967.

Klein K, Simon D. Effect of specimen composition on the strength development in cemented paste backfill. Canadian Geotechnical Journal 2006; 43:310–324.
Lee WY. Numerical modeling of blast induced liquefaction. PhD thesis. Brigham Young University, Provo, USA, 2006.
Le Roux K. In situ properties and liquefaction potential of cemented paste backfill. Ph.D. Thesis. University of Toronto, Toronto, Canada, 2004.
Li L, Aubertin M. Horizontal pressure on baerricades for backfilled stopes. Part I: Fully drained conditions. Canadian Geotechnical Journal 2009; 46: 37-46.
Lin F, Meyer C. Hydration kinetics modeling of Portland cement considering the effects of curing temperature and applied pressure. Cement and Concrete Research 2009; 39: 255-265.
Mitchell RJ, Smith JD, Libby DJ. Bulkhead pressures due to cemented hydraulic mine backfills. Canadian Geotechnical Journal 1975; 12:362-371.
Nasir O, Fall M. Coupling binder hydration, temperature and compressive strength development of underground cemented paste backfill at early ages. Tunnelling and Underground Space Technology 2010; 25(1):9–20.
Rankine RM, Sivakugan N, 2007. Geotechnical properties of cemented paste backfill from Cannington Mine, Australia. Geotechnical and Geological Engineering 25, 383-393.
Saebimoghaddam A. Liquefaction of early age cemented paste backfill. Ph.D Thesis. University of Toronto, Toronto, Canada, 2009.
Schindler AK, Folliard KJ. Heat of hydration models for cementitious materials. ACI Material Journal 2005;102(1):24–33.
Schindler AK. Effect of temperature on hydration of cementitious materials. ACI Material Journal 2004; 101(1):72–81.
Suazo G, Fourie A, Doherty J. Experimental investigation of propagation and transmission of compressional stress waves in cemented paste backfill. Journal of Geotechnical and Geoenvironmental Engineering 2016. (Available online).
Thompson BD, Bawden WF, Grabinsky MW. In situ measurements of cemented paste backfill at the Cayeli Mine. Canadian Geotechnical Journal 2012;49: 755–772.
van Gool BS. Effects of blasting on the stability of paste fill stopes at Cannington Mine. Ph.D. Thesis. James Cook University, Townville, Australia, 2007.
Witteman ML. Unsaturated flow in hydrating porous media: application to cemented paste backfill. Master Thesis. Carleton University, Ottawa, Canada, 2013.
Yumlu M, Guresci M. Paste backfill bulkhead monitoring–a case study from Inmet's Cayeli mine, Turkey. In Proceedings of the 9th International Symposium in Mining with Backfill, Montréal, Quebec, 2007.
Zelić J, Rušić D, Krstulović R. A mathematical model for prediction of compressive strength in cement–silica fume blends. Cement and Concrete Research 2004; 34(12): 2319–2328.
Zhou Q, Beaudoin JJ. Effect of applied hydrostatic stress on the hydration of Portland cement and C3S. Advanced Cement Research 2003;15: 9-16.

Chapter 3.
Literature Review – Technical Paper 1: State-of-the-Art Modelling of Soil Behaviour under Blast Loading

(Submitted)

Gongda Lu, Mamadou Fall

Abstract:

A comprehensive literature review has been carried out on existing models that characterize soil response under the impact of blast shock waves. Various models in the literature are reviewed and discussed in terms of their equations of state that account for the effect of high pressure, failure models that control the yield behaviour, and strength models that represent the effect of high strain-rates, along with a comparison of their advantages and limitations. Then, the application of different soil models to blast-induced liquefaction is elucidated and compared. Consequently, this review provides a comprehensive understanding of the fundamental and unique aspects of modelling soil response subjected to such transient impulsive loading on the grounds of increasing global interest in blast response of soils.

KEY WORDS**:** review; soil; blast; equation of state; constitutive model; liquefaction

3.1 Introduction

The issue of blast wave-soil interactions is an important subject for civil as well as defense engineering (e.g., Ivanov, 1967; Dowding and Hryciw, 1986; Wang and Lu, 2003; Wang et al., 2004a, 2004b, 2008, 2011; Lu et al., 2005; Feldgun et al., 2008a, 2008b, 2011, 2014). Over the decades, these problems have been conventionally addressed with the development of empirical relationships, and extensive experiments have been undertaken for particular types of soils at given sites (e.g. Ivanov, 1967; Henrych, 1979; Drake and Little, 1983; Bretz, 1990; Charlie et al., 1998, 2013; Ashford et al., 2004; Al-Qasimi et al., 2005; Leong et al., 2007; Kumar et al., 2014). Despite the substantial amount of time and financial costs incurred as well as the safety issues at stake, the test results are site-specific and problematic in terms of their applicability to different cases (Wang et al. 2004a, 2004b). In recent years, there has been growing interest in this area, which has led to the rational modelling of such behaviour of soils. In addition to the benefit of overcoming related costs and safety issues, the trend of using modelling has also brought about more salient insights into the problems, and helped to provide a more comprehensive appreciation of blast wave-soil interactions. This paper aims to summarize the modelling work on blast response of soils during past decades, and provide the main fundamental aspects of constitutive modelling for soil behaviours under blast loading. By presenting critical examination of the advantages and limitations of different available solutions, the comprehensive review can thus act as a reference for framing an appropriate model to address specific problems that involve blast events.

The analysis of soil response under blast loading is different from those that are found in the general concepts of soil mechanics or soil dynamics. In the latter, it has been assumed that solid particles are rigid and pore fluid incompressible in accordance with the effective stress principle. Later, Biot developed the theory of poroelasticity (Biot theory) in which both the solid grains and porous skeleton were assumed to be elastic, and the pore fluid flowing in interconnected voids is also compressible through complex coupling mechanisms, while the deformation of the system has been assumed infinitesimal (Biot, 1956a, 1956b, 1962a, 1962b). These assumptions on the compressibility of phase components were also adopted later in the generalized Biot's theory for nonlinear material behaviour, whilst the fluid-solid interactions have been generally simplified by neglecting the relative accelerations of the fluid phases with respect to the solid phase (for e.g., Ghaboussi and Kim, 1984; Zienkiewicz and Shiomi, 1984; Zienkiewicz et al., 1990a, 1990b; Li

and Zienkiewicz, 1992; Akiyoshi et al., 1993; Li et al., 1999; Schrefler and Scotta, 2001; Zhang et al., 2001; Khoei et al., 2004; Khoei and Mohammadnejad, 2011). However, in the course of a blast event, the effective stress approach might be no longer valid (Wang et al., 2004a; An et al., 2011). This is because solid particles will be compressible in this condition, and the trapped fluid phase(s) will simultaneously deform with the soil skeleton in a highly nonlinear manner, thus providing additional resistance which could possibly be even more significant than that of the matrix for the soil when subjected to blast loading with high amplitude. This can be due to the hypothesis that interstitial fluids with even higher stiffness are not able to drain during blast loading (Wang et al., 2004a; Grujicic et al., 2008a; An et al., 2011), and thus Biot theories that incorporate fluid flow are also generally not used in the modelling of blasting. Furthermore, under transient blast loading, the effects of high strain-rates should be considered as a crucial factor on the stiffness, strength and other mechanical behaviours of the soil (Casagrande and Shannon, 1948; Whitman, 1970; Jackson et al., 1980; Prapaharan et al., 1989; Yamamuro and Lade, 1993; Bolton et al., 1994; Semblat et al., 1999; Omidvar et al., 2012; etc.).

Therefore, the greatest challenge in modelling soil response under blast load conditions, compared with general dynamic problems, is developing a material model with high fidelity to characterize the response of such materials under high pressure as well as high strain-rates. To solve such transient nonlinear dynamic problems, Grujicic et al. (2008a) suggested that a complete formulation should include the following: an appropriate equation of state (EOS) which is employed to account for the effect of high pressure on soil components during blast loading, a realistic failure model to delineate the yield behaviour, as well as a strength model to incorporate the effects of a high strain rate. A variety of soil models on blast loading are available in the literature to date with different levels of advancement (e.g., Murray and Lewis, 1995; Wang et al., 2003, 2004a, 2004b, 2008; Lewis, 2004; Grujicic et al., 2006, 2008a, 2008b; Murray, 2007; Tong and Tuan, 2007; Feldgun et al., 2008a, 2008b, 2011, 2013; Karinsi et al., 2009a, 2009b; An et al., 2011; Higgins et al., 2013), and they fully or at least partially include the three aforementioned components of having an appropriate EOS, and failure and strength models. The models found in such related research works will be evaluated against these three components in this study, along with a comparison of their advantages and limitations. Following that, the application of current soil models to liquefaction induced by blasting will be summarized and discussed. It is found in the study that despite the significant advancement in rational modelling,

not all models currently used for blast response of soils have sufficiently accounted for its characteristic behaviours under such dynamic condition. Besides, the lack of quantity and diversity of experimental data has been one of the obstacles for development of more advanced models.

3.2 Equation of state for soils

An equation of state (EOS) as a thermodynamic equation, characterizes the state of a matter under given physical conditions. In impact engineering, an EOS is usually defined as a semi-empirical relationship between thermodynamic state variables (such as pressure, density or volume, internal energy, etc.) of a material for a given set of initial conditions based on experimental calibration (by using the Hugoniot curve) (Zukas, 2004). Generally, the EOS of matters is independent of the loading path. However, when introduced to soil mechanics, such loading path dependence has been augmented given the complex response of soils in the loading/unloading processes. In the case of modelling explosion in soils, different EOS is used for both the explosives and the soil itself. In this study, only EOS for soils will be discussed in this section of the literature review.

According to Henrych (1979), there are two basic types of deformation that exist in soils: the first is the deformation of the solid skeleton, while the second is the deformation of all soil phases. Their dominance is determined by the constitution of the phase components as well as the magnitude of pressure (or distance from the charge). Specifically, the former is found at low pressures for dry soils, whilst the latter prevails at high pressures and in water-bearing soils. In fact, for water-bearing soils, the inter-particle friction is quite low, thus the second type of deformation is more prevalently found, while the first type of deformation is less important and is significant only at extremely high pressures. Meanwhile, with increasing distance to a charge, the blast waves gradually attenuate and the soil also undergoes less compression. Therefore, the second type of deformation or the deformation of all soil phases is more prevalent in the vicinity of the camouflet, while the first type of deformation, that is, the deformation of the soil skeleton, is more dominant further away from the explosion (Wang and Lu, 2003; Grujicic et al., 2008a).

Given the fact that there is simultaneous deformation in all three constituent phases during blast loading, an applicable material model should include the compressibility of each phase, and be able to reproduce the different types of deformation of soils in the course of the blast event

(Henrych, 1979). In addition, due to the high pressure exerted onto soils, their deformation will no longer be linear, as shown in Figure 3.1. Therefore, EOS for soils under blast loading should incorporate pressure dependence in the soil compressibility. The available EOS in soil models for blast loading will be presented and discussed in this section, and various expressions for variable bulk moduli of soils under compaction are also included as special forms of EOS. It should be noted that although both EOS and bulk modulus characterize the volume-compaction relationship of a material, the associated algorithms are different. To be more specific, the former is used with numerical programs known as *hydrocodes*, and the pressure of each phase is usually expressed in total volumetric strain (or density); whereas for the latter, soil stresses are calculated from elastic strain components which is consistent with conventional mechanics.

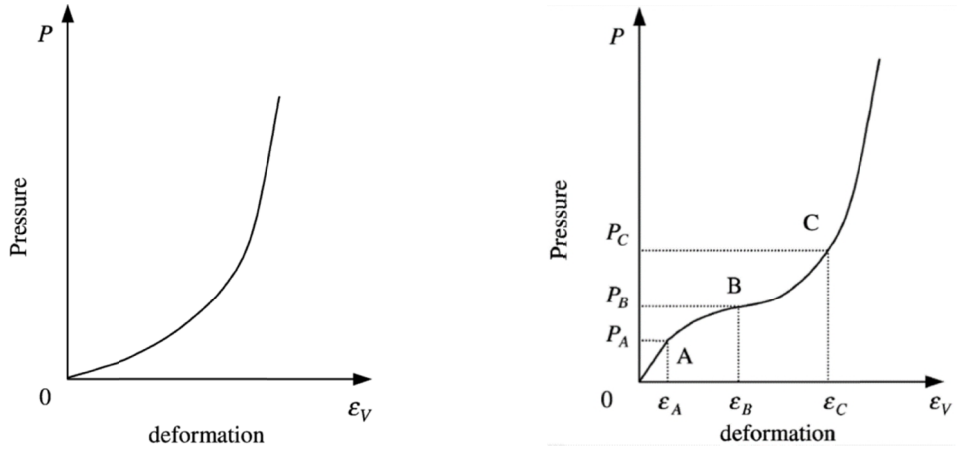

(a) Relationship for liquids, gases, etc. (b) Relationship for solids

Figure 3.1 Relationship between pressure and volumetric deformation of materials (Modified after Henrych, 1979; $0<P<P_A$: elastic wave; $P_A<P<P_B$: plastic wave; $P_B<P<P_C$: unstable shock wave; $P_C<P$: stable shock wave; and e_A, e_B, e_C are corresponding volumetric deformations)

3.2.1 Lyakhov model

One of the most frequently adopted EOS (for e.g., the Kandaur conceptual model in Henrych (1979); Wang and Lu, 2003; Wang et al., 2004a, 2004b, 2005, 2008, 2011; Lu et al., 2005; Feldgun et al. 2008b, 2011, 2014; An et al. 2011) is the Lyakhov model of soil as a three-phase medium (Lyakhov, 1974, 1977a, 1977b), which indicates that soil changes its density in accordance with:

$$\frac{r_0}{r} = a_1(\frac{p}{p_0})^{-1/k_g} + a_2\left[\frac{k_w(p-p_0)}{r_{w0}c_{w0}^2}+1\right]^{-1/k_w} + a_3\left[\frac{k_s(p-p_0)}{r_{s0}c_{s0}^2}+1\right]^{-1/k_s} \quad (3.1)$$

where p is the soil pressure; p_0 is the atmospheric pressure; r_w, r_g, and r_s are the density of the three individual phases and subscript 0 denotes the initial condition; c_{w0}, c_{g0}, c_{s0} and k_w, k_g, k_s denote the initial sound speed and isentropic exponent of the components of the three phases; r is the current density of the soil under pressure p; and a_1, a_2, a_3 are the volumetric content of the soil constituents with $a_1+a_2+a_3=1$. When the pressure is removed, then the density corresponds to the peak of the loading history.

Notably, by considering volumetric compatibility, the Lyakhov model has been modified in the three-phase soil model for blast loading (Wang et al., 2004a), and the pressure borne by each phase can be independently solved with the following EOS:

$$p_g = p_{g0}(\frac{r_g}{r_{g0}})^{k_g} \quad (3.2)$$

$$p_w = p_{w0} + \frac{r_{w0}c_{w0}^2}{k_w}[(\frac{r_w}{r_{w0}})^{k_w} - 1] \quad (3.3)$$

$$p_s = p_{s0} + \frac{r_{s0}c_{s0}^2}{k_s}[(\frac{r_s}{r_{s0}})^{k_s} - 1] \quad (3.4)$$

where p_g, p_w, p_s is the pressure of water, gas and solid in soil, respectively, and subscript 0 indicates the initial state. In addition, the Kandaur conceptual model (found in Henrych, 1979) has been adopted in the three-phase soil model, and the friction as well as bonds between the solid particles have been incorporated as contributions to the pressure borne by the skeleton. This model has been shown to explicitly and realistically represent the deformation of each phase, and thus capture the blast response of soils with different phase compositions. By introducing a damage model to assess the stress carried by bonds between solid particles, the three-phase soil model is able to simulate blast-induced liquefaction, and a detailed discussion will be provided in Section 3.4.2.1.

3.2.2 Mie-Grüneisen EOS

The Mie-Grüneisen EOS is another popular formulation that is found in almost all hydrocodes. For compressed materials, the Mie-Grüneisen EOS provides (LSTC, 2007):

$$p = \frac{r_0 C_0^2 m\{1+[1-(g_0/2)]m-(a_0/2)m^2\}}{\{1-(s_1-1)m-s_2[m^2/(m+1)]-s_3[m^3/(m+1)^2]\}} + (g_0 + a_0 m)E \quad (3.5)$$

where C_0 is the intercept between the shock velocity and particle velocity curves; s_1, s_2, and s_3 are the coefficients of the slope of the Hugoniot curve; g_0 is the Grüneisen parameter, E is the internal energy per unit initial volume; a_0 is the first order volume correction to g_0 ;and $m=(r/r_0)-1=(V_0/V)-1$with V as the volume of the soil element.

If the Hugoniot curve is assumed to be a linear relationship between the shock and particle velocities, the second and higher order terms in Equation (3.5) can be neglected, i.e. the coefficients s_2 and s_3 are taken as zero (Wang et al., 2009), and therefore reduced to:

$$p = \frac{r_0 C_0^2 m\{1+[1-(g_0/2)]m-(a_0/2)m^2\}}{(1+m-sm)^2} + (g_0 + a_0 m)E \quad (3.6)$$

where s is the slope of the shock velocity versus the particle velocity curve.

The Mie-Grüneisen EOS was used in An et al. (2011) to calculate the pressure of the three phase components of soil by using different initial parameters for solid, water, and gas, respectively. The soil density, soil bulk modulus, internal energy as well as phase deformation and composition were then updated at each time step in accordance with both the Mie-Grüneisen and Lyakhov EOS (An et al., 2011), thus allowing the mechanical response of the soil mass during blasting to remain highly coupled. This advanced algorithm and its implementation in ANSYS/LS-DYNA are found in An (2010). Otherwise, either the deformation or the pressure of different phases in a material is assumed to be the same by default in hydrocodes (e.g. ANSYS/LS-DYNA). However, the assumption that deformation for different phases is the same may cause numerical instability with unrealistic strain levels, especially when the constituent phases have distinct compressibilities (LSTC, 2007), while the assumption that the pressure is the same has also been found to be inappropriate in accordance with experimental observations; for e.g., those by Bretz (1990).

3.2.3 Shock-Hugoniot equations

Shock-Hugoniot curves are fitted and used to characterize the pressure-volume relationships of soils in the course of blast loading. According to Karinski et al. (2009b), the initial compaction of a material is defined based on linear elastic response (Segment A_1A in Figure 3.2), which is small and generally disregarded. Then, this is followed by the elastoplastic compaction process (Segment ABCD, also called active loading) with hardening caused by the shrinkage of the internal pore structure as well as denser rearrangement of the grains. In this state, the unloading and reloading processes of soils are characterized by nonlinear elastic behaviour (Segments BB_1 and CC_1), and solely determined by the maximum soil density r^* that has been obtained in the course of active loading. The aforementioned hysteresis will exist until the full compaction density r_{FC} (Point C) is exceeded, thus indicating the complete shrinkage of the internal pores. Hereafter, an increase in pressure will only lead to elastic compaction. There are three different types of loading patterns beyond full compaction, i.e. a linear pattern (CD_3), a polynomial pattern (CD_2), and a full locking pattern (CD_1) which indicates an infinite increase of pressure during compaction when approaching a fixed soil density. Most of the EOS in the literature have adopted the polynomial pattern of the Hugoniot curve which interpolates between the other two (i.e. linear and full locking) curves, while very few have taken the full locking behaviour into account. To include such an effect, the shock-Hugoniot equations in Yankelevsky et al. (2008), Karinski et al. (2009a, 2009b), and Feldgun et al. (2013) are expressed as:

$$\begin{aligned} p_L(r) &= r_0 c_0^2 \frac{e_v}{(1-be_v)^2} \\ p_U(r, r^*) &= p_L(r^*) + c_U^2(r^*)(r - r^*) \\ c_U(r^*) &= c_{FC} + \frac{r_{FC} - r^*}{r_{FC} - r_0}(c_0 - c_{FC}) \end{aligned} \tag{3.7}$$

where p_L and p_U indicate the pressure upon loading and unloading/reloading respectively; e_v the volumetric strain which is determined by $1 - r_0 / r$; $1/b$ the full locking bulk strain; $c_U(r^*)$ the current sound velocity; and c_{FC} the sound velocity at full compaction.

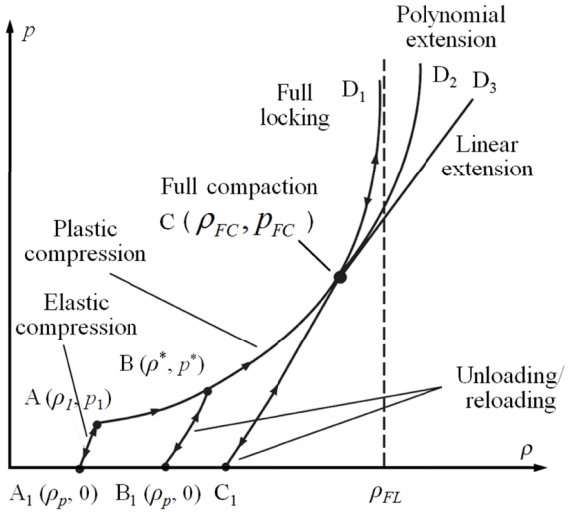

Figure 3.2 General pressure-density relationship of soils (Modified after Karinski et al., 2009b and Feldgun et al., 2013)

Shock-Hugoniot equations have also been adopted in both compaction models and modified compaction models (Laine and Sandvik, 2001; Grujicic et al., 2006, 2008b, 2009, 2010). The compaction model for dry sand found in Laine and Sandvik (2001) incorporates the essential physical basis for soil response under blast shock loading with ease of numerical implementation (Grujicic et al., 2006). The nonlinear pressure-density relationship in their model is given as piecewise linear curves with ten pairs of (p , r) values, and the last pair corresponds to the state of full compaction. Beyond full compaction, the loading becomes elastic and is expressed as:

$$p = c_{FC}^2 (r - r_{FC}) \tag{3.8}$$

Then, the nonlinear elastic unloading and reloading are governed by the following equation:

$$p = c_b^2 (r) \cdot r \tag{3.9}$$

where c_b is the bulk sound speed which is also given as a piecewise linear curve.

Since the original compaction model is only applicable to dry sand, Grujijcic et al. (2006) modified the EOS to include various degrees of saturation. They assumed that the dynamic response of unsaturated sand can be obtained as a linear combination of the corresponding dynamic material behaviours for dry and saturated sands, and the Hugoniot curve for saturated sand was also a piecewise linear curve of (p , r) values. This model was then extended to sandy gravel (Grujicic et al., 2008b), clayey sand (Grujicic et al., 2009), and sandy clay (Grujicic et al.,

2010) with a similar strategy of mixture to account for the contribution of secondary soil constituents and the role of moisture content.

3.2.4 Material Type 147 (FHWA model) in LS-DYNA

A material model was developed by Lewis (2004) to analyze the blast effect in soils and incorporated in the hydrocode LS-DYNA, which is named *MAT_FHWA_SOIL (Material Type 147) and also called a Federal Highway Administration (FHWA) model. The effect of the degree of saturation and volume changes on the stiffness of soil and pore pressure response is considered by using the following expressions:

$$K = \frac{K_i}{1 + K_i D_1 n_{cur}} \tag{3.10}$$

$$p_w = \frac{K_{sk}}{1 + K_{sk} D_2 n_{cur}} e_v \tag{3.11}$$

$$n_{cur} = \max[0, n(1-S) - e_v] \tag{3.12}$$

where K, K_i and K_{sk} are the bulk modulus for soil composites, nonporous soil material and soil without air voids, respectively; D_1 and D_2 the material constants that control the stiffness of the soil skeleton and pore water before the air voids are closed; n the porosity and S the degree of saturation, i.e. $n(1-S)$ represents the volumetric fraction of the gas phase.

This model was adopted by Lee (2006) and recently by Busch et al. (2016) to simulate the response of soil under blast loading. Lee (2006) showed that the model would underestimate the pore water pressure build-up, and attributed this phenomenon to the lack of dependence of the soil stiffness on water. To improve the performance of the model, Lee (2006) made modifications based on the prototype model, namely a transition technique that takes into consideration the soil stiffness with the compressibility of water and accounted for different magnitudes of pressures. However, a parameter related to the weight of the explosives is included in the expression for soil bulk modulus. In fact, the reason that this FHWA model tends to underestimate pore pressure response is due to the unrealistic dilation as a result of the incorporated failure model, and this will be discussed in detail in Section 3.4.2.2.

3.2.5 Other expressions for pressure-dependent bulk moduli of soils

For better flexibility in data fitting, nonlinear (variable) bulk modulus is used to replace constant modulus, with the general form of $K = K(I_1)$ or $K = K(e_v)$ (e.g., Sandler et al., 1976; Chen and Baladi, 1985; An et al., 2011; Lu and Fall, 2016, 2017). For example, in Chen and Baladi (1985), the bulk modulus is defined as:

$$K = \frac{K_i}{1 - K_1}[1 - K_1 \exp(-K_2 I_1)] \tag{3.13}$$

where K_i is the initial bulk modulus, and K_1, K_2 are the material constants; and I_1 is the first invariant of the stress tensor. More recently, An et al. (2011) derived an expression for bulk modulus by using a Mie-Grüneisen EOS which was also adopted in Lu and Fall (2016, 2017), as follows:

$$K = \frac{r_0 C_0^2 [1 + (1 - \frac{g_0}{2})m - \frac{a_0}{2} m^2][1 + \frac{2m(s-1)}{1+m-sm} + \frac{m(g_0 + a_0 m)}{(1+m)^2}] + r_0 C_0^2 m(1 - \frac{g_0}{2} - a_0 m)}{(1+m-sm)^2} + \left[\frac{(g_0 + a_0 m)^2}{(1+m)^2} + a_0\right] E^v \tag{3.14}$$

Notably, Awad (1990) and Ghassemi et al. (2010) analyzed the response of saturated soil under impulsive loading with the generalized Biot's theory. Based on the seminal work of Biot (1956a, 1956b, 1962a, 1962b), the modelling was extended to describe nonlinear material response, and can also depict the movement of interstitial fluids with Darcy's law. Awad (1990) has taken into account the pressure-dependence in stiffness of soil skeleton by using Equation (3.13), while Ghassemi et al. Ghassemi et al. (2010) used the following expression to account for the effect of the mean effective pressure (P') and relative density (D_r) on the bulk modulus of soil after compaction:

$$K = b' \exp(g D_r) \cdot p_0 (\frac{P'}{p_0})^{0.5} \tag{3.15}$$

where b' and g are the soil constants.

3.2.6 Summary and discussion

The introduction of a nonlinear pressure-volume relationship would enable soil modelling to match stress-strain curves with higher accuracy. Notably, not all of the discussed models have explicitly incorporated pressure-dependent EOS to solve pore water and pore air pressures, and thus they cannot be directly used to assess liquefaction caused by blast loading.

Due to the experimental and empirical nature of EOS, despite its theoretical and physical basis, an important consideration is that an appropriate EOS specifies only a range of pressures encountered in a specific problem, and it is erroneous to extrapolate such an EOS beyond the range from which it is developed (Zukas, 2004). According to Zukas (2004), an EOS fitted through Hugoniot data will produce reasonable results for conditions where the pressure exceeds the material strength by a large margin, but prone to provide poor results in regions where the pressure is of the same order of magnitude. This also confirms the argument that there is no single model that is able to govern the entire range of pressures (Bloom, 2006). Therefore, given the significant attenuation of shock waves with distance, the practice of applying the same EOS for the entire domain of soil may not be appropriate. To account for this concern, An et al. (2011) limited their EOS for soil elements to the vicinity of explosion, while using a soil model without an EOS for blast loadings that were not in the close range, although no general rule is provided to specify such an interface of the two domains.

3.3 Failure and strength models

Soils under the high-amplitude impact of blasting exhibit both hydrodynamic fluid behaviour as well as plastic solid behaviour (Bloom, 2006). Accordingly, the stress tensor in a representative element volume of the soil can be divided into a uniform hydrostatic component p and a deviatoric component s_{ij}. In hydrocodes, when the material is subject to explosive impact, the hydrostatic pressure is generally characterized by using an EOS, while the yield behaviour is governed by a failure model to evaluate the deviatoric stress of the system, and also a strength model to account for the strain-rate effect of impulse loading on the material (Grujicic et al., 2008a). Meanwhile, because the response of soils under transient loading is typically undrained even drainage is properly facilitated (Omidvar et al., 2012), the shear stress resistance provided by water and air in soils is generally neglected due to the absence of their relative movement to the solid phase. Hence, the shear stresses are solely resisted by the soil skeleton, and the deviatoric stress of the soil skeleton is equal to that of the total soil element (Wang et al., 2004a, 2004b; Grujicic et al., 2008a; An et al., 2011). A variety of constitutive relationships have been adopted to build up the failure and strength models for soils under blast loading, e.g. ideal plastic, viscoplastic, plastic cap, viscoplastic cap, and bounding surface plastic models, etc. These

models will be reviewed and recapitulated in this section, and their advantages and limitations will also be compared.

3.3.1 Failure models

3.3.1.1 Drucker-Prager model

The most fundamental failure criterion, *f*, upon which many of the soil models for blast loading are formulated, is either a von Mises or Drucker-Prager failure criterion, as shown in Equation (3.16), respectively:

$$\begin{cases} f = \sqrt{J_2} - k = 0 \\ f = \sqrt{J_2} - a\, I_1 - k = 0 \end{cases} \tag{3.16}$$

where a and k are the material constants related to the frictional and cohesive responses of the material, respectively, and J_2 the second invariant of the stress deviators.

Due to its inability to account for the effect of hydrostatic stress on the shearing resistance of materials, the von Mises yield criterion was modified to incorporate the first invariant of stress tensor by Drucker and Prager (Chen and Baladi, 1985). Then, it was widely adopted in characterizing the failure of geomaterials. For example, in the scope of soil response under blast loading herein, the three-phase soil model (e.g., Wang et al., 2004a) uses the Drucker-Prager yield criterion, but modified by including a strain rate term (addressed later), and strain-softening is augmented with a damage model.

Although the original Drucker-Prager yield criterion works reasonably well at low pressures with relative simplicity, its performance is not satisfactory in high pressure conditions. First of all, it is not reasonable to assume that the yield limit of a material will increase as long as I_1 is increasing. To address this problem, a yield criterion which approximates the Drucker-Prager criterion at low pressures, then acts as a von Mises criterion with asymptotic yield strength at high pressures (Bloom, 2006) was introduced. By using an exponential expression, the smooth transition of this yield function can be achieved, and it is written as (Nelson et al., 1971; Chen and Baladi, 1985):

$$f = \sqrt{J_2} - [A' - C' \exp(-B' I_1)] = 0 \tag{3.17}$$

where A', B' and C' are the material constants to be calibrated. An analogous yield criterion in terms of the smooth transition within the entire pressure spectrum is described in the Lundborg

model (Lundborg, 1968), and it is used in Yankelevsky et al. (2008), Karinski et al. (2009a, 2009b) and Feldgun et al. (2013),, which is expressed as:

$$s_Y(p) = Y_0 + m_Y p / [1 + m_Y p / (Y_{\max} - Y_0)] \tag{3.18}$$

where Y_0 is the shear cohesion, and m_Y the internal friction coefficient which correspond to the cohesion and the internal friction angle, respectively; and Y_{max} is the shear strength when the normal pressure at the surface of the rupture approaches infinity. However, despite that the material will have fixed yield strength at high pressures with this type of model, it may also exhibit only elastic behaviour upon isotropic loading, which is inappropriate in reality.

In addition, if the associated flow rule is adopted, the Drucker-Prager yield criterion cannot be effectively used to control soil dilatancy, i.e. the simulated dilatancy is much greater than that experimentally observed (Merkle and Dass, 1985). One of the most commonly used approaches to address this problem has been the use of the non-associated flow rule. For example, the three-phase soil model (Wang et al., 2004a) used the Drucker-Prager criterion with the non-associated flow rule that adopted a von Mises function as the plastic potential, but this method may lead to the problem of uniqueness of solution (Bloom, 2006a).

3.3.1.2 Mohr-Coulomb criterion

The Mohr-Coulomb yield criterion also considers the influence of hydrostatic stress on the shearing resistance of materials. To account for the influence of the intermediate principal stresses on geomaterials, the Mohr-Coulomb yield criterion in triaxial stress conditions can be written as:

$$f = -\frac{1}{3} I_1 \sin j + K(q)\sqrt{J_2} - c\cos j = 0 \tag{3.19}$$

where c and j are the cohesion and internal friction angle, respectively; q the Lode angle related to the stress state including the third invariant of the stress deviators J_3, and $K(q)$ the function of q in the deviatoric plane. Compared with the Drucker-Prager criterion which is a circular cone in a three-dimensional principal stress space, the Mohr-Coulomb criterion has the shape of a hexagonal pyramid. The resulting sharp vertices (singularities) in the octahedral plane and at the point of intersection with the hydrostatic line would lead to numerical instability.

In the FHWA model developed by Lewis (2004) in LS-DYNA (Material Type 147), the Mohr-Coulomb yield surface is modified to remove singularity at its point of intersection with the pressure axis so that it is convex and smooth, and its shape is also modified to be triangular at low pressure instead of being hexagonal. The expression of the modified Mohr-Coulomb yield criterion for the FHWA model is written as:

$$f = -\frac{1}{3} I_1 \sin j + \sqrt{J_2 K(q)^2 + \bar{m}^2 \sin^2 j} - c \cos j = 0$$
$$K(q) = \frac{4(1-l^2)\cos^2 q + (2l-1)^2}{2(1-l^2)\cos q + (2l-1)[4(1-l^2)\cos^2 q + 5l^2 - 4l]^{1/2}} \tag{3.20}$$

where $\bar{m}$ and l are the material constants. Meanwhile, the strain-hardening algorithm is implemented in the model by defining the internal friction angle as an increment function of the effective plastic strain, and strain-softening is also included by adopting a damage model. The FHWA model has been used in Lee (2006) and Busch et al. (2016). Similar to the Drucker-Prager yield criterion, the Mohr-Coulomb yield criterion also suffers from a similar inadequacy under high pressure and unrealistic dilation as stated in Section 3.3.1.1.

3.3.1.3 Failure criterion of compaction and modified compaction models

The failure behaviour of the compaction model by Laine and Sandvik (2001) as well as its modified versions for sand-based soils by Grujicic et al. (2006, 2009) and gravel-based soils by Grujicic et al. (2008b) as discussed in the previous section, is modelled by specifying a piecewise linear function. The defined yield strength increases with pressure up to a maximum value when it then becomes a constant value. A constant tensile strength is also specified and the material would fracture and lose its ability to support any stress if such a condition is satisfied, but the cracks will close up if the material is subsequently subjected to compression. Despite that these models have taken the contents of the secondary soil constituents and water into account (with the rule of mixture), in fact, they are Drucker-Prager type of models, and thus also suffer from the aforementioned limitations. Furthermore, for clay-based soils, the shear failure has only been considered to depend on the degree of saturation, while its explicit dependence on hydrostatic pressure has been neglected in the modified compaction model (Grujicic et al., 2010).

3.3.1.4 Variable moduli model

The variable moduli model has been used to describe the behaviour of soils under ground shocks (Nelson et al., 1971; Baron et al., 1973; Nelson and Baladi, 1977; Chen and Baladi, 1985; Bloom, 2006). This type of model defines the bulk and shear moduli as a function of the stress and strain invariants in an incremental form:

$$\delta p = K \delta \varepsilon_{kk} \quad \text{and} \quad \delta s_{ij} = 2G \delta e_{ij} \tag{3.21}$$

where e_{ij} is the deviatoric strain, and there is no explicit yield condition. In general, different functions G and K are defined in both the initial loading and subsequent unloading/reloading. In this type of model, the final state of strain not only depends on the final state of stress, but also on the stress path; therefore, no unique stress-strain relations can be defined by using the model (Bloom, 2006).

The variable moduli model provides satisfactory data fitting with relative simplicity in computation. Besides, it is also capable of capturing repeated cycles of loading/unloading with irreversible volume reduction. However, the model is not able to represent the dilatancy in soils, and may fail to satisfy the continuity condition for neutral loading conditions or near neutral loading conditions in shear (Chen and Baladi, 1985).

3.3.1.5 Soil hysteresis and plastic cap model

Volumetric hysteresis is a typical behaviour of soils that is significant in engineering, for example, it is a key mechanism that induces liquefaction of soils during blast loading (Fragaszy and Voss, 1981, 1986). In general, two sources contribute to the hysteresis in soils (Nelson et al., 1971; Bloom, 2006). The first is the yield of the material, which can be represented by the solid line in Figure 3.3 below. The second is from the different pressure-volume relationships upon hydrostatical loading/unloading, which can be expressed by the dashed line in Figure 3.3. Therefore, the employment of a constant bulk modulus or adoption of the same nonlinear EOS for the soil skeleton upon loading/unloading may not be always sufficient to reproduce the soil hysteresis (Nelson et al., 1971; Bloom, 2006). In order to control the amount of irreversible bulk volume compaction, some have used different prescribed bulk moduli during loading/unloading paths for the soil skeleton with a bilinear model (a special variable moduli model, for e.g. Kim and Blouin, 1984), and others have used different pressure-volume relationships to control the hydrostatic loading/unloading processes as discussed in Section 3.2.3 (e.g. Laine and Sandvik,

2001; Karinski et al., 2009b; Feldgun et al., 2013). However, a more advanced method that provides more advantages without causing additional mathematical uncertainties is the application of the plastic cap model (Nelson et al., 1971; Merkle and Dass, 1985; Bloom, 2006; etc.). The plastic cap model has been already widely adopted, for example, in the work of Awad (1990), Gu and Lee (2002) and Ghassemi et al. (2010) to simulate soil behaviour during intensive loading that originates from subsurface explosions or impulsive impact from tamping.

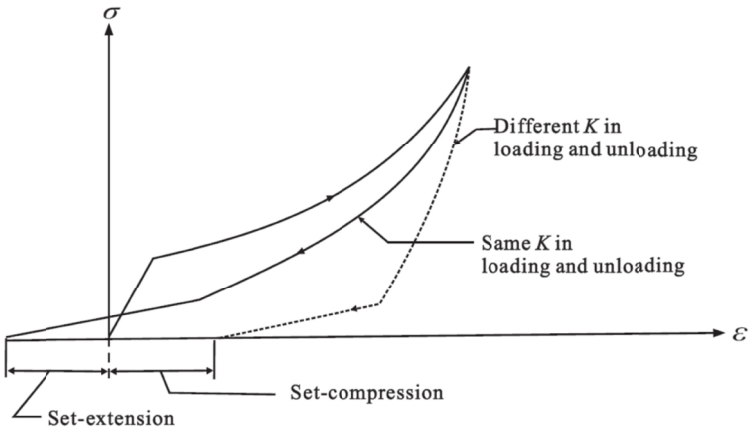

Figure 3.3 Stress vs strain curve from uniaxial testing (Modified after Nelson et al, 1971)

The plastic cap model with two variants was originally proposed by DiMaggio and Sandler (1971) and then generalized by Sandler et al. (1976) and Sandler and Rubin (1979). For isotropic materials, the yield surface characterized by the plastic cap model is in the form of:

$$f(I_1,\sqrt{J_2},k)=0 \tag{3.22}$$

where k is a hardening parameter and function of the plastic volumetric strain history e_{kk}^{p}. In general, the associated flow rule has been used for this type of modelling, and its yield surface is assumed to consist of two parts: a fixed shear failure envelope which serves to limit the maximum shear stresses, and a strain-hardening cap to describe loading processes close to the hydrostatic line (Figure 3.4). Specifically, the shear failure envelope of the yield surface is expressed as:

$$f=h(I_1,\sqrt{J_2})=\sqrt{J_2}-F_1(I_1)=0 \tag{3.23}$$

and the strain-hardening cap surface is denoted by:

$$f = H(I_1, \sqrt{J_2}, k) = \sqrt{J_2} - F_2(I_1, k) = 0 \tag{3.24}$$

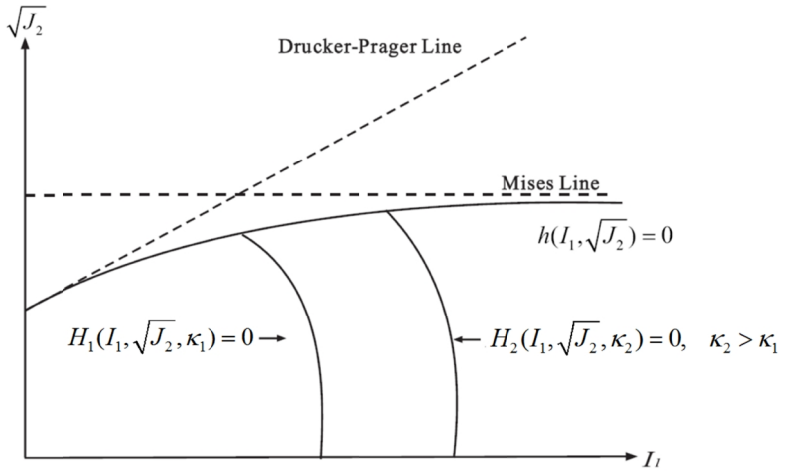

Figure 3.4 Yield surface of the plastic cap model (Modified after Chen and Baladi, 1985)

By adopting a simplified plastic cap model found in Chen and Baladi (1985) as an example, and assuming that the shear yield surface has a linear Drucker-Prager form, then the entire failure envelope can be characterized by the following equations and it is shown in Figure 3.5:

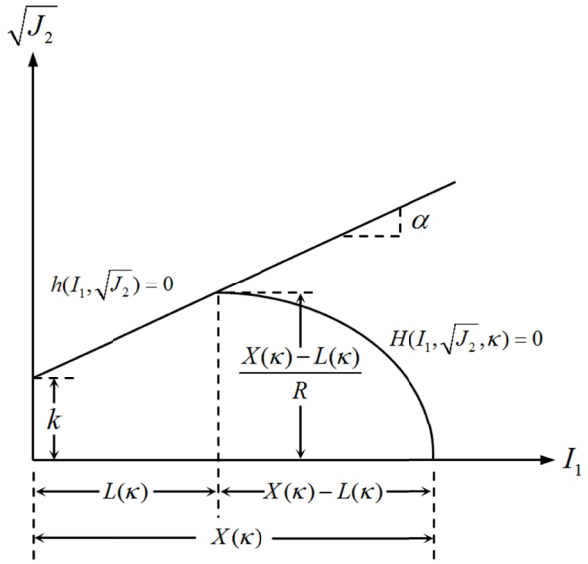

Figure 3.5 Yield surface for a simplified plastic cap model (Adopted from Chen and Baladi, 1985)

$$f=\begin{cases} h(I_1,\sqrt{J_2})=\sqrt{J_2}-a\,I_1-k=0 & \text{for } I_1<L(k) \\ H(I_1,\sqrt{J_2},k)=\sqrt{J_2}-\dfrac{1}{R}\left\{\left[X(k)-L(k)\right]^2-\left[I_1-L(k)\right]^2\right\}^{1/2}=0 & \text{for } I_1\geq L(k) \end{cases} \tag{3.25}$$

where R is the ratio of the major to the minor axis of the elliptical cap; $X(k)$ and $L(k)$ is the abscissa of intersection of the elliptical cap with the hydrostatic loading line (I_1 axis) and shear failure envelope $h(I_1,\sqrt{J_2})$, respectively; and $X(k)$ can be expressed by using a logarithmic hardening law, which was originally proposed for McCormick Ranch sand (DiMaggio and Sandler, 1971) and is written as:

$$X(k)=-(1/D')\cdot\ln\left(1-\frac{e_{kk}^{p}}{W}\right)+X_0 \tag{3.26}$$

where W indicates the maximum volumetric plastic strain of the material, and is suggested to be equal to the volumetric fraction of the gas phase (i.e. $n(1-S)$) (Chen and Baladi, 1985); D' is a shape parameter of the pressure-volume curve; and X_0 is the initial vertex of the hardening cap. These parameters can be determined from isotropic compression tests. Then, $L(k)$ can be determined by enforcing continuity of the entire envelope:

$$k=\frac{X(k)-R\cdot k}{1+R\cdot a} \tag{3.27}$$

and

$$L(k)=\begin{cases} k & k>k_0 \\ k_0 & \text{otherwise} \end{cases} \tag{3.28}$$

where k_0 is the onset of the cap.

According to the formulation, the hardening cap is not fixed in a stress space, and it will expand or contract as the plastic volumetric strain develops. For instance, during initial compaction, the location of the cap ($X(k)$) expands as e_{kk}^{p} grows; then, when the stress state satisfies the shear failure criterion, dilation occurs due to the assumption of associated flow, and the decrease in e_{kk}^{p} would thereby cause the shrinkage and movement of the elliptical cap towards the origin, and the dilatancy would continue until the cap reaches the stress point on the shear yield envelope (DiMaggio and Sandler, 1971; Tu and Lu, 2009). When this occurs, this stress point becomes the point of intersection of the shear and the cap envelopes, and the plastic

strain rate vector is vertical, so any cap movement that would result from further plastic volumetric strain is not possible. In this way, the amount of dilatancy is controlled. Besides, the existence of the cap also facilitates consideration for the yield of geomaterials under large hydrostatic pressures.

Finally, the incremental volumetric response of the soil in this case can be derived as (Chen and Baladi, 1985):

$$\frac{\mathrm{d}I_1}{\mathrm{d}e_v} = \frac{3K}{1+3KD'(W-e_{kk}^p)} = 3\bar{K} \tag{3.29}$$

where $\bar{K}$ is the apparent bulk modulus of the material. As can be identified, the hysteresis in soil will be captured by the second term in the denominator of Equation (3.29). Specifically, at low pressures, the apparent bulk modulus $\bar{K}$ will be lower than K because the denominator is greater than 1; with an increase in pressure, the term e_{kk}^p will approach W, and thus the term $W-e_{kk}^p$ gradually vanishes and $\bar{K}$ becomes comparable to the elastic bulk modulus K (Chen and Baladi, 1985). During unloading and reloading, the soil behaviour is elastic where the apparent bulk modulus is always equal to K. The aforementioned process is illustrated in Figure 3.6. It can be concluded that in addition to its ability to control dilatancy and describe the strain-hardening behaviour of geomaterials, the irreversible bulk compaction or the hysteresis effect can be reasonably captured as well.

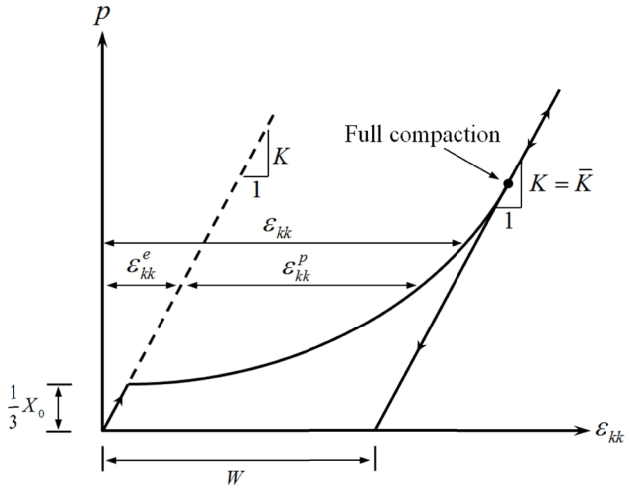

Figure 3.6 Hysteresis effect represented by cap model during compaction

(Modified after Chen and Baladi, 1985 and Murray, 2007. e_{kk}^e is elastic volumetric strain)

Furthermore, it can be observed that the pressure-volume relationship presented by the cap model in Figure 3.6 can indeed represent the EOS of a soil as shown in Figure 3.2. Specifically, in the cap model, when e_{kk}^{p} is less than W, the active loading will be elastoplastic and unloading is elastic which is similar to the curve AC in Figure 3.2. However, after W is exceeded, the loading and unloading behaviour of soil will be elastic, which is comparable to the curve CD after full compaction (Point C) in Figure 3.2.

Since the pressure-volume relationship of soil during blast loading is highly nonlinear, some researchers have enhanced the cap model by introducing variable bulk moduli (which was discussed in Section 3.2.5) to improve the accuracy of simulation compared with experimental observations (e.g. Chen and Baladi, 1985). In the meantime, the cap model has also been integrated with a Mie-Grüneisen EOS in the development of Material 145 in LS-DYNA (Murray and Lewis, 1995) and the soil model of An et al. (2011). It can be observed that, the linear pattern CD_3 in Figure 3.2 after full compaction would in fact correspond to the material response with a constant bulk modulus in the cap model. By introducing nonlinear pressure-volume relationships into the cap model, the polynomial pattern CD_2 after full compaction can be recovered.

A tension cut-off has been augmented in the cap model, for e.g., in Sandler and Rubin (1979), Katona (1984), Simo et al. (1986), Tong and Tuan (2007), and An et al. (2011). Furthermore, the third stress invariant has been included in the cap model of Murray and Lewis (1995) and Murray (2007) to improve its performance in capturing the compression and extension behaviours of geological materials (Schwer, 1994; Schwer and Murray, 1994).

Notably, traditional cap models suffered the numerical difficulties of singular corners at the point of intersection of the shear failure envelope and hardening cap. The former has a positive tangent while the latter has a horizontal slope at the singularity point. If the yield surface is not smooth, the flow direction at the point of intersection of the shear failure surface and the hardening cap is indeterminate. From a modelling point of view, this can lead to much time spent on iteration to locate the aforementioned point of intersection. To resolve this problem, a transition technique has been introduced by Schwer and Murray (1994). After multiplying the elliptical cap function by the shear surface function, the modified failure envelope would take on the same slope at this point of intersection. This model is called the smooth cap model or a

continuous surface cap model. However, in the smooth cap model, the product of a monotonically increasing shear yield function and a decreasing cap expression (with respect to I_1) would imply that the cap size and shape are ambiguous, i.e. the ratio of the major to the minor axis of the elliptical cap (R) will be variant during the hardening process, and it will be different from the R value specified by the modeller. Therefore, the volumetric dilation/compaction of materials may not be effectively controlled by using the smooth cap model.

Meanwhile, by extending the elliptical cap back into the shear failure zone until the point where they can join smoothly, Dolarevic and Ibrahimbegovic (2007) proposed a smoothing technique in which the shape of the elliptical cap is adjusted to have a smooth transition to the prescribed shear envelope. More recently, Lu and Fall (2016) developed an alternative and comparable transition approach. Instead of using a prescribed shear envelope, the elliptical cap is set to be known, while a parabolic curve is used to approximate the shear failure portion and is forced to have a horizontal slope at the point of intersection with the hardening cap to ensure a smooth transition.

3.3.1.6 Bounding surface model

A new category of failure models has been introduced by the emerging application of SANISAND models in the simulation of sand behaviour under impact loading (Higgins et al., 2013; Xu and Zhang, 2015). SANISAND denotes a family of simple anisotropic sand constitutive models under the framework of critical state soil mechanics and bounding surface plasticity (Manzari and Dafalias, 1997; Taiebat and Dafalias, 2008). SANISAND was initially developed to address the behaviour of sand which has a pronounced Bauschinger effect under cyclic and reversed types of loading. Then, the capability of capturing the constant stress ratio (h , defined as p/q) or high pressure loading conditions was supplemented into the prototype model. For the sake of simplicity and consistency in the context of blast loading, only formulations in triaxial stress space and the stress state in compression will be discussed.

In the SANISAND models, the critical state of sand plays an important role, since many features of the models and their performance rely on the distance between the current soil state and the critical state by explicitly using the state parameter $\psi = e - e_c$, where e is the current void ratio and e_c is the current void ratio of the critical state.

Initially, a conical shape yield surface was proposed in the form of (Manzari and Dafalias, 1997):

$$f = |h - a_c| - m = 0 \tag{3.30}$$

where the back-stress ratio a_c is the rotational (kinematic) hardening variable of the yield surface, and represents the slope of the bisector of the yield surface in the p–q space; m is the isotropic hardening variable, and refers to the radius of the circular yield surface in the π-plane of the stress ratio space. Generally, m is assumed to be constant, and a small value is used in order to have a narrow yield surface. According to Taiebat and Dafalias (2008), the small size (small m value) of the conical yield surface and rotation around the origin (kinematic hardening through a_c) are engineered towards the delineation of loading reversals including cyclic loading.

In addition to the yield surface, the SANISAND models incorporate three more different surfaces, namely, the bounding, critical state, and dilatancy surfaces. The layout of the surfaces in the SANISAND models is schematically illustrated in the general stress space in Figure 3.7. These surfaces appear in the triaxial space as lines that emanate from the origin, and they are linked to the back-stress ratio at the critical state a_c^c by using:

$$\begin{aligned} a_c^b &= a_c^c + k_c^b \langle -y \rangle \\ a_c^d &= a_c^c + k_c^d y \end{aligned} \tag{3.31}$$

where a_c^b, a_c^c, a_c^d are the values of the back-stress ratio a_c when the stress ratio h is at the bounding ($h = M_c^b = a_c^b + m$), critical state ($h = M_c^c = a_c^c + m$), and dilatancy ($h = M_c^d = a_c^d + m$) surfaces with subscript c denoting compression (i.e. $h > a_c$), respectively. k_c^b and k_c^d are model parameters.

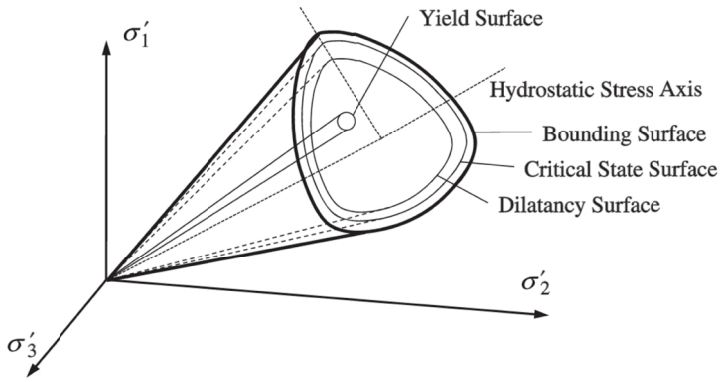

Figure 3.7 Surfaces of SANISAND models in three-dimensional stress space (Adopted from Higgins et al., 2013)

The plastic flow rule in the SANISAND model is defined as:

$$\begin{aligned} d\varepsilon_{ij}^{p} &= \langle L \rangle R_{ij} \\ R_{ij} &= R'_{ij} + \frac{1}{3} D d_{ij} \\ L &= \frac{1}{K_p} \frac{\partial f}{\partial s_{ij}} ds_{ij} \end{aligned} \tag{3.32}$$

where R_{ij} is the direction of the plastic flow which consists of a deviatoric component R'_{ij} and a hydrostatic component $(1/3)Dd_{ij}$, and D is the dilatancy coefficient defined as the ratio of the volumetric to deviatoric plastic strain rate ($D = de_v^p / \left| de_q^p \right|$) and expressed as:

$$D = z A (a_c^d - a_c) \tag{3.33}$$

where A is the dilatancy parameter, z is 1 when $h > a_c$ and -1 when $h < a_c$. It can be concluded that if a_c is inside the dilatancy surface, D will be positive and lead to contractive behaviour; if a_c is outside the dilatancy surface, it will depend on both the distance between a_c and a_c^d and the loading direction via z to determine the material contraction/dilation (Manzari and Dafalias, 1997; Taiebat and Dafalias, 2008), while a_c^d is rotating in the stress-ratio space controlled by the state parameter ψ via Equation (3.31) .

L is the loading index and has been expressed in terms of the plastic modulus K_p whose sign differentiates between hardening (+) and softening (-) responses. K_p can in turn be obtained

with a consistency condition $\dot{f} = 0$ in conjunction with the hardening laws for variables a_c and m.

As discussed, the isotropic hardening (through parameter m) option is generally not activated in applications of the prototype model. As for rotational or kinematic hardening, it is assumed to depend on the distance between the current and the projected stress ratios on the bounding surface in the deviatoric plane as:

$$\dot{a}_c = \langle L \rangle h(a_c^b - a_c) \tag{3.34}$$

where h is a positive scalar-valued function of the state. Then, the plastic modulus K_p can be determined for this case as:

$$K_p = ph(a_c^b - a_c) \tag{3.35}$$

With the formulation, the softening behaviour in the post-failure stage can be represented in addition to capturing the kinematic hardening of sand before the stress state reaches the bounding surface with Equation (3.34). To be more specific, when the stress state reaches the bounding surface ($a_c = a_c^b$), the kinematic hardening process remains momentarily stationary according to Equation (3.34). In the meantime, the bounding surface would contract for a dilatant soil in accordance with Equation (3.31), and then the stress state may be found outside the bounding surface. As the bounding surface continues to contract and converge towards the critical state surface, it then acts as a pole of attraction and a_c would be directed inwards after its peak value and converges to a_c^b from outside (Manzari and Dafalias, 1997).

The SANISAND model has proven to be satisfactory in reproducing the response of sand under cyclic as well as monotonic loadings with varying stress ratios. Notably, the dependence of $\dot{a}_c$ on the distance between a_c and its image a_c^b on the bounding surface is the essence of the bounding surface plasticity (Manzari and Dafalias, 1997). However, the projection rule which relies on the distance between the current and the projected stress states has been only considered in the deviatoric plane. This implies that the model has implicitly assumed that the plastic deformation of sand is predominantly caused by shearing. Only changes in the stress ratio h can lead to relative shearing and rolling of sand grains, which are in turn macroscopically modelled as deviatoric and volumetric plastic strains. Besides, the open conical shape of the yield surface in the stress space would mean that a loading path with a constant

stress ratio that lies inside the yield surface will only result in elastic deformation (Loukidis, 2006; Taiebat and Dafalias, 2008). The said limitations of this prototype model inhibit its fidelity to problems associated with constant stress ratios or high pressure such as blast loading. Those limitations also apply to its extension to the Perzyna type of viscoplasticity (which will be discussed later) in soil model for explosive loads developed by Higgins et al. (2013).

To address the issues of plastic strains in loose sand and high pressure conditions with grain crushing, modifications on a prototype SANISAND model was implemented by Taiebat and Dafalias (2008). Specifically, an end cap was added to the original conical yield surface, and the modified expression for the yield surface is:

$$f = (q - pa_c)^2 - m^2 p^2 \left[1 - (p / p_{c0})^{\bar{n}}\right] = 0 \tag{3.36}$$

where p_{c0} refers to a new isotropic hardening variable and represents the value of p at the tip of the cap ($h = a_c$); and $\bar{n}$ is the model parameter. The layout of the surfaces in this modified SANISAND model is schematically illustrated in the p-q stress space in Figure 3.8.

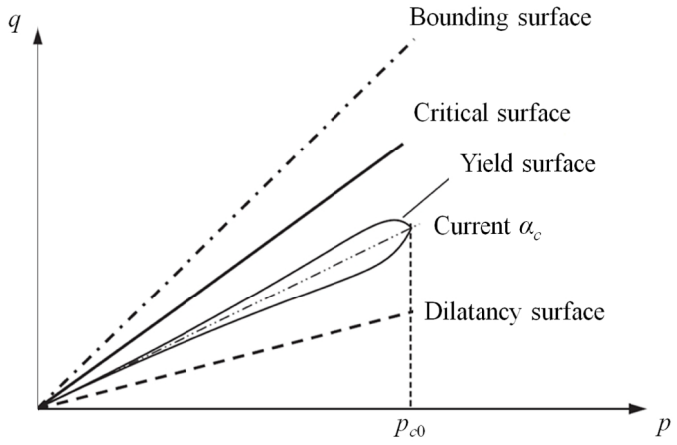

Figure 3.8 Surfaces of capped SANISAND model in p-q stress space (Adopted from Xu and Zhang, 2015)

In addition to the change made to the yield surface, the plastic flow rule has also been revised to accommodate sand behaviours under high pressure loading. Specifically, Taiebat and Dafalias (2008) assumed that the plastic volumetric strain rate consists of two parts. The first part is induced by shearing, and it may be positive or negative controlled by the dilatancy coefficient D, while the second part is caused by constant stress-ratio loading with an increase

in p and it is positive, i.e. contractive, due to pore collapse. They also assumed that only the second contribution of the plastic volumetric strain rate would contribute to isotropic hardening (through p_{c0}). A similar decomposition of the plastic deviatoric strain was carried out for consistency. The deviatoric ($\dot{\varepsilon}_q^p$) and volumetric ($\dot{\varepsilon}_v^p$) parts of the plastic flow are defined as:

$$\begin{aligned}\dot{\varepsilon}_q^p &= \langle L \rangle [z\, r_{\text{ef}} + Xh \exp(-\bar{V} r_{\text{ef}})] \\ \dot{\varepsilon}_v^p &= \langle L \rangle [D r_{\text{ef}} + \exp(-\bar{V} r_{\text{ef}})] \\ r_{\text{ef}} &= |h - a_c| = m[1-(p/p_{c0})^{\bar{n}}]^{1/2}\end{aligned} \tag{3.37}$$

where X is a positive model parameter and $\bar{V}$ is a large number. The above definition of the plastic strain components can ensure a smooth transition between two types of deformation with respect to different states of stress on the yield surface (Taiebat and Dafalias, 2008).

Similarly, hardening laws have to be specified in order to obtain the plastic modulus K_p, and thus in turn, the loading index L. To account for constant stress-ratio loading paths, the kinematic hardening of the capped SANISAND model was modified based on its prototype and expressed as:

$$\dot{a}_c = \langle L \rangle h r_{\text{ef}} (a_c^b - a_c) = \langle L \rangle \bar{a}_c \tag{3.38}$$

Just as $\dot{a}_c$ is dependent on the distance between a_c and its image stress point a_c^b on the bounding surface, the isotropic hardening process also relies on the distance d between the current confining pressure p and its image stress point on the limiting compaction curve (LCC) $p_b = p_r \exp(-1/r_c)$ within the framework of bounding surface plasticity（Taiebat and Dafalias, 2008）. LLC is generally a linear curve in a double logarithmic void ratio-effective stress space as illustrated in Figure 3.9. p_r is the reference stress (at e=1), and r_c is the slope of the linear LCC in the log e-log p space. The distance d is expressed as:

$$d = 1 - \frac{p}{p_b}\left[1 + 2\frac{a_c^{\,2}}{(g a_c^c)^2}\right] \tag{3.39}$$

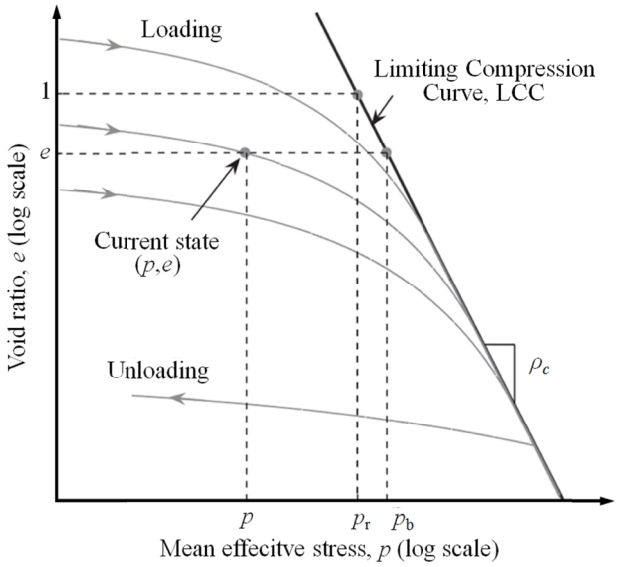

Figure 3.9 Typical limiting compression curve (Adopted from Taiebat and Dafalias, 2008)

Then, the isotropic hardening law is defined as:

$$\dot{p}_{c0} = \langle L \rangle \frac{(1+e)\, p_{c0} \exp(-\bar{V}\varepsilon_{\mathrm{ef}})}{e(r_c - (p_{c0}/p_0)^{1/3}/K_0)(1-(\mathrm{sgn}\, d)|d|^c)} = \langle L \rangle \bar{p}_{c0} \tag{3.40}$$

where K_0 and c are the model parameters, and $\mathrm{sgn}\, d$ means the sign of d.

The dilatancy coefficient D in the capped SANISAND model is consistent with its prototype model. The definition of the relationships among the bounding, critical state, and dilatancy surfaces are modified as:

$$\begin{aligned} a_c^b &= a_c^c \exp(-n^b \psi) \\ a_c^d &= a_c^c \exp(n^d \psi) \end{aligned} \tag{3.41}$$

where n^b and n^d are the model parameters. Finally, the plastic modulus K_p can be obtained as:

$$K_p = 2p(q - a_c p)\bar{a}_c + \frac{\bar{n}}{p_{c0}} m^2 p^2 \left(\frac{p}{p_{c0}}\right)^{\bar{n}} \bar{p}_{c0} \tag{3.42}$$

Recently, the capped SANISAND model was adopted in Xu and Zhang (2015) to simulate the response of sand under impulsive loading, and the strain-rate effect was also taken into account through a phenomenological method (which will be discussed later).

Note the difference in the capability of the SANISAND and traditional cap models in capturing the volumetric hysteresis during the loading/unloading process. As discussed in Section 3.3.1.5, if the stress state is located on the cap portion of the yield surface during initial

compaction, the cap envelope and the associated flow rule will cause volumetric plastic strain in compression. Since the unloading process is elastic regardless of the unloading path (the unloading path will not intersect the yield surface again), there will be irrecoverable bulk volumetric deformation associated with only the initial loading. While for SANISAND models, at initial compaction, plastic volumetric contraction takes place in conjunction with isotropic hardening. However, in the unloading process, due to the narrowness of the yield surface, it is possible that the unloading path may intersect the bottom half of the yield surface ($h < a_c$). Then, inelastic strain will develop, and the irrecoverable volumetric deformation or the hysteresis loop generated upon initial compaction may be altered due to inelastic unloading. In fact, the narrow yield surface with kinematic hardening in the SANISAND models was originally introduced to represent the inelastic unloading/reloading of sand under cyclic and reversed types of loading, while this effect is generally not considered in problems associated with blast loading as discussed in Section 3.2.3.

Finally, although both models have demonstrated sufficient ability in reproducing sand behaviour under high pressure loading conditions, the traditional cap model is considerably easier to use since a minimum of only 6 parameters are required to define the yield envelope; while in contrast, 19 parameters (including 3 generally fixed parameters independently of soil property) are required in the capped SANISAND model. However, the capped SANISAND model excels with its ability to capture the response of sand under cyclic loading, while the traditional cap model does not have such a capability.

3.3.2 Strength models

It has been demonstrated that the strain rate has a significant effect on stiffness, strength and other mechanical performance (such as pore pressure, maximum failure deformation, liquefaction resistance, particle breakage, etc.) of soils during various high-rate impact tests (Casagrande and Shannon, 1948; Whitman, 1970; Jackson et al., 1980; Prapaharan et al., 1989; Omidvar et al., 2012;). This effect has been attributed to the tensile micro-cracking during transient loading. Specifically, more microcracks will be generated from high-strain rate impacts than static loading, and more energy would be demanded to initiate major cracks and induce failure after overcoming the inertial resistance of the material (Cai et al., 2007). Very few efforts have been made to explicitly account for the effect of high strain rates on the stiffness and

strength response of soil during blast loading, and those modelling works will be presented and discussed in this section.

3.3.2.1 Model of Prapaharan et al.

Assuming that the undrained strength of soils increases linearly with the logarithm of the strain rate, a phenomenological method is proposed by Prapaharan et al. (1989) to modify the yield strength of soils under different strain rates as follows:

$$q_u = q_a(1+\bar{b}\log_{10}(\dot{\varepsilon}/\dot{\varepsilon}_{ref})) \tag{3.43}$$

where q_u is the undrained strength at a given strain rate $\dot{\varepsilon}$; q_a the undrained strength at a reference strain rate $\dot{\varepsilon}_{ref}$; and $\bar{b}$ the slope of strength against the logarithm of the strain rate curve. Then, this approach was adopted in the three-phase soil model (e.g. Wang et al., 2004a) by modifying the Drucker-Prager yield criterion for soils under blast shock loading as

$$f = \sqrt{J_2} - (a I_1 - k)(1+\bar{b}\ln\frac{\dot{\varepsilon}_{eff}}{\dot{\varepsilon}_0}) = 0 \tag{3.44}$$

where $\dot{\varepsilon}_{eff}$ is the effective strain rate defined by $\dot{\varepsilon}_{eff} = \sqrt{2\mathrm{d}\dot{\varepsilon}_{ij}\mathrm{d}\dot{\varepsilon}_{ij}/3}$; and $\dot{\varepsilon}_0$ the reference effective strain rate. Later, the effect of high strain rates on both the strength and stiffness of soil has been incorporated in work by Xu and Zhang (2015) with a similar strategy.

3.3.2.2 Modified compaction model

To further improve the performance of the original compaction model (Laine and Sandvik, 2001) in which the strain rate effect was neglected for dry sand, Grujicic et al. (2006) considered strain-rate dependence of the unsaturated soil by interpolating its pressure-density relationship between that of low and high strain rates (with a threshold of 10^{-3} s^{-1} and 10^{5} s^{-1} respectively), which is expressed as:

$$r = r_{\text{high}} + (r_{\text{low}} - r_{\text{high}})\left(\frac{\log\dot{\varepsilon} - \log\dot{\varepsilon}_{\text{high}}}{\log\dot{\varepsilon}_{\text{low}} - \log\dot{\varepsilon}_{\text{high}}}\right) \tag{3.45}$$

where the densities ρ, ρ_{high} and ρ_{low} correspond to the strain rate at $\dot{\varepsilon}$, $\dot{\varepsilon}_{\text{high}}$ and $\dot{\varepsilon}_{\text{low}}$, respectively. However, it was revealed that the formulation can be simplified to be rate independent, if model parameters correspond to higher deformation rates are used (Grujicic et al.,

2006). Therefore, the rate-dependence has not been explicitly incorporated in the series of modified compaction models in Grujicic et al. (2008a, 2008b, etc.).

3.3.2.3 Perzyna viscoplastic model

An alternative approach to consider the rate-effect on soil is to integrate the viscosity with conventional plasticity, i.e. thus resulting in the so-called viscoplasticity. Therefore, the rate-effect on both the yield limit and compressibility of soils can be simultaneously considered with more theoretical soundness (e.g. Katona, 1984; Simo et al., 1986; Tong and Tuan, 2007). The most frequently used viscoplastic constitutive model is the Perzyna (1966) type of viscoplastic model.

As is conventional in mechanics, the total strain rate vector $\dot{\varepsilon}$ can be decomposed into an elastic part $\dot{\varepsilon}^e$ and a viscoplastic part $\dot{\varepsilon}^{vp}$ as

$$\dot{\varepsilon} = \dot{\varepsilon}^e + \dot{\varepsilon}^{vp} \tag{3.46}$$

The elastic strain rate is independent of the viscosity and can be obtained as:

$$\dot{\varepsilon}^e = C^{-1}\dot{\sigma} \tag{3.47}$$

where $\dot{\sigma}$ is the stress rate tensor and C the elastic stiffness matrix.

For the viscoplastic strain rate, the viscoplastic flow rule is generally expressed as:

$$\dot{\varepsilon}^{vp} = h_0 \langle f(f) \rangle \frac{\partial f}{\partial s} \tag{3.48}$$

where h_0 is a material constant termed fluidity parameter; $\langle\ \rangle$ the Macaulay bracket; f the yield function; and $f(f)$ is a dimensionless scaling function, commonly expressed in the form of:

$$f(f) = \left(\frac{f}{f_0}\right)^N \quad \text{or} \quad f(f) = \exp\left(\frac{f}{f_0}\right)^N - 1 \tag{3.49}$$

where N is the exponent and f_0 the normalizing constant with the same unit as f. Associated flow rule is generally employed in this type of model, and the direction of $\dot{\varepsilon}^{vp}$ is given by f and it is in the outward normal direction of the yield surface. Therefore, to incorporate the Perzyna type of viscosity into a plastic formulation, three additional material parameters (h_0, N and f_0) are introduced to the original plastic model, and they can be determined by trial and error (Katona, 1984; Tong and Tuan, 2007). As can be concluded, in the overstress theory of Perzyna for delineating the viscoplastic behaviour of materials, $f(f)$ acts to quantify the overstress, i.e. the

distance between the current viscoplastic stress state and the yield surface. According to Equation (3.48), the material response will be purely elastic when $h_0 \rightarrow 0$, but simply corresponds to inviscid plasticity when $h_0 \rightarrow \infty$.

The Perzyna model has been successfully integrated with the plastic cap model for capturing the impact response of geological materials, e.g. in Katona (1984), Simo et al. (1986) and later by Tong and Tuan (2007), An et al. (2011), Aráoz and Luccioni (2015) and Lu and Fall (2016, 2017). It has been demonstrated that such a viscoplastic cap model has the capability of not only reproducing the behaviours of soils under high strain rate conditions, such as ground shock, but also capturing other time-dependent processes, such as creep with low strain rates. More recently, Higgins et al. (2013) also integrated the Perzyna model with bounding surface plasticity to model sand behaviour under blast loading. Although the overstress theory by Perzyna has provided significant convenience in determining the loading index L (which corresponds to the scalar factor of proportionality $d\,l$ in conventional plasticity) in bounding surface plasticity, the model in Higgins et al. (2013) suffers from inadequacies associated with the incorporated failure model, namely the SANISAND model. A detailed discussion on its strength and weakness in terms of its applicability to blast loading conditions was provided in Section 3.3.1.6.

3.3.2.4 Duvaut-Lions viscoplastic model

Another formulation of viscoplasticity that has been increasingly popular in recent years is the Duvaut-Lions viscoplastic formulation (Duvaut and Lions, 1972). This formulation has been adopted by Simo et al. (1988), and hereafter implemented in LS-DYNA as Material Types 145 (Murray and Lewis, 1995) and 159 (Murray, 2007) with a continuous surface cap model, and Material Type 147 (Lewis, 2004) with a modified Mohr-Coulomb model. To incorporate the Duvaut-Lions viscosity model, only one additional material parameter h_0 (fluidity coefficient) is needed based on the original plasticity, while extra constants can be introduced to enhance its flexibility in data fitting. In the Duvaut-Lions viscoplastic model, the viscoplastic stress s_{ij}^{VP} is revised by interpolating between the elastic trial stress s_{ij}^{T} and the inviscid stress s_{ij}^{P} (without rate effects) as (Murray, 2007):

$$s_{ij}^{VP} = (1-g)s_{ij}^{T} + g s_{ij}^{P} \tag{3.50}$$

and

$$g = \frac{\Delta t / h_0}{1+\Delta t / h_0} \tag{3.51}$$

where Δt is the time step, and when $h_0 \to 0$, the inviscid stress is obtained so that the solution is independent of the strain rate. As $h_0 \to \infty$, the elastic trial stress is obtained. Therefore, the viscoplastic stress in the Duvaut-Lions model is bounded between the current rate-independent stress and the elastic trial stress, and also allows the viscoplastic stress state to lie outside the yield surface.

A comparable performance has been reported on the Duvaut-Lions and Perzyna viscoplasticity models (Schwer, 1994; An, 2010). A detailed comparison between the Duvaut-Lions and the Perzyna viscoplastic formulation is available in Schwer (1994) with respect to their algorithms and performance. However, from a practical point of view, the former is easier in numerical implementation, as the Duvaut-Lions formulation is in fact a revised inviscid formulation. In contrast, the latter provides more flexible data fitting as there are more viscous parameters included, although its solution algorithm is inevitably complicated as it requires more matrix operations (An, 2010).

3.3.3 Summary and discussion

Despite that the influence of strain rate on soils is widely acknowledged, not all blast models for soils have incorporated a strength model to explicitly account for the strain rate effect. As for failure models, although the inadequacy of Drucker-Prager or Mohr-Coulomb type of models in modelling soil response under blast loading are quite evident, they are still widely in use primarily due to their relative simplicity. Nevertheless, it is necessary to include isotropic hardening caps in constitutive laws, since they can serve to account soil failure under high pressure, control soil dilatancy, reproduce volumetric hysteresis as well as capture the pore crushing process, which are all vital ingredients for a rational description of soil behaviour under blast loading. Meanwhile, many of foregoing failure models have not accounted for the effect of the third stress invariant.

Although various models for the seismic behaviour of sand (original and capped SANISAND models) have been recently extended to simulate its blast response, they are also subject to different limitations, and more research is required to verify their applicability and fidelity to blast loading conditions.

Given the drastic attenuation of blast waves with distance to a charge, it is therefore evident that there may not be a single constitutive model that can describe the soil response for the entire spectrum of pressures either. For instance, although SANISAND types of models may have limitations in capturing the blast response of soils compared with the cap models, they represent an excellent means of reproducing soil behaviour at the far end of an explosion event where seismic waves prevail, which cannot be readily modelled by cap models.

3.4 Application of soil models to blast-induced liquefaction

There are numerous cases of increases in residual excess pore pressure or liquefaction caused by blasting or high-pressure compression reported and discussed in literature. These phenomena can occur in cohesionless soils (sand, silt) and are usually observed during human induced activities, such as in-situ soil improvement processes, military high-explosive testing, laboratory experiments, accidental explosions, and terrorist attacks (e.g. Ivanov, 1967; Fragaszy and Voss, 1981, 1986; Dowding and Hryciw, 1986; Charlie et al., 1988, 1996, 2013; Bretz, 1990; Veyera and Charlie, 1990; Bolton et al., 1994; Veyera et al., 2002; Ashford et al., 2004; Al-Qasimi et al., 2005; Charlie and Doehring, 2007). Among the different definitions of liquefaction, they all commonly indicate a condition where an increase in the pore water pressure leads to a decrease in the effective stress and thus loss of the shear strength of a soil mass (Charlie, 1988).

Analyses of blast-induced liquefaction are generally consistent with that caused by earthquakes, but there are pronounced differences between the two of them. From a physical point of view, earthquake-induced liquefaction is considered to result from slowly increasing pore water pressure caused by shear waves that vertically propagate toward the ground surface, which in general have relatively low peak accelerations, while blast-induced liquefaction is caused by compression waves. Meanwhile, the predominant frequency of a blast wave usually demonstrates orders of magnitude that are more than 2 times greater than those of an earthquake wave, and its amplitude of pressure is large, whereas the loading period is extremely short (Charlie et al., 1996; Wang et al., 2008). Therefore, from a modelling point of view, a different

mechanism with respect to the occurrence of liquefaction in blast events should be taken into account. Besides, due to the intensive impact, the soil response during the compression process under shock loading will demonstrate pressure dependence as well as a rate-effect. The effect of strain rate on liquefaction resistance or pore pressure response of granular soils has been demonstrated in Yamamuro and Lade (1993) and Bolton et al. (1994). Furthermore, as blast waves have rapid attenuation, the loading condition can drastically vary within a certain distance from the charge. Consequently, the modelling strategy for blast-induced liquefaction should be different from that for earthquake-induced liquefaction, and such an analysis should be conducted with a competent soil model for blast loading. In this section, the mechanism of blast-induced liquefaction will be briefly elucidated. Then, the application of current soil models to blast-induced liquefaction is summarized, and their different methods and performance in reproducing the pore water pressure build-up are compared.

3.4.1 Mechanism of blast-induced liquefaction

For saturated loose materials such as sandy and silty soils, the volume reduction caused by blast-induced compression is prevented by increases in the pore water pressure, since there is insufficient time for relative movement of pore fluid and soil skeleton. If the increase in the pore water pressure is large enough, liquefaction would occur. Meanwhile, the undrained blast loading would impose a volume compatibility condition for a saturated soil, i.e., the volumetric strain of the pore fluid should be equivalent to that of soil skeleton (Puebla et al., 1977). In this condition, blast-induced liquefaction is generally attributed to the elastic deformation of the pore water in saturated soils, whilst the skeleton exhibits plastic behaviour (Schapermeier, 1978; Fragaszy and Voss, 1981, 1986; Kim and Blouin, 1984; Charlie, 1988). To be more specific, given this hysteresis in the stress-strain path of the material, it is therefore possible that the effective stress could drop to zero after unloading, while the pore water pressure is kept at a certain positive value higher than its initial condition due to the irrecoverable compaction. The mechanism is shown in Figure 3.10 below.

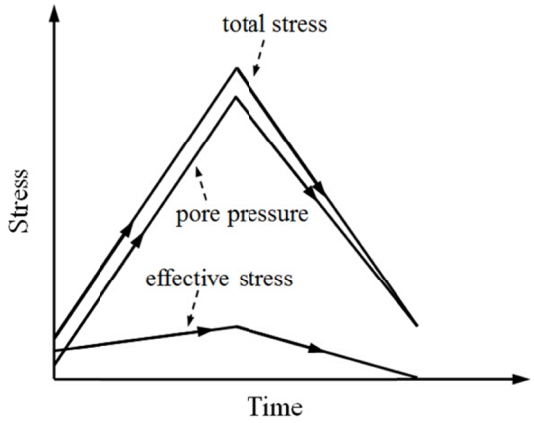

(a) stress-time curve of a saturated soil during quasi-static loading (Adopted from Fragaszy and Voss, 1986)

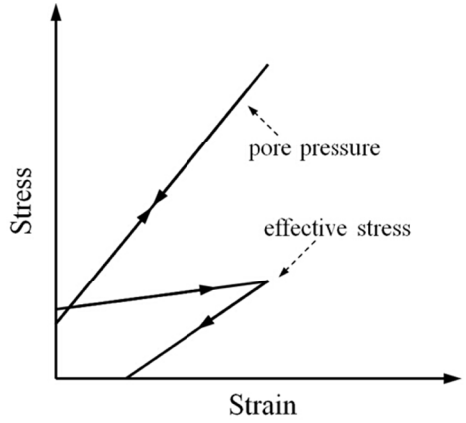

(b) stress-strain curve of saturated soil during quasi-static loading (Adopted from Fragaszy and Voss, 1981)

Figure 3.10 Sketch of the mechanism of blast-induced liquefaction

3.4.2 Application of soil models to blast-induced liquefaction

3.4.2.1 Simulation with the three-phase soil model

The most noticeable example of modelling blast-induced liquefaction is the application of the three-phase soil model by Wang et al. (2008, 2011). In their modelling work, a model for damage in a parallel bar system (Krajcinovic, 1996) was used to cause excess pore water pressure. One component of pressure in the soil skeleton is borne by the bonds between the solid particles (p_c), and these bonds are represented by a series of elastic brittle filaments. Each filament is a two-force structural element endowed only with axial stiffness and strength, and the bonding pressure p_c is determined by (Wang et al., 2004a):

$$p_c = E_0(1-\bar{D})\cdot\Delta V \tag{3.52}$$

and

$$\bar{D}=1-\exp\left[-\frac{1}{\bar{h}}(\bar{B}e)^{\bar{h}}\right] \tag{3.53}$$

where E_0 is the initial modulus of the bonds; $\bar{D}$ the damage variable; and $\bar{B}, \bar{h}$ the constants related to the properties of the soil. As a result, the damage of the soil skeleton gradually accumulates during the passage of blast waves. Thus, its stiffness will be reduced and may become sufficiently low such that when the soil is unloaded to the initial condition, the skeleton cannot bear as much as its initial pressure, and more pressure will be borne by the liquid phase in

this condition (Wang et al., 2008). Then, there is build-up of excess pore water pressure and liquefaction may take place. It is worth mentioning that liquefaction has been generally assumed to occur only in saturated soils. However, the three-phase soil model has also shown that the closure of air-filled pores during blast-induced compression can also bring the soil from an unsaturated state to saturation (Wang and Lu, 2003). Thus, liquefaction may also occur in unsaturated soils with high water content in the vicinity of explosion where the loading has considerable intensity.

3.4.2.2 Simulation with the FHWA model

The FHWA model adopted in Lee (2006) to simulate the process of blast-induced liquefaction introduces volumetric hysteresis with different bulk moduli upon isotropic loading/unloading (with Equation (3.10)), and the term $q_a - e_v$ in the denominator indeed works in a way similar way as the cap model (Equation (3.29)). Meanwhile, the model estimates the pore water pressure based on the total volumetric strain of the soil mass (Equation (3.11)), i.e. the volumetric deformation of water is assumed to equal to that of the soil skeleton. As discussed, this assumption is only valid when the soil is fully saturated.

In the work of Lee (2006), the FHWA model was found to underestimate pore water pressure build-up, and it had been attributed to the lack of dependence of the soil stiffness on water. However, this inadequacy of the model should be associated with the incorporated failure model. To be more specific, the yield surface of the FHWA model is a modified Mohr-Coulomb yield surface. As discussed in Sections 3.3.1.1 and 3.3.1.2, this will lead to unrealistic dilation during initial loading. Therefore, the total volumetric strain that is used to calculate the pore water pressure may be underestimated, and thus the resultant pore pressure response will be unrealistic and lower than experimental results.

3.4.2.3 Simulation with a bilinear model

To reproduce the hysteresis effect and capture liquefaction due to transient impact loading, Kim and Blouin (1984) used the generalized Biot's theory and applied a bilinear model with different prescribed loading and unloading bulk moduli of the soil skeleton. However, the bilinear model, which is a special variable moduli model with no explicit yield surface, cannot account for soil dilatancy and may fail to satisfy continuity conditions regardless of its

computational simplicity (Chen and Baladi, 1985; Bloom, 2006). Besides, the strain-rate effect associated with blast loading has not been included in their model either.

3.4.2.4 Simulation with a cap model

As discussed in Section 3.3.1.5, the cap model is theoretically feasible to capture the hysteretic behaviour in the hydrostatic response of soils, and it has also been demonstrated to satisfy all rigorous theoretical requirements and avoid mathematical uncertainties (DiMaggio and Sandler, 1971; Nelson et al., 1971; Bloom, 2006). Therefore, the cap model can be employed to analyze the liquefaction triggered by explosions where hydrostatic pressure dominates.

Examples can be found in the work by Awad (1990) and Ghassemi et al. (2010) where a cap model with two invariants has been applied to reproduce the dynamic response of saturated soils under impulsive loading, and the pressure dependence of soil compressibility has also been considered. However, the strain-rate effect has not been included. Notably, the Perzyna type of viscoplastic cap model has been used to simulated blast response of soils by An et al. (2011), and an appropriate EOS for each constitutive phase in soils has also been incorporated. Nevertheless, only unsaturated soils were studied in such work, while the liquefaction phenomenon was not examined. Therefore, despite its theoretical feasibility, the effectiveness of a cap model in capturing blast-induced liquefaction should be further studied within a more rigorous scheme.

3.4.3 Summary and discussion

Despite the fact that the model of Wang et al (2008) has realistically captured the liquefaction induced by dynamic compression and blast loading, the simulated pore pressure response has not yet been validated against experimental data that involve varied strain rates. According to Fragaszy and Voss (1986), the compressive waves generated by an explosion will significantly contribute only to the development of liquefaction near the explosive source, while other factors, such as contribution from shear waves similar to those of earthquakes, may be more predominant with increasing distance. Therefore, a single material model may not be available to reproduce liquefaction for the entire range of pressures during a blast event.

3.5 Final remarks

Although there is no model that can account for the entire range of pressures during blast loading, this is generally not problematic if only high pressures are of interest. To date, the modelling strategies for the blast response of soils have gradually improved and become more extensive and prudent. For example, focus has been given to the valid range of an EOS, and different material models have been applied in a single problem. The variations of soil constitution, bulk modulus, and soil energy during blast loading have been considered and then updated through iterations in a highly coupled manner. Moreover, advanced constitutive relations that are more practical in capturing the behaviours of soils under high-frequency loading conditions have also been developed. However, there still remain problems and challenges, such as determining the valid range for a given EOS model in a specific problem; the inclusion of the strain-rate effect and the third stress invariant in soil models; supplement of end caps to conical yield envelopes to account for inelastic soil behaviour under high pressure; further verification of emerging models; and the application and improvement of soil models in estimating blast-induced liquefaction.

Besides these issues from a modelling perspective, the limitation in availability of experimental data has also hindered the development of more advanced models. Specifically, first of all, the experimental studies conducted for examining the blast response of soils are quite scarce compared with those for other types of loading (i.e. quasi-static and cyclic), and the influence of very limited intrinsic properties of soils have been studied. In fact, under the perception that all soils exhibit similar contractive behaviour during intensive blast loading, only the effect of (relative) density, degree of saturation, and stiffness on blast response of soils have been experimentally investigated to date, while other controlling factors such as soil type, overconsolidation ratio, and anisotropy have been generally disregarded. In the meantime, due to the intensity and destructive nature of blast tests, very few parameters, such as total and pore pressure as well as particle velocity, can be measured, and thus limited details of the constitutive behaviours of soils can be provided for model development and validation purposes. As a result, soil models have been generally developed on a phase basis and applied to assess its blast response regardless of the differences in soil type and a few other properties.

As prevalent throughout this literature review, the guideline provided in the beginning of this paper should be taken into consideration in addressing the problem of soil response under blast loading, i.e., a holistic formulation should incorporate an appropriate EOS, failure model,

as well as strength model. The discussed soil models for blast loading are summarized in Table 3.1 with respect to their integral components as required by the aforementioned criterion, and their mechanisms for modelling blast-induced liquefaction or volumetric hysteresis are also presented.

Table 3.1 Summary and comparison of existing soil models for blast loading

Source	Material stiffness	Failure model	Strength model	Application to liquefaction	Additional comments
Lee (2006); Busch et al. (2016)	Soil stiffness is modified to include pressure dependence	Modified Mohr-Coulomb model	Duvaut-Lions viscoplasticity model	Modified Mohr-Coulomb model could result in unrealistic dilation	Based on *MAT_147 model in LS-DYNA; underestimate pore water pressure due to dilation
Xu and Zhang (2015)	Soil stiffness is modified to include pressure dependence	Capped SANISAND model	Modify stiffness and failure model in accordance with Prapaharan et al. (1989)	Generate hysteresis effect with capped SANISAND model	-
Higgins et al. (2013)	Soil stiffness is modified to include pressure dependence	Original SANISAND model	Perzyna viscoplasticity model	Generate hysteresis effect with SANISAND model	Inelastic deformation is only due to shearing; insufficient in high pressure conditions
Yankelevsky et al. (2008); Karinski et al. (2009a, 2009b); Feldgun et al. (2013)	Shock–Hugoniot	Lundborg model	Not included	Generate hysteresis effect with different volume-pressure relations for loading and unloading	-
An et al. (2011)	Mie-Grüneisen model	Cap model	Perzyna viscoplasticity model	Generate hysteresis effect by using cap model	Soil density, composition, bulk modulus and internal energy are updated, and lower limits of EOS are considered
The three-phase soil model (e.g. Wang et al., 2004a, 2008, 2011)	Lyakhov model	Drucker-Prager model	Modify the yield strength according to Prapaharan et al. (1989)	Cause liquefaction by introducing a damage model	Based on the conceptual model of Kandaur in Henrych (1979)
Feldgun et al. (2008b, 2011)	Lyakhov model	Lundborg model	Not included	Generate hysteresis effect with different volume-pressure relations for loading and unloading	-
Ghassemi et al. (2010); Awad (1990)	Soil stiffness is modified to include pressure dependence	Plastic cap model	Not included	Generate hysteresis effect by the cap model	Generalized Biot's formulation for saturated condition
Grujicic et al. (2006; 2008a; 2008b; 2009; 2010)	Piecewise shock–Hugoniot curves	Piecewise yield stress curves	Implicitly considered	Generate hysteresis effect with different volume-pressure relations for loading and unloading	-
Kim and Blouin (1984)	Bilinear model	No explicit yield condition	Not included	Generate hysteresis effect by assigning different loading and unloading moduli	Generalized Biot's formulation for saturated condition

Although a variety of models are available to date for a rational characterization of soil behaviour under blast loading, there is no model that is able to capture the blast response of

evolutive granular material, such as hydrating cemented tailings backfill. Therefore, to reliably capture its dynamic behaviour, multiphysics modelling of the blast response of CTB is conducted in this PhD research and it is presented in Chapter 4.

3.6 References

Akiyoshi T, Fuchida K, Matsumoto H, Hyodo T, Fang HL. Liquefaction analyses of sandy ground improved by sand compaction piles. Soil Dynamics and Earthquake Engineering 1993;12:299–307.

Al-Qasimi EMA, Charlie WA, Woeller DJ. Canadian liquefaction experiment (CANLEX): Blast–induced ground motion and pore pressure experiments. Geotechnical Testinng Journal 2005; 28(1): 1–13.

An J, Tuan CY, Cheeseman BA, Gazonas GA. Simulation of soil behaviour under blast loading. International Journal of Geomechanics, ASCE 2011; 11:323–334.

An J. Soil behaviour under blast loading. PhD thesis. University of Nebraska–Lincoln, Lincoln, NE, USA, 2010.

Aráoz G, Luccioni B. Modeling concrete like materials under sever dynamic pressures. International Journal of Impact Engineering 2015; 76:139–154.

Ashford SA, Rollins KM, Lane JD. Blast–Induced liquefaction for full–scale foundation testing. Journal of Geotechnical and Geoenvironmental Engineering, ASCE 2004; 8: 798–806.

Awad AA. A numerical model for blast–induced liquefaction using displacements–pore pressure formulations. PhD thesis. Colorado State University, Fort Collins, CO, USA, 1990.

Baron ML, Nelson I, Sandler I. Influence of constitutive models on ground motion predictions. Journal of the Engineering Mechanics Division 1973; 99: 1181–1200.

Biot MA. Theory of propagation of elastic waves in a fluid saturated porous solid. I. Low frequency range. Journal of the Acoustical Society of America 1956a; 28(2): 168–178.

Biot MA. Theory of propagation of elastic waves in a fluid saturated porous solid. II. Higher–frequency range. Journal of the Acoustical Society of America 1956b ; 28(2): 179–191.

Biot MA. Mechanics of deformation and acoustic propagation in porous media. Journal of Applied Physics 1962a; 33(4): 1482–1498.

Biot MA. Generalized theory of acoustic propagation in porous dissipative media. Journal of the Acoustical Society of America 1962b; 34(5): 1254–1264.

Bloom F. Constitutive models for wave propagation in soil. Applied Mechanics Reviews 2006; 59:146–175.

Bolton JM, Durnford DS, Charlie WA. One–dimensional shock and quasi–static liquefaction of silt and sand. Journal of Geotechnical Engineering, ASCE 1994; 120:1874–1888.

Bretz TE. Soil liquefaction resulting from blast-induced spherical stress waves. Final Rep. No. WL-TR-89-100, Weapons Laboratory, Air Force Systems Command, 1990.

Busch CL, Aimone–martin CT, Tarefder RA. Experimental evaluation and finite–element simulations of explosive airblast tests on clay soils. International Journal of Geomechanics, ASCE 2016. (Available online).

Cai M, Kaiser PK, Suorineni F, Su K. A study on the dynamic behaviour of the Meuse/Haute–Marne argillite. Physics and Chemistry of the Earth 2007; 32:907–916.

Casagrande A, Shannon WL. Strength of soils under dynamic loads. Proceedings of the American Society of Civil Engineers 1948; 74(4):591–608.
Charlie WA, Doehring DO. Ground water table mounding, pore pressure, and liquefaction induced by explosions: Engery–ditance relations. Reviews of Geophysics 2007; 45: 1–9.
Charlie WA, Doehring DO, Veyera GE, Hassen HA. Blast induced liquefaction of soils: Laboratory and field tests. Final Rep., USAF Office of Scientific Research, Bolling AFB, Washington, DC, 1988.
Charlie W, Veyera GE, Durnford DS, Doehring DO. Porewater pressure increases in soil and rock from underground chemical and nuclear explosions. Engieering Geology 1996; 43(4):225–236.
Charlie WA, Bretz TE, Schure LA, Doehring DO. Blast–induced pore pressure and liquefaction of saturated sand. Journal of Geotechnical and Geoenvironmental Engineering, ASCE 2013; 139(8):1308–1319.
Chen WF, Baladi GY. Soil Plasticity: Theory and Implementation. Elsevier: Amsterdam, 1985.
DiMaggio FL, Sandler IS. Material models for granular soils. Journal of the Engineering Mechanics Division 1971; 97:935–950.
Dolarevic S, Ibrahimbegovic A. A modified three–surface elasto–plastic cap model and its numerical implementation. Computers and Structures 2007; 85: 419–430.
Dowding CH, Hryciw RD. A laboratory study of blast densification of saturated sand. Journal of Geotechnical Engineering 1986; 112(2):187–99.
Drake JL., Little CD. Ground shock from penetrating conventional weapons. Proceedings of Symposium on the Interaction of Non-Nuclear Munitions with Structures, US Air Force Academy, Colorado Springs, Colorado, 1983, 1–6.
Duvaut G, Lions JL. Les Inequations en Mechanique et en Physique. Dunos, Paris, 1972.
Feldgun VR, Kochetkov AV, Karinski YS, Yankelevsky DZ. Internal blast loading in a buried lined tunnel. International Journal of Impact Engineering 2008a; 35(3):172–183.
Feldgun VR, Kochetkov AV, Karinski YS, Yankelevsky DZ. Blast response of a lined cavity in a porous saturated soil. International Journal of Impact Engineering 2008b; 35(9):953–966.
Feldgun VR, Karinski YS, Yankelevsky DZ. Blast pressure distribution on a buried obstacle in a porous wet soil. International Journal of Protective Structures 2011; 2(1): 45–70.
Feldgun VR, Karinski YS, Yankelevsky DZ. A coupled approach to simulate the explosion response of a buried structure in a soil–rock layered medium. International Journal of Protective Structures 2013; 4(3):231–292.
Feldgun VR, Karinski YS, Yankelevsky DZ. Riemann solver for irreversibly compressible three–phase porous media. International Journal for Numerical and Analytical Methods in Geomechanics 2014; 38:406–440.
Fragaszy RJ, Voss ME. Laboratory verification of blast–induced liquefaction mechanism. Final Report ADA109000, US Air Force Office of Scientific Research. Washington, DC. 1981.
Fragaszy RJ, Voss ME. Undrained compression behaviour of sand. Journal of Geotechnical Engineering, ASCE 1986; 112(3): 334–347.
Ghaboussi J, Kim KJ. Quasistatic and dynamic analysis of saturated and partially saturated soils. In: C.S. Desai and R.H. Gallagher (Editors), Mechanics of Engineering Materials, Wiley, Somerset, N.J., USA, 1984, 277–296.
Ghassemi A, Pak A, Shahir H. Numerical study of the coupled hydro–mechanical effects in dynamic compaction of saturated granular soils. Computers and Geotechnics 2010; 37:10–24.

Grujicic M, Pandurangan B, Cheeseman BA. The effect of degree of saturation of sand on detonation phenomena associated with shallow–buried and ground–laid mines. Shock and Vibration 2006; 13:41–61.

Grujicic M, Pandurangan B, Cheeseman BA, Roy WN, Skaggs RR, Gupta R. Parameterization of the porous–material model for sand with various degrees of water saturation. Soil Dynamics and Earthquake Engineering 2008a; 28:20–35.

Grujicic M, Pandurangan B, Coutris N, Cheeseman BA, Roy WN, Skaggs RR. Computer–simulations based development of a high strain–rate, large–deformation, high–pressure material model for STANAG 4569 sandy gravel. Soil Dynamics and Earthquake Engineering 2008b; 28:1045–1062.

Grujicic M, Pandurangan B, Coutris N, Cheeseman BA, Roy WN, Skaggs RR. Derivation and validation of a material model for clayey sand for use in landmine detonation computational analysis. Multidiscipline Modeling in Materials and Structures 2009; 5:311–344.

Grujicic M, Pandurangan B, Coutris N, Cheeseman BA, Roy WN, Skaggs RR. Derivation, parameterization and validation of a sandy–clay material model for use in landmine detonation computational analyses. Journal of Materials Engineering and Performance 2010; 19(3):434–450.

Gu Q, Lee FH. Ground response to dynamic compaction of dry sand. Géotechnique 2002; 52(7):481–493.

Henrych J. The Dynamics of explosion and its use. Elsevier: New York, 1979.

Higgins W, Chakraborty T, Basu D. A high strain–rate constitutive model for sand and its application in finite–element analysis of tunnels subjected to blast. International Journal for Numerical and Analytical Methods in Geomechanics 2013; 37(15):2590–2610.

Ivanov PL. Compaction of noncohesive soils by explosions. US Department of the Interior, Bureau of Reclamation and Natrual Science Foundation, Washington, DC, 1967.

Jackson JG, Rohani B, Ehrgot JQ. Loading rate effects on compressibility of sand. Journal of Geotechnical Engineering Division 1980; 106(8):839–852.

Karinski YS, Feldgun VR, Yankelevsky DZ. Explosion–induced dynamic soil–structure interaction analysis with the coupled Godunov–Variational Difference Approach. International Journal for Numerical Methods in Engineering 2009a; 77:824–851.

Karinski YS, Feldgun VR, Yankelevsky DZ. Effect of soil locking on the cylindrical shock wave's peak pressure attenuation. Journal of Engineering Mechanics, ASCE 2009b; 135(10):1166–1180.

Katona MG. Evaluation of viscoplastic cap model. Journal of Geotechnical Engineering, ASCE 1984; 110(8):1106–1125.

Khoei AR, Mohammadnejad T. Numerical modeling of multiphase fluid flow in deforming porous media: A comparison between two– and three–phase models for seismic analysis of earth and rockfill dams. Computers and Geotechnics 2011; 38:142–166.

Khoei AR, Azami AR, Haeri SM. Implementation of plasticity based models in dynamic analysis of earth and rockfill dams: A comparison of Pastor–Zienkiewicz and cap models. Computers and Geotechnics 2004; 31(5):384–409.

Kim KJ, Blouin SE. Response of saturated porous nonlinear materials to dynamic loadings, Final Report ADA148528, US Air Force Office of Scientific Research. Washington, DC. 1984.

Krajcinovic D. Damage Mechanics, Elsevier, New York, NY, USA, 1996.

Kumar R, Choudhury D, Bhargava K. Prediction of blast-Induced vibration parameters for soil sites. International Journal of Geomechanics, ASCE 2014; 14(3):341–349.

Laine P, Sandvik A. Derivation of mechanical properties for sand. Proceedings of the 4–th Asia–Pacific Conference on Shock and Impact Loads on Structures, Singapore, 2001; 361–368.
Lee WY. Numerical modeling of blast induced liquefaction. PhD thesis, Brigham Young University, Provo, UT, USA, 2006.
Leong EC, Anand S, Cheong HK, Lim CH. Reexamination of peak stress and scaled distance due to ground shock.International Journal of Impact Engineering 2007; 34(9):1487–1499.
Lewis BA. Manual for LS–DYNA Soil Material Model 147. Federal Highway Administration. Publication No. FHWA–HRT–095. McLean, VA, USA, 2004.
Li X, Zienkiewicz OC. Multiphase flow in deforming porous media and finite element solutions. Computers and Structures 1992; 45:211–227.
Li X, Thomas HR, Fan Y. Finite element method and constitutive modeling and computation for unsaturated soils. Computer Methods in Applied Mechanics and Engineering 1999; 169:135–159.
Livermore Software Technology Corporation (LSTC). LS–DYNA Keyword user's manual, Version 971, Livermore, CA, USA, 2007.
Loukidis D. Advanced constitutive modeling of sands and applications to foundation engineering. PhD thesis, Purdue University, West Lafayette, IN, USA, 2006.
Lu G, Fall M. A coupled chemo–viscoplastic cap model for simulating the behaviour of hydrating cemented tailings backfill under blast loading. International Journal for Numerical and Analytical Methods in Geomechanics 2016; 40: 1123–1149.
Lu G, Fall M. Modelling blast wave propagation in a subsurface geotechnical structure made of an evolutive porous material. Mechanics of Materials 2017; 108:21–39.
Lu Y, Wang Z, Chong K. A comparative study of buried structure in soil subjected to blast load using 2D and 3D numerical simulations. Soil Dynamics and Earthquake Engineering 2005; 25:275–288.
Lundborg N. Strength of rock–like materials. International Journal of Rock Mechanics and Mining Sciences 1968; 5: 427–454.
Lyakhov GM. Fundamentals of the dynamics of detonation waves in soils and rock. Nedra, Moscow, 1974.
Lyakhov GM, Okhitin VN. Nonstationary plane waves in media with bulk viscosity. Journal of Applied Mechanics and Technical Physics 1977a; 18(5): 693–700.
Lyakhov GM, Okhitin VN. Plane waves in nonlinear viscous multicomponent media. Journal of Applied Mechanics and Technical Physics 1977b; 18(2): 241–248.
Manzari MT, Dafalias YF. A critical state two–surface plasticity model for sands. Géotechnique 1997; 47(2): 255–272.
Merkle DH, Dass WC. Fundamental Properties of Soils for Complex Dynamic Loadings. Final Report ADA164206, US Air Force Office of Scientific Research. Washington, DC. 1985.
Murray YD, Lewis BA. Numerical simulation of damage in concrete. Report DNA–TR–94–190, Defense Nuclear Agency. Alexandria, 1995.
Murray YD. Users manual for LS–DYNA concrete material model 159. Report FHWA–HRT–05–062, Federal Highway Administration. McLean, 2007.
Nelson I, Baladi GY. Outrunning ground shock computed with different models. Journal of the Engineering Mechanics Division 1977; 103(3): 377–393.
Nelson I, Baron ML, Sandler I. Mathematical models for geological materials for wave–propagation studies. Report DASA2672, Defense Nuclease Agency. Washington, DC. 1971.

Omidvar M, Iskander M, Bless S. Stress–strain behaviour of sand at high strain rates. International Journal of Impact Engineering 2012; 49:192–213.
Perzyna P. Fundamental problems in viscoplasticity. Advances in Applied Mechanics 1966; 9:243–377.
Prapaharan S, Chameau JL, Holtz RD. Effect of strain rate on undrained strength derived from pressuremeter tests. Geotechnique 1989; 39(4):615–624.
Puebla H, Byrne PM, Phillips R. Analysis of CANLEX liquefaction embankments: prototype and centrifuge models. Canadian Geotechnical Journal 1997; 34: 641–657.
Sandler IS, DiMaggio FL, Baladi GY. Generalized cap model for geological materials. Journal of the Geotechnical Engineering Division 1976; 102:683–699.
Sandler IS, Rubin D. An algorithm and a modular subroutine for the cap model. International Journal for Numerical and Analytical Methods in Geomechanics 1979; 3:173–186.
Schapermeier E. Liquefaction produced by compressional waves. Proc, Int. Workshop on Blast–Induced Liquefaction, Dames and Moore/US Air Force Maidenhead, UK, 1978, 57–64.
Schrefler BA, Scotta R. A fully coupled dynamic model for two–phase fluid flow in deformable porous media. Computer Methods in Applied Mechanics and Engineering 2001, 190: 3223–3246.
Schwer LE, Murray YD. A three–invariant smooth cap model with mixed hardening. International Journal for Numerical and Analytical Methods in Geomechanics 1994; 18:657–688.
Schwer LE. Viscoplastic augmentation of the smooth cap model. Nuclear Engineering and Design 1994; 150:215–223.
Semblat JF, Luong MP, Gary G. 3d-Hopkinson bar: new experiments for dynamic testing on soils. Soils and Foundations 1999; 39(1):1–10.
Simo JC, Wu JW, Pister KS, Taylor RL. Assessment of cap model: Consistency return algorithms and rate–dependent extension. Journal of Engineering Mechanics, ASCE 1986; 114(2):191–218.
Simo JC, Kennedy JG, Govindjee S. Non–smooth multisurface plasticity and viscoplasticity. Loading/unloading conditions and numerical algorithms. International Journal for Numerical Methods in Engineering 1988; 26:2161–2185.
Taiebat M, Dafalias YF. SANISAND: Simple anisotropic sand plasticity model. International Journal for Numerical and Analytical Methods in Geomechanics 2008; 32(8): 915–948.
Tong X, Tuan CY. Viscoplastic cap model for soils under high strain rate loading. Journal of Geotechnical and Geoenvironmental Engineering, ASCE 2007; 133(2):206–214.
Tu Z, Lu Y. Evaluation of typical concrete material models used in hydrocodes for high dynamic response simulations. International Journal of Impact Engineering 2009; 36(1): 132–146.
Veyera GE, Charlie WA. Laboratory study of compressional liquefaction. Journal of Geotechnical Engineering 1990; 116:790–804.
Veyera GE, Charlie WA, Hubert ME. One–dimensional shock–induced pore pressure response in saturated carbonate sand. Geotechcal Testing Journal 2002; 25(3):277–288.
Wang Z, Lu Y. Numerical analysis on dynamic deformation mechanism of soils under blast loading. Soil Dynamics and Earthquake Engineering 2003; 23:705–714.
Wang Z, Hao H, Lu Y. A three–phase soil model for simulating stress wave propagation due to blast loading. International Journal for Numerical and Analytical Methods in Geomechanics 2004a; 28:33–56.

Wang Z, Lu Y, Hao H. Numerical investigation of effects of water saturation on blast wave propagation in soil mass. Journal of Engineering Mechcanics, ASCE 2004b; 130(5):551–561.
Wang Z, Lu Y, Bai C. Numerical analysis of blast–induced liquefaction of soil. Computers and Geotechnics 2008; 5:196–209.
Wang Z, Lu Y, Bai C. Numerical simulation of explosion–induced soil liquefaction and its effect on surface structures. Finite Elements in Analysis and Design 2011; 47(9):1079–1090.
Wang ZL, Konietzky H, Huang RY. Elastic–plastic–hydrodynamic analysis of crater blasting in steel fiber reinforced concrete. Theoretical and Applied Fracture Mechanics 2009; 52:111–116.
Whitman RV. The response of soils to dynamic loading. Final Report AD708625, US Army Engineer Waterways Experiment Station. Vicksburg, 1970.
Xu TH, Zhang LM. Numerical implementation of a bounding surface plasticity model for sand under high strain–rate loadings in LS–DYNA. Computers and Geotechnics 2015; 66:203–218.
Yamamuro JA, Lade PV. 1993. Effects of strain rate on instability of granular soils. Geotechnical Testing Journal, 16(3): 304–313.
Yankelevsky DZ, Feldgun VR, Karinski YS. Underground explosion of a cylindrical charge near a buried wall. International Journal of Impact Engineering 2008; 35(8):905–919.
Zhang HW, Sanavia L, Schre BA. Numerical analysis of dynamic strain localisation in initially water saturated dense sand with a modified generalized plasticity model. Computers and Structures 2001;79:441–459.
Zienkiewicz OC, Chan AHC, Pastor M, Paul DK, Shiomi T. Static and dynamic behaviour of soils: a rational approach to quantitative solution, I. Fully saturated problems. Proceedings of the Royal Society of London 1990a; 429: 285–309.
Zienkiewicz OC, Xie YM, Schrefler BA, Ledesma A, Bicanic, N. 1990b. Static and dynamic behaviour of soils: a rational approach to quantitative solution, II. Semi–saturated problems. Proceedings of the Royal Society of London 1990b; 429: 311–321.
Zienkiewicz OC, Shiomi T. Dynamic behaviour of saturated porous media: the generalized Biot formulation and its numerical solution. International Journal for Numerical and Analytical Methods in Geomechanics 1984; 8: 71–96.
Zukas JA. Introduction to hydrocodes. Elsevier: Kidlington, 2004.

Chapter 4.
Multiphysics Models for CTB Response under Blast Loading

4.1 Introduction

To achieve full ore recovery, the CTB in the field is often exposed to mine blasts during the extraction of remnant ore pillars. However, there is limited understanding of CTB behaviour under blast loading, and the current design practice considering only static stress equilibrium has contributed to a number incidents of backfill system failures. Therefore, to ensure mine safety and profitability, a rational characterization of CTB response during blasting is required. Nevertheless, based on the literature review of research work on modelling granular media (soils) behaviours subjected to blast loading (Chapter 3), there is no existing tool that can capture the blast response of hydrating CTB undergoing multiphysics processes. Therefore, fundamental multiphysics models are developed to assess blast response of hydrating CTB in this chapter. Specifically, a novel coupled chemo-viscoplastic cap model is developed to characterize the rate-dependence, irrecoverable compaction, and nonlinear hydrostatic behaviour of CTB under blast loading (Section 4.2). The model can also capture the evolutive blast response of CTB in the hydration process with a binder hydration model. Moreover, the performance of CTB is not only affected by the hydration of binders (chemical, C), but is also significantly influenced by the thermal (T), hydraulic (H), and mechanical (M) factors contributing in its curing process. Therefore, a new multiphysics-viscoplastic cap model is then developed to characterize the blast response of CTB under the impact of complex THMC processes (Section 4.3). Consequently, the behaviour of CTB under blast loading can be evaluated under any time and curing conditions of interest. Furthermore, the early-age CTB with no or negligible cementation is also subjected to the risk of blast-induced liquefaction. Thus, a new total-stress viscoplastic cap model is developed to account for the volumetric constraints imposed by pore water and capture excess pore pressure development due to inelastic deformation during blast loading (Section 4.4). The developed multiphysics models are validated against a series of laboratory and field experiments,

and the effectiveness and predictive ability of the models are verified by good agreement between the simulated and measured results.

4.2 Technical Paper 2: A coupled chemo-viscoplastic cap model for simulating the behaviour of hydrating cemented tailings backfill under blast loading

Published in *International Journal for Numerical and Analytical Methods in Geomechanics* 40(8), 2016, 1123-1149.

Gongda Lu, Mamadou Fall

Abstract

Although the use of blasting has become a routine in contemporary mine operations, there is a lack of knowledge on the response of cement tailings backfills subjected to sudden dynamic loading. To rationally describe such a phenomenon, a new coupled chemo-viscoplastic cap model is proposed in the present study to describe the behaviour of hydrating cemented tailings backfill under blast loading. A modified Perzyna type of visco-plasticity model is adopted to represent the rate-dependent behaviour of the cemented tailings backfill under blast loading. A modified smooth surface cap model is consequently developed to characterize the yield of the material, which also facilitates hysteresis and full compaction as well as dilation control. Then, the viscoplastic formulation is further augmented with a variable bulk modulus derived from a Mie-Grüneisen equation of state, in order to capture the nonlinear hydrostatic response of cemented backfills subjected to high pressure. Subsequently, the material properties required in the viscoplastic cap model are coupled with a chemical model, which captures and quantifies the degree of cement hydration. Thus, the behaviour of hydrating cemented backfills under the impact of blast loading can be evaluated under any curing time of interest. The validation results of the developed model show a good agreement between the experimental and the predicted results. The authors believe that the proposed model will contribute to a better understanding of the performance of cemented backfills under mine blasting, and contribute to evaluating and managing the risk of failure of backfill structures under such a dynamic condition.

KEY WORDS: cemented paste backfill; tailings; viscoplastic cap model; hydration model; coupling; blast

4.2.1 Introduction

Two main types of cemented tailings backfill technologies are prevailing in nowadays mining industry, namely, cemented hydraulic and paste backfills, among which, the cemented paste backfill (CPB) is becoming an increasingly popular backfill technique compared to its alternatives. It is also intensively used in underground mine operations worldwide (Fall et al., 2010a). This is because CPB is more cost-effective in terms of the mechanical performance per unit of cement consumption (Landriault, 2001; Fall et al., 2010b). CPB is a mixture of dewatered mine tailings produced by mineral extraction, binder additives (such as cement, fly ash, slag, etc.) to meet the mechanical stability requirements of backfilling, and water to reach the desired consistency to transport the paste to underground mine openings or stopes (Yilmaz et al., 2009). The application of CPB has been benefiting the mining industry by providing a safe subsurface environment for mine workers by controlling caving and roof falls, thus helping with the effective disposal of mining waste in a more eco-friendly way, and also enhancing the recovery of ore pillars (Bussière B, 2004; Klein and Simon, 2006; Nasir and Fall, 2009, 2010; Huang et al., 2011; Ghirian and Fall, 2013, 2014).

To obtain better knowledge of the performance of CPB in actual mining sequences, especially the process of its strength gain which is associated with the issue of stability as the primary concern, a variety of experiments have been conducted (Fall et al., 2005, 2007; Kesimal et al., 2005; Klein and Simon, 2006; Fall and Samb, 2009; Yilmaz et al., 2009; Fall et al., 2010b; Abdul–Hussain and Fall, 2012; Ghirian and Fall, 2013, 2014). These experiments have helped to provide a better understanding of the mechanical behaviour of CPB under the coupled influence of the environment (e.g. ambient temperature, moisture migration, stress, etc.) and the intrinsic ingredients of the backfill itself (e.g., tailings fineness, density and sulphate content, types of binders, and also mix proportions). Notably, these experiments have been commonly carried out under quasi-static conditions. This is because in practice, self-weight stresses often govern backfill design, and the traditional criterion has been a freestanding wall that requires unconfined compressive strength (UCS) that is at least equal to the overburden stress at the bottom of the filled stope (Emad et al., 2014). However, as field backfills may be subject to mining blasts, rock bursts, as well as earthquake excitations, therefore, an ideal backfill design should accommodate both static loading due to gravity and dynamic loading due to vibration. Hence, it is of paramount importance to determine the response of this type of material under such dynamic

loading conditions, preferably with tantamount consideration for the influence of environmental and other intrinsic factors. Unfortunately, very limited efforts have been made for this purpose in the open literature. van Gool (2007) studied the attenuation of blast waves in cemented backfill at both the laboratory and field scales. Huang et al. (2011) obtained the stress-strain curves of CPB with different curing times and cement contents under high strain rates by using a modified Split-Hopkinson pressure bar (SHPB) system, and strength enhancement was observed. Le Roux (2004) and Saebimoghaddam (2010) investigated the liquefaction of CPB with monotonic and cyclic tests, and the response of field CPB under seismic loading was also determined. However, far-field dynamic events, where low-frequency shear waves are predominant, have been often studied, while details on the response of CPB in the near-field of blast loading where high-frequency compressive waves are dominant (Fragaszy and Voss, 1981, 1986; Charlie et al., 1996; Wang et al., 2008a) remain to be examined thoroughly.

The objective of the current study is therefore to develop and validate a mathematical model that is capable of evaluating the response of hydrating CPB under blast loading. A brief sketch of the interaction between the blast and cemented backfill is illustrated in Figure 4.1. Unlike any other natural material, CPB, especially at the early ages, has material properties that are highly time-dependent mainly due to the cement hydration process. Thus, its mechanical response will be significantly influenced by such a chemical process. There are quite a few models for cement-based materials in which coupled chemo-mechanical processes are considered at the time of writing. Kuhl et al. (2004a, 2004b) and Nguyen et al. (2007a, 2007b) simulated the effect of calcium leaching and damage on the mechanical degradation of cementitious materials, and the deterioration results from thermo-induced desalination and dehydration was investigated by Li et al. (2006). However, time-evolutive hydration process has not been considered in those works. Although the evolutive cement hydration is incorporated in some other researches, the mechanical model has been developed only to recapture the creep (Cervera et al., 1999a, 1999b; Sercombe et al., 2000; Gawin et al., 2006a, 2006b; Li et al., 2015), shrinkage (Ulm and Coussy, 1995; Gawin et al., 2006a, 2006b; Pichler et al., 2007; Li et al., 2015), or cracking behaviours (Zhang et al., 2013; Li et al., 2015) of those materials under quasi-static conditions, and there is no model available at present that can evaluate the response of a cement-based material under transient blast loading.

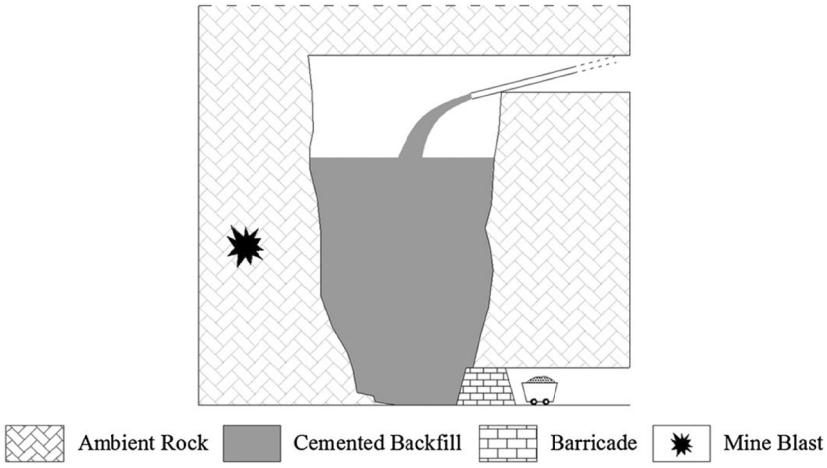

Figure 4.1 Schematic diagram of production blast in mining with cemented backfill

Therefore, to assess such a coupled chemo-mechanical process of cemented backfill, the task of this study should be twofold: first, a model for quasi-static condition of CPB should be developed to quantify the variation of its material properties against curing time; subsequently, a dynamic model for CPB should be developed to characterize its response under blast loading at the time of the curing concerned.

In terms of a mathematical model to describe the quasi-static behaviour of cemented backfill in the course of curing, Nasir and Fall (2009) proposed a thermo-chemical (TC) model to predict the temperature evolution in CPB against the hydration process, and then, this model was extended to quantify the UCS development of CPB (Nasir and Fall, 2010). Wu et al. (2012, 2014) developed a coupled thermo-hydro-chemical (THC) model to evaluate heat transfer and fluid migration during the hydration progress of CPB, and Wu et al. (2013) also developed a similar thermo-mechanical-chemical (TMC) model where the mechanical (M) component was limited to characterizing the rheological behaviour of CPB. In this study, however, unless otherwise specified, the chemical process (C) refers to only the effect of binder hydration.

As for a blast model for backfills, considering that CPB is similar to soils in terms of its phase composition and relatively low levels of diagenetic cementation, therefore, the strategy of modeling soil response under blast loading seems to be extendable for CPB. Given that the primary discrepancy between blast events and static or conventional dynamic problems (e.g. earthquake-related issues) lies in the occurrence of high pressure (or large deformation) and high strain rate, according to Grujicic et al. (2008a), the holistic formulation to solve such transient

nonlinear dynamic problems should include: an appropriate equation of state (EOS) to account for the effect of high pressure on the material during blasting, a realistic failure model to describe the yield behaviour of the system, as well as a strength model to allow the material to incorporate the effects of a high strain rate. Noticeably, Emad et al. (2012, 2014) simulated the blasting response of cemented rockfill. However, the time-dependent evolution of cemented rockfill properties has not been included in their research. Moreover, the Mohr-Coulomb criterion was used, which has been proven inappropriate for high pressure loading conditions, such as blasting (Bloom, 2006), and a constant bulk modulus was considered instead of utilizing a nonlinear pressure-volume relationship for such high magnitude loadings. The study also did not account for the strain rate effect. Similar limitations are found in the work of van Gool (2007). Therefore, although a variety of soil models for blasting are available in the literature to date with good outcomes (Kim and Blouin, 1984; Awad, 1990; Gu and Lee, 2002; Wang and Lu, 2003; Wang et al., 2004a, 2004b, 2005, 2008a, 2011; Lu et al., 2005; Grujicic et al., 2006, 2008a, 2008b, 2009, 2010; Feldgun et al., 2007, 2008a, 2008b, 2011, 2013, 2014; Yankelevsky et al., 2008; Karinski et al., 2009a, 2009b; Ghassemi et al., 2010; Osinov, 2011; An, 2010; An et al., 2011; Higgins et al., 2013; Xu and Zhang, 2015), these models are not applicable to hydrating CPB. A model that is directly applicable to CPB is urgently needed, given the fact that production blast remains the routine in the current operations of mines. Hence, much work needs to be done to characterize the behaviour of cemented backfill in the course of a blast event, compared to the well-developed theories and practices for soils.

The remainder of this paper is organized as follows: the general modeling approach including the assumptions and methodology adopted in the study are first briefly introduced in Section 4.2.2. In Section 4.2.3, a mechanical model used to characterize the response of CPB during blast loading is developed, and coupled with a chemical model to recapture the variation of its material properties with time of curing. Subsequently, the developed model is validated against laboratory experiments in Section 4.2.4. Finally, a discussion on the determination of model parameters and concluding remarks are presented in Sections 4.2.5 and 4.2.6.

4.2.2 Modelling approach

To evaluate the response of hydrating CPB under blast loading, a viscoplastic cap model (mechanical model) is employed and coupled with a chemical model (binder hydration model) which quantifies the progress of binder hydration.

The chemical model has the ability to describe and capture chemical reactions (binder hydration) that occur within the CPB. The progress of the binder hydration can be captured by predicting the degree of binder hydration. The degree of binder hydration is the measure of hydration product formation on a microscopic scale, and associated with the development of mechanical and other properties of cementitious materials at the macroscopic level. To evaluate the process of the binder hydration in CPB, the model of Schindler (2004) and Schindler and Folliard (2005) is adopted. The influence of temperature and moisture migration is not included in the present study, and binder hydration is considered as the only chemical process in the CPB. The effect of sulphate attack on CPB is excluded, because not all tailings and CPB mixing waters contain sulphate ingredients, and also the reactivity of sulphide minerals in a CPB system is negligible as CPB has a high degree of water saturation, and the resulting reduction in porosity and hydration products act as a physical barrier against oxygen during the cement hydration process (Fall et al., 2005; Fall and Pokharel, 2011). Meanwhile, since blast loading is characterized by high intensity as well as short duration, the hydration process, which in general takes a longer time span to induce a pronounced influence on the CPB, is neglected in the course of blasting. Finally, the effects of the mechanical process due to gravity and blasting on the binder hydration are not considered here for the sake of simplicity.

A mechanical model based on viscoplastic cap models is adopted in the current study as the constitutive law to characterize the response of CPB under blast loading. This type of model works well for geomaterials under high pressure, and is capable of recapturing the strain rate effect. It has been utilized and validated in Katona (1984), Simo et al. (1986), Tong and Tuan (2007), An et al. (2011), Aráoz and Luccioni (2015), etc. for both high and low strain rate phenomena. In addition, a variable bulk modulus is also employed herein to account for the nonlinear pressure-volume relationship (EOS) of CPB under high amplitude impact. Details and formulation of the model will be elucidated in Section 4.2.3. All of the material properties used in the variable-modulus viscoplastic cap model of the CPB are coupled with the degree of binder hydration, i.e. to the chemical model. Finally, the developed model is implemented into the

commercial software COMSOL Multiphysics (COMSOL AB, Stockholm, Sweden) for finite element simulation.

4.2.3 Formulation of the model

4.2.3.1 Formulation of model for binder hydration

In order to quantify the evolution of the binder hydration process, as mentioned above, the equation for the degree of binder hydration proposed by Schindler (2004) and Schindler and Folliard (2005) for cementitious materials is adopted. This equation has been successfully applied to predict the progress of binder hydration for CPB (e.g. Wu et al., 2012, 2014), and is expressed as

$$x = x_u \cdot \exp\left[-\left(\frac{t}{t_e}\right)^b\right] \tag{4.1}$$

where x is the degree of binder hydration which represents the fraction of the binder that has reacted at an equivalent age t_e, t is the hydration time parameter at the current temperature of the cement-based material, b is the hydration shape parameter, and x_u the ultimate degree of binder hydration, which depends only on the water-binder ratio (*w/c*) and has been modified by Wu et al. (2012, 2014) as

$$x_u = \begin{cases} \dfrac{1.031 w/c}{0.194 + w/c}, & w/c < 6.258 \\ 1, & w/c \geq 6.258 \end{cases} \tag{4.2}$$

To account for the effect of the curing temperature on the rate of hydration, the equivalent age maturity function based on the Arrhenius definition can be used. It converts the chronologic curing age t of the cement based material at any temperature T_c to the equivalent age t_e at the reference temperature T_r, and can be expressed as (Schindler and Folliard, 2005):

$$t_e(T_r) = \sum_0^t \exp\left(\frac{E_a}{R_a}\left(\frac{1}{273+T_r} - \frac{1}{273+T_c}\right)\right)\Delta t \tag{4.3}$$

where R_a is a universal gas constant, and E_a is the apparent activation energy (J/mol). Since the effect of temperature is not considered in the current study, the equivalent age t_e will be equal to the chronologic curing age t.

4.2.3.2 Formulation of the mechanical model for blast loading

4.2.3.2.1. Perzyna type of viscoplastic formulation

It has been revealed that the strain rate effect has a significant influence on the stiffness, strength and other mechanical behaviours (such as pore pressure response, maximum failure strain, liquefaction resistance and particle breakage) of soils, during experiments of uniaxial, triaxial, plate impact and split Hopkinson pressure bar (SHPB) tests, etc. (Casagrande et al., 1948; Whitman, 1970; Jackson et al., 1980; Prapaharan et al., 1989; Bolton et al., 1994; Sheahan et al., 1996; Zhu and Yin, 2000; Omidvar et al., 2012; Torisu et al., 2012). Recently, the strain rate effect has been also observed for CPB (Huang et al., 2011). Some attribute the stiffness and strength improvement to the resulting undrained condition from the impact of high-strain rates, and the pore water pressure would decrease and the effective stress increase due to material dilation (Omidvar et al., 2012). However, it is more convincing that this should be associated with the mechanism of micro-cracking development during transient loading. To be more specific, compared with static loading, more micro-cracks will be generated from high-strain rate impact, and it would require more energy to initiate major cracks or failure after overcoming the inertial resistance of the material (Cai et al., 2007).

Very few attempts have been made to explicitly characterize the effect of high strain rates on soft porous materials (like soil or CPB) in the course of blasting. A three phase soil model (Wang et al., 2004a, 2004b) has accounted for the strength enhancement of soil under blast shocks with a phenomenological method. Later, the effect of high strain rates on both the strength and stiffness of soil was incorporated in work by Xu and Zhang (2015) with a similar strategy. Alternatively, to take the effect of high strain rates into account for both strength and stiffness, formulations of viscosity have been integrated with conventional plasticity, i.e. resulting in the so-called viscoplasticity. There are two popular viscoplastic models to account for the high strain rate phenomenon in the literature, the viscoplastic formulations of Duvaut-Lions (Simo et al., 1988; Schwer, 1994; Schwer and Murray, 1994; Motamedi and Foster, 2015) and Perzyna (Perzyna, 1966; Katona, 1984; Simo et al., 1986; Tong and Tuan, 2007; An et al., 2011; Higgins et al., 2013).

A detailed comparison between the viscoplasticity model of Duvaut-Lions and the more popular model of Perzyna can be found in Schwer (1994) in terms of their algorithms and performances. However, from a practical point of view, the former should be easier in terms of

numerical implementation, as it is in fact an extension of the inviscid formulation, while the latter appears to provide more flexibility for data fitting because it involves more viscosity parameters, although the solution algorithm is inevitably more complicated as it requires matrix operations (An, 2010).

The current study adopts a viscoplastic formulation for CPB that is based on the Perzyna model. As is the convention in mechanics, it is possible to decompose the total strain rate vector $\dot{\boldsymbol{\varepsilon}}$ into an elastic part $\dot{\boldsymbol{\varepsilon}}^{e}$ and a viscoplastic (inelastic) part $\dot{\boldsymbol{\varepsilon}}^{vp}$ as

$$\dot{\boldsymbol{\varepsilon}} = \dot{\boldsymbol{\varepsilon}}^{e} + \dot{\boldsymbol{\varepsilon}}^{vp} \tag{4.4}$$

The elastic strain rate is independent of viscosity and expressed as

$$\dot{\boldsymbol{\varepsilon}}^{e} = \mathbf{D}^{-1}\dot{\boldsymbol{\sigma}} \tag{4.5}$$

where $\dot{\boldsymbol{\sigma}}$ is the stress rate tensor, and $\mathbf{D}$ the elastic stiffness matrix which for isotropic material can be defined in terms of bulk and shear moduli K and G as

$$\mathbf{D} = \begin{bmatrix} K+\frac{4G}{3} & K-\frac{2G}{3} & K-\frac{2G}{3} & 0 & 0 & 0 \\ K-\frac{2G}{3} & K+\frac{4G}{3} & K-\frac{2G}{3} & 0 & 0 & 0 \\ K-\frac{2G}{3} & K-\frac{2G}{3} & K+\frac{4G}{3} & 0 & 0 & 0 \\ 0 & 0 & 0 & G & 0 & 0 \\ 0 & 0 & 0 & 0 & G & 0 \\ 0 & 0 & 0 & 0 & 0 & G \end{bmatrix} \tag{4.6}$$

Due to the formation and evolution of the microstructure of the CPB during the binder hydration progress, K and G will not be constants in the CPB but will vary with time. In order to capture the variation of the elastic constants that pertain to the degree of binder hydration, the model of Cui and Fall (2015, 2016) is adopted, and expressed as

$$\frac{E(x)}{E_u} = \left(\frac{x - x_0}{x_u - x_0} \right)^{A} \tag{4.7}$$

where $E(x)$ is the elastic modulus at a given degree of binder hydration x ; E_u and x_u are the ultimate elastic modulus and degree of hydration, respectively; x_0 indicates the reference degree of hydration below which no development of elastic constants occurs; and A is a material

constant. Furthermore, to characterize the variation of the Poisson's ratio, v, with degree of hydration, the following expression is (Cui and Fall, 2015, 2016)

$$n(x) = 0.5\exp(B_1 x) + B_2 x^{B_3}\exp(B_4 x^{B_5}) \tag{4.8}$$

where B_1, B_2, B_3, B_4 and B_5 are the fitting parameters. Then, E and v are related to K and G as

$$K = \frac{E}{3(1-2v)} \quad , \quad G = \frac{E}{2(1+v)} \tag{4.9}$$

For the viscoplastic strain rate, the viscoplastic flow rule is generally expressed as:

$$\dot{\boldsymbol{\varepsilon}}^{vp} = h\left\langle f(f)\right\rangle \frac{\partial f}{\partial \boldsymbol{\sigma}} \tag{4.10}$$

where h is a fluidity parameter that is a material constant; $\langle\ \rangle$ is the Macaulay bracket defined as $\langle x\rangle = x + |x|/2$, f is the yield function and will be introduced in the following subsection, and $f(f)$ is a dimensionless viscous flow function, which is commonly expressed in one of the two following forms:

$$\begin{aligned} f(f) &= \left(\frac{f}{f_0}\right)^N \quad \text{(a)} \\ f(f) &= \exp\left(\frac{f}{f_0}\right)^N - 1 \quad \text{(b)} \end{aligned} \tag{4.11}$$

where N is the exponent and f_0 is the normalizing constant with the same unit as f. The direction of $\dot{\boldsymbol{\varepsilon}}^{vp}$ is given by f and in the outward normal direction of a dynamic yield surface, i.e. the associated flow rule is used for the viscous behaviour of the material. As can be observed, in the overstress theory of Perzyna for characterizing the viscoplastic behaviour of materials, $f(f)$ is used to quantify the overstress, i.e. the distance between the viscoplastic stress state and the yield surface (Higgins et al., 2013). The Equation (4.11a) is used in the present study, and the parameters h , N and f_0 can be determined by trial and error (Katona, 1984; Tong and Tuan, 2007).

The application of the Perzyna model on viscosity for cementitious material is rare in the literature (Simo et al., 1986; Ning et al., 2008; Aráoz and Luccioni, 2015). To simplify the modeling, N and f_0 are assumed to be constant in the present study, while h will vary with the hydration process, and will be determined by developing a function that relates its value to the degree of binder hydration based on the experimental data. According to Equation (4.10), the

material response will be purely elastic when $h \rightarrow 0$, while it corresponds to simple inviscid plasticity when $h \rightarrow \infty$.

4.2.3.2.2 Modified plastic cap model

Monotonous yield functions that pertain to I_1 (the first invariant of the stress tensor) have been widely used in soil models, or even in cement backfill models for blast loading, for example, the Drucker-Prager (Wang et al., 2004a, 2004b, 2008a, etc.), Mohr-Coulomb (Emad et al., 2014), and Lundborg criteria (Feldgun et al., 2008, 2011, 2013, etc.), etc. Although they work reasonably well at low pressures, the performance of these types of models is not satisfactory in high pressure conditions. First, it is not reasonable to assume that the yield limit of a geomaterial will increase as long as I_1 is increasing. Furthermore, if the associated flow rule is used in the plastic flow scheme, those models will produce excessive and unrealistic dilatancy than those experimentally observed. An effective approach to control dilatancy is to adopt a non-associated flow rule. However, this treatment may lead to the problem of uniqueness of solution (Bloom, 2006).

Although the bounding surface plasticity theory has been successfully extended to describe the high-rate impact of soils (Higgins et al., 2013; Xu and Zhang, 2015), it suffers from the difficulty in determining a large number of parameters for the yield envelope. In contrast, plastic cap models are superior in this regard and do not suffer from the said previous issues. Thus, a plastic cap model will be utilized in the current study to characterize the yield behaviour of CPB under blast loading. Details and advantages of plastic cap models over their counterparts will be elucidated in the following, and the extension of plastic cap models to incorporate the progress of binder hydration will be discussed.

i) Smooth strain-hardening cap model

The two-invariant cap model was originally proposed by DiMaggio and Sandler (1971) and then generalized by Sandler et al. (1979) and Sandler and Rubin (1979). For isotropic materials, the yield surface that is characterized by a plastic cap model has the form

$$f(I_1, \sqrt{J_2}, k) = 0 \tag{4.12}$$

where J_2 is the second invariant of the stress deviators, and k is a hardening parameter and a function of the history of the volumetric plastic strain e_{kk}^{p} . In general, its yield surface is assumed to consist of two parts combined: a fixed ultimate (shear) failure envelope and a strain-hardening elliptic cap (Chen and Baladi, 1985) (Figure 4.2), while in its later modifications, a tension cutoff was added.

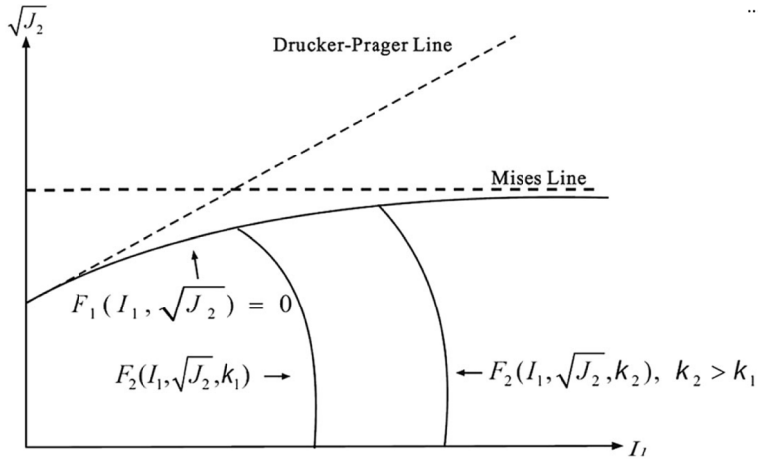

Figure 4.2 Yield surface of the plastic cap model (modified after Chen and Baladi, 1985)

Two different forms of shear yield functions have been widely used in cap models. In the first expression, the fixed shear yield surface approximates the linear Drucker-Prager criterion at low pressures, and joins smoothly to a von Mises condition at high pressures (Equation (4.13a)), while the second expression simply adopts a linear Drucker-Prager criterion as the shear failure envelope (Equation (4.13b)).

$$F_1(I_1, \sqrt{J_2}) = \sqrt{J_2} - [A' - C' \exp(-B' I_1) + D' I_1] \quad \text{(a)}$$
$$F_1(I_1, \sqrt{J_2}) = \sqrt{J_2} - a\, I_1 - k \quad \text{(b)} \qquad (4.13)$$

where a and k, and A', B', C' and D' are the material constants to be calibrated. A comparison has been made on the influence of these two different functions in cap models, and their effect has been found to be negligible when the pressure is high (Ghassemi et al., 2010).

Notably, traditional cap models suffer from the numerical complexity of singular corners, and these are located at the intersection of the shear failure envelope and hardening cap, where the former has a positive tangent while the latter is horizontal at that point. To alleviate such a

problem, a transition technique has been introduced by Schwer (1994) and Schwer and Murray (1994). By multiplying the cap ellipse function by the shear surface function, the complete failure envelope would take on the same slope at such intersection. This model has been termed as a smooth cap model or a continuous surface cap model (CSCM), and similar treatment for such an intersection point has been widely used (Foster et al., 2005; Sun et al., 2014; Motamedi and Foster, 2015). However, in this type of model, the product of a monotonically increasing shear yield function and a decreasing cap expression (with respect to I_1) would mean that the range of the cap is ambiguous, i.e. the ratio of the major to the minor axis of the elliptic cap (R) will not be constant during the hardening process, and will be different from the R value that is specified by the modeller. Therefore, the volumetric dilation/compaction behaviour of materials cannot be effectively controlled.

In order to avoid this problem, and in the meantime treat such singular corners with relative simplicity, a new transition approach will be introduced in the present model. In considering the insignificant influence from the shape of the shear envelope under high pressure, such a shear yield surface is assumed to have the same intercept with $\sqrt{J_2}$ axis as the Drucker-Prager criterion at the beginning; then, it is forced to turn absolutely horizontal at the intersection with the hardening cap. This can be realized with a parabolic curve and the following restrictions:

$$\begin{cases} F_1(I_1,\sqrt{J_2}) = \sqrt{J_2} - Y = \sqrt{J_2} - (aI_1^2 + bI_1 + c) \\ Y(I_1 = 0) = k \\ -\dfrac{b}{2a} = L(k) \\ Y(I_1 = L(k)) = \dfrac{1}{R}[X(k) - L(k)] \end{cases} \tag{4.14}$$

where $L(k)$ and $X(k)$ is the abscissa of the intersection of the elliptic cap with the shear failure envelope and the hydrostatic loading line (I_1 axis), respectively. Then, the shear envelope can be obtained as

$$F_1(I_1,\sqrt{J_2}) = \sqrt{J_2} - \frac{k-[X(k)-L(k)]/R}{L(k)^2} I_1^2 + 2\cdot\frac{k-[X(k)-L(k)]/R}{L(k)} I_1 - k \tag{4.15}$$

where k for the Drucker-Prager criterion can be related to the Mohr-Coulomb criterion by

$$a = \frac{2\sin j}{\sqrt{3}(3+\sin j)}, \quad k = \frac{6c\cos j}{\sqrt{3}(3+\sin j)} \tag{4.16}$$

where c and j is the cohesion and internal friction angle, respectively.

The hardening cap will be defined by following the conventional:

$$F_2(I_1,\sqrt{J_2},k)=\sqrt{J_2}-\frac{1}{R}\left\{\left[X(k)-L(k)\right]^2-\left[I_1-L(k)\right]^2\right\}^{1/2} \tag{4.17}$$

where $X(k)$ can be expressed with a logarithmic hardening law as

$$X(k)=-(1/D)\cdot\ln\left(1-\frac{e_{kk}^{p}}{W}\right)+X_0 \tag{4.18}$$

where W indicates the maximum volumetric plastic strain of the material, D is a shape parameter of the volume-pressure curve, and X_0 is the initial vertex of the hardening cap. These parameters can be determined from isotropic compression tests. Then, $L(k)$ can be obtained by enforcing continuity:

$$k=\frac{X(k)-R\cdot k}{1+R\cdot a} \tag{4.19}$$

and

$$L(k)=\begin{cases} k & k>k_0 \\ k_0 & \text{otherwise} \end{cases} \tag{4.20}$$

where k_0 is the onset of the cap.

According to the formulation, the hardening cap in a plastic flow scheme is not fixed in a stress space, and will expand or contract as the plastic volumetric strain varies. For example, during initial compaction, the location of the cap ($X(k)$) expands as e_{kk}^{p} grows; after that, when the stress state satisfies the shear yield criterion, dilatancy takes place due to the associated flow assumption, and the decrease in e_{kk}^{p} would thereby lead to the shrinkage and movement of the ellipse cap against the origin point, and the dilation would continue until the cap reaches the stress point on the shear yield surface (DiMaggio and Sandler, 1971; Bloom, 2006; Tu and Lu, 2009; Gu and Lee, 2009). When this occurs, this stress point becomes the intersection of the shear yield and the cap surface, and the plastic strain rate vector is absolutely vertical, so any cap motion that would result from further plastic volumetric strain is precluded; in this way, the amount of dilatancy is controlled. Besides, the existence of the cap also facilitates consideration for the yield of geomaterials under large hydrostatic pressure, i.e. in such extreme loading conditions where soils or CPB behaves similar to a fluid state, the yield condition should be essentially independent of I_1 (DiMaggio and Sandler, 1971), instead of growing without limit.

According to Chen and Baladi (1985), the hysteresis effect, which is a typical behaviour of geomaterials with great engineering significance, can be recaptured by applying the cap model. The hysteresis effect is considered to be the key mechanism that leads to the liquefaction of soils during blast loading (Fragaszy and Voss, 1981; 1986). In general, there are two main scenarios that contribute to the hysteresis effect (Nelson et al., 1971; Bloom, 2006). The first is from the yield of the material, and the second is from the different pressure-volume relationships upon hydrostatical loading and unloading. However, the hysteresis generated by the latter is considered to be predominant in soft porous materials like soil or CPB (Nelson et al., 1971; Bloom, 2006), especially given the wide range of pressures encountered during blast loading. Therefore, according to Nelson et al. (1971) and Bloom (2006), the use of a constant bulk modulus, or application of a path-independent and nonlinear EOS for porous skeletons upon loading and unloading is not sufficient in reproducing the material hysteresis. In order to control the amount of hysteresis during blasts independently of the yield conditions, some researchers have used different prescribed bulk moduli in the loading and unloading paths for soil skeletons with a bilinear model (Kim and Blouin, 1984), and others have used different functions to control the loading and unloading processes (Yankelevsky et al., 2008; Karinski et al., 2009a, 2009b; Laine and Sandvik, 2001). However, a more sophisticated method without any mathematical uncertainties, and at the same time, one that better fits experimental data (Nelson et al., 1971; Merkle et al., 1985; Bloom, 2006), is the plastic cap model. It has already been adopted, e.g. in Awad (1990), Gu and Lee (2002), Ghassemi et al. (2010), An et al. (2011), etc. for modeling soil response during dynamic loading which originates from subsurface explosions or impulsive impacts from blows by tamping. Specifically, if the stress state is located on the cap portion of the yield surface during initial compaction, the cap envelope and the associated flow will cause volumetric plastic strain in compression. Since unloading is elastic, there will be unrecoverable bulk deformation and the hysteresis effect is thus realized (Figure 4.3).

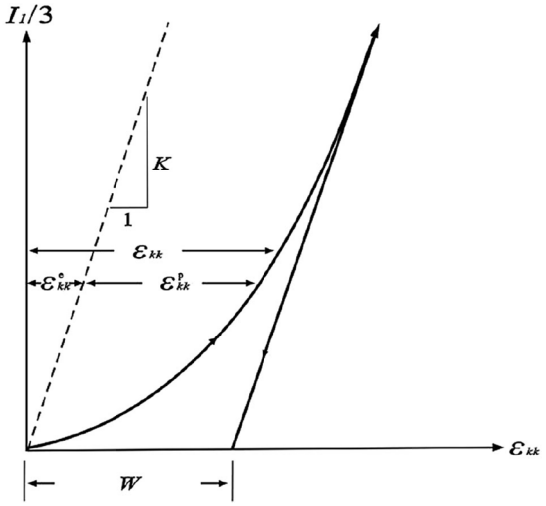

Figure 4.3 Hysteresis effect represented by the cap model

(Modified after Chen and Baladi, 1985 and Murray, 2007; where *K* is bulk modulus, and e_{kk} and e_{kk}^{e} are total and elastic volumetric strain, respectively)

ii) Chemical hardening extension

During the process of binder hydration, the microstructure of the CPB develops and the strength parameters will increase as macroscopic manifestations. As a result, the yield surface will evolve in the stress space (hardening due to chemical reaction). The yield function in the regard will be denoted by $f(I_1,\sqrt{J_2},k,x)$, which consists of a chemical hardening shear failure portion $F_1(I_1,\sqrt{J_2},x)$, and a chemical and strain hardening cap portion $F_2(I_1,\sqrt{J_2},k,x)$. For the chemical hardening of the shear failure envelopes, the model by Cui and Fall (2015, 2016) is adopted here to quantitatively recapture the growth of the cohesion and internal friction angle of CPB with respect to the degree of binder hydration:

$$\begin{cases} c(x) = M_1 x^{M_2} \\ j(x) = N_1 x^{N_2} + N_3 x \end{cases} \tag{4.21}$$

and

$$a(x) = \frac{2\sin j(x)}{\sqrt{3}\left[3+\sin j(x)\right]}, \qquad k(x) = \frac{6c(x)\cos j(x)}{\sqrt{3}\left[3+\sin j(x)\right]} \tag{4.22}$$

where M_1 and M_2, and N_1, N_2 and N_3 are the fitting constants. Therefore, the shear failure surface can be rewritten as

$$F_1(I_1,\sqrt{J_2},x)=\sqrt{J_2}-\frac{k(x)-[X(k)-L(k)]/R}{L(k)^2}I_1^2+2\cdot\frac{k(x)-[X(k)-L(k)]/R}{L(k)}I_1-k(x) \quad (4.23)$$

For the cap portion of the yield function, the chemical hardening due to binder hydration is augmented to the original strain hardening formulation. Isotropic compression testing (Green and Swanson, 1973) and numerical applications of the cap models for concrete (Simo et al., 1986; Murray, 2007; Jiang and Zhao, 2015) are summarized (see Figure 4.4), in order to capture the evolution of the parameters required to define the chemo-plastic hardening cap envelope with the hydration process. By following the work in Murray (2007) and Jiang and Zhao (2015), and given that the curing time is not known, all of the cap parameters were calibrated against the UCS. Besides, in considering that fresh cemented tailings backfill may behave in a similar manner as saturated sandy soil when just placed and its strength has not been developed yet, the parameters of a cap model used for saturated sandy soil (An et al., 2011) have also been used. In numerical cases where a nonlinear Drucker-Prager criterion has been used (e.g. Equation (4.13a)), the initial linear portion of such envelope is adopted to determine c and j , thus determining the UCS in accordance with the Mohr-Coulomb criterion.

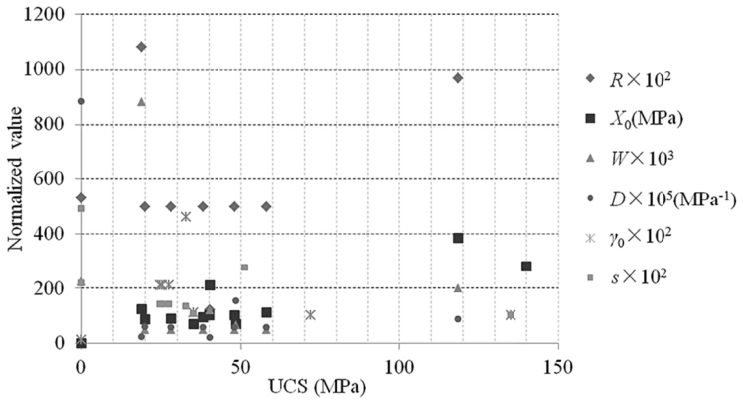

Figure 4.4 Variation of cap and Mie–Grüneisen equation of state parameters against unconfined compressive strength of cementitious material (concrete)

As can be concluded from Figure 4.4, no general trend can be identified for R, W, and D, while an obvious increase is observed for X_0 with respect to the UCS. Therefore, in the chemo-plastic hardening cap, only X_0, i.e. the initial location of the cap, will be treated to vary with UCS (or degree of hydration) of the cementitious material, while the other parameters are assumed to be constant. Thus, the function of the hardening cap can be rewritten as:

$$F_2(I_1,\sqrt{J_2},k,x)=\sqrt{J_2}-\frac{1}{R}\left\{\left[X(k,x)-L(k,x)\right]^2-\left[I_1-L(k,x)\right]^2\right\}^{1/2} \tag{4.24}$$

Accordingly, the hardening law will be recaptured by

$$X(k,x)=-(1/D)\cdot\ln\left(1-\frac{e_{kk}^{p}}{W}\right)+X(x)_0 \tag{4.25}$$

Then, the intersection of the cap and the shear envelope can be obtained by using

$$k(x)=\frac{X(k,x)-R\cdot k(x)}{1+R\cdot a(x)} \tag{4.26}$$

and

$$L(k,x)=\begin{cases} k(x) & k(x)>k(x)_0 \\ k(x)_0 & \text{otherwise} \end{cases} \tag{4.27}$$

The remaining task, obviously, is to relate the UCS of cementitious materials to the degree of binder hydration. Once the internal friction angle and cohesion of the CPB during the process of hydration are obtained (with Equation (4.21)), its UCS (f_c) can be evaluated with the Mohr-Coulomb criterion:

$$f_c=2c(x)\tan[45^{\circ}+\frac{j(x)}{2}] \tag{4.28}$$

Thus, all parameters in the yield function have been directly or indirectly coupled with x. Finally, the modified cap model $f(I_1,\sqrt{J_2},k,x)$ is used as the yield function f in Equation (4.10), and the inelastic volumetric strain ($e_{kk}^{inelastic}$) obtained from such a viscous flow rule will contribute to the strain hardening of cap envelope in the modified cap model.

4.2.3.2.3 Nonlinear pressure-volume relationship (EOS)

Under extremely intensive compactions during blast shocks, the pressure-volume relationship of a material would be typically nonlinear (Henrych, 1979). Various expressions of equation of state (EOS) have been adopted to represent this nonlinear bulk behaviour of soil in hydrocodes. Some examples are the Lyakhov's model of the soil as a three-phase medium (Henrych, 1979; Wang et al., 2003, 2004a, 2004b, 2008a; Feldgun et al., 2008, 2014; An et al., 2011), Mie-Grüneisen type of EOS (An et al., 2011), Shock-Hugoniot EOS (Karinski et al., 2009a, 2009b; Feldgun et al., 2013), etc. An equation of state is a thermodynamic equation to characterize the state of matter under given physical conditions. More practically, in impact

engineering, an EOS is usually defined as a semi-empirical relationship between thermodynamic state variables (such as pressure, density or volume, internal energy, etc.) of a material for a given set of initial conditions based on experimental calibrations (the Rankine-Hugoniot curve) (Zukas, 2004). However, since the current research will not be carried out with a hydrocode, and an updated pressure-volume algorithm is not directly available, the variable-bulk-modulus approach will be utilized instead of an EOS for CPB. In fact, this strategy has been adopted by Nelson et al. (1971), Sandler et al. (1976), Chen and Baladi (1985) and Murray and Lewis (1995) among others, and supplemented with a plastic cap model to acquire better flexibility in data fitting.

The expression for the variable bulk modulus used in the present study is derived from a Mie-Grüneisen EOS, and written as (An et al., 2011):

$$K = \frac{r_0 C_0^2 [1+(1-\frac{g_0}{2})m - \frac{a_0}{2}m^2][1+\frac{2m(s-1)}{1+m-sm}+\frac{m(g_0+a_0 m)}{(1+m)^2}] + r_0 C_0^2 m(1-\frac{g_0}{2}-a_0 m)}{(1+m-sm)^2} + \left[\frac{(g_0+a_0 m)^2}{(1+m)^2}+a_0\right]E^v \quad (4.29)$$

where r_0 is the material density; C_0 is the sound speed of CPB at an ambient pressure and temperature; s is the slope of the shock velocity against the particle velocity curve; g_0 is the Grüneisen parameter, E^v is the internal energy per unit initial volume; a_0 is the first order volume correction to g_0 and often set to 0; and $\mu=(V_0/V) - 1$ with V and V_0 as the current and initial volumes of an element.

Obviously, the pressure-volumetric strain relationship derived from the cap model in Figure 4.3 would in fact represent the EOS of the material. It should be emphasized that in addition to the hysteresis behaviour, the plastic cap model is also capable of recapturing the full compaction phenomenon of porous materials. Full compaction indicates a state of complete closure of the internal pores in a porous mass (Karinski et al., 2009a), and this corresponds to e_{kk}^{p} approaching W in the cap model, and the hysteresis effect can exist until the associated full compaction density is exceeded. According to Karinski et al. (2009a), there are three different types of loading patterns beyond full compaction, i.e. the simplistic linear, full locking (an infinite increase of pressure during compaction approaching a fixed density), and polynomial patterns, in which the latter interpolates between the former two and is the most widely accepted in EOS for porous materials. It can be observed that, such linear pattern in fact would correspond to the material response with a constant bulk modulus in the cap model (see in Figure 4.3). Moreover,

by augmenting the feature of variable bulk modulus into the cap model, the polynomial pattern can be recovered and has been illustrated in Murray and Lewis (1995).

During the process of binder hydration, the density of CPB will be mainly controlled by the migration of water, i.e. drainage and evaporation. In other words, its density will be affected by the boundary conditions of curing. For the sake of simplicity, and given that the variation of CPB density with time is generally insignificant (less than 10% in Ghirian and Fall (2013)), r_0 will be assumed to be constant in the present study. In order to obtain the evolution of the Grüneisen parameters g_0 and s with the hydration process, Hugoniot data (Gebbeken et al., 2006; Wang et al., 2008b) and numerical applications of Mie-Grüneisen EOS for concrete (Ning et al., 2008; Riedel et al., 2008; Wang et al., 2009) are summarized and expressed in terms of the UCS (see Figure 4.4). Besides, considering that fresh cemented tailings backfill may behave relatively similar to saturated sandy soil, those two parameters acquired from high pressure tests (Wardlaw et al., 1996), and those used in a numerical case (An et al., 2011) of saturated sand have also been added. Due to the lack of data on strength, the UCS of saturated sand in the latter case is assumed to be identical to that in the former case.

As can be observed from Figure 4.4, no general trend can be recognized for g_0. Furthermore, since the Grüneisen parameter g_0 is generally a function of material density (Rice et al., 1958; Murray and Lewis, 1995), thus it is also assumed to be a constant in the current study. In contrast, a more obvious pattern of reduction in s vs. UCS can be noticed. Considering that, in general, water content is negatively proportional to the UCS of hydrating cementitious materials, and s of the simulant sand at low water saturation is similar to that of dry sand, but becomes sensitive to water content at higher degrees of water saturation (Chapman et al., 2006), an exponential expression can be employed to relate s to the UCS of a cementitious material.

Then, the value of C_0 can be chosen so that the K value when μ=0 defined by Equation (4.29) equals to that of the initial value provided by Equations (4.7) – (4.9) (i.e. C_0 is hydration-dependent). Consequently, Equation (4.29) can be rewritten as:

$$K(x)=\frac{r_0 C(x)_0^2[1+(1-\frac{g_0}{2})m-\frac{a_0}{2}m^2][1+\frac{2m[s(x)-1]}{1+m-s(x)m}+\frac{m(g_0+a_0m)}{(1+m)^2}]+r_0C(x)_0^2m(1-\frac{g_0}{2}-a_0m)}{[1+m-s(x)m]^2} + \left[\frac{(g_0+a_0m)^2}{(1+m)^2}+a_0\right]E^v \tag{4.30}$$

4.2.3.2.4 Arbitrary Lagrangian-Eulerian formulation

Partial differential equations (PDEs) that are used to solve multi-physics problems are generally expressed in either the Eulerian (spatial) coordinate or Lagrangian (material) coordinate system. In the former, the coordinate axes are fixed in space, and it is the most widely adopted in soil mechanics or multi-physics analysis in which the physical state at fixed points in space is the primary concern. However, the Eulerian coordinate system is inherently lacking in its ability to treat moving boundaries, and suffers from mesh entanglement and accuracy problems when the mesh distortion is severe. In the course of blast loading, there can be large material deformations, which may cause the mapping from the mesh to the spatial coordinates to become ill-conditioned, thus leading to the aforementioned mesh entanglement and accuracy problems. In contrast, the Lagrangian coordinate system is fixed to the material, and moves along with the transport of the material particles, and therefore does not have the issues of the Eulerian coordinate system, although it is more computationally intensive (ANSYS Inc., 2009; COMSOL AB, 2009). In considering these factors, an arbitrary Lagrangian-Eulerian formulation (ALE) is used in the present CPB model for blast loading. The previous numerical issues can be addressed through the remeshing feature in the ALE method, i.e. it can suspend calculations before the mesh degrades to unacceptable levels, build a new mesh system in the current domain, then map all of the model quantities to the new mesh and restart calculation. The ALE method incorporates the advantages of the Eulerian and Lagrangian formulations, and allows the moving of boundaries and analyzing of physical states of materials at fixed points in space (COMSOL AB, 2009).

4.2.4 Model validation

4.2.4.1. Introduction

The chemo-viscoplastic cap model developed in this study is parameterized and validated against a set of SHPB tests on hydrating CPB, and will be discussed in this section, in terms of the peak axial stress, and the strain-stress history. To demonstrate its versatility, the model is then employed to simulate the stress-strain response of other types of cementitious materials, and mortar is used an example. In addition, blast tests on a soil have also been numerically reproduced in the validation, in order to demonstrate the applicability of the model developed in

this study to uncemented tailings backfills as well as comparability to previous viscoplastic cap models.

4.2.4.2 Simulations of high strain rate experiments on CPB

Huang et al. (2011) studied the dynamic response of CPB at different curing times and cement contents under high strain rates by using a modified split Hopkinson pressure bar (SHPB), and enhancement in strength was observed in their laboratory tests. Some of their quasi-static data can be found in Klein and Simon (2006). Their experimental results are adopted to validate the developed chemo-viscoplastic cap model in this study.

In accordance with the cement type and mix proportion (5% cement content) used, the empirical parameters in Equation (4.1) can be obtained with t =13.69, b = 0.905 (Schindler, 2004), and x_u = 1. By using the data from quasi-static experiments for CPB with 5% cement content (Klein and Simon, 2006), the fitting constants in Equation (4.7) can be determined with E_u = 282.3 MPa, x_0 = 0.09, and A= 36.3. Since there was no measurement for the Poisson's ratio, the original fitting parameters provided in Cui and Fall (2015, 2016) are adopted for Equation (4.8), with B_1 = -0.2, B_2= -15000, B_3 = 7, B_4= -10.98 and B_5 = 0.7. Due to the unavailability of knowledge on the cohesion ($c(x)$) and internal friction angle ($j(x)$) in their experiments, $j(x)$ is assumed to be a constant and equal to 38^o based on the experimental evidence which shows its low sensitivity to the degree of binder hydration (Ghirian and Fall, 2014). Then, $c(x)$ can be determined in accordance with the Mohr-Coulomb criterion and the associated UCS. The fitting constants in Equation (4.21) are subsequently obtained by using a regression analysis, with M_1 = 0.234 MPa and M_2= 30.3. A previous simulation has been conducted to determine the relationships between the UCS (f_c, in MPa) and the variables h , X_0 and s required in the modeling. The results for this studied CPB can be expressed as

$$X(x)_0\,(\mathrm{MPa}) = 52.9\ln(0.03 f_c + 0.236) + 75.5 \tag{4.31}$$

with a correlation coefficient of 0.83 for the data shown in Figure 4.4; and

$$s(x)(1) = 2.06\exp(-4.38 f_c + 0.779) + 1.5 \tag{4.32}$$

with a correlation coefficient of 0.84 for the data shown in Figure 4.4; and

$$h(x)(\mathrm{s}^{-1}) = 48.2 \cdot (f_c + 0.224)^{-3.51} + 0.002 \tag{4.33}$$

The tested specimens in Huang et al. (2011) are cylindrical with 22 mm in diameter and 10 mm in height. In the simulation, only one quarter of those specimens is modelled with axially symmetric elements. To simplify the modeling process, the typical loading history pattern in the SHPB tests for CPB in Huang et al. (2011) is used (Figure 4.5). Axial velocity increments are applied at one end of the specimen while the other end is fixed, and it is not laterally confined according to the experiment configuration. With the information obtained for the material properties versus the degree of binder hydration (direct or indirect), the simulated results for the peak axial stress of CPB cured for 15 and 30 days with a 5% cement content are presented in Figures 4.6 and 4.8 with various strain rates, and the associated stress-strain curves are shown in Figures 4.7 and 4.9 with the use of the proposed viscoplastic cap model. Parameters used in the simulation are listed in Table 4.1. The numerically obtained stress-strain curves have not been compared with experimental data since the latter are not available.

Table 4.1 Material properties of CPB with 5% cement content.

Curing time	r_0 (kg/m^3)	x_u	t (hour)	b	w/c	h (μsec^{-1})	N	f_0 (Pa)	K(MPa)
15 d	1840	1	13.69	0.905	7.77	9×10^{-4}	2.5	2×10^5	16.9
30 d	1840	1	13.69	0.905	7.77	2×10^{-4}	2.5	2×10^5	44.5
G(MPa)	a	k(MPa)	R	D (MPa^{-1})	W	X_0(MPa)	C_0(m/s)	g_0	s
15.5	0.1966	0.0367	8	8×10^{-2}	0.1	0.3	96	1	3.39
40.4	0.1966	0.0764	8	8×10^{-2}	0.1	3	155	1	2.23

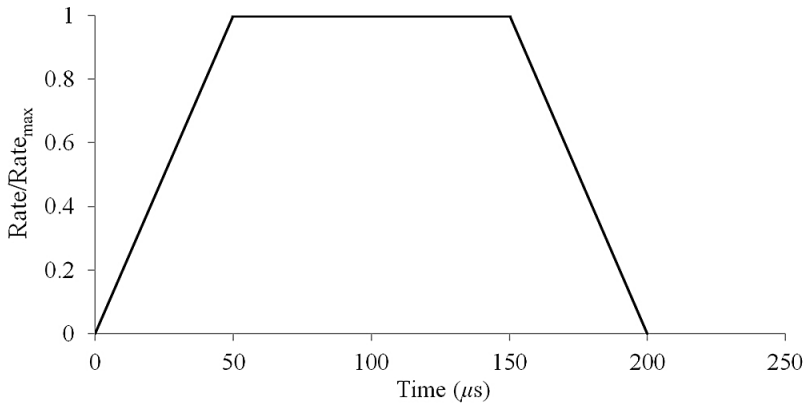

Figure 4.5 Strain rate-time history exerted on the model

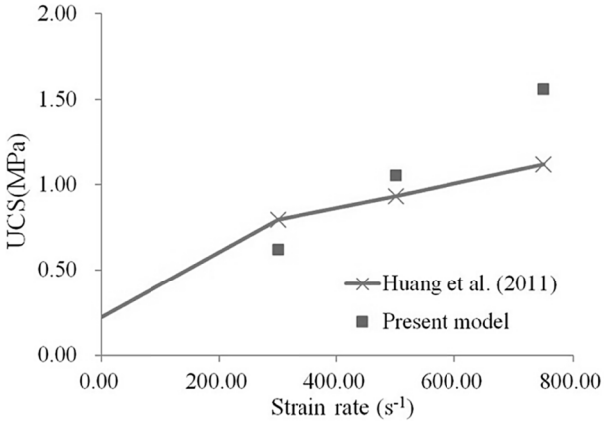

Figure 4.6 Comparison between tested and simulated peak axial stress for cemented paste backfill at 15th day with 5% cement

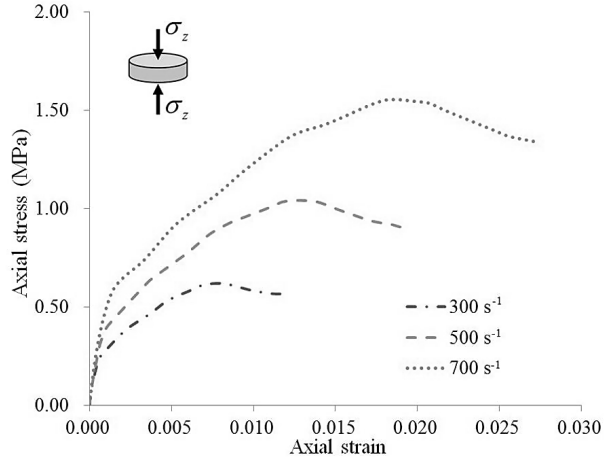

Figure 4.7 Simulated stress–strain curves for cemented paste backfill at 15th day with 5% cement

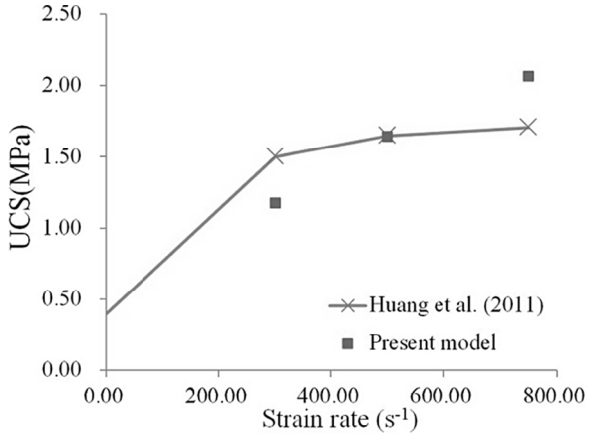

Figure 4.8 Comparison between tested and simulated peak axial stress for cemented paste backfill at 30th day with 5% cement. UCS, unconfined compressive strength

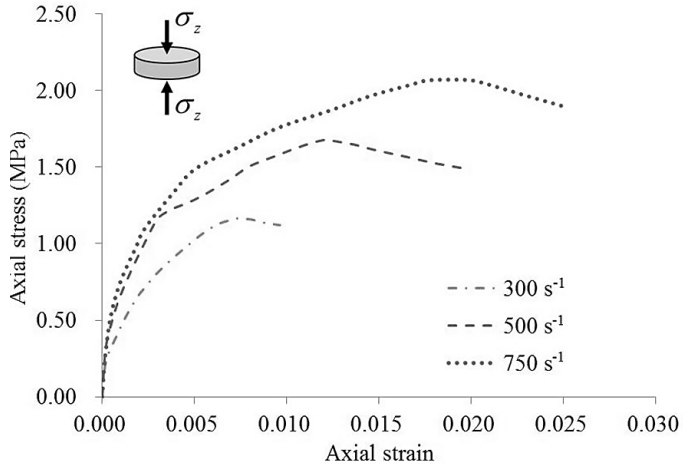

Figure 4.9 Simulated stress–strain curves for unconfined compressive strength at 30th day with 5% cement

As can be concluded from Figures 4.6 and 4.8, the model can capture the rate-dependence of the material strength quite well, and indicates an increasing trend of the UCS against strain rate within the range of the strain rate studied. According to Figures 4.7 and 4.9, in addition to the strength increase, the viscoplastic cap model can also account for the apparent stiffness enhancement due to high strain rates; unfortunately, no experiment data is available to provide a comparison. It should be emphasized that the softening process is not incorporated in traditional cap models. However, the softening behaviour has been taken into consideration in the proposed model. In fact, this phenomenon has also been taken into consideration by Katona (1984) and

Simo et al. (1986), and is a time-dependent effect of the viscoplastic overstress formulation. Specifically, the stress state is still well above the cap envelope at such a yield point, and subsequently, the stress would decrease as a result of additional inelastic strain accumulation.

To compare the simulated stress-strain curves with experimental results, dynamic tests on CPB cured for 15 days with 3% and 10% cement content respectively (Huang, 2009; Huang et al., 2011) were reproduced. The quasi-static data for these two mix proportions were obtained by using the results of Fall et al. (2008).

An empirical expression to relate the elastic modulus to the UCS was used, and is written as (Fall et al., 2005)

$$E = h(f_c)^i \tag{4.34}$$

where f_c is in the KPa and E in the MPa in the equation, and the fitting coefficients h and i can be determined by using quasi-static data found in Klein and Simon (2006) with h = 0.0324 and i = 1.32.

Finally, a comparison between the simulated stress-strain curves and experimental results in this case can be made and is shown in Figure 4.10. The material properties used in the example are listed in Table 4.2. From Figure 4.10, it can be observed that there is a good agreement between the experimental and the predicted results.

Table 4.2 Material properties of CPB with 3% and 10% cement content.

Cement content (curing time)	r_0 (kg/m^3)	x_u	t (hour)	b	w/c	h (μsec^{-1})	N	f_0 (Pa)	K(MPa)
3%(15d)	1840	1	13.69	0.905	12.96	2×10^{-3}	2.5	2×10^{5}	8.9
10%(15d)	1840	0.982	13.69	0.905	3.88	1×10^{-5}	2.5	2×10^{5}	104.8
3%(30d)	1840	1	13.69	0.905	12.96	7.5×10^{-4}	2.5	2×10^{5}	23.5
G(MPa)	a	k(MPa)	R	D (MPa^{-1})	W	X_0(MPa)	C_0(m/s)	g_0	s
8.1	0.1966	0.0309	8	8×10^{-2}	0.1	0.1	70	1	4.12
95	0.1966	0.1472	8	8×10^{-2}	0.1	4	238	1	1.62
21.3	0.1966	0.0471	8	8×10^{-2}	0.1	0.4	113	1	2.97

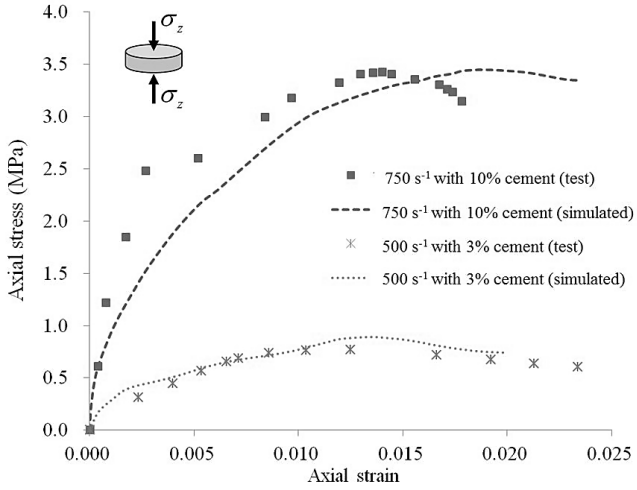

Figure 4.10 Comparison between simulated and tested stress–strain curves for unconfined compressive strength at 15th day

Comparisons between the measured and predicted UCS in all of the previous examples are shown in Figure 4.11. The case of CPB with *w*= 3% cured for 30 days under various strain rates is also provided, and the material properties are also listed in Table 4.2. From this figure, it can be concluded that the coupled chemo-viscoplastic cap model is able to adequately characterize the transient mechanical behaviour of hydrating CPB under shock loading.

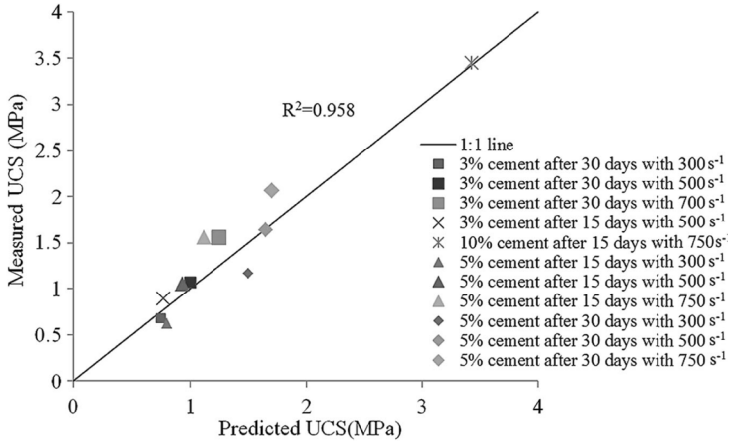

Figure 4.11 Comparison between measured and predicted unconfined compressive strength (UCS) of cemented paste backfill

4.2.4.3 Simulations of high strain rate experiments on other types of cementitious materials

To demonstrate the capability of the model developed in this study in capturing the rate-dependent response of other types of cementitious materials, SHPB tests with various strain rates conducted by Grote et al. (2001) on mortar are adopted. Similar to CPB, mortar also comprises solid aggregates, water, air and binder, and its material properties also evolve with time. It is noted that the ratio of enhancement over the stiffness and strength of cementitious materials with respect to the strain rate is not constant (Bischoff and Perry, 1991); therefore, only two of the tests in Grote et al. (2001) with an equivalent magnitude of strain rate (290/s and 620/s) as the experiments on CPB in section 4.2.4.2 are employed in the validation testing that will be carried out here. The two tested cylindrical samples are 11.9 mm and 11.6 mm in diameter, and 11.7 mm and 5.9 mm in height, respectively, and they are modelled with axially symmetric elements. A typical strain rate history in Grote et al. (2001) is adopted and applied as axial velocity increments at one end of the specimen, while the other end is fixed, and no lateral constraint is used according to the experiment configuration. The UCS, elastic modulus and Poisson's ratio are also obtained from the work by Grote et al. (2001), and the internal friction angle is assumed to be 55^{o}, so that the associated cohesion can be determined with the UCS. X_0, s and h can be determined with Equations (4.31) – (4.33), while other material parameters remain the same as in section 4.2.4.2. All of the parameters used in this example are listed in Table 4.3. A comparison between the tested and simulated stress-strain curves is shown in Figure 4.12. The results indicate that the model can also capture the shock response of mortar reasonably well, which is used as an example as one of the cementitious materials.

Table 4.3 Material properties of mortar used in the model

r_0 (kg/m^3)	h ($m$sec^{-1})	N	f_0 (MPa)	E(GPa)	v	a	k(MPa)	R	D (MPa^{-1})	W	X_0(MPa)	C_0(m/s)	g_0	s
2100	2	2.5	0.2	20	0.2	0.247	3.693	8	8×10^{-2}	0.1	100	2300	1	1.5

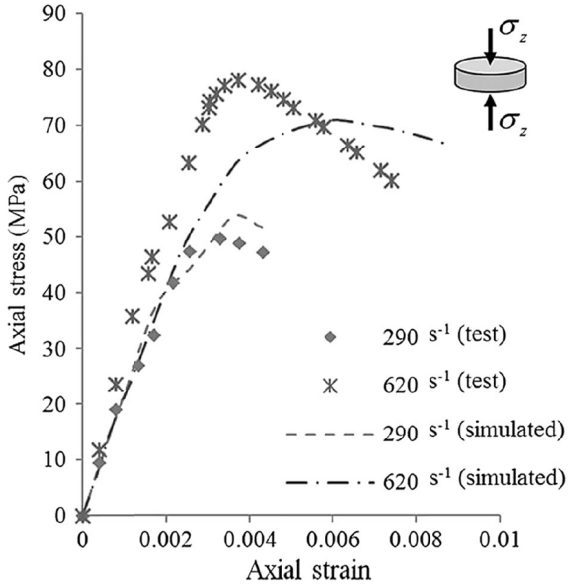

Figure 4.12 Comparison between tested and simulated stress–strain curves for mortar

4.2.4.4 Simulations of laboratory blast experiments on soils

By considering the fact that not all backfills contain cement, e.g. uncemented mine tailings backfill, and that they are similar to soil which consists of solid particles, water and air without the binder hydration process, impact tests performed on clayey sand by Jackson et al. (1980) are therefore adopted and numerically reproduced in this study. The maximum strain rate in related dynamic tests can reach as high as 200/s. The tested soil is molded into a thin disk-shaped specimen, with 12.7 mm in height and a height-to-diameter ratio of 1:7.6, at the bottom of an oil-filled rigid chamber. An explosive charge is used to load the piston at the top of the chamber, and the piston, in turn, produces a planar pressure pulse in the oil-filled chamber which uniformly pressurizes the surface of the membrane-sealed soil specimen. The soil specimen is modelled with axially symmetric elements, and the interactions between the explosives, piston and oil are not considered. Instead, the recorded axial stress history (Figure 4.13) adopted from Jackson et al. (1980) is applied at one end of the soil while the other end is fixed, and it is laterally constrained according to the experiment setup. Such experiments are also found in Katona (1984) and Tong and Tuan (2007) in the validation of their viscoplastic cap models. To demonstrate the consistency and comparability of the proposed model with those of previous efforts, identical material properties as those outlined in Tong and Tuan (2007) are used, and shown in Table 4.4. A comparison between the tested and simulated stress-strain curves for the soil obtained by the

model is shown in Figure 4.14. According to the results, the model in this study is comparable to previous viscoplastic cap models, and also comparable enough for application to capture the response of uncemented backfills under blast loading.

Table 4.4 Material properties of soil used in the modeling.

r_0 (kg/m^3)	h ($m$sec^{-1})	N	f_0 (MPa)	K (GPa)	G (GPa)	a	k (MPa)	R	D (MPa^{-1})	W	X_0 (MPa)	C_0 (m/s)	g_0	s
1430	0.002	1.5	1	2.5	1.5	0.2735	0.154	1.5	5×10^{-2}	0.109	0.3	1322	0.11	1.64

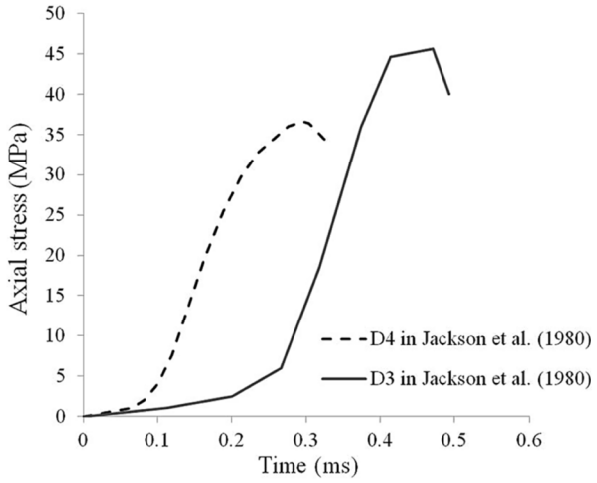

Figure 4.13 Stress history of the dynamic loading

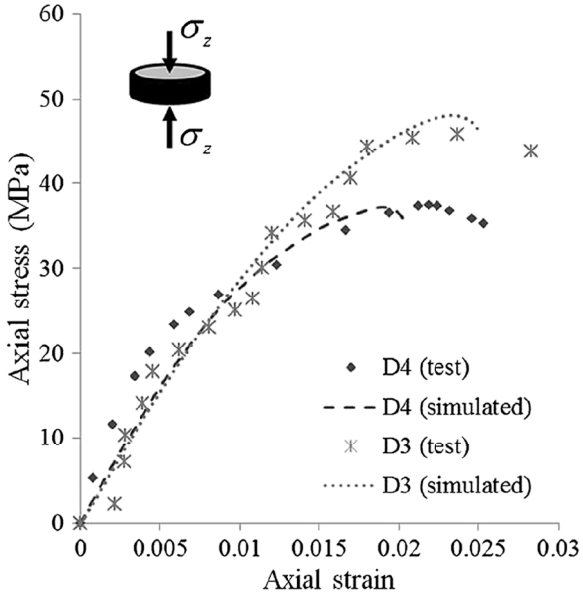

Figure 4.14 Comparison between tested and simulated stress–strain curves for a clayey sand

4.2.5 Discussion on the determination of model parameters

The presented coupled chemo-viscoplastic cap model contains a number of parameters, for characterizing both the hydration process and mechanical behaviour of cemented paste subjected to blast load. A discussion on the determination of model parameters is outlined below. A concise summary of incorporated parameters is listed at the end of discussion in Table 4.5, and a flow chart showing the update of parameters in the model is also presented in Figure 4.15.

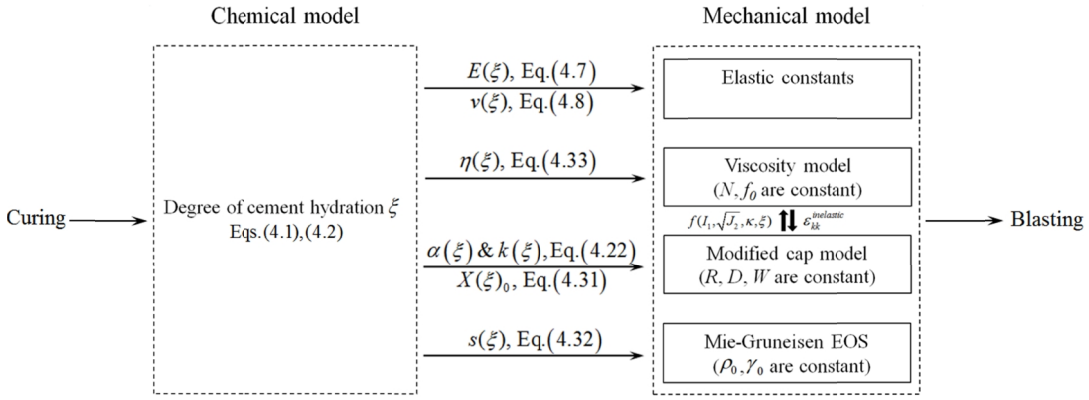

Figure 4.15 Parameters update in the proposed coupled chemo-viscoplastic cap model

Table 4.5 Summary of model parameters

Parameter	Physical meaning	Variant / Constant	Method of determination
w/c	Water-binder ratio	Variant	Known from the recipe of a cemented paste
x_u	Ultimate degree of binder hydration	Variant	Equation (4.2)
t (hour)	Hydration time parameter	Variant	Determine by the type of binder used
b	Hydration shape parameter	Variant	Determine by the type of binder used
K(MPa)	Bulk modulus	Variant	UCS test
G (MPa)	Shear modulus	Variant	UCS test
h (μsec^{-1})	Fluidity parameter	Variant	Equation (4.33)
N	Constant in viscous flow rule	Constant	-
f_0 (Pa)	Constant in viscous flow rule	Constant	-
a	Constant in Drucker-Prager criteria	Variant	Triaxial test or direct shear test
k	Constant in Drucker-Prager criteria	Variant	Triaxial test or direct shear test
R	Ratio of major to minor axis of the cap	Constant	-
D	Shape parameter of P - e_{kk} curve	Constant	-
W	Maximum volumetric plastic strain	Constant	-
X_0(MPa)	Initial vertex of the hardening cap	Variant	Equation (4.31)
r_0 (kg/m^3)	Density	Constant	Wax seal method, etc.
C_0(m/s)	Sound speed of CPB	Variant	K (μ=0) defined by Equation (4.29) should equal to that provided by Equations (4.7) - (4.9)
g_0	Grüneisen parameter	Constant	-
s	Slope of shock velocity - particle velocity curve	Variant	Equation (4.32)

In order to be applied for a particular problem, the curing recipe and the type of binder used should be provided as the first step, so that the hydration process can be uniquely quantified by the degree of binder hydration x using Equations (4.1) and (4.2). With the characterization of x, the evaluation of time evolutive parameters in the proposed viscoplastic cap model will be possible as elucidated in the following.

For the elastic constants of the material, UCS tests should be conducted at different time of curing. By fitting the obtained Young's modulus and Poisson's ratio to Equations (4.7) and (4.8), the time evolution of the material stiffness can be evaluated. In case the Young's modulus is not provided while UCS is available, Equation (4.34) could be adopted for an estimation of material stiffness.

The parameters N and f_0 in the viscous flow scheme are assumed constant in the current study, and only h has been treated variant and can be estimated by Equation (4.33) as a function of UCS. Their combination has been proved competent in recapturing the rate-dependence of the

material in the context. The inelastic volumetric strain obtained from the viscous flow rule will contribute to the strain hardening of cap envelope in the modified cap model.

To determine the evolutive yield surface used in the viscous flow scheme, triaxial compression tests or direct shear tests should be performed at different time of curing. The acquired cohesion and internal friction angle should be fitted to Equation (4.21) in order to capture the strength gain of the material against binder hydration process, and they will also be used to determine the parabolic shear envelope with Equation (4.23). As for the hardening cap, parameters R, D, and W are assumed constant in the study, and X_0 can be estimated with the empirical Equation (4.31). Then, the evolutive cap envelope is finalized with Equations (4.24) – (4.27).

For parameters in the variable bulk modulus of the Mie-Grüneisen type, density r_0 is assumed invariable for a given cementitious material, and g_0 is kept constant, while C_0 should be determined by ensuring the K value when μ=0 defined by Equation (4.29) equals to that provided by Equations (4.7) – (4.9). Then, s can be obtained with Equation (4.32) as a function of UCS.

Notably, the practice of characterizing parameters h , X_0 and s of cemented backfills based on their UCS exhibit a straightforward manner in model parameterization, since it is one of the most easily accessible data for those materials. This is also feasible and reasonable, because the strength gain of a given cementitious material is directly controlled by the binder hydration process, thus UCS would provide a good indication of the evolutive nature of cementitious materials. In fact, this concept has already been adopted in Murray (2007) and Jiang and Zhao (2015), where material properties of different concretes have been related to their UCS respectively.

4.2.6 Conclusions

A coupled chemo-viscoplastic cap model with variable bulk modulus has been developed for simulating the behaviour of hydrating cemented paste under blasting, and the proposed model is implemented into the commercial software COMSOL Multiphysics for finite element simulation. The developed model has been validated against various experimental high strain rate and blast tests. The good agreement between the simulated and measured results suggests

that the model is not only able to capture the blasting response of hydrating CPB, but also applicable to other cementitious materials, such as mortar and uncemented tailings.

Compared with previous modeling efforts on cemented backfills, where the time-dependent evolution of the material properties, strain rate effect, plastic volumetric compaction as well as nonlinear hydrostatic behaviour have not been taken into consideration, the evolution of cemented backfill properties with the progress of binder hydration can be reasonably determined by the model developed in this study. By using these as the input parameters, the viscoplastic cap model can also adequately model the transient mechanical process with the strain rate effect on both material strength as well as stiffness.

This developed model could be a potential tool to assess and understand the behaviour of hydrating cemented tailings backfill structures when subjected to mine blasts, and thus contribute to the design of cost-effective CPB structures.

Despite the results obtained, it should be emphasized that the hysteresis effect, although inherent in the cap models, has not been examined in the current study, and will be discussed in detail in subsequent research. Moreover, it is noted that the effect of the strain rate on cementitious materials is not linear, i.e. the ratio of enhancement over the strength and stiffness of the material with respect to the strain rate is not a constant. Therefore, despite its effectiveness in the study here, caution must be taken when extending the proposed coupled chemo-viscoplastic cap model to higher or even lower levels of strain rates, as in such conditions, the constants in the viscous flow rule might vary from case to case.

4.2.7 References

Abdul–Hussain N, Fall M. Thermo–hydro–mechanical behaviour of sodium silicate–cemented paste tailings in column experiments. Tunnelling and Underground Space Technology 2012; 29:85–93.

An J, Tuan CY, Cheeseman BA, Gazonas GA. Simulation of soil behaviour under blast loading. International Journal of Geomechanics, ASCE 2011; 11:323–334.

An J. Soil behaviour under blast loading, Ph.D. Thesis. University of Nebraska –Lincoln, Lincoln, USA, 2010.

Aráoz G, Luccioni B. Modeling concrete like materials under sever dynamic pressures. International Journal of Impact Engineering 2015; 76:139–154.

Awad AA. A numerical model for blast–induced liquefaction using displacements–pore pressure formulations. Ph.D. Thesis. Colorado State University, Colorado, USA, 1990.

Bischoff PH, Perry SH. Compressive behaviour of concrete at high strain rates. Materials and Structures 1991; 24:425–450.

Bloom F. Constitutive models for wave propagation in soil. Applied Mechanics Reviews 2006; 59:146–175.
Bolton JM, Durnford DS, Charlie WA. One–dimensional shock and quasi–static liquefaction of silt and sand. Journal of Geotechnical Engineering, ASCE 1994; 120:1874–1888.
Bussière B. Colloquium 2004: Hydrogeotechnical properties of hard rock tailings from metal mines and emerging geoenvironmental disposal approaches. Canadian Geotechnical Journal 2007; 44(9):1019–1052.
Cai M, Kaiser PK, Suorineni F, Su K. A study on the dynamic behaviour of the Meuse/Haute–Marne argillite. Physics and Chemistry of the Earth 2007; 32:907–916.
Casagrande A, Shannon WL. Strength of soils under dynamic loads. Proceedings of the American Society of Civil Engineers 1948; 74(4):591–608.
Cervera M, Oliver J, Prato T. Thermo-chemo-mechanical model for concrete. I: Hydration and aging. Journal of Engineering Mechcanics, ASCE 1999a; 125(9): 1018–1027.
Cervera M, Oliver J, Prato T. Thermo-chemo-mechanical model for concrete. II: Damage and creep. Journal of Engineering Mechcanics, ASCE 1999b; 125(9): 1028–1039.
Chapman DJ, Tsembelis K, Proud WG. Behaviour of water saturated sand under shock–loading. Proceedings of SEM Annual Conference and Exposition on Experimental and Applied Mechanics, St. Louis, 2006; 400–406.
Charlie W, Veyera GE, Durnford DS, Doehring DO. Porewater pressure increases in soil and rock from underground chemical and nuclear explosions. Engieering Geology 1996; 43(4):225–236.
Chen WF, Baladi GY. Soil Plasticity: Theory and Implementation. Elsevier: Amsterdam, 1985.
COMSOL Multiphysics User's Guide, Version 3.5a, COMSOL AB, Stockholm, Sweden, 2009.
Cui L, Fall M. A coupled thermo–hydro-mechanical–chemical model for underground cemented tailings backfill. Tunnelling and Underground Space Technology 2015; 50: 396–414.
Cui L, Fall M. An evolutive elasto–plastic model for cemented paste backfill. Computer and Geotechnics 2016; 71: 19-29.
DiMaggio FL, Sandler IS. Material models for granular soils. Journal of the Engineering Mechanics Division 1971; 97:935–950.
Emad MZ, Mitri H, Kelly C. Effect of blast–induced vibrations on fill failure in vertical block mining with delayed backfill. Canadian Geotechnical Journal 2014; 51:975–983.
Emad MZ, Mitri HS, Henning JG. Effect of blast vibrations on the stability of cemented rockfill. International Journal of Mining, Reclamation and Environment 2012; 26(3):233–243.
Fall M, Belem T, Benzaazoua M. The compressive and tensile properties of underground paste backfill. Proceedings of 58-th Canadian Geotechnical Conference, Saskatoon, 2005; 1–7.
Fall M, Belem T, Samb S, Benzaazoua M. Experimental characterization of the stress–strain behaviour of cemented paste backfill in compression. Journal of Material Science 2007; 42(11):3914–3922.
Fall M, Benzaazoua M, Ouellet S. Experimental characterization of the influence of tailings fineness and density on the quality of cemented paste backfill. Mineral Engineering 2005; 18(1):41–44.
Fall M, Benzaazoua M, Saa EG. Mix proportioning of underground cemented tailings backfill. Tunnelling and Underground Space Technology 2008; 23:80–90.
Fall M, Célestin JC, Han FS. Potential use of polymer–pastefill as waste containment barrier materials. Journal of Waste Management 2010a; 30: 2570–2578.

Fall M, Célestin JC, Pokharel M, Touré M. A contribution to understanding the effects of curing temperature on the mechanical properties of mine cemented tailings backfill. Engineering Geology 2010b;114:397–413.
Fall M, Pokharel M. Strength development and sorptivity of tailings shotcrete under various thermal and chemical loads. Canadian Journal of Civil Engineering 2011; 38:772–784.
Fall M, Samb SS. Effect of high temperature on strength and microstructural properties of cemented paste backfill. Fire Safety Journal 2009; 44(4):642–651.
Feldgun VR, Karinski YS, Yankelevsky DZ. A coupled approach to simulate the explosion response of a buried structure in a soil–rock layered medium. International Journal of Protective Structures 2013; 4(3):231–292.
Feldgun VR, Karinski YS, Yankelevsky DZ. Blast pressure distribution on a buried obstacle in a porous wet soil. International Journal of Protective Structures 2011; 2(1): 45–70.
Feldgun VR, Karinski YS, Yankelevsky DZ. Riemann solver for irreversibly compressible three–phase porous media. International Journal for Numerical and Analytical Methods in Geomechanics 2014; 38:406–440.
Feldgun VR, Kochetkov AV, Karinski YS, Yankelevsky DZ. A coupled simulation of an explosion inside a lined cavity surrounded by a plastic compressible medium. International Journal for Numerical Methods in Engineering 2007; 72:1135–1156.
Feldgun VR, Kochetkov AV, Karinski YS, Yankelevsky DZ. Blast response of a lined cavity in a porous saturated soil. International Journal of Impact Engineering 2008a; 35(9):953–966.
Feldgun VR, Kochetkov AV, Karinski YS, Yankelevsky DZ. Internal blast loading in a buried lined tunnel. International Journal of Impact Engineering 2008b; 35(3):172–183.
Foster CD, Regueiro RA, Fossum AF, Borja RI. Implicit numerical integration of a three-invariant, isotropic/kinematic hardening cap plasticity model for geomaterials. Computer Methods in Applied Mechanics and Engineering 2005; 194: 5109–5138.
Fragaszy RJ, Voss ME. Laboratory verification of blast–induced liquefaction mechanism. Final Report ADA109000, US Air Force Office of Scientific Research. Washington, DC. 1981.
Fragaszy RJ, Voss ME. Undrained compression behaviour of sand. Journal of Geotechnical Engineering, ASCE 1986; 112(3): 334–347.
Gawin D, Pesavento F, Schrefler BA. Hygro-thermo-chemo-mechanical modelling of concrete at early ages and beyond. Part I: Hydration and hygro-thermal phenomena. International Journal for Numerical Methods in Engineering 2006a; 67: 299–331.
Gawin D, Pesavento F, Schrefler BA. Hygro-thermo-chemo-mechanical modelling of concrete at early ages and beyond. Part II: Shrinkage and creep of concrete. International Journal for Numerical Methods in Engineering 2006b; 67: 332–363.
Gebbeken N, Greulich S, Pietzsch A. Hugoniot properties for concrete determined by full–scale detonation experiments and flyer plate–impact tests. International Journal of Impact Engineering 2006; 32(12):2017–2031.
Ghassemi A, Pak A, Shahir H. Numerical study of the coupled hydro–mechanical effects in dynamic compaction of saturated granular soils. Computers and Geotechnics 2010; 37:10–24.
Ghirian A, Fall M. Coupled thermo–hydro–mechanical–chemical behaviour of cemented paste backfill in column experiments. Part I: Physical, hydraulic and thermal processes and characteristics. Engineering Geology 2013; 164:195–207.

Ghirian A, Fall M. Coupled thermo–hydro–mechanical–chemical behaviour of cemented paste backfill in column experiments. Part II : Mechanical, chemical and microstructural processes and characteristics. Engineering Geology 2014; 170:11–23.
Green SJ, Swanson SR. Static constitutive relations for concrete. Report AD761820, Air Force Weapons Laboratory. Kirtland, 1973.
Grote DL, Park SW, Zhou M. Dynamic behaviour of concrete at high strain rates and pressures: I. experimental characterization. International Journal of Impact Engineering 2001; 25(9):869–886.
Grujicic M, Pandurangan B, Cheeseman BA, Roy WN, Skaggs, RR, Gupta, R. Parameterization of the porous–material model for sand with various degrees of water saturation. Soil Dynamics and Earthquake Engineering 2008a; 28:20–35.
Grujicic M, Pandurangan B, Cheeseman BA. The effect of degree of saturation of sand on detonation phenomena associated with shallow–buried and ground–laid mines. Shock and Vibration 2006; 13:41–61.
Grujicic M, Pandurangan B, Coutris N, Cheeseman BA, Roy WN, Skaggs RR. Computer–simulations based development of a high strain–rate, large–deformation, high–pressure material model for STANAG 4569 sandy gravel. Soil Dynamics and Earthquake Engineering 2008b; 28:1045–1062.
Grujicic M, Pandurangan B, Coutris N, Cheeseman BA, Roy WN, Skaggs RR. Derivation and validation of a material model for clayey sand for use in landmine detonation computational analysis. Multidiscipline Modeling in Materials and Structures 2009; 5:311–344.
Grujicic M, Pandurangan B, Coutris N, Cheeseman BA, Roy WN, Skaggs RR. Derivation, parameterization and validation of a sandy–clay material model for use in landmine detonation computational analyses. Journal of Materials Engineering and Performance 2010; 19(3):434–450.
Gu Q, Lee FH. Ground response to dynamic compaction of dry sand. Géotechnique 2002; 52(7):481–493.
Henrych J. The Dynamics of Explosion and Its Use. Elsevier: New York, 1979.
Higgins W, Chakraborty T, Basu D. A high strain–rate constitutive model for sand and its application in finite–element analysis of tunnels subjected to blast. International Journal for Numerical and Analytical Methods in Geomechanics 2013; 37(15):2590–2610.
Huang S, Xia K, Qiao L. Dynamic tests of cemented paste backfill: effects of strain rate, curing time, and cement content on compressive strength. Journal of Material Science 2011; 46(15):5165–5170.
Huang S. Dynamic testing of soft and ultra–soft materials. Master Thesis. University of Toronto, Toronto, Canada, 2009.
Jackson JG, Rohani B, Ehrgot JQ. Loading rate effects on compressibility of sand. Journal of Geotechnical Engineering Division 1980; 106(8):839–852.
Jiang H, Zhao J. Calibration of the continuous surface cap model for concrete. Finite Elements in Analysis and Design 2015; 97:1–19.
Karinski YS, Feldgun VR, Yankelevsky DZ. Effect of soil locking on the cylindrical shock wave's peak pressure attenuation. Journal of Engineering Mechanics, ASCE 2009b; 135(10):1166–1180.
Karinski YS, Feldgun VR, Yankelevsky DZ. Explosion–induced dynamic soil–structure interaction analysis with the coupled Godunov–Variational Difference Approach. International Journal for Numerical Methods in Engineering 2009a; 77:824–851.

Katona MG. Evaluation of viscoplastic cap model. Journal of Geotechnical Engineering, ASCE 1984; 110(8):1106–1125.
Kesimal A, Yilmaz E, Ercikdi B, Alp I, Deveci H. Effect of properties of tailings and binder on the short– and long–term strength and stability of cemented paste backfill. Materials Letters 2005; 59(28):3703–3709.
Kim KJ, Blouin SE. Response of saturated porous nonlinear materials to dynamic loadings, Final Report ADA148528, US Air Force Office of Scientific Research. Washington, DC. 1984.
Klein K, Simon D. Effect of specimen composition on the strength development in cemented paste backfill. Canadian Geotechnical Journal 2006; 43:310–324.
Kuhl D, Bangert F, Meschke G. Coupled chemo-mechanical deterioration of cementitious materials. Part I: Modeling. International Journal of Solids and Structures 2004a; 41:15–40.
Kuhl D, Bangert F, Meschke G. Coupled chemo-mechanical deterioration of cementitious materials. Part II: Numerical methods and simulations. International Journal of Solids and Structures 2004b; 41:41–67.
Laine P, Sandvik A. Derivation of mechanical properties for sand. Proceedings of the 4-th Asia–Pacific Conference on Shock and Impact Loads on Structures, Singapore, 2001; 361–368.
Landriault D. Backfill in underground mining. In Underground Mining Methods Engineering Fundamentals and International Case Studies. SME, 2001; 601–614.
Le Roux K. In situ properties and liquefaction potential of cemented paste backfill. Ph.D. Thesis. University of Toronto, Toronto, Canada, 2004.
Li H, Liu J, Wang Y, Yao T, Tian Q, Li S. Deformation and cracking modeling for early-age sidewall concrete based on the multi-field coupling mechanism. Construction and Building Materials 2015; 88: 84–93.
Li X, Li R, Schrefler RA. A coupled chemo-thermo-hygro-mechanical model of concrete at high temperature and failure analysis. International Journal for Numerical and Analytical Methods in Geomechanics 2006; 30: 635–681.
Lu Y, Wang Z, Chong K. A comparative study of buried structure in soil subjected to blast load using 2D and 3D numerical simulations. Soil Dynamics and Earthquake Engineering 2005; 25:275–288.
Merkle DH, Dass WC. Fundamental Properties of Soils for Complex Dynamic Loadings. Final Report ADA164206, US Air Force Office of Scientific Research. Washington, DC. 1985.
Motamedi MH, Foster CD. An improved implicit numerical integration of a non-associated, three-invariant cap plasticity model with mixed isotropic–kinematic hardening for geomaterials. International Journal for Numerical and Analytical Methods in Geomechanics 2015.
Murray YD, Lewis BA. Numerical simulation of damage in concrete. Report DNA–TR–94–190, Defense Nuclear Agency. Alexandria, 1995.
Murray YD. Users manual for LS–DYNA concrete material model 159. Report FHWA–HRT–05–062, Federal Highway Administration. McLean, 2007.
Nasir O, Fall M. Coupling binder hydration, temperature and compressive strength development of underground cemented paste backfill at early ages. Tunnelling and Underground Space Technology 2010; 25(1):9–20.
Nasir O, Fall M. Modeling the heat development in hydrating CPB structures. Computers and Geotechnics 2009; 36(7):1207–1218.
Nelson I, Baron ML, Sandler I. Mathematical models for geological materials for wave–propagation studies. Report DASA2672, Defense Nuclease Agency. Washington, DC. 1971.

Nguyen VH, Colina H, Torrenti JM, Boulay C, Nedjar B. Chemo-mechanical coupling behaviour of leached concrete Part I: Experimental results. Nuclear Engineering and Design 2007a; 237:2083–2089.

Nguyen VH, Nedjar B, Torrenti JM. Chemo-mechanical coupling behaviour of leached concrete Part II: Modelling. Nuclear Engineering and Design 2007b; 237:2090–2097

Ning JG, Liu HF, Shang L. Dynamic mechanical behaviour and the constitutive model of concrete subjected to impact loadings. Science in China Series G: Physics, Mechanics & Astronomy 2008; 51(11):1745–1760.

Omidvar M, Iskander M, Bless S. Stress–strain behaviour of sand at high strain rates. International Journal of Impact Engineering 2012; 49:192–213.

Osinov VA. Blast–induced waves in soil around a tunnel. Archive of Applied Mechanics 2011; 81:543–559.

Perzyna P. Fundamental problems in viscoplasticity. Advances in Applied Mechanics 1966; 9:243–377.

Pichler C, Lackner R, Mang HA. A multiscale micromechanics model for the autogenous-shrinkage deformation of early-age cement-based materials. Engineering Fracture Mechanics 2007; 74: 34–58.

Prapaharan S, Chameau JL, Holtz RD. Effect of strain rate on undrained strength derived from pressuremeter tests. Geotechnique 1989; 39(4):615–624.

Rice MH, McQueen RG, Walsh JM. Compression of solids by strong shock waves. In Solid State Physics. Academic Press: New York, 1958; 6:1–63.

Riedel W, Wicklein M, Thoma K. Shock properties of conventional and high strength concrete: Experimental and mesomechanical analysis. International Journal of Impact Engineering 2008; 35(3):155–171.

Saebimoghaddam A. Liquefaction of early age cemented paste backfill. Ph.D Thesis. University of Toronto, Toronto, Canada, 2009.

Sandler IS, DiMaggio FL, Baladi GY. Generalized cap model for geological materials. Journal of the Geotechnical Engineering Division 1976; 102:683–699.

Sandler IS, Rubin D. An algorithm and a modular subroutine for the cap model. International Journal for Numerical and Analytical Methods in Geomechanics 1979; 3:173–186.

Schindler AK, Folliard KJ. Heat of hydration models for cementitious materials. ACI Material Journal 2005; 102(1):24–33.

Schindler AK. Effect of temperature on hydration of cementitious materials. ACI Material Journal 2004; 101(1):72–81.

Schwer LE, Murray YD. A three–invariant smooth cap model with mixed hardening. International Journal for Numerical and Analytical Methods in Geomechanics 1994; 18:657–688.

Schwer LE. Viscoplastic augmentation of the smooth cap model. Nuclear Engineering and Design 1994; 150:215–223.

Sercombe J, Hellmich C, Ulm FJ, Mang H. Modeling of early-age creep of shotcrete. I: Model and model parameters. Journal of Engineering Mechcanics, ASCE 2000; 126(3): 284–291.

Sheahan TC, Ladd CC, Germaine JT. Rate–dependent undrained shear behaviour of saturated clay. Journal of Geotechnical Engineering, ASCE 1996; 122(2):99–108.

Simo JC, Wu JW, Pister KS, Taylor RL. Assessment of cap model: Consistency return algorithms and rate–dependent extension. Journal of Engineering Mechanics, ASCE 1986; 114(2):191–218.

Simo JC, Kennedy JG, Govindjee S. Non–smooth multisurface plasticity and viscoplasticity. Loading/unloading conditions and numerical algorithms. International Journal for Numerical Methods in Engineering 1988; 26:2161–2185.
Sun W, Chen Q, Ostien JT. Modeling the hydro-mechanical responses of strip and circular punch loadings on water-saturated collapsible geomaterials. Acta Geotechnica 2014; 9: 903–934.
Theory Reference for the Mechanical APDL and Mechanical Applications, ANSYS Release 12.0, ANSYS Inc., Canonsburg, Pennsylvania, 2009.
Tong X, Tuan CY. Viscoplastic cap model for soils under high strain rate loading. Journal of Geotechnical and Geoenvironmental Engineering, ASCE 2007; 133(2):206–214.
Torisu SS, Pereira JM, De Gennaro V, Delage P, Puech A. Strain–rate effects in deep marine clays from the Gulf of Guinea. Geotechnique 2012; 62(9):767–775.
Tu Z, Lu Y. Evaluation of typical concrete material models used in hydrocodes for high dynamic response simulations. International Journal of Impact Engineering 2009; 36(1): 132–146.
Ulm FJ, Coussy O. Modeling of thermochemomechanical couplings of concrete at early ages. Journal of Engineering Mechcanics, ASCE 1995; 121(7): 785–794.
van Gool BS. Effects of blasting on the stability of paste fill stopes at Cannington Mine. Ph.D. Thesis. James Cook University, Townville, Australia, 2007.
Wang Z, Hao H, Lu Y. A three–phase soil model for simulating stress wave propagation due to blast loading. International Journal for Numerical and Analytical Methods in Geomechanics 2004a; 28:33–56.
Wang Z, Lu Y, Bai C. Numerical analysis of blast–induced liquefaction of soil. Computers and Geotechnics 2008a; 5:196–209.
Wang YG, Zhang YP, Wang LL. Experimental study on the shock Hugoniot relationship and the Grüneisen–type equation of state for C30 concrete. Acta Physica Sinica 2008b; 57(12):7789–7793. (in Chinese)
Wang Z, Lu Y, Bai C. Numerical simulation of explosion–induced soil liquefaction and its effect on surface structures. Finite Elements in Analysis and Design 2011; 47(9):1079–1090.
Wang Z, Lu Y, Hao H, Chong K. A full coupled numerical analysis approach for buried structures subjected to subsurface blast. Computers and Structures 2005; 83:339–356.
Wang Z, Lu Y, Hao H. Numerical investigation of effects of water saturation on blast wave propagation in soil mass. Journal of Engineering Mechcanics, ASCE 2004b; 130(5):551–561.
Wang Z, Lu Y. Numerical analysis on dynamic deformation mechanism of soils under blast loading. Soil Dynamics and Earthquake Engineering 2003; 23:705–714.
Wang ZL, Konietzky H, Huang RY. Elastic–plastic–hydrodynamic analysis of crater blasting in steel fiber reinforced concrete. Theoretical and Applied Fracture Mechanics 2009; 52:111–116.
Wardlaw AB, McKeown R, Chen H. Implementation and application of the P–α equation of state in the DYSMAS code. Report NSWCDD/TR–95/107, Naval Surface Warfare Center. Dahlgren, 1996.
Whitman RV. The response of soils to dynamic loading. Final Report AD708625, US Army Engineer Waterways Experiment Station. Vicksburg, 1970.
Wu D, Fall M, Cai S. Coupled modeling of temperature distribution and evolution in cemented tailings backfill structures that contain mineral admixtures. Geotechnical and Geological Engineering 2012; 30(4):935–961.

Wu D, Fall M, Cai S. Coupling temperature, cement hydration and rheological behaviour of fresh cemented paste backfill. Mineral Engineering 2013; 42:76–87.
Wu D, Fall M, Cai S. Numerical modelling of thermally and hydraulically coupled processes in hydrating cemented tailings backfill columns. International Journal of Mining, Reclamation and Environment 2014; 28(3):173–199.
Xu TH, Zhang LM. Numerical implementation of a bounding surface plasticity model for sand under high strain–rate loadings in LS–DYNA. Computers and Geotechnics 2015; 66:203–218.
Yankelevsky DZ, Feldgun VR, Karinski YS. Underground explosion of a cylindrical charge near a buried wall. International Journal of Impact Engineering 2008; 35(8):905–919.
Yilmaz E, Benzaazoua M, Belem T, Bussière B. Effect of curing under pressure on compressive strength development of cemented paste backfill. Mineral Engineering 2009; 22:772–785.
Zhang Y, Pichler C, Yuan Y, Zeiml M, Lackner R. Micromechanics-based multifield framework for early-age concrete. Engineering Structures 2013: 47: 16–24.
Zhu J, Yin J. Strain–rate–dependent stress–strain behaviour of overconsolidated Hong Kong marine clay. Canadian Geotechnical Journal 2000; 37:1272–1282.
Zukas JA. Introduction to Hydrocodes. Elsevier: Kidlington, 2004.

4.3 Technical Paper 3: A multiphysics–viscoplastic cap model for simulating the blast response of cemented tailings backfill

Published in *Journal of Rock Mechanics and Geotechnical Engineering* 9, 2017, 551-564.
Gongda Lu, Mamadou Fall, Liang Cui

Abstract:

Although a large number of previous researches have significantly contributed to the understanding of the quasi-static mechanical behaviour of cemented tailings backfill, an evolutive porous medium used in underground mine cavities, very few efforts have been made to improve the knowledge on its response under sudden dynamic loading during the curing process. In fact, there is a great need for such information given that cemented backfill structures are often subjected to blast loadings due to mine exploitations. In this study, a coupled thermo-hydro-mechanical-chemical (THMC)-viscoplastic cap model is developed to describe the behaviour of cementing mine backfill material under blast loading. A THMC model for cemented backfill is adopted to evaluate its behaviour and evolution of its properties in curing processes with coupled thermal, hydraulic, mechanical and chemical factors. Then, the model is coupled to a Perzyna type of viscoplastic model with a modified smooth surface cap envelope and a variable bulk modulus, in order to reasonably capture the nonlinear and rate-dependent behaviours of the cemented tailings backfill under blast loading. All of the parameters required for the variable-modulus viscoplastic cap model were obtained by applying the THMC model to reproduce the evolution of CPB properties in the curing process. Thus, the behaviour of hydrating cemented backfill under high-rate impacts can be evaluated under any curing time of concern. The validation results of the proposed model indicate a good agreement between the experimental and the simulated results. The authors believe that the proposed model will contribute to a better understanding of the performance of hydrating cemented backfill under blasting, and also to practical risk management of backfill structures associated with such a dynamic condition.

KEY WORDS: THMC coupling; multiphysics processes; tailings; paste backfill; cap model; blast

4.3.1 Introduction

Cemented hydraulic and paste backfills represent two main types of cemented tailings backfill technologies in nowadays mining industry for tailings disposal and ground control. Due to its superior mechanical performance per unit of cement consumption, cemented paste backfill (CPB) has become increasingly popular (Landriault, 2001; Fall et al., 2010a, 2010b). As a cementitious evolutive geotechnical material, CPB is a mixture of dewatered mine tailings (fine aggregates), binder additives (e.g. Portland cement, fly ash, slag, etc.), and water. Although the majority of research focus has been placed on the quasi-static mechanical behaviour of CPB (Kesimal et al., 2005; Klein and Simon, 2006; Yilmaz et al., 2009; Abdul-Hussain and Fall, 2012; Ghirian and Fall, 2013, 2014; etc.), knowledge of its dynamic response is equally important, as field backfills are often subjected to dynamic excitations such as mining blasts, rock bursts, as well as earthquake loadings.

Unlike any other natural porous medium (natural soil, rock, etc.), cemented backfill has material properties that are highly time-dependent, mainly due to the cement hydration process. Thus, its mechanical response will be significantly influenced by such a chemical process. To evaluate the response of hydrating CPB under blast loading, a coupled chemo-viscoplastic cap model has been developed (Lu and Fall, 2016), and validated against experiments on various types of cementitious materials. Specifically, in this model, a modified Perzyna viscoplastic formulation is employed to represent the rate-dependence in the behaviour of cemented tailings backfill under blast loading. A modified smooth surface cap model is then developed to delineate the failure of the material, and can also control the material dilation and account for the hysteresis as well as full compaction effects. Then, the viscoplastic formulation is further enhanced with a variable bulk modulus derived from a Mie-Grüneisen equation of state (EOS), in order to characterize the nonlinear hydrostatic behaviour of cemented backfill subjected to high pressure. In the model, the material properties required for the viscoplastic cap model have been coupled with a chemical model, which captures and quantifies the degree of cement hydration. Thus, the behaviour of hydrating cemented backfill under blast loading can be evaluated at any curing time of concern. However, the evolution of material properties of CPB is not only a function of the degree of cement hydration, but also all of the thermal (T), hydraulic (H), mechanical (M) and chemical (C) factors and their interactions to which the CPB is subjected during its curing (Ghirian and Fall, 2013, 2014) (Figure 4.16). Thus, the coupled

chemo-viscoplastic cap model proposed in Lu and Fall (2016) is not sufficient to capture the blast response of CPB when cured under the influence of complex THMC factors.

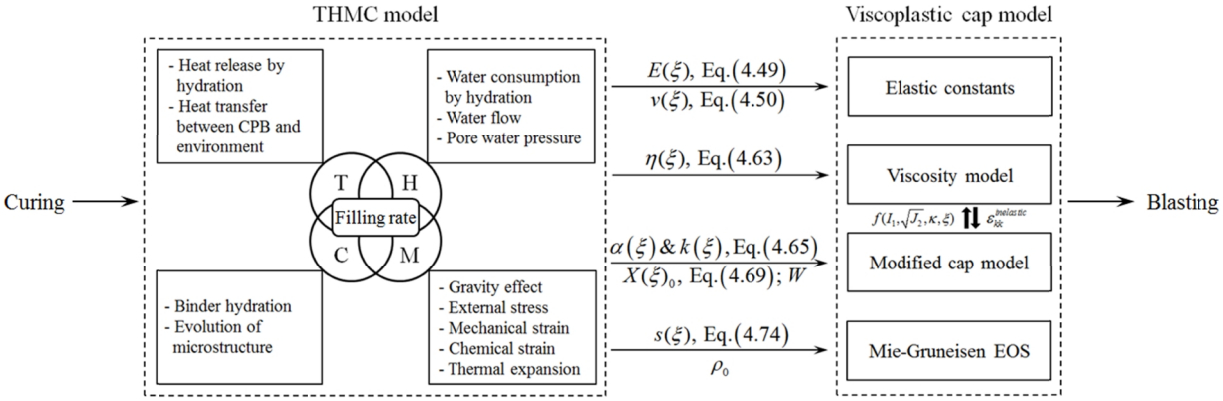

Figure 4.16 Component interactions and parameter update in the coupled THMC-viscoplastic cap model

Moreover, according to Henrych (1979), dry and water-bearing loose materials have distinct behaviour under blast loading. This difference in water content is represented by the maximum volumetric plastic strain (parameter W) in the cap model, which is a measure of the volumetric gas content of the material (Chen and Baladi, 1985). Therefore, W should be a variant in the cement hydration process as the interstitial water is gradually consumed. The same applies to the material density (r_0 , used in the Mie-Grüneisen EOS) if drainage or evaporation occurs. In contrast, W and r_0 have been assumed to be constant in this prototype of the chemo-viscoplastic cap model for cemented tailings backfill (Lu and Fall, 2016). This simplification was appropriate because the CPB samples in Lu and Fall (2016) had been only cured at the early ages, and the volumetric gas contents and densities of those samples should be almost constant according to the analogous experiment in Ghirian and Fall (2013). However, this will not be the case if CPB samples are cured for a longer period of time, and the volumetric gas content and density of CPB would significantly deviate from younger samples at a more mature stage (Ghirian and Fall, 2013). Furthermore, matric suction develops as cement hydration takes place. Most models for porous media (including CPB) under blast loading have neglected the influence of suction. However, this is important for soft cementitious materials, such as CPB. As the cement hydration process can generate up to hundreds of kPa of suction (Ghirian and Fall, 2013) due to self-

desiccation, which is large scale compared to both the static and dynamic strengths of CPB which are usually less than 1 and 3 MPa, respectively (Klein and Simon, 2006; Huang et al., 2011; Ghirian and Fall, 2014). Thus, in order to recapture the mechanical response of more mature cemented backfill under blast loading, a chemical model alone would not be sufficient to quantify all of the incorporated (time-evolutive) parameters in the viscoplastic cap model, and a model that can further reproduce the hydraulic process during cement hydration is needed. The same also applies to the thermal and mechanical factors, and they will also affect the evolution of the material properties including the W and r_0 of CPB. A detailed description on the coupling mechanisms of multiphysics processes that occur during the curing of cemented backfill is presented in Section 4.3.2.

Therefore, to describe these multiphysics processes, the coupled thermo-hydro-mechanical-chemical (THMC) model for cemented backfill developed by Cui and Fall (2015) is adopted. By using this THMC model, the evolution of parameters required in the prototype viscoplastic cap model can be obtained with more rational considerations of the influence of the environment and intrinsic ingredients of the backfill itself. Noticeably, there has been no shortage of models for cement-based materials in which at least two components of coupled THMC processes are considered. However, their mechanical components have been developed only to capture the creep (e.g., Cervera et al., 1999a,1999b; Sercombe et al., 2000; Gawin et al., 2006a, 2006b; Li et al., 2015), shrinkage (Ulm and Coussy, 1995; Pichler et al., 2006; Gawin et al., 2006a, 2006b; Li et al., 2015), cracking (e.g., Zhang et al., 2013; Li et al., 2015) or uniaxial/triaxial compression (e.g., Cui and Fall, 2015) behaviours of cement-based materials under quasi-static conditions, and they cannot evaluate the response of an evolutive cement-based material under transient blast loading. In the remainder of the paper, considerations for the coupled THMC processes and the modeling approach of the present model are briefly outlined. Then, formulations of the coupled THMC model for recapturing the variation of CPB properties are presented, and it is coupled with a viscoplastic cap model to characterize the response of CPB during blast loading. Finally, the developed model is validated against laboratory experiments.

4.3.2 Considerations for coupled THMC processes in cemented backfill

The performance of cemented backfill is significantly influenced by complex coupled multiphysics, including thermal (T), hydraulic (H), mechanical (M) and chemical (C) processes

(Ghirian and Fall, 2013, 2014). Their interplays are conceptually illustrated in Figure 4.16. Therefore, the heat transfer, liquid flow, gas migration, skeleton deformation, and binder hydration processes and their mutual coupling effects are taken into account, and their roles in the curing process are elucidated as follows (Dutt et al., 2012; Verma et al., 2013; Cui and Fall, 2015; Verma et al., 2015; Gautam et al., 2016; and Verma et al., 2016).

4.3.2.1 Chemical process

Binder hydration initiates right after the CPB is mixed. The progression of the chemical reaction influences CPB properties and behaviour with four key mechanisms: (i) as the chemical reaction proceeds, the resultant hydration products precipitate and refine the capillary pore space between tailings particles. This would then lead to significant microstructural evolution, and consequently contribute to the change of material properties including thermal conductivity, hydraulic conductivity and some mechanical properties (Ghirian and Fall, 2013, 2014); (ii) interstitial water is gradually consumed during the binder hydration process. This will not only reduce the degree of saturation, but also result in the build-up of matric suction; (iii) the heat released by exothermic binder hydration will affect the temperature distribution in the CPB structure, thus boost the rate of binder hydration (Schindler, 2004; Schindler and Folliard, 2005); and (iv) since the volume of the hydration products is less than the combined volume of the reacted cement and water (Powers and Brownyard, 1947), binder hydration will result in mechanical deformation through chemical shrinkage. The effect of sulphate on CPB is excluded in the consideration of chemical processes as not all CPB contains sulphate.

4.3.2.2 Hydraulic process

The changes in the water content of CPB structure are generally attributed to binder hydration, evaporation, water flow and drainage (Abdul-Hussain and Fall, 2011; Ghirian and Fall, 2013). Variation in the water content can strongly affect other physics, such as: (i) the unhydrated binder can be coated with precipitated hydration products. This will inhibit pore water from diffusing inward to reach the unhydrated cement cores, thus consequently decrease the hydration rate (Cui and Fall, 2015); (ii) loss of water can result in the development of matric suction within the backfill mass, which will influence the effective stress distribution, and thus in turn, modifies the strength and mechanical performance of CPB (Ghirian and Fall, 2014); and (iii)

the hydraulic processes will cause variations in the temperature distribution by convection and changes in the thermal properties (e.g. thermal conductivity), as a result of different phase compositions.

4.3.2.3 Thermal process

The main source of heat in CPB systems is the heat generated by binder hydration (Fall et al., 2010b). The variation in the temperature within a CPB structure can also have tremendous effects on other physics, such as: (i) the rate of hydration is temperature-dependent. Specifically, higher temperature is generally associated with a faster hydration rate (Schindler, 2004; Schindler and Folliard, 2005); (ii) due to the geothermal gradient, the temperature of the ambient rocks increases with depth, and could lead to mechanical deformations through thermal expansion; and (iii) the temperature of curing will also have an impact on the surface evaporation (Ghirian and Fall, 2013).

4.3.2.4 Mechanical process

Field CPB is subjected to self-weight, confining pressure from the ambient rock mass, and thermal stress, etc. Thus, CPB could experience deformation through elastoplastic strain, thermal expansion as well as chemical shrinkage. The resultant volumetric deformation could in turn give rise to variations in the porosity, thus affect a few properties of the CPB, such as hydraulic conductivity (Davis and Davis, 1999) and thermal conductivity (Ghirian and Fall, 2013). The impact of mechanical processes on binder hydration is neglected, since it is minimal considering the relatively low stress levels in CPB structures.

4.2.2.5 Filling rate

The filling rate refers to the speed at which the CPB materials are pumped into the stope, and it can differ from one mine or stope to another due to various filling strategies used in the field (Nasir and Fall, 2010). In mining industry, backfilling with multiple stages and different filling rates are often adopted as a balance of safety, cost, and productivity concerns. The backfilling rate and strategies have been found to not only affect the stress distribution within the CPB, but also influence the pore water pressure (PWP) imposed on the barricade (Thompson et al., 2012; Doherty et al., 2015).

4.3.3 Modeling approach

To evaluate the response of hydrating CPB under blast loading, a viscoplastic cap model is employed and coupled with a THMC model which quantifies the variation of the material properties during the curing process.

As discussed in Section 4.3.2, the performance of cemented backfill is significantly influenced by the concerted action of the THMC processes. Therefore, the characterization of the coupled THMC processes that occur in CPB is crucial for reliably assessing and predicting the behaviour of CPB structures under blast loading. The coupled THMC model developed by Cui and Fall (2015) for cemented tailings backfill is adopted in this study, and it has been proven sufficient to account for the interactions among the multiple physical processes listed in Section 4.3.2. Details and formulation of the model will be elucidated in Section 4.3.4.

The modified viscoplastic cap model developed by Lu and Fall (2016) is adopted in the current study as the constitutive law to characterize the response of CPB under blast loading. This model works well for geomaterials under high pressure, and is capable of recapturing the strain rate effect. It has been utilized and validated for both high and low strain rate phenomena (Katona, 1985; Simo et al., 1986; Tong and Tuan, 2007; An et al., 2011; Aráoz and Luccioni, 2015; etc.). Details and formulation of the model will be elucidated in Section 4.3.5.

All of the material properties required in the variable-modulus viscoplastic cap model of CPB are obtained from the coupled THMC model for cemented backfill. The coupling strategy and parameter update are illustrated in Figure 4.16. Finally, the developed coupled THMC-viscoplastic cap model is implemented into a commercial software package, COMSOL Multiphysics (COMSOL AB, Stockholm, Sweden), for finite element simulation.

4.3.4 Formulations of the coupled THMC model for cemented backfill

4.3.4.1 General assumptions

To develop the governing equations for the coupled THMC model, the following assumptions are made:

(i) The three phase (solid, water, and dry air) constituents in CPB are three independent overlapping continua in the context of the theory of mixtures. Water is the wetting phase while dry air is not and is considered as an ideal gas.

(ii) The water and gas migrate in the interconnected voids of the solid. Since the temperature within CPB is relatively low, the phase transition of liquid water is not considered.

(iii) Solid particles and liquid water are incompressible, while the porous skeleton is deformable. The stress is considered tension positive, while the pore fluid pressure is considered compression positive.

(iv) Local thermal equilibrium is assumed for the three-phase system.

(v) The solid skeleton is assumed chemically inert, and the only chemical process that takes place is the hydration of the binder additives.

4.3.4.2 Binder hydration model

The binder hydration model proposed by Schindler (2004) and Schindler and Folliard (2005) for cementitious materials is adopted in this study, and it has already been used to quantify the progress of binder hydration for CPB, e.g. in Cui and Fall (2016) and Wu and Fall (2013), and is expressed as:

$$x\left(t_e\right)=x_u\cdot\exp\left[-\left(\frac{t}{t_e}\right)^b\right] \tag{4.35}$$

with

$$\begin{cases} x_u=\dfrac{1.031\cdot w/c}{0.194+w/c}+0.5\cdot X_{FA}+0.30\cdot X_{slag} \\ t_e=\int_0^t \exp\left[-\dfrac{E_a}{R_a}\left(\dfrac{1}{T}-\dfrac{1}{T_r}\right)\right]dt \end{cases}$$

and

$$E_a\left(T\right)=\begin{cases} 33500+1470\times\left(293.15-T\right) & T<293.15\,\mathrm{K} \\ 33500 & T\geq 293.15\,\mathrm{K} \end{cases}$$

where x is the degree of binder hydration, and x_u the ultimate degree of hydration; t stands for the hydration time parameter (hours), b represents the hydration shape parameter, t_e is the equivalent age of CPB at the reference temperature T_r (K), T denotes the temperature of the

CPB (K), t is the chronologic curing age, E_a is the activation energy (J/mol), R_a represents the natural gas constant (8.314 J/mol/K), w/c is the water-cement ratio, and X_{FA} and X_{slag} refer to the mass fraction of the corresponding minerals with respect to the total binder.

4.3.4.3 Fluid flow model

The mass conservation equations for a CPB system are defined as (Cui and Fall, 2015):

$$fS\frac{\partial r_w}{\partial t}+fr_w\frac{\partial S}{\partial t}+Sr_w\left[\frac{\partial e_v}{\partial t}+\frac{(1-f)}{r_s}\frac{\partial r_s}{\partial t}\right]-fSm_{hydr}\left(\frac{r_w}{r_s}S-1\right)=-\nabla\cdot\left(fSr_w\mathbf{v}^{rw}\right) \tag{4.36}$$

$$f(1-S)\frac{\partial r_a}{\partial t}-fr_a\frac{\partial S}{\partial t}+(1-S)r_a\left[\frac{(1-f)}{r_s}\frac{\partial r_s}{\partial t}+\frac{\partial e_v}{\partial t}-\frac{fS}{r_s}m_{hydr}\right]=-\nabla\cdot f(1-S)r_a\mathbf{v}^{ra} \tag{4.37}$$

where r_i refers to the density and the subscript i denotes the an individual phase (air, water and solid), f is the porosity, $S=q/f$ is the degree of saturation of the liquid phase, q is the volumetric water content, $\mathbf{v}_s$ and $\mathbf{v}^{ri}$ denote the solid phase velocity with respect to the (fixed) Eulerian coordinate, and the relative apparent velocity of the fluids in the porous medium, respectively, e_v indicates the total volumetric strain.

m_{hydr} refers to the rate of water consumption due to binder hydration, and can be estimated by using (Cui and Fall, 2015):

$$\begin{aligned}m_{hydr}=2m_{hc-initial}&\left(0.187x_{C_3S}+0.158x_{C_2S}+0.665x_{C_3A}+0.2130x_{C_4AF}\right)\\&\times\left\{\left(\frac{t}{t_e}\right)^b\left(\frac{b}{t_e}\right)x(t_e)\exp\left[\frac{E_a}{R_a}\left(\frac{1}{273+T_r}-\frac{1}{273+T}\right)\right]\right\}\end{aligned} \tag{4.38}$$

where $m_{hc-initial}$ is the initial cement mass, and x_i is the mass fraction of the corresponding compound with respect to the total cement content.

The $\mathbf{v}^{ri}$ of fluid phases can be characterized by using Darcy's law, which is expressed as:

$$\mathbf{v}^{ri}=-\mathbf{k}\frac{k_{ri}}{m_i}\nabla\left(P_i-r_ig\right) \tag{4.39}$$

where $\mathbf{k}$ is the intrinsic permeability tensor of the medium with the intrinsic permeability $k_0=K_{sat}m_i/r_ig$, K_{sat} represents the (saturated) hydraulic conductivity, m_i stands for the fluid dynamic viscosity, k_{ri} denotes the relative permeability with respect to each fluid phase, and P_i

refers to the pore fluid pressure. Meanwhile, K_{sat} of CPB will change with time, and it can be written in terms of x as (Ghirian and Fall, 2013):

$$K_{sat} = K_T \exp\left(C_1 x^{C_2}\right) \tag{4.40}$$

where K_T is the saturated hydraulic conductivity of the tailings in CPB, and fitting constants C_1 =-8.173 and C_2 =4.035 based on the experimental results reported in Ghirian and Fall (2013).

The relative permeability can be evaluated based on the model of van Genuchten (1980):

$$\begin{cases} k_{rw}\left(S_{eff}\right) = \sqrt{S_{eff}}\left[1-\left(1-S_{eff}^{1/m_{VG}}\right)^{m_{VG}}\right]^2 \\ k_{ra}\left(S_{eff}\right) = \sqrt{1-S_{eff}}\left(1-S_{eff}^{1/m_{VG}}\right)^{2m_{VG}} \end{cases} \tag{4.41}$$

with

$$S_{eff} = \frac{1}{\left\{1+\left[a_{VG}(P_a-P_w)\right]^{\frac{1}{1-m_{VG}}}\right\}^{m_{VG}}} \tag{4.42}$$

By introducing the time evolution of the fitting parameters into the model of van Genuchten (1980) during the hydration process of CPB, a_{VG} and m_{VG} can be estimated by using (Abdul-Hussain and Fall, 2011):

$$\begin{cases} m_{VG} = f_1 x^{f_2} + f_3 \\ a_{VG} = f_4 e^{f_5 x} \end{cases} \tag{4.43}$$

where the fitting constants, f_1 =0.0415, f_2 =4.231, f_3=0.4073, f_4 =0.2103 kPa^{-1} and f_5 =-6.921, are based on the measured data reported in Abdul-Hussain and Fall (2011) and Ghirian and Fall (2013). Then, the volumetric water content q can be calculated by using:

$$q = q_r + S_{eff}(q_s - q_r) \tag{4.44}$$

where q_s and q_r represent the saturated and residual water contents, respectively. Meanwhile, the evolution of q_r due to hydration can be related to x by using (Abdul-Hussain and Fall, 2011):

$$q_r = R_1 \cdot \exp(-R_2 \cdot x) \tag{4.45}$$

where R_1 and R_2 are the fitting parameters and equal to 1.314 and 7.538, respectively.

To introduce the temperature-dependence of fluid properties, the following expressions are adopted (Cui and Fall, 2015):

$$\begin{cases} m_w = 0.6612\left(T-229\right)^{-1.562} \\ r_w = 314.4+685.6\left\{1-\left[\left(T-273.15\right)/374.14\right]^{1/0.55}\right\}^{0.55} \\ m_a = 1.716\times10^{-5}\cdot\left(T/273\right)^{1.5}\cdot\left[384/\left(T+111\right)\right] \\ r_a = \dfrac{M_a}{R_a T}P_a \end{cases} \tag{4.46}$$

where m_w and m_a are dynamic viscosity, and r_w and r_a are density of water and air, respectively; M_a is the molar mass of air.

4.3.4.4 Model of mechanical equilibrium

The momentum conservation of the system can be written as:

$$\nabla\cdot\left(\frac{\partial\boldsymbol{\sigma}_{ij}}{\partial t}\right)+\frac{\partial\left[\left(1-f\right)r_s+fSr_w+f\left(1-S\right)r_a\right]}{\partial t}\mathbf{g}=0 \tag{4.47}$$

where $\boldsymbol{\sigma}_{ij}$ is the total stress tensor, and can be defined based on the effective stress concept as

$$\boldsymbol{\sigma}_{ij}=\boldsymbol{\sigma}'_{ij}-aP\boldsymbol{\delta}_{ij} \tag{4.48}$$

where the Biot's coefficient $a=1-K/K_s$ with K and K_s denoting the bulk modulus of the porous skeleton and solid grains; the mean pore pressure P exerted by the fluid phases on the solid grains is defined by the averaging technique as $P=SP_w+\left(1-S\right)P_a$ (e.g., Khoei and Mohammadnejad, 2011). Notably, K will evolve in time during the binder hydration process, and can be estimated by using (Cui and Fall, 2016):

$$\frac{E(x)}{E_u}=\left(\frac{x-x_0}{x_u-x_0}\right)^A \tag{4.49}$$

$$n(x)=0.5\exp(B_1x)+B_2x^{B_3}\exp(B_4x^{B_5}) \tag{4.50}$$

where $E(x)$ stands for the elastic modulus at a given degree of binder hydration x ; E_u and x_u denote the ultimate elastic modulus and degree of hydration, respectively; x_0 refers to the reference degree of hydration below which no development of elastic constants occurs; and A is a material constant. B_1, B_2, B_3, B_4 and B_5 are the fitting parameters for determining the Poisson's ratio v; then, bulk modulus of the backfill can be obtained as $K=E(x)/[3(1-2v(x)]$.

The effective stress can be obtained based on Hooke's law as

$$\boldsymbol{\sigma}' = \mathbf{D}\boldsymbol{\varepsilon}_{\mathbf{e}} = \mathbf{D}\left(\boldsymbol{\varepsilon} - \boldsymbol{\varepsilon}_{\mathbf{p}} - \boldsymbol{\varepsilon}_{\mathbf{T}} - \boldsymbol{\varepsilon}_{\mathbf{c}}\right) \tag{4.51}$$

where $\mathbf{D}$ is the stiffness tensor, and $\boldsymbol{\varepsilon}$ is the total strain, which consists of elastic, $\boldsymbol{\varepsilon}_e$, plastic, $\boldsymbol{\varepsilon}_p$, thermal, $\boldsymbol{\varepsilon}_T$, and chemical, $\boldsymbol{\varepsilon}_c$, strains under the theory of superposition. The components $\boldsymbol{\varepsilon}_p$, $\boldsymbol{\varepsilon}_T$, $\boldsymbol{\varepsilon}_c$ can be obtained based on the failure model, coefficient of thermal expansion a_T, and coefficient of the chemical shrinkage b_{ch} for CPB, respectively, which are defined in Cui and Fall (2015, 2016).

4.3.4.5 Heat transfer model

The heat transfers in CPB mainly with two mechanisms, namely, through heat conduction and convection. Meanwhile, heat is also released by the exothermic binder hydration. Under the isothermal assumption, the energy conservation for CPB can be written as

$$\left[(1-f)\, r_s C_s + f S\, r_w C_w + f\,(1-S)\, r_a C_a\right]\frac{\partial T}{\partial t} + Q_{cv} + Q_{cd} = Q_{hydr} \tag{4.52}$$

where C_i is the specific heat capacity with i=a, w, and s, Q_{cv} and Q_{cd} are the amount of heat transfer by convection and conduction, respectively, and Q_{hydr} denotes the heat release as a result of the exothermic binder hydration.

The convection of heat is caused by the migration of both liquid water and dry air, and it can be expressed as

$$Q_{cv} = \left(r_w C_w \mathbf{v}^{rw} + r_a C_a \mathbf{v}^{ra}\right)\cdot \nabla T \tag{4.53}$$

The conduction of heat can be evaluated with Fourier's law as

$$Q_{cd} = -k_{eff}\nabla T \tag{4.54}$$

where k_{eff} is the effective thermal conductivity of the CPB, and it can be evaluated by using (Cui and Fall, 2015)

$$k_{eff} = k_{dry} + \sqrt{S_{eff}}\left(k_{sat} - k_{dry}\right) \tag{4.55}$$

where k_{sat} and k_{dry} are the thermal conductivity of the CPB in the saturated and a completely dry condition, respectively. k_{sat} can be evaluated by (Côté and Konrad, 2005; Ghirian and Fall, 2013):

$$k_{sat} = k_{tailings}^{1-f} k_w^f \tag{4.56}$$

where $k_{tailings}$ and k_w represent the thermal conductivity of the tailings and water, respectively. An analogous expression for k_{dry} can be expressed as

$$k_{dry} = k_{tailings}^{1-f} k_a^f \tag{4.57}$$

where k_a is the thermal conductivity of air.

The heat released by exothermic binder hydration can be evaluated by using (Schindler, 2004; Schindler and Folliard, 2005)

$$Q_{hydr} = H_T \left(\frac{t}{t_e}\right)^b \cdot \left(\frac{b}{t_e}\right) \cdot x\left(t_e\right) \cdot \exp\left[\frac{E_a}{R_a}\left(\frac{1}{273+T_r} - \frac{1}{273+T}\right)\right] \tag{4.58}$$

with

$$\begin{cases} H_T = \left(H_{cem} \cdot X_{cem} + 461 \cdot X_{slag} + 1800 \cdot x_{CaO/FA} \cdot X_{FA}\right) C_b \\ H_{cem} = 500x_{C_3S} + 260x_{C_2S} + 866x_{C_3A} + 420x_{C_4AF} + 624x_{SO_3} + 1186x_{FreeCaO} + 850x_{MgO} \end{cases}$$

where H_T denotes the total heat available for binder hydration, H_{cem} is the heat from the hydration of cement, and C_b is the apparent binder density with regard to the total volume of the CPB.

4.3.5 Formulation of viscoplastic cap model for cemented backfill under blast loading

4.3.5.1 Perzyna type of viscoplastic formulation

The Perzyna type of viscoplastic formulation is adopted in current study to represent the rate-dependence in the material behaviour. In Perzyna's model, the total strain rate vector $\dot{\boldsymbol{\varepsilon}}$ is decomposed into an elastic $\dot{\boldsymbol{\varepsilon}}^e$ and a viscoplastic (inelastic) component $\dot{\boldsymbol{\varepsilon}}^{vp}$ as

$$\dot{\boldsymbol{\varepsilon}} = \dot{\boldsymbol{\varepsilon}}^e + \dot{\boldsymbol{\varepsilon}}^{vp} \tag{4.59}$$

The elastic strain rate independently of the viscosity is expressed as

$$\dot{\boldsymbol{\varepsilon}}^e = \mathbf{D}^{-1}\dot{\boldsymbol{\sigma}} \tag{4.60}$$

where $\dot{\boldsymbol{\sigma}}$ is the stress rate tensor, and the elastic constants in the stiffness matrix $\mathbf{D}$ can be obtained by Equations (4.49) and (4.50).

The viscoplastic strain rate is generally defined by the viscoplastic flow rule:

$$\dot{\boldsymbol{\varepsilon}}^{vp} = h\left\langle f(f)\right\rangle \frac{\partial f}{\partial \boldsymbol{\sigma}} \tag{4.61}$$

where h is a material parameter called fluidity parameter; $\langle\ \rangle$ is the Macaulay bracket defined as $\langle x \rangle = (x + |x|)/2$, f is the yield function and will be defined in the following subsection, and $f(f)$ is a dimensionless scaling function which is expressed as

$$f(f) = \left(\frac{f}{f_0} \right)^N \tag{4.62}$$

where N is the exponent and f_0 is the normalizing constant with the same unit as f. The associated flow rule is used for the viscous behaviour of the material, and the direction of $\dot{\varepsilon}^{vp}$ is given by f and in the outward normal direction of the yield surface.

To simplify the modeling, N and f_0 are assumed to be constant, while h is related to the degree of binder hydration as (Lu and Fall, 2016):

$$h(x)(\mathrm{s}^{-1}) = 48.2 \cdot (f_c + 0.224)^{-3.51} + 0.002 \tag{4.63}$$

where f_c (in MPa) is the unconfined compressive strength (UCS) of the material as a function of the degree of binder hydration and will be explained below.

4.3.5.2 Modified plastic cap model

The plastic cap model with associated flow rule is adopted in this study to recapture the yield behaviour of cemented tailings backfill. As discussed in Lu and Fall (2016), this model not only can avoid the problems of unreasonable strength development under increasing pressure, and unrealistic dilation that a Drucker-Prager or Mohr-Coulomb criteria would suffer, but is also free from the problem of solution uniqueness in the non-associated flow scheme. Besides, it has far fewer model parameters to calibrate than bounding surface plasticity.

It has been noted that traditional cap models suffer from the numerical complexity due to singular corners, which locate at the intersection of the shear failure envelope with a positive tangent and hardening cap with a horizontal tangent. In order to treat such singular corners with relative simplicity, and at the same time, effectively control the volumetric dilation/compaction behaviour of the materials, a new transition approach has been introduced in Lu and Fall (2016), and it is also adopted in this study. A conceptual comparison between the original cap model (Chen and Baladi, 1985), Continuous Surface Cap Model (Murray an Lewis, 1995) and the cap model used in the study are presented in Figure 4.17, and the parameters used for these yield envelopes are the same in this illustration.

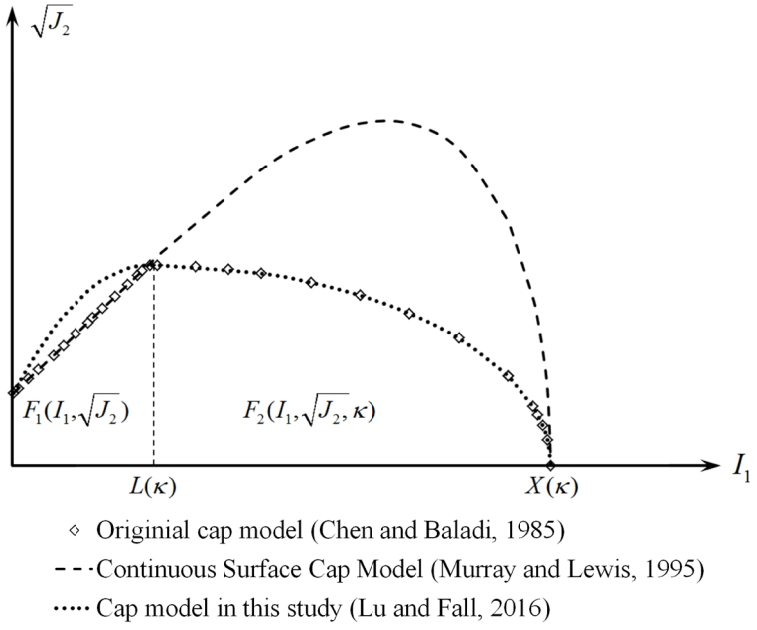

Figure 4.17 Comparison between shapes of different cap models

The cap model adopted in the study defines the shear envelope as

$$F_1(I_1,\sqrt{J_2},x)=\sqrt{J_2}-\frac{k(x)-[X(k,x)-L(k,x)]/R}{L^2(k,x)}I_1^2+2\cdot\frac{k(x)-[X(k,x)-L(k,x)]/R}{L(k,x)}I_1-k(x) \quad (4.64)$$

where k is the strain hardening parameter, $L(k,x)$ and $X(k,x)$ are the abscissa of the intersection of the elliptic cap with the shear failure envelope and the hydrostatic loading line, respectively, R is the ratio of the major to the minor axis of the elliptic cap, and $k(x)$ is the Drucker-Prager parameter defined by

$$a(x)=\frac{2\sin j(x)}{\sqrt{3}\left[3+\sin j(x)\right]},\quad k(x)=\frac{6c(x)\cos j(x)}{\sqrt{3}\left[3+\sin j(x)\right]} \quad (4.65)$$

where $c(x)$ and $j(x)$ are the cohesion and internal friction angle as functions of the degree of binder hydration (Cui and Fall, 2016):

$$c(x)=M_1x^{M_2},\quad j(x)=N_1x^{N_2}+N_3x \quad (4.66)$$

where M_1 and M_2, and N_1, N_2 and N_3 are the fitting constants.

Then, the hardening cap can be written as:

$$F_2(I_1,\sqrt{J_2},k,x)=\sqrt{J_2}-\frac{1}{R}\left\{\left[X(k,x)-L(k,x)\right]^2-\left[I_1-L(k,x)\right]^2\right\}^{1/2} \tag{4.67}$$

The hardening of the cap due to the plastic volumetric strain, e_{kk}^{p}, can be defined by the following law:

$$X(k,x)=-(1/D)\cdot\ln\left(1-\frac{e_{kk}^{p}}{W}\right)+X(x)_0 \tag{4.68}$$

where W indicates the maximum plastic volumetric strain of the material, and can be determined by $W=f(1-S)$ (Chen and Baladi, 1985). D is the shape parameter of the volume-pressure curve, and $X(x)_0$ is the initial vertex of the hardening cap, which can be estimated by using (Lu and Fall, 2016)

$$X(x)_0\,(\text{MPa})=52.9\ln(0.03f_c+0.236)+75.5 \tag{4.69}$$

and the UCS of the material can be evaluated based on the Mohr-Coulomb criterion:

$$f_c=2c(x)\tan[45^{\circ}+\frac{j(x)}{2}] \tag{4.70}$$

Then, the intersection of the cap and the shear envelope can be obtained by considering continuity:

$$k(x)=\frac{X(k,x)-R\cdot k(x)}{1+R\cdot a(x)} \tag{4.71}$$

and

$$L(k,x)=\begin{cases} k(x) & k(x)>k(x)_0 \\ k(x)_0 & \text{otherwise} \end{cases} \tag{4.72}$$

Thus, all time-evolutive parameters in the yield function have been defined as functions of x. Finally, the modified cap envelope $f(I_1,\sqrt{J_2},k,x)$ which is a combination of $F_1(I_1,\sqrt{J_2},x)$ and $F_2(I_1,\sqrt{J_2},k,x)$ is used as the yield function f in Equations (4.61) and (4.62), and the accumulated inelastic volumetric strain acquired by such a viscous flow will contribute to the hardening of the cap envelope in the stress space.

Details on the mechanisms of how the plastic cap model can control the material dilation and account for the hysteresis effect in hydrostatic loading/unloading can be found in Lu and Fall (2016).

4.3.5.3 Nonlinear pressure-volume relationship (EOS)

Under extremely intensive loading conditions such as blasting, the pressure-volume behaviour of a material would be typically nonlinear (Henrych, 1979). In the current study, the variable-bulk-modulus approach will be utilized to capture the nonlinear pressure-volume relationship of CPB, and is derived from a Mie-Grüneisen EOS (An et al., 2011) expressed as (Lu and Fall, 2016)

$$K(x)=\frac{r_0 C(x)_0^2[1+(1-\frac{g_0}{2})m-\frac{a_0}{2}m^2][1+\frac{2m[s(x)-1]}{1+m-s(x)m}+\frac{m(g_0+a_0m)}{(1+m)^2}]+r_0C(x)_0^2m(1-\frac{g_0}{2}-a_0m)}{[1+m-s(x)m]^2}+\left[\frac{(g_0+a_0m)^2}{(1+m)^2}+a_0\right]E^v \quad (4.73)$$

where r_0 is the material density, which can be determined by tracking the loss of water via evaporation or drainage, and calculating the volume change of the CPB in the curing process; $C(x)_0$ is the sound speed of the CPB at an ambient pressure and temperature, and its value can be chosen so that the $K(x)$ at μ=0 as defined by Equation (4.73) equals to that provided by Equations (4.49) and (4.50); g_0 is the Grüneisen parameter, E^v is the internal energy per unit initial volume; a_0 is the first order volume correction to g_0 and generally set to 0; $m=e_v/(1-e_v)$; and $s(x)$ is the slope of the shock velocity against the particle velocity curve, which can be estimated by using (Lu and Fall, 2016)

$$s(x)(1)=2.06\exp(-4.38f_c+0.779)+1.5 \quad (4.74)$$

4.3.5.4 Arbitrary Lagrangian-Eulerian formulation

During blast loading, materials may experience large deformations, and this would make the mapping from the mesh to the spatial coordinates to be ill-conditioned, then lead to mesh entanglement and accuracy issues when there is severe mesh distortion. Therefore, an arbitrary Lagrangian-Eulerian (ALE) formulation is used in the CPB model here for blast loading. Previous numerical problems can be solved by the remeshing mechanism of the ALE method. Specifically, when the mesh degrades to an unacceptable level, the ALE method can suspend the calculations, then build a new mesh system in the current domain, subsequently map all of the model quantities to the new mesh system and resume calculation. Therefore, the ALE method embodies the advantages of both Eulerian and Lagrangian formulations, and allows the movement of boundaries and evaluation of physical states at fixed points in space, although it is relatively more intensive in computation (COMSOL AB, 2009; ANSYS Inc., 2009).

4.3.6 Model validation

4.3.6.1 Simulation of high column experiments on hydrating CPB (Case Study 1)

Ghirian and Fall (2013, 2014) conducted experiments with high columns to investigate the coupled THMC behaviour of CPB during the curing process. A backfilling strategy with 3 layers (50 cm each in height) has been employed and the high columns of CPB were completed in 3 days. Each backfilling stage was finished within 5 minutes, and one-day delay between each lift was adopted. The experiments were conducted under insulated-undrained conditions, and extensive laboratory measurements and testing were performed during the curing of CPB. The monitoring points were located at the centre of each lift, i.e. 25 cm, 75 cm, and 125 cm from the bottom, respectively. Further details of the experimental program can be found in Ghirian and Fall (2013, 2014).

The high column tests on hydrating CPB were reproduced with the coupled THMC model, in order to show its validity in the evaluation of the THMC behaviour of CPB during the hydration process. The cylinder column was simulated with axisymmetric elements, and the configuration of the model is illustrated in Figure 4.18. The delayed backfilling of each lift was simulated in a layer-by-layer manner, and each stored solution of the previous sequence was set as the initial condition of the field variables in the next stage of simulation. The input parameters, boundary conditions and initial values used for the numerical simulation are listed in Table 4.6.

Table 4.6 Input parameters, boundary conditions and initial values of simulated curing tests

	Case Study 1	Case Study 3		
Cement content	4.5%	5%	7%	10%
w/c ratio	7.6	7.77	5.55	3.88
Height of specimen	0.5 m for each of 3 layers	0.07 m	0.07 m	0.07 m
Insulation materials				
Category	Thermal insulating foam		CPVC	
Thermal conductivity (W/(m k))	0.024		0.1	
Heat capacity (J/(kg k))	1400		1050	
Density (kg/m^3)	30		1760	
Mechanical module				
Top surface	Free		Free	
Lateral sides	Roller		Roller	
Bottom side	Fixed		Fixed	
Volume force	Gravity		Gravity	
Hydraulic module				
Top surface	Mass flux		No flux	
Lateral sides	No flux		No flux	
Bottom side	No flux		No flux	
Volume force	Gravity		Gravity	
Initial value	Hydraulic head=0		Hydraulic head=0	
Thermal module				
Top side (°C)	20.75		25	
Lateral sides (°C)	20.75		25	
Bottom side (°C)	20.75		25	
Initial temperature (°C)	20.75		25	

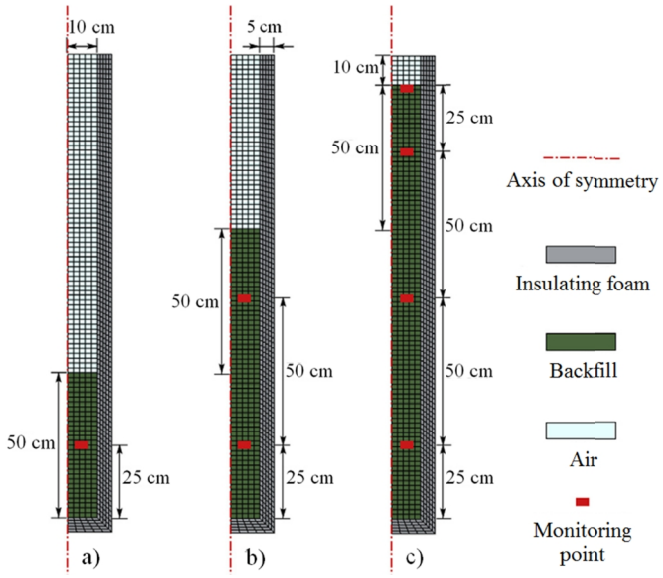

Figure 4.18 Configuration of the model for high column test

a) 1st stage of backfilling; b) 2nd stage of backfilling; and c) 3rd stage of backfilling

A comparison between the simulated and measured temperature within the CPB column for both short-term and long-term curing is shown in Figure 4.19. It can be observed that there is

good agreement between the simulated and measured variation of temperature in terms of both the peak values and trend of evolution. Note that the fluctuation in the measured temperature is caused by the variation of room temperature during the test program.

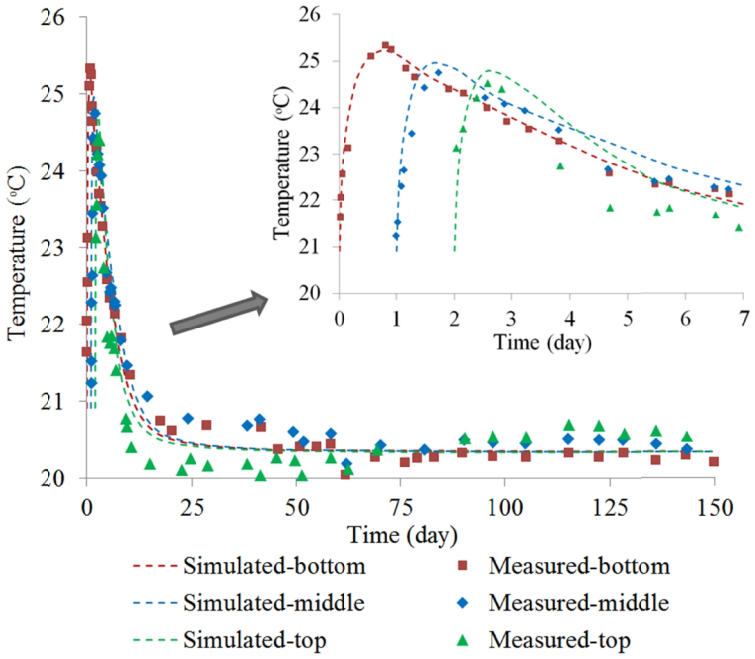

Figure 4.19 Comparison between simulated and measured temperatures at monitored points

Figure 4.20 shows both the short-term and long-term evolution of pore water pressure (PWP) in CPB. As can be observed, there is also good agreement between the simulated and experimental results. Specifically, at roughly 16 hrs after placement, a negative PWP starts to develop rapidly in the column, and this is due to the advancement of binder hydration which consumes the pore water. It is also noticeable that the PWP of the bottom layer jumps back to a positive value once an upper backfill layer is placed into the column, and this phenomenon should be attributed to the downward drainage of water from the initially saturated upper layer due to gravity. After approximately 7 days, the PWP in the column exhibits a much slower rate of decrease, and the PWP of the three monitoring points evolve asymptotically to approximately -100 kPa, -150 kPa, and -200 kPa for the for the bottom, middle and top layer, respectively.

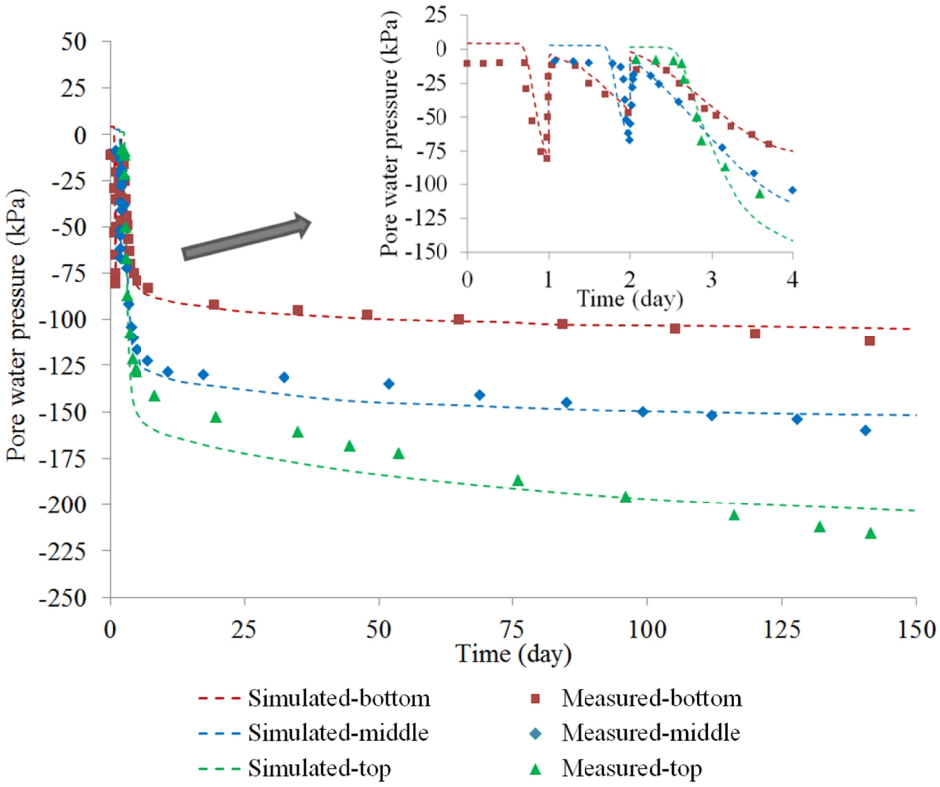

Figure 4.20 Comparison between simulated and measured PWP at monitored points

A series of quasi-static UCS tests were performed on the CPB specimens extracted from the column after 7, 28, 90 and 150 days of curing. To validate the mechanical component of the coupled THMC model, a comparison between the simulated and experimental stress-strain curves in the quasi-static UCS tests of CPB is presented in Figure 4.21 below. As can be observed, there is a good agreement between the simulated and experimental results. Specifically, the model can reproduce well the chemical and strain softening–hardening behaviour of CPB. Note that all axial stresses in simulated stress–strain curves of the present study are total stress. More details on the features of the mechanical behaviours of CPB under quasi-static loading conditions are discussed in Cui and Fall (2016).

It can be thus concluded that the coupled THMC model in this work is valid and reliable in estimating the THMC behaviour of CPB in the hydration process. More examples on simulated properties of CPB in this high column test and more other case studies for the validation of the coupled THMC model can be found in Cui and Fall (2015).

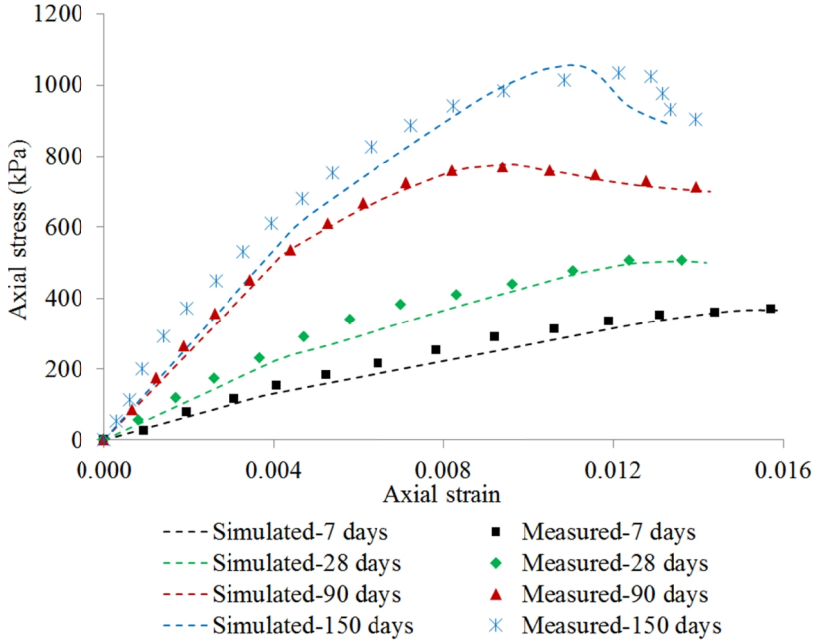

Figure 4.21 Comparison between simulated and measured stress-strain curves of hydrating CPB in quasi-static UCS tests

4.3.6.2 Simulation of SHPB tests on another cementitious material with varied water content (Case Study 2)

To verify the validity of the inclusion of variable gas contents (affecting parameter W and r_0) in the prototype viscoplastic cap model, and also to show its ability to capture the strain rate-dependent behaviour of other types of cementitious materials, SHPB tests performed on concrete with various degrees of saturation (Ross et al., 1995, 1996) are adopted and reproduced.

In an effort to experimentally determine the effects of moisture coupled with strain rate on concrete strength, high strain rate tests were conducted on completely saturated, partially saturated, and completely dry concrete specimens by using SHPB (Ross et al., 1995, 1996). After the concrete specimens were cured in air for 24 h, they were then submerged into tap water for 30 days. Then, the completely dry and partially saturated specimens were prepared by drying them in the oven at 230 F (110◦C) for 72 h and 7 h, respectively, with successive timed weighing. Prior to the dynamic tests, quasi-static tests were performed on each type of specimen to determine the quasi-static compression and tensile strength, and this information was also used to normalize the dynamic strength and acquire the dynamic increase factor (DIF) which is defined as the ratio of dynamic to static strength for each type of specimen in the SHPB tests. The tests

on completely dry and partially saturated specimens are reproduced in this study, while the response of fully saturated concrete during high-rate impacts will be addressed in a separate paper.

In the numerical simulation of the SHPB tests, the internal friction angle and cohesion of each type of specimen were determined based on quasi-static compression and tensile strength by using the Mohr–Coulomb criterion (López Cela, 2002). The Poisson's ratio was assumed to be fixed at 0.2 (Ross et al., 1996) and Young's modulus was estimated by using $E = 4785\sqrt{f_c}$ (Neville, 1973; Ross et al., 1996). The density of a fully saturated specimen was assumed to be 2350 kg/m^3, and the volumetric gas content (W) and density (r_0) of the completely dry and partially saturated specimens could be obtained by the measured drying curve in the test (Ross et al., 1995). The parameters h , X_0 and s required in the viscoplastic cap model for blast loading are obtained with Equations (4.63), (4.69) and (4.74), respectively. The samples in the SHPB test are 51 mm in length and 51 mm in diameter, and modeled with axisymmetric elements in the simulation. To simplify the modeling process, the typical loading history pattern in the SHPB tests was used (Tedesco et al., 1989). Axial velocity increments were applied at one end of the specimen while the other end was fixed, and it is not laterally confined according to the experiment configuration. The simulated DIFs are compared with the measured values of concrete in the SHPB tests in Figure 4.22, and the material properties used in the simulation are presented in Table 4.7.

Table 4.7 Material properties of concrete used in the simulation of SHPB test

Drying method	UCS (MPa)	Tensile strength (MPa)	r_0 (kg/m^3)	h (sec^{-1})	N	f_0 (Pa)	K(GPa)	G(GPa)
Oven-7 h	35.12	1.95	2246.6	1.1×10^{-3}	2.5	2×10^5	15.75	11.82
Oven-72 h	42.88	2.54	2105.6	9.5×10^{-4}	2.5	2×10^5	17.41	13.06
a	k(MPa)	R	D (MPa^{-1})	W	X_0(MPa)	C_0(m/s)	g_0	s
0.2653	1.6405	8	8×10^{-2}	0.103	145	2648	1	1.5
0.2638	2.1358	8	8×10^{-2}	0.244	155	2875	1	1.5

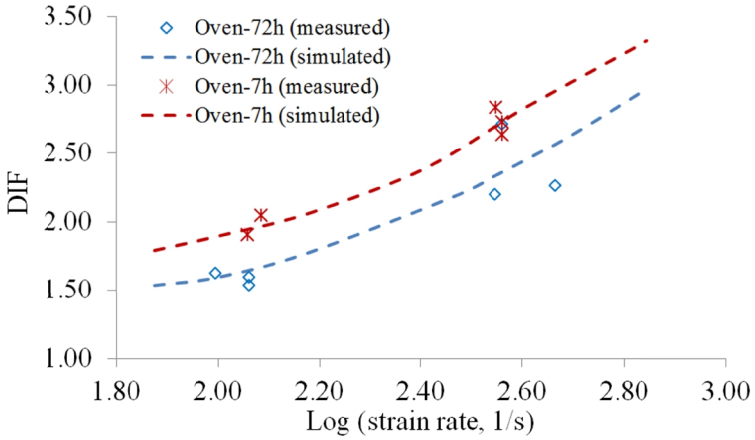

Figure 4.22 Comparison between simulated and measured DIFs of concrete in SHPB tests

As can be observed in Figure 4.22, there is a good agreement between the simulated and measured DIFs of each type of concrete over the range of the strain rates tested. Therefore, by supplementing the influence of the gas content, the modified viscoplastic cap model presented in the study is capable of evaluating the rate-dependent behaviour of cementitious materials such as concrete under the coupled influence of the moisture content and strain rate. Notably, as suggested in Figure 4.22, the DIF of the dry specimens is generally lower than that of the wetter ones. This is due to the effect of the moisture content on its strain rate sensitivity. Specifically, according to Ross et al. (1995, 1996), wetter concrete generally shows more strength increase as opposed to dry concrete in all ranges of the strain rates tested.

4.3.6.3 Simulation of SHPB tests on hydrating CPB (Case Study 3)

Huang (2009) and Huang et al. (2011) investigated the response of CPB at different curing times and cement contents under high strain rates with a modified SHPB system. To validate the developed THMC-viscoplastic cap model, test data of CPB with 5% cement content at different curing ages (15, 30, 60 days and dry samples) were used and reproduced. It is assumed that those dry samples were obtained after 180 days of curing. Prior to the simulation of the behaviour of hydrating CPB under high-rate impact with a viscoplastic cap model, the first step was to obtain the material properties of the CPB with the coupled THMC model. Some of the quasi-static data for the material used can be found in Klein and Simon (2006).

The CPB prepared in the test had an initial water content of 28% and cement content of 5% of the total solid mass, and fresh CPB was poured into PVC pipes with an inner diameter of 22

mm, outer diameter of 25 mm and height of 70 mm. The samples were sealed with water-resistant tape and cured at approximately 100% humidity and 25 $^{\circ}C$ (Huang, 2009). The input parameters, boundary conditions and initial values used for the numerical simulation of the curing process are listed in Table 4.6. In the simulation, the fitting parameters used in Equations (4.49), (4.50) and (4.66) are identical to those in Lu and Fall (2016), and they are obtained from the average values of the elastic constants and UCS reported in the quasi-static experiments by Klein and Simon (2006). With the simulated average strength parameters, elastic constants, volumetric gas content and pore pressure obtained by the coupled THMC model, it was possible to simulate the response of the CPB under high-rate loading with the viscoplastic cap model at the time of interest.

In the SHPB tests performed on CPB cured for 15, 30, 60 and 180 days, the specimens were taken from the curing pipes, and trimmed into cylinders that were 22 mm in diameter and 10 mm in height. They were then subjected to high strain rate impacts of 300 s^{-1} - 750 s^{-1}. The simulated pore pressure acquired from the THMC model was applied onto the specimen prior to the SHPB testing as the initial stress. In the simulation of the SHPB tests, only a quarter of those specimens were modeled with axially symmetric elements. To simplify the modeling process, a typical loading history pattern in the SHPB tests on CPB was used (Huang, 2009; Lu and Fall, 2016). Axial velocity increments were applied at one end of the specimen while the other end was fixed, and it was not laterally confined according to the experiment configuration.

The simulated peak axial stress of CPB with 5% cement content (by using the average UCS and elastic constants) at various ages under different loading rates in the SHPB tests were compared with the measured average dynamic strength of CPB as shown in Figure 4.23. The parameters used in the impact loading simulation were obtained from the THMC model and are listed in Table 4.8. The simulated stress-strain curves are not presented here, since experimental data are not available.

Table 4.8 Material properties of CPB with 5% cement content

Curing time	r_0 (kg/m^3)	h (μsec^{-1})	N	f_0 (Pa)	K(MPa)	G(MPa)	a
15 d	1847.0	1.05×10^{-3}	2.5	2×10^5	16.9	15.5	0.1966
30 d	1848.4	1.4×10^{-4}	2.5	2×10^5	44.5	40.4	0.1966
60 d	1849.5	1.4×10^{-4}	2.5	2×10^5	75.0	67.9	0.1966
180 d	1851.1	2.6×10^{-5}	2.5	2×10^5	109.3	98.6	0.1966
k(MPa)	R	D (MPa^{-1})	W	X_0(MPa)	C_0(m/s)	$\dot{g}_0$	s
0.0367	8	8×10^{-2}	0.078	0.3	96	1	3.39
0.0764	8	8×10^{-2}	0.094	2.2	155	1	2.23
0.1129	8	8×10^{-2}	0.123	2.2	202	1	1.80
0.1498	8	8×10^{-2}	0.326	5.5	244	1	1.62

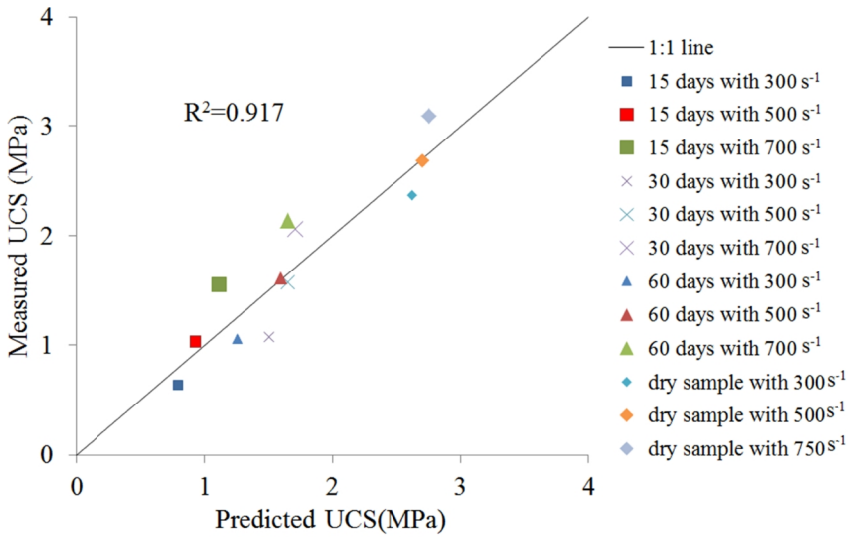

Figure 4.23 Comparison between simulated and measured average dynamic UCS of CPB with 5% cement content

As can be concluded from the good agreement between the simulated and measured results shown in Figure 4.23, the presented model can capture the time-evolution and rate-dependence of the material strength quite well, and indicates an increasing trend in the UCS against the strain rate for a given curing time within the range of the strain rates studied.

To further validate the proposed model, SHPB tests conducted on CPB with 7% and 10% cement content (Huang, 2009) were also reproduced. The curing process was also simulated by using the coupled THMC model with changes in the initial cement content, while other boundary and initial conditions were the same as those of the previous case with 5% cement content. As for the time-evolution of the average UCS of the CPB with 7% and 10% cement content, due to the lack of experimental data, it was estimated by increasing the UCS values of CPB with 5%

cement content by a ratio of increment in the cement content, since the strength of cementitious materials is generally proportional to the cement content (Fall et al., 2008; Chian et al., 2011). Then, the evolution of the average Young's modulus can be recaptured by the empirical rule as (Fall et al., 2005):

$$E = h(f_c)^i \tag{4.75}$$

where f_c is in the KPa and E in the MPa in the equation, and the fitting coefficients h = 0.0324 and i = 1.32 (Lu and Fall, 2016).

With the simulated average strength parameters, elastic constants, volumetric gas content and pore pressure obtained by the coupled THMC model, it was also possible to reproduce the response of the CPB with 7% and 10% cement content in the SHPB tests. These samples were also cured and tested at the same curing times and loading rates as those with 5% cement content, and also simulated by using the viscoplastic cap model with the same configurations.

A comparison between the simulated and measured average peak axial stress for CPB with 7% and 10% cement content in the SHPB tests are shown in Figures 4.24 and 4.25. The material parameters used in the simulation are obtained from the coupled THMC model and listed in Tables 4.9 and 4.10.

Table 4.9 Material properties of CPB with 7% cement content

Curing time	r_0 (kg/m^3)	h (μsec^{-1})	N	f_0 (Pa)	K(MPa)	G(MPa)	a
15 d	1847.7	8.0×10^{-4}	2.5	2×10^5	26.4	23.8	0.1966
30 d	1849.9	2.3×10^{-4}	2.5	2×10^5	68.6	61.9	0.1966
60 d	1850.8	7.0×10^{-5}	2.5	2×10^5	116.7	105.3	0.1966
180 d	1853.0	1.1×10^{-5}	2.5	2×10^5	169.5	152.9	0.1966
k(MPa)	R	D (MPa^{-1})	W	X_0(MPa)	C_0(m/s)	g_0	s
0.0513	8	8×10^{-2}	0.104	0.9	120	1	2.83
0.1057	8	8×10^{-2}	0.125	1.4	193	1	1.86
0.1579	8	8×10^{-2}	0.167	3.4	252	1	1.60
0.2096	8	8×10^{-2}	0.464	9.0	303	1	1.53

Table 4.10 Material properties of CPB with 10% cement content

Curing time	r_0 (kg/m^3)	h (μsec^{-1})	N	f_0 (Pa)	K(MPa)	G(MPa)	a
15 d	1847.9	2.5×10^{-4}	2.5	2×10^5	42.5	38.3	0.1966
30 d	1850.0	3.5×10^{-5}	2.5	2×10^5	111.7	100.7	0.1966
60 d	1851.9	1.5×10^{-5}	2.5	2×10^5	187.1	168.8	0.1966
180 d	1854.6	5×10^{-6}	2.5	2×10^5	272.3	245.6	0.1966
k(MPa)	R	D (MPa^{-1})	W	X_0(MPa)	C_0(m/s)	g_0	s
0.0732	8	8×10^{-2}	0.142	1.7	152	1	2.28
0.1525	8	8×10^{-2}	0.169	5.0	246	1	1.62
0.2250	8	8×10^{-2}	0.226	6.4	319	1	1.52
0.2997	8	8×10^{-2}	0.476	14.0	385	1	1.50

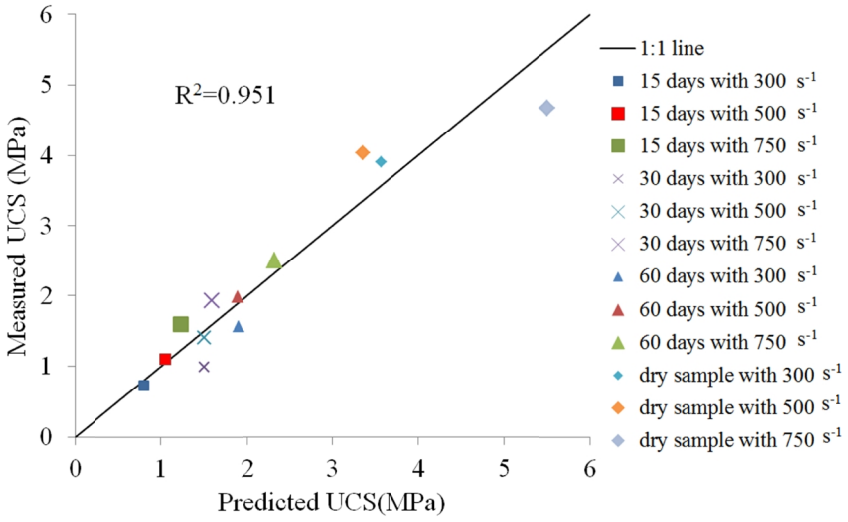

Figure 4.24 Comparison between simulated and measured average dynamic UCS of CPB with 7% cement content

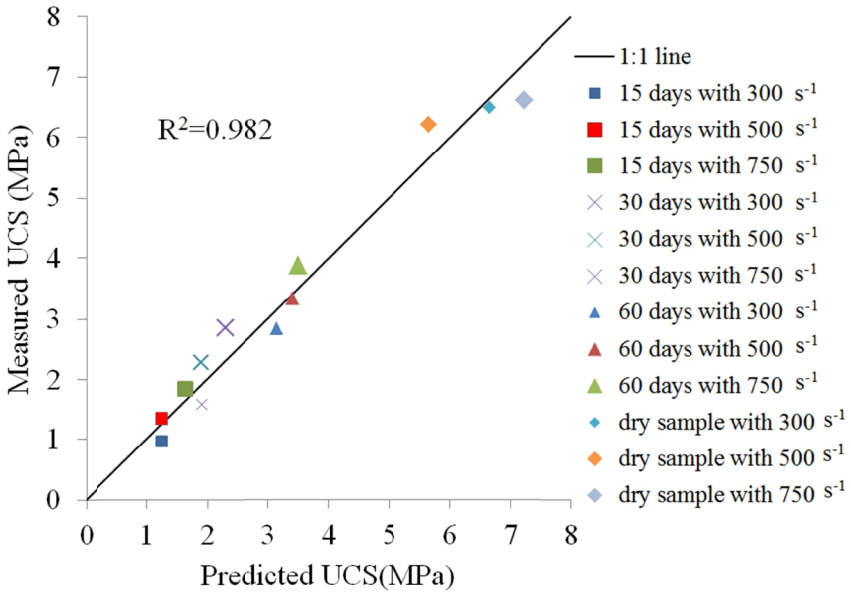

Figure 4.25 Comparison between simulated and measured average dynamic UCS of CPB with 10% cement content

As observed from Figures 4.24 and 4.25, there is also a good agreement between the simulated and measured average UCS of CPB in the SHPB tests, and thus the capability of the presented model to represent the time-evolutive and rate-dependent material strength under high-rate impact is again confirmed.

Stress-strain curves for individual CPB samples with 7% and 10% cement content are provided in Huang (2009) and Huang et al. (2011). In order to obtain simulated stress-strain curves and compare them with the experimental data, it was assumed that CPB specimens at a given cement content and curing time have an identical DIF at a given strain rate. Then, the quasi-static UCS of an individual sample can be estimated by comparing the peak of its stress-strain curve in the SHPB test, with the average dynamic strength of the CPB at a corresponding cement content, curing time and loading rate. With the use of this method, four simulated stress-strain curves of CPB samples with 7% or 10% cement content at various ages under different loading rates were obtained and compared with the available data, see Figure 4.26, and the material properties used in the viscoplastic cap model are presented in Table 4.11.

Table 4.11 Material properties of CPB samples used to obtain stress-strain curves

Cement content	Curing time	Strain rate (s^{-1})	DIF	UCS (MPa)	r_0 (kg/m^3)	h (μsec^{-1})	N	f_0 (Pa)	K (MPa)
7%	30d	500	2.63	0.49	1849.9	8×10^{-4}	2.5	2×10^5	54.8
7%	30 d	750	2.79	0.55	1849.9	7×10^{-4}	2.5	2×10^5	65.2
10%	15 d	300	3.14	0.85	1847.9	7×10^{-6}	2.5	2×10^5	114.7
10%	15 d	750	4.12	0.83	1847.9	9×10^{-6}	2.5	2×10^5	111.2
G(MPa)	a	k(MPa)	R	D (MPa^{-1})	W	X_0(MPa)	C_0(m/s)	g_0	s
49.4	0.1966	0.0891	8	8×10^{-2}	0.125	0.7	173	1	2.04
58.5	0.1966	0.1019	8	8×10^{-2}	0.125	0.9	188	1	1.90
104.1	0.1966	0.1567	8	8×10^{-2}	0.142	5.0	250	1	1.60
100.9	0.1966	0.1529	8	8×10^{-2}	0.142	5.0	246	1	1.62

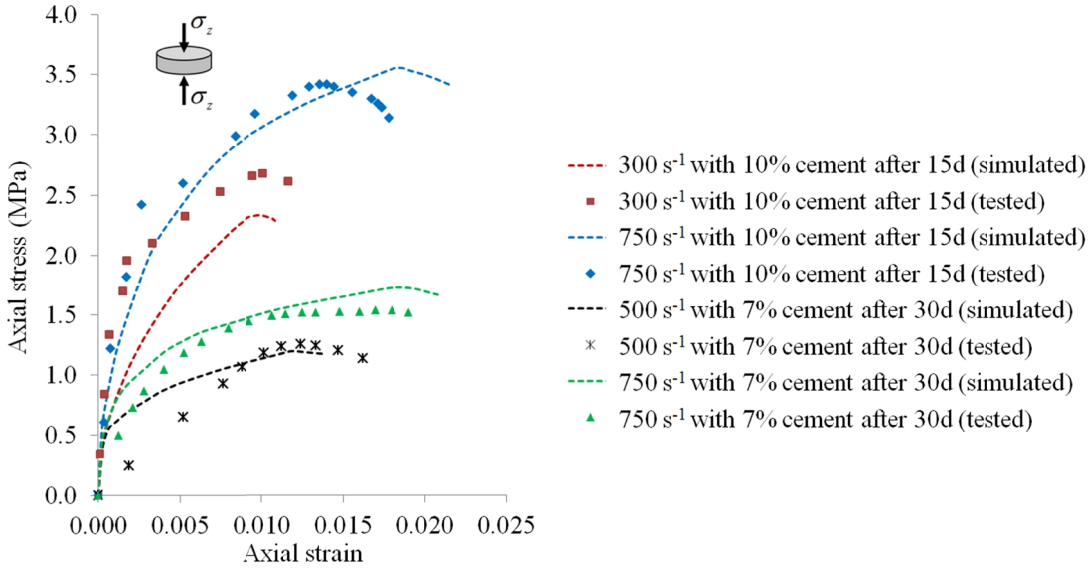

Figure 4.26 Comparison between simulated and measured stress-strain curves of individual CPB samples in SHPB tests

As shown by the good agreement between the simulated and measured results in Figure 4.26, the presented model can reproduce the mechanical behaviour of CPB under high-rate loading reasonably well. It should be noted that in addition to the strength increase, the viscoplastic cap model can also account for the apparent stiffness enhancement due to high strain rates.

Therefore, as concluded from the previous examples, the coupled THMC-viscoplastic cap model is able to adequately characterize the transient mechanical response of hydrating CPB under blast loading.

It should be noted that the softening process is not considered in traditional cap models. However, the softening behaviour has been captured by the viscoplastic cap model in this study. In fact, this phenomenon has also been captured in Katona (1985) and Simo et al. (1986), and is a time-dependent effect of the viscoplastic overstress formulation. To be more specific, the stress state is still above the cap envelope at such a yield point, and then, the stress would decrease (softening) as a result of additional inelastic strain development in the viscoplastic formulation.

4.3.7 Conclusions

To better understand the response of cemented backfill under sudden blast loading in the curing process, a coupled THMC-viscoplastic cap model has been developed. The THMC model is first validated against high column tests on hydrating CPB, in order to prove the capability of the THMC component of the coupled model to predict the time-evolutive material properties of CPB. Then, to verify the validity of the inclusion of variable gas contents into the prototype viscoplastic cap model, a set of SHPB tests performed on concrete with various water contents are reproduced. Finally, the developed model is used to reproduce a set of SHPB tests on hydrating CPB, and all material property input for the viscoplastic cap model is obtained from the THMC model to which it is coupled. The good agreement between the simulated and measured results suggests that the model is competent in capturing the blast response of hydrating CPB.

Compared with the previous chemo-viscoplastic cap model for cemented backfill, in addition to the consideration of time-evolutive mechanical properties, strain rate effect, plastic volumetric compaction as well as nonlinear hydrostatic response, the effect of variation in the volumetric gas content, density and pore pressure due to the hydration process on its blast response is further augmented in the presented model. Furthermore, all of the material properties required by the viscoplastic cap model to simulate the blast response of CPB are obtained from the coupled THMC model, which has rigorous consideration for the concerted action of multiphysics factors. By applying the coupled THMC-viscoplastic cap model, the transient mechanical behaviour of hydrating cemented backfill under high-rate impact can be evaluated under any curing time of concern. Thus, the developed model could be used as a potential tool for understanding and assessing the behaviour of hydrating cemented backfills subjected to mine blasts.

4.3.8 References

Abdul-Hussain N, Fall M. Unsaturated hydraulic properties of cemented tailings backfill that contains sodium silicate. Engineering Geology 2011; 123:288–301.

Abdul–Hussain N, Fall M. Thermo–hydro–mechanical behaviour of sodium silicate–cemented paste tailings in column experiments. Tunnelling and Underground Space Technology 2012; 29:85–93.

An J, Tuan CY, Cheeseman BA, Gazonas GA. Simulation of soil behaviour under blast loading. International Journal of Geomechanics, ASCE 2011; 11:323–334.

Aráoz G, Luccioni B. Modeling concrete like materials under sever dynamic pressures. International Journal of Impact Engineering 2015; 76:139–154.

Cervera M, Oliver J, Prato T. Thermo-chemo-mechanical model for concrete. I: Hydration and aging. Journal of Engineering Mechcanics, ASCE 1999a; 125(9): 1018–1027.

Cervera M, Oliver J, Prato T. Thermo-chemo-mechanical model for concrete. II: Damage and creep. Journal of Engineering Mechcanics, ASCE 1999b; 125(9): 1028–1039.

Chen WF, Baladi GY. Soil Plasticity: Theory and Implementation. Elsevier: Amsterdam, 1985.

Chian SC, Nguyen ST, Phoon KK. Extended strength development model of cement-treated clay. Journal of Geotechnical and Geoenvironmental Engineering, ASCE 2011;142(2):1–7.

COMSOL Multiphysics User's Guide, Version 3.5a, COMSOL AB, Stockholm, Sweden, 2009.

Côté J, Konrad JM. A generalized thermal conductivity model for soils and construction materials. Canadian Geotechnical Journal 2005; 42: 443–458.

Cui L, Fall M. A coupled thermo–hydro-mechanical–chemical model for underground cemented tailings backfill. Tunnelling and Underground Space Technology 2015; 50: 396–414.

Cui L, Fall M. An evolutive elasto–plastic model for cemented paste backfill. Computer and Geotechnics 2016; 71: 19-29.

Davis JP, Davis DK. Stress-dependent permeability: characterization and modeling. Society of Petroleum Engineers, 1999; SPE Paper no. 56813.

Doherty JP, Hasan A, Suazo GH, Fourie A. Investigation of some controllable factors that impact the stress state in cemented paste backfill. Canadian Geotechnical Journal 2015;12:1–12.

Dutt A, Saini MS, Singh TN, Verma AK, Bajpai RK. Analysis of thermo-hydrologic-mechanical impact of repository for high-level radioactive waste in clay host formation: an Indian reference disposal system. Environmental Earth Sciences 2012; 66 (8): 2327-2341.

Fall M, Belem T, Benzaazoua M. The compressive and tensile properties of underground paste backfill. Proceedings of 58-th Canadian Geotechnical Conference, Saskatoon, 2005; 1–7.

Fall M, Benzaazoua M, Saa EG. Mix proportioning of underground cemented tailings backfill. Tunnelling and Underground Space Technology 2008; 23:80–90.

Fall M, Célestin JC, Han FS. Potential use of polymer–pastefill as waste containment barrier materials. Journal of Waste Management 2010a; 30: 2570–2578.

Fall M, Célestin JC, Pokharel M, Touré M. A contribution to understanding the effects of curing temperature on the mechanical properties of mine cemented tailings backfill. Engineering Geology 2010b;114:397–413.

Gawin D, Pesavento F, Schrefler BA. Hygro-thermo-chemo-mechanical modelling of concrete at early ages and beyond. Part I: Hydration and hygro-thermal phenomena. International Journal for Numerical Methods in Engineering 2006a; 67: 299–331.

Gawin D, Pesavento F, Schrefler BA. Hygro-thermo-chemo-mechanical modelling of concrete at early ages and beyond. Part II: Shrinkage and creep of concrete. International Journal for Numerical Methods in Engineering 2006b; 67: 332–363.

Ghirian A, Fall M. Coupled thermo–hydro–mechanical–chemical behaviour of cemented paste backfill in column experiments. Part I: Physical, hydraulic and thermal processes and characteristics. Engineering Geology 2013; 164:195–207.

Ghirian A, Fall M. Coupled thermo–hydro–mechanical–chemical behaviour of cemented paste backfill in column experiments. Part II : Mechanical, chemical and microstructural processes and characteristics. Engineering Geology 2014; 170:11–23.

Gautam PK, Verma AK, Maheshwar S, Singh TN. Thermomechanical analysis of different types of sandstone at elevated temperature. Rock Mechanics and Rock Engineering 2016; 49 (5):1985-1993.

Henrych J. The dynamics of explosion and its use. Elsevier, New York, USA, 1979.

Huang S, Xia K, Qiao L. Dynamic tests of cemented paste backfill: effects of strain rate, curing time, and cement content on compressive strength. Journal of Material Science 2011; 46(15):5165–5170.

Huang S. Dynamic testing of soft and ultra–soft materials. Master Thesis. University of Toronto, Toronto, Canada, 2009.

Katona MG. Evaluation of viscoplastic cap model. Journal of Geotechnical Engineering, ASCE 1984; 110(8):1106–1125.

Kesimal A, Yilmaz E, Ercikdi B, Alp I, Deveci H. Effect of properties of tailings and binder on the short– and long–term strength and stability of cemented paste backfill. Materials Letters 2005; 59(28):3703–3709.

Khoei AR, Mohammadnejad T. Numerical modeling of multiphase fluid flow in deforming porous media: A comparison between two- and three-phase models for seismic analysis of earth and rockfill dams. Computers and Geotechnics 2011;38:142-166.

Klein K, Simon D. Effect of specimen composition on the strength development in cemented paste backfill. Canadian Geotechnical Journal 2006; 43:310–324.

Landriault D. Backfill in underground mining. In Underground Mining Methods Engineering Fundamentals and International Case Studies. SME, 2001; 601–614.

Li H, Liu J, Wang Y, Yao T, Tian Q, Li S. Deformation and cracking modeling for early-age sidewall concrete based on the multi-field coupling mechanism. Construction and Building Materials 2015; 88: 84–93.

López Cela JJ. Material identification procedure for elastoplastic Drucker–Prager model. Journal of Engineering Mechanics 2002;128:586–591.

Lu G, Fall M. A coupled chemo-viscoplastic cap model for simulating the behaviour of hydrating cemented tailings backfill under blast loading. International Journal for Numerical and Analytical Methods in Geomechanics 2016;40:1123–1149.

Murray YD, Lewis BA. Numerical simulation of damage in concrete. Report DNA–TR–94–190, Defense Nuclear Agency. Alexandria, 1995.

Nasir O, Fall M. Coupling binder hydration, temperature and compressive strength development of underground cemented paste backfill at early ages. Tunnelling and Underground Space Technology 2010; 25(1):9–20.

Neville AM. Properties of concrete. New York: Wiley & Sons; 1973.

Pichler C, Lackner R, Mang HA. A multiscale micromechanics model for the autogenous-shrinkage deformation of early-age cement-based materials. Engineering Fracture Mechanics 2007; 74: 34–58.
Powers TC, Brownyard TL. Studies of the physical properties of hardened Portland cement paste. ACI Journal Proceedings 1947; 249–336.
Ross CA, Jerome DM, Tedesco JW, Hughes ML. Moisture and strain rate effects on concrete strenght. ACI Materials Journal 1996;93:293–300.
Ross CA, Tedesco JW, Kuennen ST. Effects of strain rate on concrete strenght. ACI Materials Journal 1995;92:31–47.
Schindler AK, Folliard KJ. Heat of hydration models for cementitious materials. ACI Material Journal 2005;102(1):24–33.
Schindler AK. Effect of temperature on hydration of cementitious materials. ACI Material Journal 2004; 101(1):72–81.
Sercombe J, Hellmich C, Ulm FJ, Mang H. Modeling of early-age creep of shotcrete. I: Model and model parameters. Journal of Engineering Mechcanics, ASCE 2000; 126(3): 284–291.
Simo JC, Wu JW, Pister KS, Taylor RL. Assessment of cap model: Consistency return algorithms and rate–dependent extension. Journal of Engineering Mechanics, ASCE 1986; 114(2):191–218.
Tedesco JW, Ross CA, Brunair RM. Numerical analysis of dynamic split cylinder tests. Computers and Structures 1989;32:609–624.
Theory Reference for the Mechanical APDL and Mechanical Applications, ANSYS Release 12.0, ANSYS Inc., Canonsburg, Pennsylvania, 2009.
Thompson BD, Bawden WF, Grabinsky MW. In situ measurements of cemented paste backfill at the Cayeli Mine. Canadian Geotechnical Journal 2012;49:755–772.
Tong X, Tuan CY. Viscoplastic cap model for soils under high strain rate loading. Journal of Geotechnical and Geoenvironmental Engineering, ASCE 2007; 133(2):206–214.
Ulm FJ, Coussy O. Modeling of thermochemomechanical couplings of concrete at early ages. Journal of Engineering Mechcanics, ASCE 1995; 121(7): 785–794.
van Genuchten MT. A closed-form equation for predicting the hydraulic conductivity of unsaturated soils. Soil Science Society of America Journal 1980;44:892–898.
Verma AK, Singh TN, Bajpai RK . Study of Thermo-Hydro-Mechanical Processes at the Potential Site of an Indian Nuclear Waste Repository, ISRM International Symposium-EUROCK 2013.
Verma AK, Gautam P, Singh TN, Bajpai RK. Discrete element modelling of conceptual deep geological repository for high-level nuclear waste disposal. Arabian Journal of Geosciences 2015; 8 (10): 8027-8038.
Verma AK, Jha MK, Maheshwar S, Singh TN, Bajpai RK. Temperature-dependent thermophysical properties of Ganurgarh shales from Bhander group, India. Environmental Earth Sciences 2016;75 (4): 1–11.
Wang Z, Lu Y, Hao H. Numerical investigation of effects of water saturation on blast wave propagation in soil mass. Journal of Engineering Mechcanics, ASCE 2004b; 130(5):551–561.
Wu D, Fall M, Cai S. Numerical modelling of thermally and hydraulically coupled processes in hydrating cemented tailings backfill columns. International Journal of Mining, Reclamation and Environment 2014; 28(3):173–199.

Yilmaz E, Benzaazoua M, Belem T, Bussière B. Effect of curing under pressure on compressive strength development of cemented paste backfill. Mineral Engineering 2009; 22:772–785.
Zhang Y, Pichler C, Yuan Y, Zeiml M, Lackner R. Micromechanics-based multifield framework for early-age concrete. Engineering Structures 2013: 47: 16–24.

4.4 Technical Paper 4: Predicting blast-induced liquefaction of natural and man-made granular soils with viscoplastic cap model

(Submitted)

Gongda Lu, Mamadou Fall

Abstract:

A modified viscoplastic cap model has been developed in this study to capture the liquefaction caused by blasting. This model can account for the effect of high-rate impacts by incorporation of viscosity, capture the nonlinearity in volumetric deformation under high pressure with an equation of state, and also simulate the volumetric hysteresis effect with a cap model. The stiffness matrix of saturated granular soils is modified by incorporating the compressibility of pore fluid to characterize the generation of excess pore pressure during undrained blast loading. The proposed model is validated against laboratory impact tests as well as field explosion tests on saturated natural and man-made granular soils (e.g., sand, silt, tailings). The simulated results indicate good agreement with the experimental data in terms of peak pressure, ground motion as well as liquefaction. Moreover, the simulated irrecoverable compaction can represent well the build-up of residual excess pore water pressure, and it is consistent with the mechanism of blast-induced liquefaction. The applicability of viscoplastic cap models for simulating blast-induced liquefaction is thus verified in the study, and the developed model is also found applicable to capture liquefaction of saturated tailings backfills caused by mine blasting as is a primary concern in underground mining.

KEY WORDS: granular soil; tailings; liquefaction; blast; viscoplastic cap model

4.4.1 Introduction

Understanding and predicting the liquefaction susceptibility of soils under blast loading are important topics in civil, mining, defensive and protection engineering. Numerous cases of increases in residual excess pore pressure or liquefaction caused by blasting or high-pressure compression have been reported in the literature. These phenomena can occur in natural granular soils (e.g. sand, silt) and are usually associated with human induced activities, such as in-situ soil improvement processes, military high-explosive tests, laboratory experiments, accidental explosions, and terrorist attacks (Ivanov, 1967; Fragaszy and Voss, 1981, 1986; Dowding and Hryciw, 1986; Charlie et al., 1988, 1996, 2013; Veyera and Charlie, 1990; Bolton et al. 1994; Veyera et al. 2002; Ashford et al. 2004; Al-Qasimi et al. 2005; Charlie and Doehring, 2007). Due to the complex interactions among the constituent phases of soils in the course of liquefaction caused by blasting, such problems have been conventionally described over decades by developing empirical relationships for particular types of soils at given sites (e.g. Charlie et al. 1996, 2013; Ashford et al. 2004; Al-Qasimi et al. 2005). Despite the substantial amount of time and financial costs as well as safety concerns, the test results are only site-specific and limited in applicability to different cases.

Furthermore, it has long been recognized that mining geotechnical structures constructed of man-made granular soils, such as tailings impoundments, fresh cemented and uncemented tailings backfill (paste and hydraulic backfill (PB and HB)), also present the risk of liquefaction caused by mine blast routines. Liquefaction of tailings backfills could result in breach of their retaining structures, and thus cause casualties and loss of mine production (Ferdosi et al., 2015). However, previous research work on the liquefaction susceptibility of these man-made granular soils have mainly focused only on that caused by seismic loading (Aref, 1988; Le Roux, 2004; Saebimoghaddam, 2010; Ferdosi et al., 2015), and thus liquefaction caused by blasting has yet to be thoroughly examined.

In recent years, there has been growing interest in the modelling of soil response under blast loading (e.g. Awad, 1990; Wang and Lu, 2003; Grujicic et al., 2006; An et al., 2011; Higgins et al., 2013; Feldgun et al., 2014; Busch et al., 2016). In addition to the benefits of overcoming the costs and safety issues associated with physical testing, modelling has also provided more salient insights into the problems of blast wave-soil interactions (e.g. Wang and Lu, 2003). However, studies on the mathematical modelling of blast-induced liquefaction are extremely rare.

According to Wang et al. (2008), blast-induced liquefaction has pronounced differences with that caused by earthquakes. In fact, in the course of a blast event, the fluid phase(s) entrapped will simultaneously deform with the soil skeleton in a highly nonlinear manner under high pressure, thus providing additional resistance which could be even more significant than that of the matrix for the material when subjected to blast loading. This can be attributed to the hypothesis that interstitial fluids with even higher stiffness are not able to drain during the instantaneous loading condition (Wang and Lu, 2003; Wang et al. 2004a, 2004b; Grujicic et al. 2008a; An et al. 2011). Furthermore, with transient blast loading, the strain-rate effect should be considered as a crucial factor on the stiffness, strength and other mechanical behaviours of the material (Casagrande and Shannon, 1948; Whitman, 1970; Prapaharan et al. 1989; Bolton et al. 1994). Therefore, as blast events generally involve processes with large deformations and high strain rates, a rational soil model for blast loading should include the following: an equation of state (EOS) to account for the effect of high pressure, a failure model to delineate the yield behaviour, as well as a strength model to incorporate the strain-rate effect (Grujicic et al., 2008a).

As for the mechanism for modelling blast-induced liquefaction, Fragaszy and Voss (1981, 1986) verified that the volumetric hysteresis of saturated soil during compressive loading/unloading can lead to residual excess pore pressure. One way of incorporating such a hysteresis effect is to use different pressure-volume relationships (Bloom, 2006), and this method has been adopted in Lee (2006) and Wang et al. (2008, 2011) for capturing soil liquefaction under blast loading. However, these studies have employed Mohr-Coulomb type of yield criteria that would result in unrealistic dilation (Bloom, 2006), thus have been shown to underestimate pore pressure caused by blasting (Lee, 2006).

Another effective approach to simulating the volumetric hysteresis is to use a cap yield criterion (Nelson et al. 1971; Chen and Baladi, 1985; Merkle and Dass, 1985; Bloom, 2006). Cap models have been employed to simulate blast response of soils by Awad (1990), Ghassemi et al. (2010) and An et al. (2011). Nevertheless, only unsaturated soils have been studied in An et al. (2011), while the strain-rate effect and compaction of water during blasting of saturated soils have not been considered in the other studies.

Therefore, no model is available at present that captures the blast-induced liquefaction within a rigorous scheme. Despite its theoretical feasibility, the effectiveness of a cap model in simulating blast-induced liquefaction also needs to be further examined. A brief summary and

comparison of previous research work on simulating the pore pressure response of soils during blast loading are presented in Table 4.12.

Table 4.12 Summary and comparison of soil models for pore pressure response during blast loading

Source	Material stiffness	Failure model	Strength model	Source of hysteresis deformation	Additional comments
Busch et al. (2016); Lee (2006)	Soil stiffness is modified to include pressure dependence	Modified Mohr-Coulomb model	Duvaut-Lions viscoplasticity model	Modified Mohr-Coulomb model could result in unrealistic dilation	Underestimate pore water pressure due to dilation induced by Mohr-Coulomb type of model
An et al. (2011)	Mie-Grüneisen EOS	Cap model	Viscoplasticity of the Perzyna type	Cap model	Has not been applied to liquefaction
Ghassemi et al. (2010); Awad (1990)	Soil stiffness is modified to include pressure dependence	Cap model	Not included	Cap model	Generalized Biot's formulation
Wang et al. (2008)	Lyakhov model of soil as a three-phase medium	Drucker-Prager model	Modify the yield strength in accordance with Prapaharan et al. (1989)	Damage model	Suffer the inadequacies of Drucker-Prager model; uncertainty in capturing strain rate-effect
Kim and Blouin (1984)	Bilinear model	No explicit yield condition	Not included	Different loading and unloading moduli	Generalized Biot's formulation; suffer the inadequacies of bilinear model (Bloom, 2006)

The aim of the study is to demonstrate the validity of cap model for simulating blast-induced liquefaction in saturated granular porous media, such as natural and man-made soils. Recently, the authors have developed a viscoplastic cap model to describe the blast response of porous media (Lu and Fall, 2016, 2017), and it satisfies all three required components (i.e. EOS, failure and strength model) for modelling blast loading. This model is modified in the current study for simulating blast-induced liquefaction, and it is validated against liquefaction tests on natural granular soils (sand and silt). Meanwhile, given the correlation between grain size distribution (GSD) and liquefaction susceptibility (Ishihara, 1993), the model is then validated against liquefaction tests in a backfill deposit of tailings as a typical man-made granular soil with similar GSD to sand and silt. Therefore, the proposed model can also be generalized to capture the liquefaction of early-age tailings backfills (e.g. HB, PB) in a saturated state caused by production blasts which is one primary concern in backfilling operation of underground mining.

4.4.2 Mechanism of blast-induced liquefaction

For saturated loose materials, such as sandy and silty soils, the volume reduction caused by

blast-induced compression is prevented by the impedance of both matrix and pore fluid. This is due to insufficient time for relative movement of soil skeleton and pore water, and drainage is typically precluded in the blast loading process. Meanwhile, the volume compatibility in the undrained condition also necessitates that the volumetric strain of the pore fluid should be equivalent to that of soil skeleton (Naylor, 1974; Griffiths, 1985; Fragaszy and Voss, 1986; Griffiths and Li, 1989; Puebla et al., 1997). In this condition, blast-induced liquefaction could occur attributed to the inelastic stress-strain behaviour of soil skeleton, whilst the deformation of pore water is elastic (Fragaszy and Voss, 1981, 1986; Kim and Blouin, 1984; Charlie et al. 1988). To be more specific, with the volumetric hysteresis, it is therefore possible that the effective stress could drop to initial value after unloading, while the pore pressure is still maintained at a certain value greater than its initial condition due to the irrecoverable compaction. The discussed mechanism is illustrated in Figure 4.27.

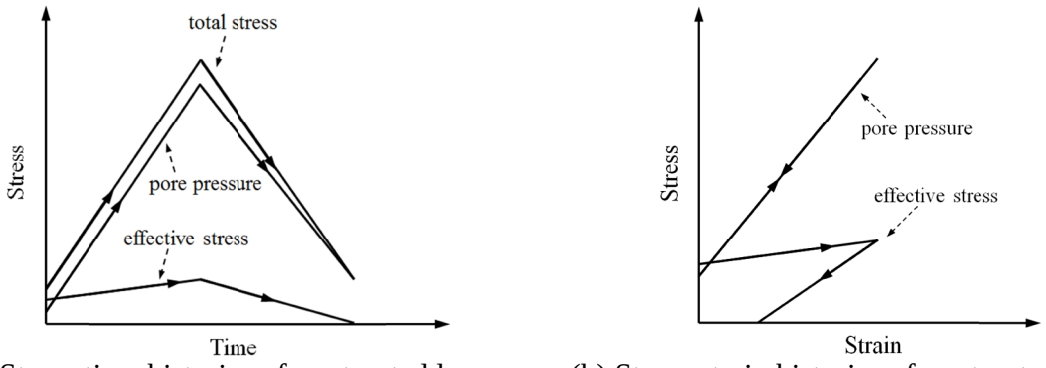

(a) Stress-time histories of a saturated loose material under blast loading (Adopted from Fragaszy and Voss, 1986)

(b) Stress-strain histories of a saturated loose material under blast loading (Adopted from Fragaszy and Voss, 1981)

Figure 4.27 Mechanism of blast-induced liquefaction

Whether liquefaction will take place also depends on the initial stress state, magnitude of the total stress increase, loading and unloading moduli of the material, drainage conditions, etc. (Fragaszy and Voss, 1986). Meanwhile, according to Fragaszy and Voss (1986), the compressive wave from an explosion will only significantly contribute to the development of liquefaction near the explosive source, and other mechanisms, such as contribution from shear waves, may be dominant further away from source. Therefore, the validity of such a mechanism for blast-induced liquefaction is restricted to a certain range of pressure in the vicinity of a camouflet, as beyond this range, the effects of shear stress are no longer negligible and different mechanisms

should be considered.

4.4.3 Formulation of model for simulating blast-induced liquefaction of granular porous media

4.4.3.1 Introduction

The viscoplastic cap model in Lu and Fall (2016, 2017) is adopted as the benchmark model for simulating the blast-induced liquefaction of granular porous media. It can account for the effects of high-rate impacts as the model takes viscosity into consideration, captures the nonlinearity in volumetric deformation with an equation of state, and also addresses the hysteresis effect with a cap model. In fact, this type of model has been proven effective for various geomaterials under high rate and high pressure conditions (e.g. Katona, 1984; Simo et al. 1988; Tong and Tuan, 2007; An et al. 2011; Aráoz and Luccioni, 2015). The formulation of the viscoplastic cap model is briefly introduced in this section. Then, the model is modified by rationally incorporating the compressibility of pore fluid to capture the pore pressure response in the undrained dynamic condition. Finally, the developed model is implemented into commercial software, COMSOL Multiphysics (COMSOL AB, Stockholm, Sweden). The model is applied to perform transient response analyses of soils subjected to time-dependent excitation that is explicitly defined in the time domain, and the problems are solved in the software using the Newton–Raphson algorithm with a Backward Euler method.

4.4.3.2 Perzyna type of viscoplastic formulation

It has been demonstrated that the strain rate has a significant effect on the stiffness and strength of various materials. However, very few efforts have been made to explicitly account for the effect of high strain rates on loose materials during blasting. A three-phase soil model (Wang et al. 2004a) and the work of Xu and Zhang (2015) have accounted for the stiffness or/and strength enhancement of soil under blast shocks with a phenomenological method. Alternatively, to take the effects of high strain rates into account for both strength and stiffness, formulations of viscosity have been integrated with conventional plasticity, resulting in the so called viscoplasticity. There are two popular viscoplastic models that are used to account for high strain rates in the literature, namely, the viscoplastic formulation of the Duvaut-Lions type (e.g. Simo et al. 1988; Schwer, 1994; Murray and Lewis, 1995; Motamedi and Foster, 2015) and Perzyna type

(e.g. Katona, 1984; Simo et al. 1988; Tong and Tuan, 2007; An et al. 2011; Higgins et al. 2013; Aráoz and Luccioni, 2015).

The Perzyna type of viscoplastic formulation (Perzyna, 1966) is adopted in current study to represent the rate-dependence in the material behaviour. As is conventional in mechanics, the total strain rate vector $\dot{\boldsymbol{\varepsilon}}$ can be decomposed into an elastic part $\dot{\boldsymbol{\varepsilon}}^{e}$ and a viscoplastic (inelastic) part $\dot{\boldsymbol{\varepsilon}}^{vp}$ as

$$\dot{\boldsymbol{\varepsilon}} = \dot{\boldsymbol{\varepsilon}}^{e} + \dot{\boldsymbol{\varepsilon}}^{vp} \tag{4.76}$$

The elastic strain rate is independent of viscosity and can be obtained as

$$\dot{\boldsymbol{\varepsilon}}^{e} = \mathbf{D}^{-1}\dot{\boldsymbol{\sigma}} \tag{4.77}$$

where $\dot{\boldsymbol{\sigma}}$ is the stress rate tensor, and $\mathbf{D}$ the elastic stiffness matrix.

For the viscoplastic strain rate, the viscoplastic flow rule is generally expressed as:

$$\dot{\boldsymbol{\varepsilon}}^{vp} = h\left\langle f(f)\right\rangle \frac{\partial f}{\partial \boldsymbol{\sigma}} \tag{4.78}$$

where h is a fluidity parameter; $\langle\ \rangle$ is the Macaulay bracket; f is the yield function and will be introduced in the following subsection; and $f(f)$ is a dimensionless scaling function conventionally defined as (e.g. Katona, 1984; Tong and Tuan, 2007):

$$f(f) = \left(\frac{f}{f_0}\right)^{N} \tag{4.79}$$

where N is the exponent and f_0 is a normalizing constant with the same unit as f. The associated flow rule has been conventionally employed in Perzyna type of viscoplasticity (Perzyna, 1966), and it has been verified by Katona (1984), Simo et al. (1986), Tong and Tuan (2007) and An et al. (2011) for simulating material behaviour under impact and blast loading. The function $f(f)$ is used here to quantify the overstress, i.e., the distance between the viscoplastic stress state and the yield surface, in accordance with the overstress theory of Perzyna (1966). According to Equation (4.78), the material response will be purely elastic when $h \to 0$, and simply corresponds to inviscid plasticity when $h \to \infty$.

4.4.3.3 Modified plastic cap model

The plastic cap model is adopted in this study to capture the yield behaviour of granular porous media. This type of model can avoid the unreasonable strength development under

increasing pressure and excessive dilation associated with a Mohr-Coulomb type criterion, and it has far less model parameters to calibrate than bounding surface plasticity (Lu and Fall, 2016).

The yield surface defined by the plastic cap model generally has two parts: a fixed ultimate failure envelope and a strain-hardening elliptical cap (see Figure 4.28). However, traditional cap models suffer from the numerical difficulties of singular corners, and these are located at the intersection of the shear failure envelope and hardening cap, where the former has a positive tangent while the latter has a horizontal slope at the singularity point. As a result, the flow direction at the intersection is indeterminate, which means that there is numerical instability, and a significant amount of time will be required for iteration (Ferdosi et al. 2015). To address this problem, Schwer and Murray (1994) provided a model that smooths the intersection of the shear failure envelope and strain-hardening surface called the continuous surface cap model (CSCM, see Figure 4.28). The CSCM has been widely adopted to date, for example, in work by Murray and Lewis (1995), Murray (2007), Aráoz and Luccioni (2015), and Motamedi and Foster (2015). However, in the CSCM, the product of a monotonically increasing shear yield function and a decreasing cap function with respect to I_1 would imply that the size and shape of the cap vary. This means the ratio of the major to the minor axis of the elliptical cap (coefficient R) will be variant and different from the R value specified by the modeller during the hardening process. Besides, the shear yield portion of the envelope might be too large and the actual cap portion could be too small due to the transition strategy. Therefore, the volumetric dilation/compaction of materials may not be effectively controlled with the use of the CSCM.

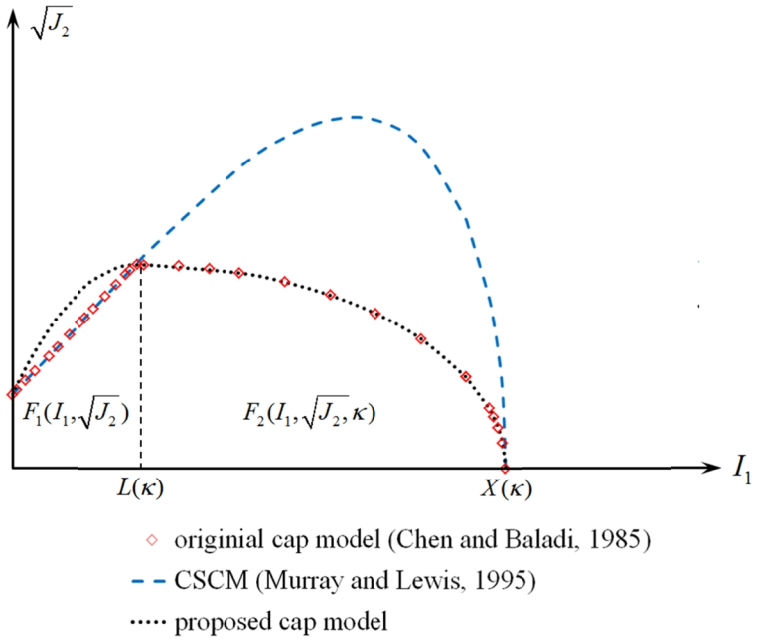

Figure 4.28 Comparison between different cap models

In order to avoid this problem and numerically treat singular corners with relative simplicity, a new approach is provided in Lu and Fall (2016). Specifically, the shear yield surface is assumed to have the same intercept with the $\sqrt{J_2}$ axis as the Drucker-Prager criterion at the beginning. Then, the shear yield surface is forced to have a horizontal slope at the intersection with the hardening cap by using a parabolic expression. Then, the shear yield surface is defined as:

$$F_1(I_1,\sqrt{J_2}) = \sqrt{J_2} - \frac{k-[X(k)-L(k)]/R}{L(k)^2} I_1^2 + 2\cdot\frac{k-[X(k)-L(k)]/R}{L(k)} I_1 - k \tag{4.80}$$

where $L(k)$ and $X(k)$ refer to the abscissa of the intersection of the elliptical cap with the shear failure envelope and the hydrostatic loading line (I_1 axis), respectively; and k is the Drucker-Prager criterion parameter that can be related to the Mohr-Coulomb criterion by using:

$$a = \frac{2\sin j}{\sqrt{3}(3+\sin j)}, \qquad k = \frac{6c\cos j}{\sqrt{3}(3+\sin j)} \tag{4.81}$$

where c and j are the cohesion and internal friction angle, respectively.

The isotropic hardening cap is defined by following Chen and Baladi (1985):

$$F_2(I_1,\sqrt{J_2},k) = \sqrt{J_2} - \frac{1}{R}\left\{[X(k)-L(k)]^2 - [I_1-L(k)]^2\right\}^{1/2} \tag{4.82}$$

where translation of $X(k)$ can be expressed with a logarithmic hardening law as

$$X(k) = -(1/D) \cdot \ln\left(1 - \frac{e_{kk}^{p}}{W}\right) + X_0 \tag{4.83}$$

where constant W denotes the maximum volumetric plastic strain that the material can undergo, D is a shape parameter of the volume-pressure curve, and X_0 is the initial vertex of the hardening cap. These parameters can be acquired from isotropic compression tests. Then, $L(k)$ can be determined by enforcing continuity of the entire yield envelope:

$$k = \frac{X(k) - R \cdot k}{1 + R \cdot a} \tag{4.84}$$

and

$$L(k) = \begin{cases} k & k > k_0 \\ k_0 & \text{otherwise} \end{cases} \tag{4.85}$$

where k_0 is the onset of the cap.

A conceptual comparison between the shape of the original cap model, continuous surface cap model and the cap model used in the study are presented in Figure 4.28, and the parameters used for the shear and cap envelopes are the same for the three different models in this example.

The hardening cap is not fixed in the stress space, and it can expand or contract with the plastic volumetric strain. For instance, during initial compaction, the cap expands as e_{kk}^{p} develops. Then, when the stress state lies the shear failure envelope, dilation would occur and the decrease in e_{kk}^{p} would thus cause the shrinkage and movement of the cap back against the origin. The dilatancy would continue until the cap reaches the stress point on the shear yield envelope. This condition implies the stress point becomes the joint point of the shear and the cap envelopes where the plastic strain rate vector is vertical. Therefore, any cap movement that would result from further plastic volumetric strain is precluded, and the amount of dilatancy is controlled in a cap model (DiMaggio and Sandler, 1971; Gu and Lee, 2002; Bloom, 2006; Tu and Lu, 2009).

Meanwhile, according to Chen and Baladi (1985), the volumetric hysteresis can also be captured by the cap model. As discussed in Section 4.4.2, the hysteresis effect is considered to be a key mechanism that leads to the liquefaction of saturated loose materials during blast loading, and it is generally attributed to two main sources (Nelson et al. 1971; Bloom, 2006). The first is from the yield of the material, and the second is from the different pressure-volume relations upon hydrostatic loading/unloading. To represent the volumetric hysteresis under blast loading,

some have used different bulk moduli during the loading/unloading processes for soil skeletons with a bilinear model (e.g. Kim and Blouin, 1984), and others have used different functions to control the loading/unloading processes (e.g. Laine and Sandvik, 2001; Grujicic et al. 2006, 2008b, 2009, 2010; Wang et al. 2008, 2011; Yankelevsky et al. 2008; Karinski et al. 2009a, 2009b; Feldgun et al. 2013). However, a more stable and effective method to account for hysteresis behaviour is the use of plastic cap model (Nelson et al. 1971; Merkle and Dass, 1985; Bloom, 2006). Specifically, if the stress state lies on the cap portion of the yield envelope during initial compaction, the cap envelope and the associated flow will result in volumetric plastic strain in compression. Since unloading is purely elastic, there will be irrecoverable bulk deformation and the hysteresis effect is thus realized (see Figure 4.29).

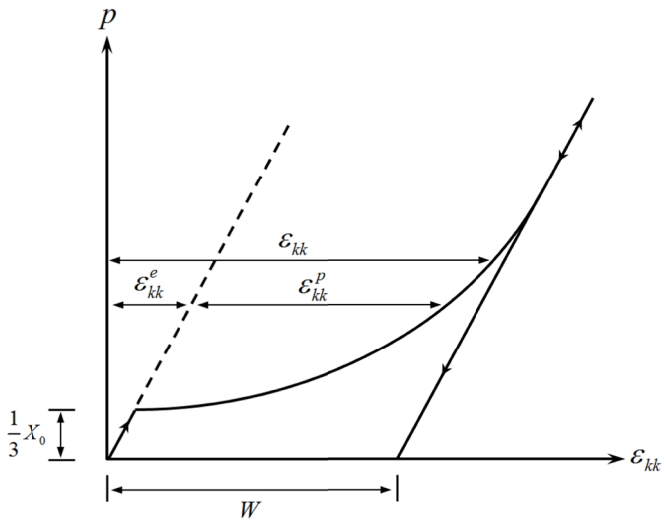

Figure 4.29 Hysteresis effect represented by the cap model

(Modified after Chen and Baladi, 1985 and Murray, 2007; where e_{kk} and e^e_{kk} are total and elastic volumetric strain, respectively)

4.4.3.4 Modified nonlinear pressure-volume relation for saturated porous media in undrained condition

Under intensive loading conditions such as blasting, the pressure-volume relationship of a material would be typically nonlinear (Henrych, 1979). The variable-bulk-modulus approach is adopted in this study to account for such an effect. In fact, this method has been used by Nelson et al. (1971), Sandler et al. (1976), Chen and Baladi (1985) and Murray and Lewis (1995) among others, and integrated with a plastic cap model to obtain better data fitting flexibility (Sandler et

al. 1976). The nonlinearity in stiffness of soil skeleton (K_s) and pore water (K_w) is determined in the study by using the Mie-Grüneisen EOS as (An et al., 2011):

$$K_i = \frac{r_{i0}C_{i0}^2[1+(1-\frac{g_{i0}}{2})m_i - \frac{a_{i0}}{2}m_i^{\,2}][1+\frac{2m_i(s_i-1)}{1+m_i-s_im_i}+\frac{m_i(g_{i0}+a_{i0}m_i)}{(1+m_i)^2}]+r_{i0}C_{i0}^2m_i(1-\frac{g_{i0}}{2}-a_{i0}m_i)}{(1+m_i-s_im_i)^2}+\left[\frac{(g_{i0}+a_{i0}m_i)^2}{(1+m_i)^2}+a_{i0}\right]E_i^v \tag{4.86}$$

where $i = s$ or w, r_{i0} is the material density; C_{i0} is the p-wave velocity of the material; s_i is the slope of the shock velocity against the particle velocity curve; g_{i0} is the Grüneisen parameter, E_i^v is the internal energy per unit initial volume; a_{i0} is the first order volume correction to g_{i0}; and $m_i = e_{kk}/(1-e_{kk})$.

Notably, despite a cap model is applicable to characterize the volumetric hysteresis of soil under blast loading, further modifications to introduce the impedance of pore fluid are required to capture its coupled hydro-mechanical behaviour and build-up of excess pore pressure in the undrained condition. As discussed, the skeleton and pore water of a saturated porous medium will be compressed concurrently at the same magnitude during blast loading. According to Naylor (1974) and Griffiths and Li (1989), the increase of pore pressure of a saturated porous medium in undrained condition can be determined as

$$dP_w = K_a de_{kk} \tag{4.87}$$

where K_a represents the apparent bulk modulus of the pore fluid, and it can be obtained as (Naylor, 1974):

$$\frac{1}{K_a} = \frac{n}{K_w} + \frac{1-n}{K_p} \tag{4.88}$$

where n is the porosity; and K_p is the bulk modulus of solid particles.

Then, the undrained response of the saturated porous medium can be characterized by combining the apparent pore fluid bulk modulus and the elastic matrix of the skeleton (Naylor, 1974; Griffiths, 1985). By considering the inelastic strain of skeleton, the modified undrained bulk modulus of the saturated mixture (K_m) can be obtained in the study as

$$dP = dP_s + dP_w = K_s de_{kk}^e + K_a de_{kk} = (K_s + K_a \frac{de_{kk}}{de_{kk}^e}) de_{kk}^e = K_m de_{kk}^e \tag{4.89}$$

Finally, the Poisson's ratio v_m also needs to be modified for the undrained condition as (Naylor, 1974; Griffiths, 1985):

$$v_m = \frac{(1-2v)(1+v)+Ev/K_a}{2(1-2v)(1+v)+E/K_a} \tag{4.90}$$

where E and ν are elastic modulus and Poisson's ratio of the porous skeleton. Thus, by using Equations (4.86)-(4.90), the stiffness matrix of the saturated porous medium in undrained condition can be obtained.

4.4.4 Model validation

4.4.4.1 Introduction

To demonstrate the validity of the developed model in simulating the response of saturated granular porous media (natural and man-made soils) under blast loading, particularly the build-up of excess pore pressure or liquefaction, simulations of laboratory ramp and shock loading tests on sand and silt are carried out. Then, simulations of field explosion tests on sand and tailings are conducted respectively to show the applicability of the developed model to large scale experiments.

4.4.4.2 Simulation of ramp loading on undrained saturated sand

The ramp loading experiments conducted by Fragaszy and Voss (1981, 1986) on saturated Eniwetok sand were adopted and simulated. The tests were conducted in a triaxial cell, and the saturated soil samples with a height of 110 mm and a diameter of 35.6 mm were subjected to ramp loading with an oil pump system. In the test, the cell pressure was increased to a predetermined level, then returned to its initial value. The porosity of the soils was determined from their grain and dry densities, and was approximately 0.47. The drained compression test conducted prior to the ramp loading showed that the soil skeleton has a bulk modulus of 100 MPa (Fragaszy and Voss, 1981; Wang et al. 2008).

The configuration of the numerical model is illustrated in Figure 4.30 below. It is simulated by using 2D symmetry, and only vertical displacement is allowed along the symmetrical axis. 4-node quadrilateral elements with maximum size of 1.5 mm are used in generating the mesh. A monitored point (M) is placed in the middle of the sample. The loading pattern is shown in Figure 4.31 below and is adopted from Wang et al. (2008). The pressure is assumed to increase to a peak within 0.1 ms, and kept constant for about 5 ms. Then the pressure is reduced to the initial value within 0.1 ms and stays at this level for a period of time. The pattern is determined through trial calculations so that there is sufficient time for the transient response to die out, and the steady state is reached after a few oscillations of the wave in the sample (Wang et al., 2008).

Two sets of experiments in Fragaszy and Voss (1981, 1986) are adopted herein, and the peak pressure is 34.48 MPa and 20.69 MPa, respectively. The material properties used in the simulation are based on the experimental data in Fragaszy and Voss (1981, 1986) and those used in Wang et al. (2008), see Tables 4.13 and 4.14. The simulated strain and pressure time histories of the monitored point in both cases are presented in Figures 4.32-4.33, and details of the simulated results are compared with the experimental data provided in Table 4.15, where PPR is the pore pressure ratio, defined as the ratio of the residual excess pore pressure over the initial mean effective stress in accordance with Fragaszy and Voss (1981, 1986).

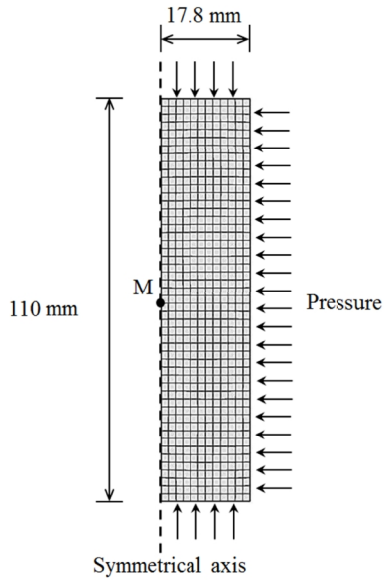

Figure 4.30 Configuration of numerical model for ramp loading tests

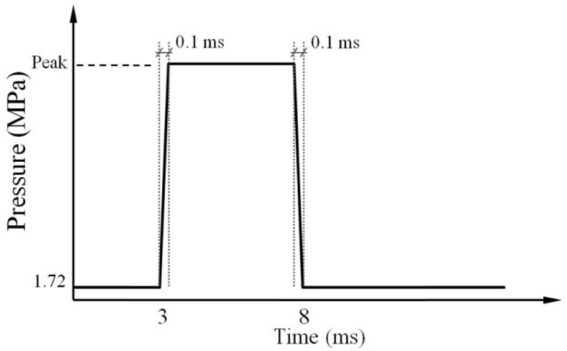

Figure 4.31 Load pattern of numerical simulation for ramp loading tests

Table 4.13 Material properties used in the model for ramp loading tests on saturated sand

Test	Initial confining pressure (MPa)	Initial pore water pressure (MPa)	Peak pressure (MPa)	Density (kg/m^3)	h (μsec^{-1})	N
Case 1	1.72	0.69	34.48	1959	4×10^{-5}	1
Case 2	1.72	0.69	20.69	1959	4×10^{-5}	1
f_0 (Pa)	a	k(MPa)	R	D (MPa^{-1})	W	X_0(MPa)
1×10^6	0.25	0	8	1×10^{-3}	0.0027	5
1×10^6	0.25	0	8	1×10^{-3}	0.0027	5

Table 4.14 Material properties used for undrained response of saturated sand in ramp loading tests

n	r_{s0} (kg/m^3)	r_{w0} (kg/m^3)	C_{s0} (m/s)	C_{w0} (m/s)	s_s	s_w	g_{s0}	g_{w0}	$\underline{\nu}$	$\underline{K_p}$ (GPa)
0.47	1490	1000	260	1460	1.64	2	0.11	0.6	0.33	54

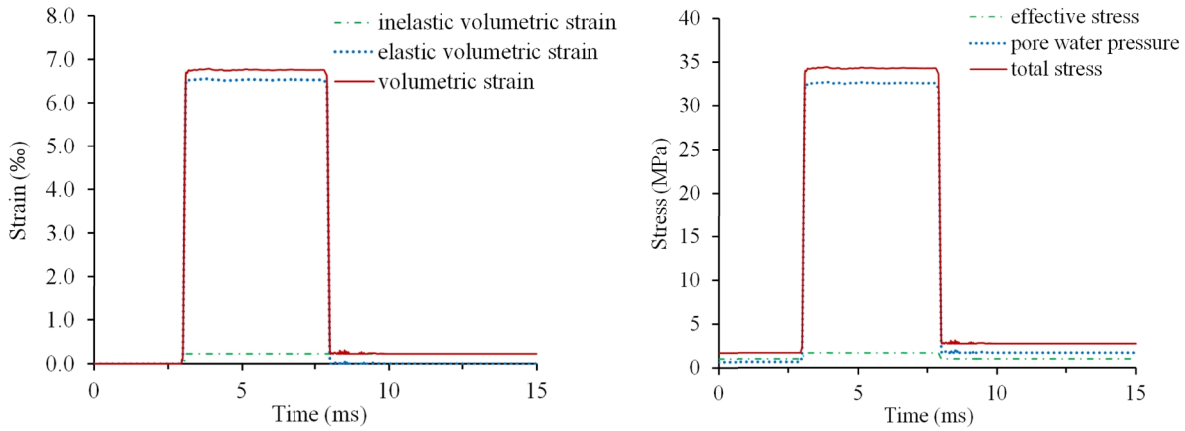

(a) (b)

Figure 4.32 Simulated loading histories of the monitoring point M in Case 1: (a) strain-time; (b) pressure-time

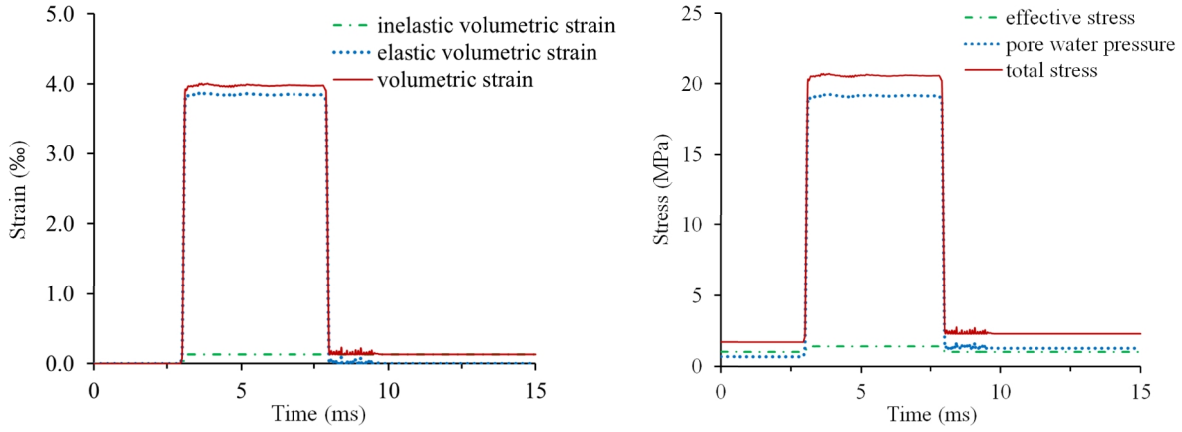

(a) (b)

Figure 4.33 Simulated loading histories of the monitoring point M in Case 2: (a) strain-time; (b) pressure-time

Table 4.15 Comparison between simulated and experimental results for ramp loading tests on saturated sand

Test	Peak p.w.p. change (MPa)		Residual p.w.p. (MPa)		PPR	
	Tested	Simulated	Tested	Simulated	Tested	Simulated
Case 1	31.10	31.90	1.72	1.70	1	0.97
Case 2	16.38	18.40	1.30	1.29	0.59	0.58

As can be observed from Figures 4.32(b)-4.33(b), when the saturated sand is subjected to sudden blast loading, the majority of the applied load is borne by the water due to its high resistance in the undrained condition, while that carried by the soil skeleton is negligible. This is in accordance with the deformation mechanism of water-bearing soil subjected to blast loading found in Henrych (1979). After the passage of blast waves, the pore water pressure is kept at a higher value than its initial condition because of the irrecoverable strain, which is supported by the strain-time histories shown in Figures 4.32(a)-4.33(a), and this is consistent with the mechanism of blast-induced liquefaction discussed in Section 4.4.2.

The details of simulation results are summarized in Table 4.15, and they have shown good agreement with the experimental data. Therefore, with the proposed strategy to include the compressibility of the interstitial water, the modified viscoplastic cap model can well capture the deformation mechanism of saturated soils subjected to blast loading, and the response of the pore water pressure that corresponds with the volumetric deformation of soil can also be effectively reproduced.

4.4.4.3 Simulation of shock loading on saturated sand and silt

A series of shock loading experiments were conducted by Charlie et al. (1985) and Bolton et al. (1994) on saturated specimens of Monterey sand and Bonny silt to study blast-induced liquefaction. Their test results are adopted and numerically reproduced in this study to validate the proposed model.

Shock loading was carried out in a laterally fixed cylinder container, and the soil samples in the container had a height of 152.5 mm and a diameter of 68 mm. Axial shock compression was applied on the top of the sample with various amplitudes. The shock loading can be simplified as triangular pulse loading in the simulation which reaches its peak and then reduces back in half a millisecond as shown in Figure 4.34 below, and it is determined based on the monitored pressure time histories in the experimental tests. The porosity of sand and silt is approximately 0.41 and 0.48, respectively, and is determined from their grain and dry densities. The drained compression test conducted on Monterey sand prior to the shock loading showed that the sand skeleton has a bulk modulus of 138 MPa (Bolton et al. 1994; Wang et al. 2008), while the information on Bonny silt is not available. Bonny silt is a wind-blown deposit of clayey silt and is typical of loess deposits found in central-west US (Charlie et al., 1988), and an empirical bulk modulus of 66.5 MPa is used based on Kezdi (1974).

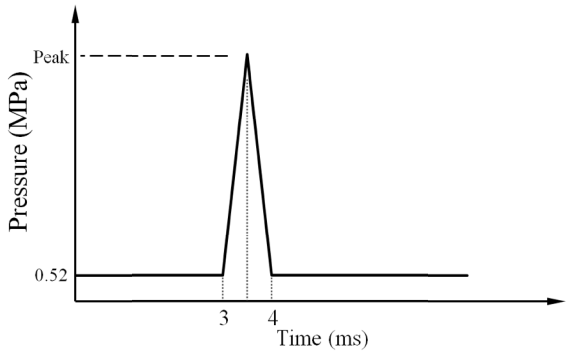

Figure 4.34 Load pattern of numerical simulation for shock loading tests

The configuration of the numerical model is shown in Figure 4.35 and it is simulated by using 2D symmetry, and only vertical displacement is allowed along the symmetrical axis. 4-node quadrilateral elements with maximum size of 3 mm are used in generating the mesh. A monitored point (N) is placed in the middle of the sample. The model is laterally confined so that

the radial displacement is restrained, and the low-reflective boundary condition is used at the bottom of the model to ensure that waves pass out from the model without reflection in the transient analysis. Two sets of experiments on Monterey sand and one on Bonny silt as found in Bolton et al. (1994) are adopted, and the peak pressure is 5.04 MPa (Case 1) and 7.39 MPa (Case 2) for the sand, respectively, and 2.66 MPa for the silt (Case 3). The material properties used in the simulation are based on the experimental data in Bolton et al. (1994) and Wang et al. (2008), which are listed in Tables 4.16 and 4.17. The simulated strain and pressure time histories of the monitored point in all cases are presented in Figures 4.36-4.38.

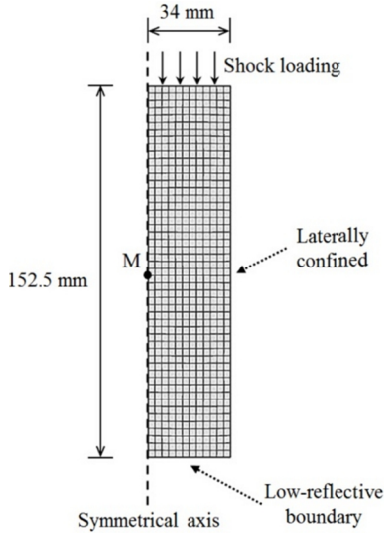

Figure 4.35 Configuration of the numerical model for shock loading test

Table 4.16 Material properties used in the model for shock tests on saturated sand and silt

Test	Initial effective stress (MPa)	Initial pore water pressure (MPa)	Peak pressure (MPa)	Density (kg/m^3)	h (μsec^{-1})	N
Case 1 (sand)	0.172	0.35	5.04	1970	3.5×10^{-6}	1
Case 2 (sand)	0.172	0.35	7.39	1970	5.2×10^{-6}	1
Case 3 (silt)	0.172	0.35	2.66	1848	1.3×10^{-5}	1
f_0 (Pa)	a	k(MPa)	R	D (MPa^{-1})	W	X_0(MPa)
1×10^6	0.25	0	8	4×10^{-3}	0.0011	1
1×10^6	0.25	0	8	4×10^{-3}	0.0011	1
1×10^6	0.225	0	8	4×10^{-3}	0.0011	1

Table 4.17 Material properties used for undrained response of saturated sand and silt in shock tests

Test	n	r_{s0} (kg/m^3)	r_{w0} (kg/m^3)	C_{s0} (m/s)	C_{w0} (m/s)	s_s	s_w	g_{s0}	g_{w0}	$\underline{\nu}$	$\underline{K_p}$ (GPa)
Cases 1-2 (sand)	0.41	1563	1000	310	1460	1.64	2	0.11	0.6	0.33	54
Case 3 (silt)	0.48	1367	1000	221	1460	1.64	2	0.11	0.6	0.33	54

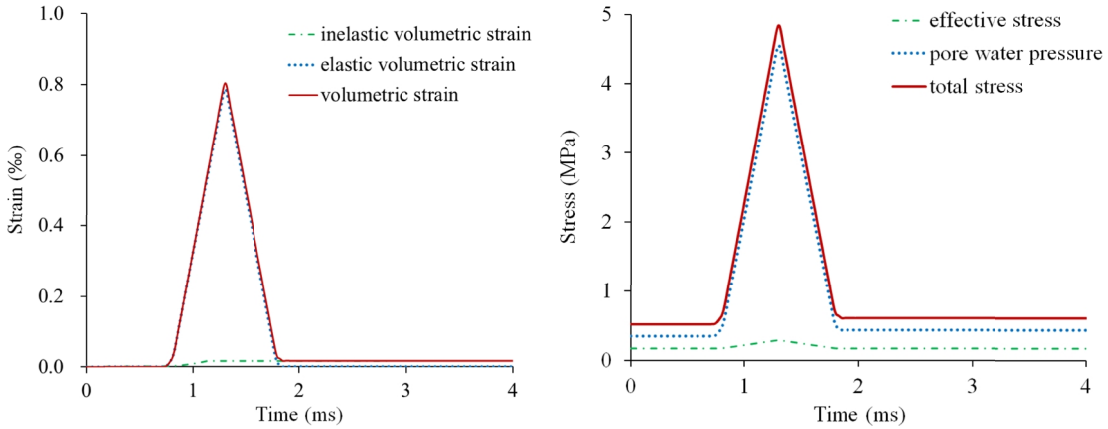

(a) (b)

Figure 4.36 Simulated loading histories of the monitoring point N in Case 1 (sand): (a) strain-time; (b) pressure-time

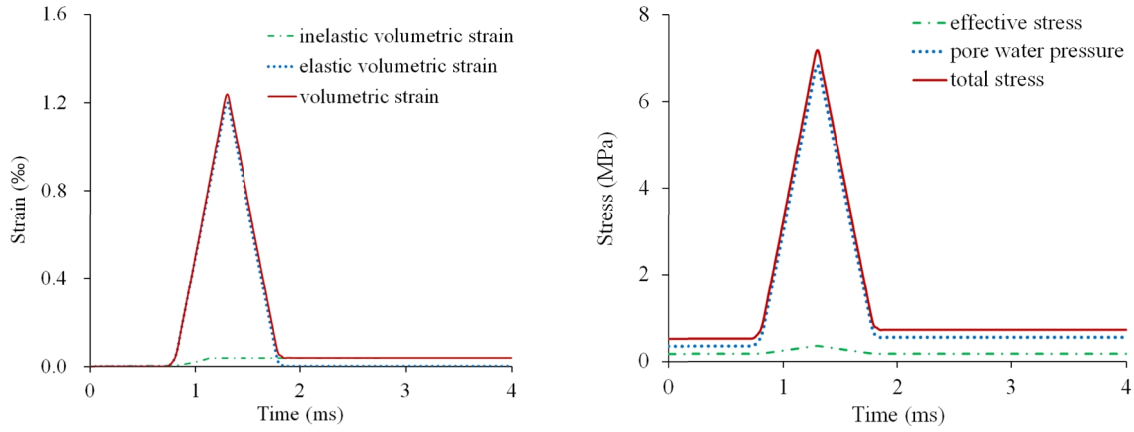

(a) (b)

Figure 4.37 Simulated loading histories of the monitoring point N in Case 2 (sand): (a) strain-time; (b) pressure-time

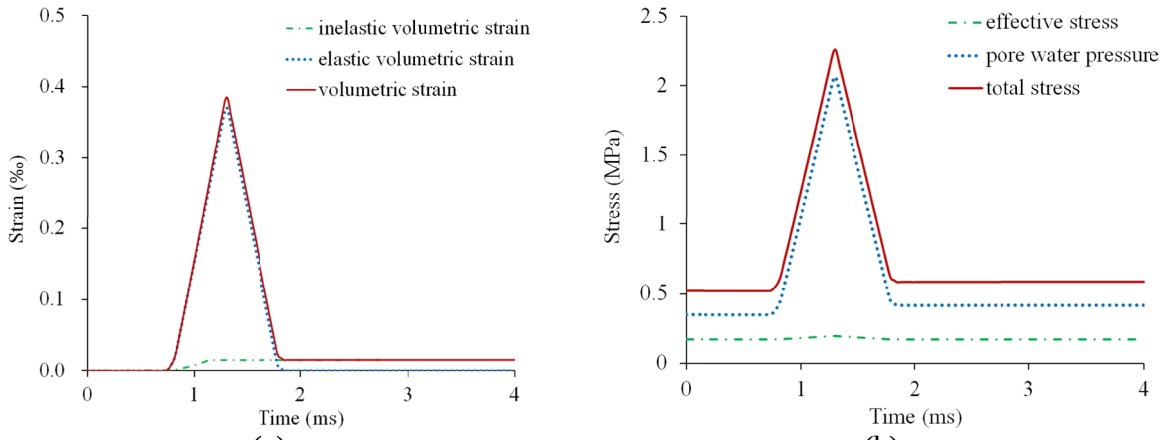

(a) (b)

Figure 4.38 Simulated loading histories of the monitoring point N in Case 3 (silt): (a) strain-time; (b) pressure-time

As can be observed from Figures 4.36(b)-4.38(b), the majority of the applied pressure is borne by the pore water during the shock impact, while in contrast, the resistance of the soil skeleton to the imposing load is insignificant. After the passage of the stress waves, the elastic strain of soils would recover, while the pore pressure is still above its initial value due to the hysteresis effect. Figures 4.36(a)-4.38(a) also show that there is irrecoverable volumetric strain after unloading, and it is responsible for the build-up of residual excess pore water pressure caused by blast loading. Details of simulated results are summarized and compared with experimental data in Table 4.18, where PPR is defined as the ratio of residual excess pore pressure over initial mean effective stress according to Bolton et al. (1994), and it has shown that they are also consistent to the experimental results.

Table 4.18 Comparison between simulated and experimental results for shock tests on the saturated sand and silt

Test	Peak p.w.p. change (MPa)		Residual p.w.p. (kPa)		PPR	
	Tested	Simulated	Tested	Simulated	Tested	Simulated
Case 1 (sand)	4.52	4.20	436	437	0.50	0.51
Case 2 (sand)	6.87	6.50	548	547	1.15	1.14
Case 3 (silt)	2.13	1.81	415	417	0.38	0.39
Case 1A (0.75 ms)	/	4.25	/	484	/	0.78
Case 1B (1 ms)	/	4.29	/	526	/	1.02

The simulated pore pressure histories of saturated sand in shock loading tests are compared with experimental data in Figure 4.39, while those for silt are not available. As can be observed,

there is also good agreement between simulation and experimental results in terms of peak and residual values of pore pressure.

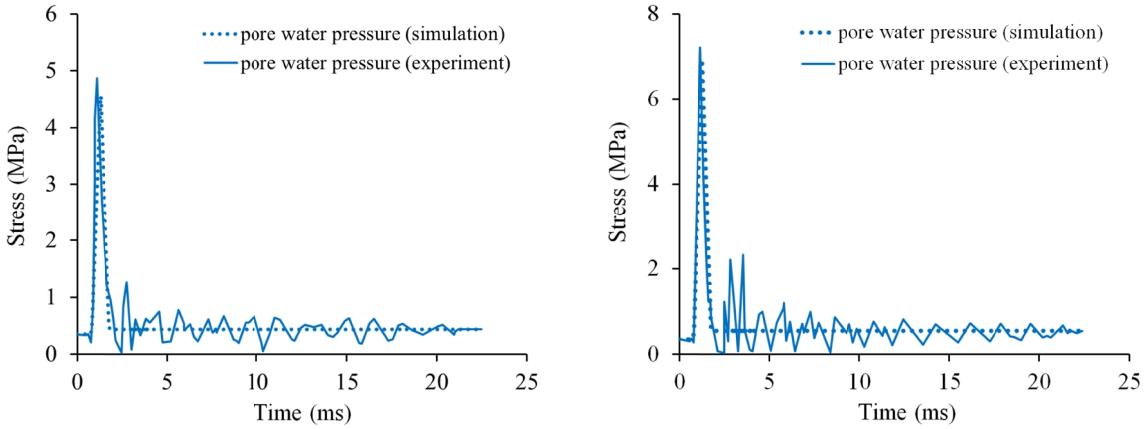

Figure 4.39 Comparison between simulated and measured pore pressure response of sand in the shock tests: (a) Case 1; (b) Case 2

Therefore, it can be concluded that the developed model is also able to characterize the behaviours of saturated sand and silt subjected to shock loading, and the response of the pore water pressure can be reasonably captured as well.

To examine the effect of viscosity in the model for capturing the strain rate effect, the soil response with two different loading patterns is also reproduced for Case 1. Specifically, the peak pressure of each test is kept the same (5.04 MPa), while the duration of the loading and unloading stages is increased from 0.5 ms to 0.75 ms (Case 1A) and 1 ms (Case 1B), respectively, and model parameters remain the same. The simulated pressure time histories of the same monitoring point are presented in Figure 4.40, and details obtained from those curves are listed in Table 4.18.

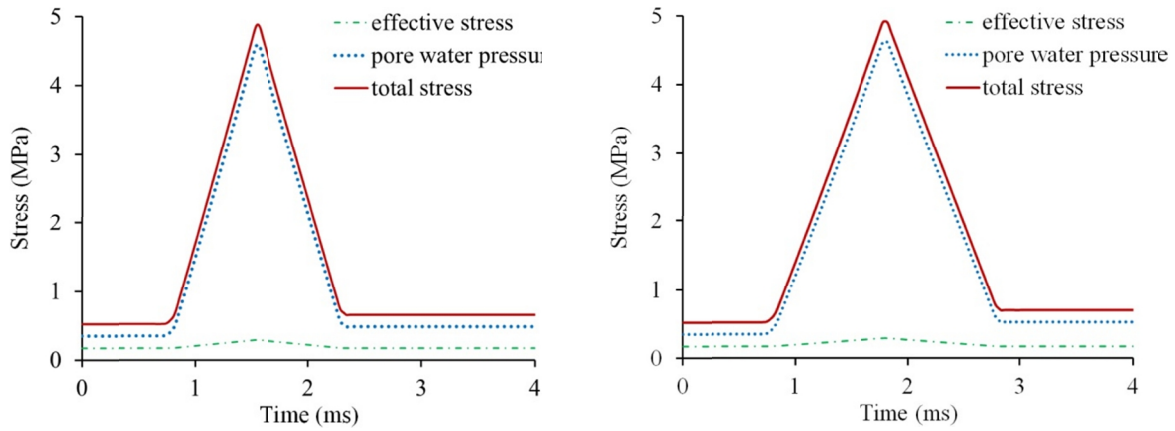

(a) (b)

Figure 4.40 Simulated pressure histories of the monitoring point N in (a) Case 1A; (b) Case 1B

As can be observed, with a more rapid loading, the peak and residual pore pressure both decreased. This is because a shorter duration to reach the same stress magnitude would provide less time for inelastic volumetric strain to develop, thus the irrecoverable deformation will be lower for a higher loading rate. In other words, a saturated soil is less prone to be liquefied by shock loadings with higher strain rates as is indicated by the PPR values shown in Table 4.18. Noticeably, this phenomenon observed from simulation results of the model is consistent to experimental studies by Yamamuro and Lade (1993) and Sheahan et al. (1996), where saturated soils were found to be less compressive and develop less pore pressure with increasing loading rates. In fact, the development of irrecoverable volumetric deformation in soils is related to pore crushing and particle rearrangement. At high loading rates, there is not sufficient time for these irreversible processes to take place, and thus the soil appears less compressible and the pore pressure would be decreased (Yamamuro and Lade, 1993). By utilizing viscoplasticity, the discussed effect of an increased strain rate on reducing irrecoverable soil compaction and pore pressure can be captured by the developed model reasonably well. In contrast, the effect of strain rate on pore pressure response presented by the soil model for blast-induced liquefaction in Wang et al. (2008) is not deterministic, or even opposite to these experimental observations.

4.4.4.4 Simulation of liquefaction in saturated sand in field explosion test

To demonstrate the validity of the proposed model for field conditions, an explosion test documented in Charlie et al. (2013) is adopted. The profile of the field test is shown in Figure 4.41. The saturated sand to be tested was placed in the bottom of the pit in a container, which is

4.27 m in diameter and 1.83 m in height, and the explosive charge was detonated 1.8 m above the sand surface in water. The model is considered to be symmetrical, and only vertical displacement is allowed along the symmetrical axis. 4-node quadrilateral elements with maximum size of 1 cm are used in generating the mesh. The field measurements verified that the reflective stress waves are small, and most of the waves could pass through the saturated sand and container, and then into the *in situ* clay. Therefore, a low-reflective boundary is used at the bottom and the sides of the saturated sand specimen.

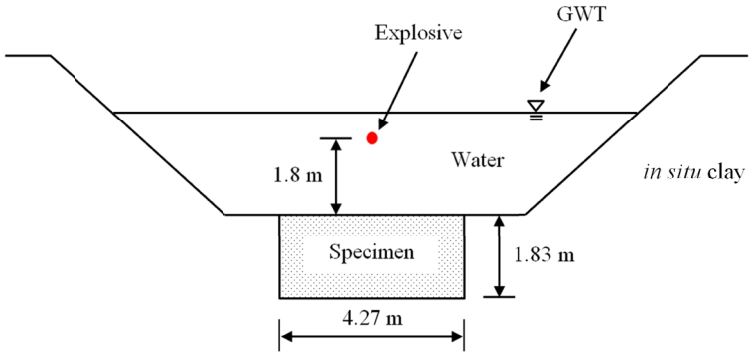

Figure 4.41 Cross section of the test site

The peak particle velocity (V_p, in m/s) of the sand caused by the spherical blast wave generated by the underwater explosion can be determined with the following equation developed for the test site (Charlie et al., 2013):

$$V_p = 12.3(R_c / Q^{1/3})^{-1.5} \tag{4.91}$$

where Q (m) and R_c (kg) are the weight of the explosive charge and the distance to the detonation, respectively. Then, the loading pattern (time history) of the incident shock wave, see Figure 4.42, is simulated with the following function modified from Jiang et al. (1995):

$$V(t) = V_0 t^{n_c} e^{-bt} \tag{4.92}$$

where $V_0 = V_p(be/n_c)^{n_c}$ with peak velocity V_p determined by Equation (4.91), and $V(t)$ would take this peak value at $t = n_c / b$ (Sainoki and Mitri, 2016); n_c and β are coefficients that define the shape of the impulse, and they are set as 1 and 6000, respectively, in this example based on monitored stress wave histories in the test. Finally, the shock impact obtained by combining Equations (4.91) and (4.92) is exerted on the surface of the saturated sand by considering different distances to the explosion, and only the perpendicular component of the wave to the

sand base is applied on the model boundary.

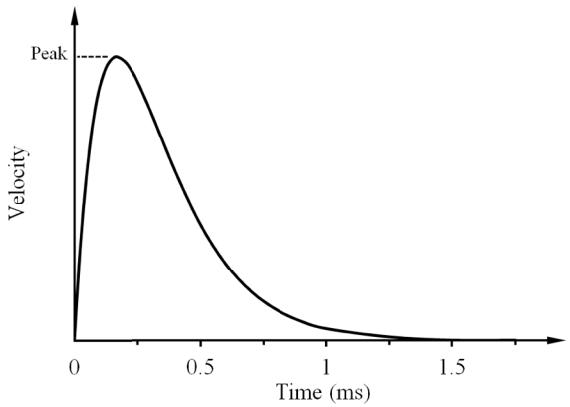

Figure 4.42 Load pattern of numerical simulation for the field explosion test

The material properties used in the simulation are based on those reported in Charlie et al. (2013) and the simulation work of Wang et al. (2008) for the same test, and are listed in Tables 4.19 and 4.20. The weight of the explosive charge in the example is 0.76 kg.

Table 4.19 Material properties used in the model for the field explosion test on sand

Density (kg/m^3)	h (μsec^{-1})	N	f_0 (Pa)	a	k (MPa)	R	D (MPa^{-1})	W	X_0 (MPa)
2138	1.8×10^{-6}	1	1×10^{6}	0.25	0	8	4×10^{-4}	0.002	1

Table 4.20 Material properties used for undrained response of saturated sand in field explosion test

n	r_{s0} (kg/m^3)	r_{w0} (kg/m^3)	C_{s0} (m/s)	C_{w0} (m/s)	s_s	s_w	g_{s0}	g_{w0}	$\underline{v}$	$\underline{K_p}$ (GPa)
0.31	1828	1000	287	1460	1.64	2	0.11	0.6	0.33	54

The time histories of the simulated pore water pressure are compared with the monitored data (Bretz, 1990) at points buried 0.22 m and 1.55 m beneath the sand surface on the vertical centre line in Figure 4.43. As can be observed, both the peak value of pore pressure and the arrival time of the shock wave obtained from simulation agree well with field data. Therefore, the proposed model is also able to reproduce the propagation of blast wave in the saturated sand.

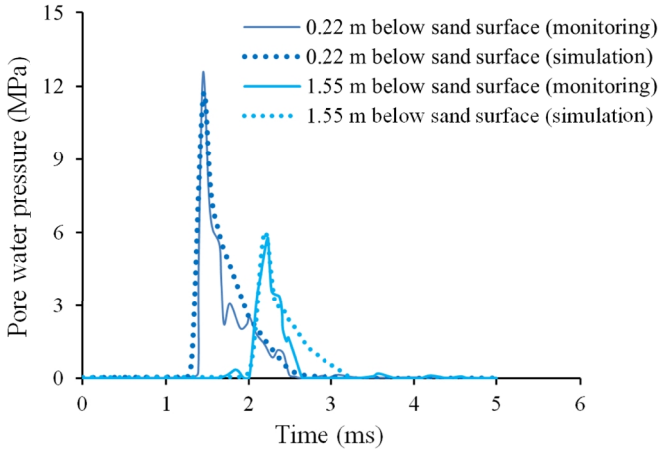

Figure 4.43 Comparison between simulated and monitored pore pressure in the field explosion test

Meanwhile, based on residual excess pore pressure measurements at 1.7 m below the center of sand surface, the PPR, defined in terms of initial vertical effective stress, at this location with 0.76 kg explosives in the field test is approximately 0.99 (Charlie et al., 2013). Thus, the depth of liquefaction in this test is approximately 1.7 m. The simulated PPR by the proposed model for the field explosion test is illustrated in Figure 4.44, and it has shown that the saturated sand was liquefied (PPR>=1) within 1.65 m in the vertical direction from the center of sand surface. Therefore, the developed model is also competent and can be used as a tool to determine the occurrence of liquefaction in saturated loose materials in the field.

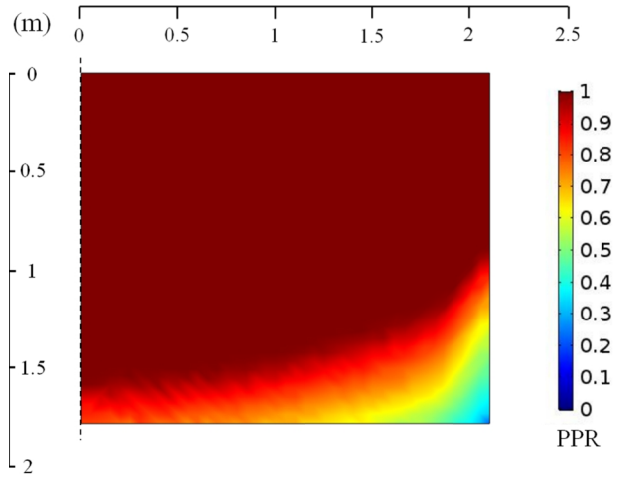

Figure 4.44 Simulated range of liquefaction after the explosion

4.4.4.5 Simulation of liquefaction in a tailings deposit by field explosion test

Typical man-made granular soils include tailings. As widely used waste management technologies in contemporary mining industry, they are disposed in underground mine cavities (stopes) in the form of cemented or uncemented HB and PB, or stored at the mine surface in tailings impoundments (Landriault, 2001). The tailings from hard rock mines stored in the impoundments mainly constitute of loose to medium dense silty sands and sandy silts. They generally contain sufficient water to be susceptible to dynamic (seismic, blast) liquefaction. On the other hand, the tailings of HB predominantly constitute of sand-size particles, while that of PB are mainly composed of silt-size particles. HB and PB are prepared with excess water in order to enable their transport from the backfill plant to the mine cavity. Their high water content also makes these tailings backfills susceptible to liquefaction caused by mine blast routines, particularly at early ages, when there is no or weak cementation. The liquefaction of tailings backfills by mine blasting is a major concern in backfill operation due to its severe consequences of casualties and production loss, while no reliable tool is available at present to address the issue.

It has been well acknowledged that the grain size distribution (GSD) has a significant impact on the liquefaction potential of saturated granular soils. Figure 4.45 is a comparison of the GSDs of natural sand and silt used in the above validation examples, and typical GSDs of tailings of HB and PB as well as those from tailings impoundments. From this figure, it can be observed that the silt used in the liquefaction testing in Bolton et al. (1994) has a roughly similar GSD as tailings in PB and tailings impoundment in the lower end of the GSD spectrum. Meanwhile, the GSDs of sand used in Fragaszy and Voss (1981, 1986), Bolton et al. (1994) and Charlie et al. (2013) represent approximately the upper portion of the GSD of HB in the spectrum. In other words, the GSDs of natural sand and silt can well represent and include those of typical tailings of HB and PB and in tailings impoundments. This would suggest that the proposed model can also be applied to the blast-induced liquefaction of geotechnical structures made of those man-made soils. To verify this assumption, the proposed model is validated against data from the field explosion tests conducted on a tailings deposit in the CANLEX program (Pathirage, 2000; Al-Qasimi et al. 2005). The GSD of tailings in the CANLEX program (Robertson et al. 2000; Al-Qasimi et al. 2005) is also shown in Figure 4.45, and it lies in the

middle of the GSD range of HB.

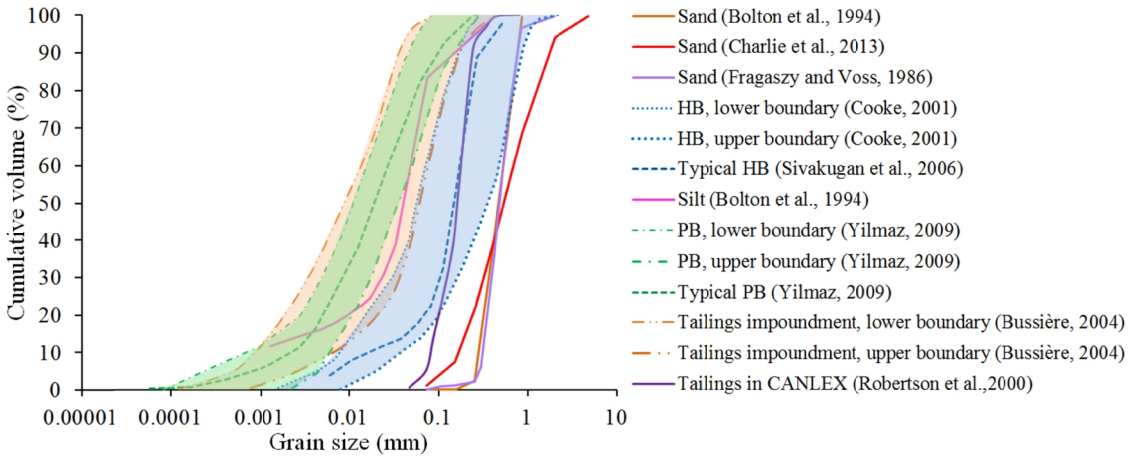

Figure 4.45 Comparison of GSDs of natural sand and silt with those of typical tailings of tailings backfills (PB, HB) and in impoundments

After a full-scale statically-induced liquefaction experiment in the CANLEX program, explosive charges were detonated in a flat deposit of mine tailings to determine blast-induced ground motion and pore pressure response (Al-Qasimi et al. 2005). Accelerometers and pore pressure transducers were installed at 10 to 50 m distance from detonations. The test site was hydraulically filled with poorly graded, sand size, loose mine tailings with a thickness of 10 m, and the groundwater was 0.5 m below the leveled ground surface.

The configuration of the model for the field test is shown in Figure 4.46, it is simulated by using 2D symmetry, and 4-node quadrilateral elements with maximum size of 2.5 cm are used. Low-reflecting boundaries are applied at the bottom and far end of the model, and a constant stress is applied on the top to represent the overburden from unsaturated tailings. Based on the setup of the field test and the spectrum of monitored data, the range of model simulation is determined as 5.5 m to 18 m from the explosion of 1.5 kg charge detonated at a buried depth of 6 m. This model size is determined to avoid extrapolation of measured field data, while the comparison of site response is possible and the effect of boundary condition is negligible.

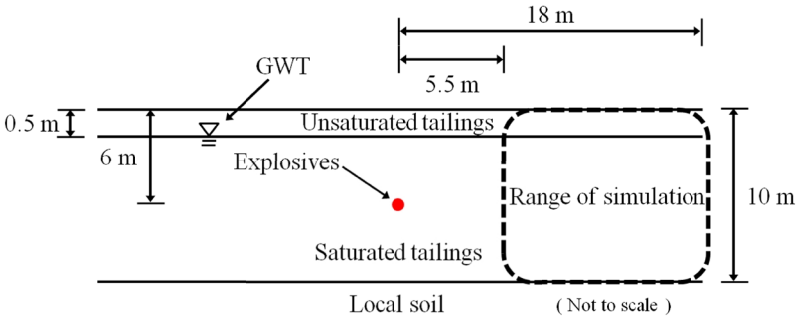

Figure 4.46 Configuration of the model for explosion in the tailings deposit

The peak particle velocity of incident blast wave that arrives at the model boundary is obtained in the simulation by the following equation developed for the test site (Al-Qasimi et al., 2005):

$$V_p = 47.64\,[R_c / Q^{1/3}]^{-2.34} \tag{4.93}$$

The time-varying pattern of the incident wave is assumed to be the same as Case Study 3 with peak velocity obtained by Equation (4.93). The positional relationship between locations along the model boundary and explosive charge is considered in the simulation, and only normal component of the wave to the boundary is applied on the model. The material properties employed in the simulation are obtained from studies on the tested tailings by Puebla et al. (1997), Robertson et al. (2000) and Al-Qasimi et al. (2005), and they are listed in Tables 4.21 and 4.22.

Table 4.21 Material properties used in the model for the field explosion test on tailings

Density (kg/m^3)	h (μsec^{-1})	N	f_0 (Pa)	a	k (MPa)	R	D (MPa^{-1})	W	X_0 (MPa)
1950	1.5×10^{-5}	1	1×10^{6}	0.18	0	8	1×10^{-2}	0.001	1

Table 4.22 Material properties used for undrained response of tailings in the field explosion test

n	r_{s0} (kg/m^3)	r_{w0} (kg/m^3)	C_{s0} (m/s)	C_{w0} (m/s)	s_s	s_w	g_{s0}	g_{w0}	$\underline{v}$	$\underline{K_p}$ (GPa)
0.43	1493	1000	219	1460	1.64	2	0.11	0.6	0.3	54

The simulated attenuation of peak particle velocity and peak pore water pressure against scaled distance is compared with test data in Figures 4.47-4.48. As can be observed, the magnitudes of simulated results lie in the middle of the spectrum of measured site response, and their simulated rates of attenuation also agree reasonably well with field data.

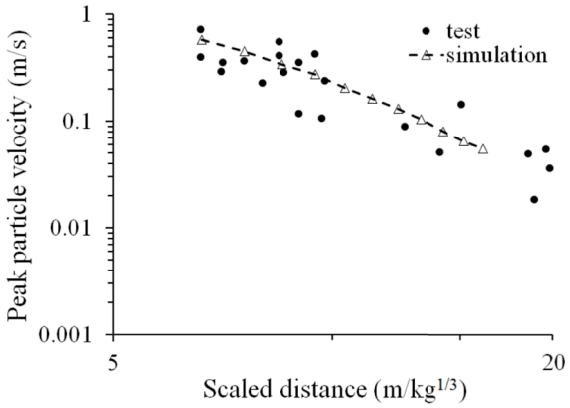

Figure 4.47 Comparison between simulated and measured attenuation of peak particle velocity against scaled distance

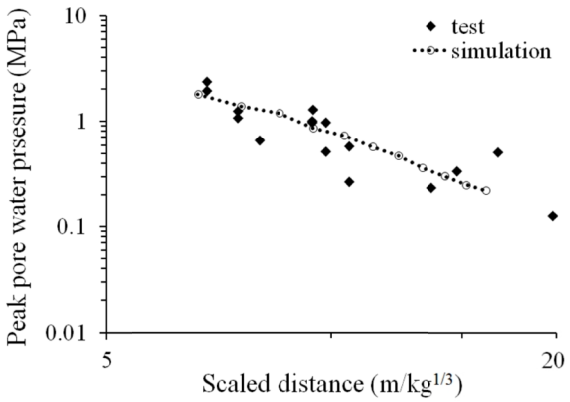

Figure 4.48 Comparison between simulated and measured attenuation of peak water pore pressure against scaled distance

Meanwhile, the field tests also showed that the tailings deposit was liquefied within 6.6 m from the detonation of 1.5 kg explosives at the buried depth of 6 m adopted in the study (Al-Qasimi et al., 2005). The simulation of liquefaction by the model after the blast is illustrated in Figure 4.49, and it indicates that the deposit is liquefied within 6.3 m from the explosion at the examined depth. The simulated attenuation of PPR, defined in terms of initial vertical effective stress (Al-Qasimi et al., 2005), against scaled distance at this depth is presented in Figure 4.50, and it is also consistent with the empirical law developed for the test site (Al-Qasimi et al., 2005).

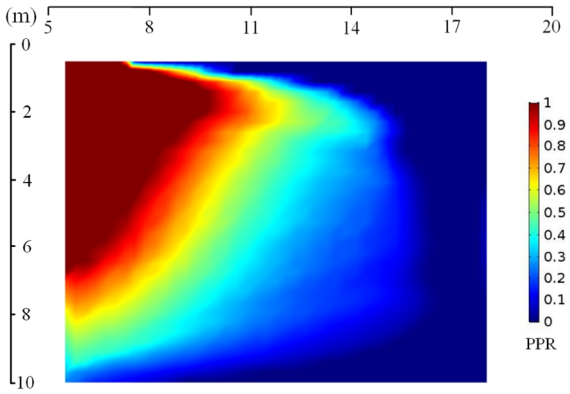

Figure 4.49 Simulated distribution of liquefaction zone in the tailings deposit

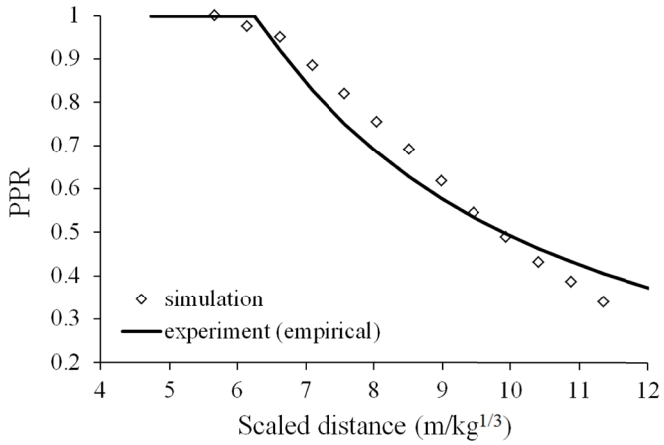

Figure 4.50 Comparison between simulated and measured attenuation of PPR against scaled distance

Therefore, the overall comparability between the measured and simulated results verifies the assumption that the proposed model can also be applied to capture the blast wave propagation and resulting liquefaction of geotechnical structures made of tailings, such as HB and PB at the early ages (with no or weak cementation) and in tailings impoundment in saturated conditions.

4.4.5 Conclusions

A new viscoplastic cap model with a variable bulk modulus is developed for simulating the blast-induced liquefaction in natural and man-made granular soils in the study. This model can account for the effect of high strain rate by taking into consideration the viscosity, capture the nonlinearity in volumetric deformation with an equation of state, and also characterize the

volumetric hysteresis that contributes to excess pore pressure with a cap model. To address the generation of excess pore pressure during blast loading, the stiffness matrix of the saturated mixture is modified by incorporating a pressure-dependent compressibility of pore fluid in the undrained condition.

The proposed model is validated against laboratory and field impact tests on saturated sand and silt. The simulated results compare well with the experimental data in terms of the peak pressure, arrival time as well as the residual excess pore pressure or range of liquefaction. Furthermore, the growth of irrecoverable compaction obtained from the volumetric strain histories can explain well the build-up of residual excess pore pressure, and the process is consistent with the mechanism of blast-induced liquefaction. Therefore, the developed model is reliable in capturing the blast wave propagation and resulting liquefaction of natural granular soils, and the applicability of viscoplastic cap models for simulating blast-induced liquefaction is verified in a rigorous scheme in the study.

Finally, given the similarity of GSDs of natural soils in the adopted liquefaction tests with those of tailings backfills, the proposed model is then extended to reproduce the liquefaction in typical tailings backfills caused by field explosion. Fairly good agreement is also found between simulation and experimental data. The validation results thus verify that the model can also be applied to capture the blast-induced liquefaction of man-made granular porous media, such as fresh HB and PB, and in saturated tailings impoundments as is a primary concern in underground mining.

4.4.6 References

Al-Qasimi EMA, Charlie WA, Woeller DJ. Canadian liquefaction experiment (CANLEX): Blast–induced ground motion and pore pressure experiments. Geotechnical Testing Journal 2005, 28(1): 1–13.

An J, Tuan CY, Cheeseman BA, Gazonas GA. Simulation of soil behaviour under blast loading. International Journal of Geomechanics, ASCE 2011; 11:323–334.

Aráoz G, Luccioni B. Modeling concrete like materials under sever dynamic pressures. International Journal of Impact Engineering 2015; 76:139–154.

Aref L. A study of the geotechnical characteristics and liquefaction potential of paste backfill. PhD Thesis, University of McGill, Montreal, Canada, 1998.

Ashford SA, Rollins KM, Lane JD. Blast-induced liquefaction for full-scale foundation testing. Journal of Geotechnical and Geoenvironmental Engineering, ASCE 2004; 8: 798–806.

Awad AA. A numerical model for blast–induced liquefaction using displacements–pore pressure formulations. Ph.D. Thesis. Colorado State University, Colorado, USA, 1990.

Bloom F. Constitutive models for wave propagation in soil. Applied Mechanics Reviews 2006; 59:146–175.
Bolton JM, Durnford DS, Charlie WA. One–dimensional shock and quasi–static liquefaction of silt and sand. Journal of Geotechnical Engineering, ASCE 1994; 120:1874–1888.
Bretz TE. Soil liquefaction resulting from blast–induced spherical stress waves. Final Rep. No. WL–TR–89–100, Weapons Laboratory, Air Force Systems Command, 1990.
Busch CL, Aimone-martin CT, Tarefder RA. Experimental evaluation and finite-element simulations of explosive airblast tests on clay soils. International Journal of Geomechanics, ASCE 2016; 16(4): 1–21.
Bussière B. Colloquium 2004: Hydrogeotechnical properties of hard rock tailings from metal mines and emerging geoenvironmental disposal approaches. Canadian Geotechnical Journal 2007; 44(9):1019–1052.
Casagrande A, Shannon WL. Strength of soils under dynamic loads. Proceedings of the American Society of Civil Engineers 1948; 74(4):591–608.
Charlie WA, Doehring DO. Ground water table mounding, pore pressure, and liquefaction induced by explosions: Energy-distance relations. Reviews of Geophysics 2007; 45: 1–9.
CharlieWA, Bretz TE, Schure LA, Doehring DO. Blast–induced pore pressure and liquefaction of saturated sand. Journal of Geotechnical and Geoenvironmental Engineering, ASCE 2013; 139(8):1308–1319.
Charlie W, Veyera GE, Durnford DS, Doehring DO. Porewater pressure increases in soil and rock from underground chemical and nuclear explosions. Engieering Geology 1996; 43(4):225–236.
Charlie, WA, Doehring, DO, Veyera GE. Blast induced liquefaction of soils: laboratory and field tests. Washington, DC: USAF Office of Scientific Research, Bolling AFB, 1988.
Charlie WA, Veyera GE, Doehring DO, Abt SR. Blast induced liquefaction potential and transient pore water pressure response of saturated sands. Technical report. Fort Collins: Colorado State University; 1985.
Chen WF, Baladi GY. Soil Plasticity: Theory and Implementation. Elsevier: Amsterdam, 1985.
COMSOL Multiphysics User's Guide, Version 3.5a, COMSOL AB, Stockholm, Sweden, 2009.
Cooke R. Design procedure for hydraulic backfill distribution systems. Journal of South African Institute of Mining and Metallurgy 2001; 101(2): 97–102.
DiMaggio FL, Sandler IS. Material models for granular soils. Journal of the Engineering Mechanics Division 1971; 97:935–950.
Dowding CH, Hryciw RD. A laboratory study of blast densification of saturated sand. Journal of Geotechnical Engineering 1986; 112(2):187-99.
Feldgun VR, Karinski YS, Yankelevsky DZ. A coupled approach to simulate the explosion response of a buried structure in a soil–rock layered medium. International Journal of Protective Structures 2013; 4(3):231–292.
Feldgun VR, Karinski YS, Yankelevsky DZ. Riemann solver for irreversibly compressible three–phase porous media. International Journal for Numerical and Analytical Methods in Geomechanics 2014; 38:406–440.
Ferdosi B, James M, Aubertin M. Numerical simulations of the seismic and post–seismic behaviour of tailings. Canadian Geotechnical Journal 2015; 52: 1–8.
Fragaszy RJ, Voss ME. Laboratory verification of blast–induced liquefaction mechanism. Final Report ADA109000, US Air Force Office of Scientific Research. Washington, DC. 1981.
Fragaszy RJ, Voss ME. Undrained compression behaviour of sand. Journal of Geotechnical

Engineering, ASCE 1986; 112(3): 334–347.
Ghassemi A, Pak A, Shahir H. Numerical study of the coupled hydro–mechanical effects in dynamic compaction of saturated granular soils. Computers and Geotechnics 2010; 37:10–24.
Griffiths DV, Li CO. Accurate pore pressure calculation in undrained analysis. Engineering Computation 1989; 6(4), 339–342.
Griffiths DV. The effect of pore fluid compressibility on failure loads in elasto–plastic soil. International Journal for Numerical and Analytical Methods in Geomechanics 1985; 9(3), 253–59.
Grujicic M, Pandurangan B, Cheeseman BA, Roy WN, Skaggs, RR, Gupta, R. Parameterization of the porous–material model for sand with various degrees of water saturation. Soil Dynamics and Earthquake Engineering 2008a; 28:20–35.
Grujicic M, Pandurangan B, Cheeseman BA. The effect of degree of saturation of sand on detonation phenomena associated with shallow–buried and ground–laid mines. Shock and Vibration 2006; 13:41–61.
Grujicic M, Pandurangan B, Coutris N, Cheeseman BA, Roy WN, Skaggs RR. Computer–simulations based development of a high strain–rate, large–deformation, high–pressure material model for STANAG 4569 sandy gravel. Soil Dynamics and Earthquake Engineering 2008b; 28:1045–1062.
Grujicic M, Pandurangan B, Coutris N, Cheeseman BA, Roy WN, Skaggs RR. Derivation and validation of a material model for clayey sand for use in landmine detonation computational analysis. Multidiscipline Modeling in Materials and Structures 2009; 5:311–344.
Grujicic M, Pandurangan B, Coutris N, Cheeseman BA, Roy WN, Skaggs RR. Derivation, parameterization and validation of a sandy–clay material model for use in landmine detonation computational analyses. Journal of Materials Engineering and Performance 2010; 19(3):434–450.
Gu Q, Lee FH. Ground response to dynamic compaction of dry sand. Géotechnique 2002; 52(7):481–493.
Henrych J. The dynamics of explosion and its use. Elsevier, New York, USA, 1979.
Higgins W, Chakraborty T, Basu D. A high strain–rate constitutive model for sand and its application in finite–element analysis of tunnels subjected to blast. International Journal for Numerical and Analytical Methods in Geomechanics 2013; 37(15):2590–2610.
Ishihara K. Liquefaction and flow failure during earthquakes. Geotechnique 1993; 43(3): 351 – 415.
Ivanov PL. Compaction of noncohesive soils by explosions. US Department of the Interior, Bureau of Reclamation and Natrual Science Foundation, Washington, DC, 1967.
Jiang J, Blair DP, Baird GR. Dynamic response of an elastic and viscoelastic full–space to a spherical source. International Journal for Numerical and Analytical Methods in Geomechanics 1995; 19:181–193.
Karinski YS, Feldgun VR, Yankelevsky DZ. Effect of soil locking on the cylindrical shock wave's peak pressure attenuation. Journal of Engineering Mechanics, ASCE 2009b; 135(10):1166–1180.
Karinski YS, Feldgun VR, Yankelevsky DZ. Explosion–induced dynamic soil–structure interaction analysis with the coupled Godunov–Variational Difference Approach. International Journal for Numerical Methods in Engineering 2009a; 77:824–851.
Katona MG. Evaluation of viscoplastic cap model. Journal of Geotechnical Engineering, ASCE

1984; 110(8):1106–1125.
Kezdi A. Handbook of soil mechanics. Elsevier, Amsterdam, 1974.
Kim KJ, Blouin SE. Response of saturated porous nonlinear materials to dynamic loadings, Final Report ADA148528, US Air Force Office of Scientific Research. Washington, DC. 1984.
Laine P, Sandvik A. Derivation of mechanical properties for sand. Proceedings of the 4-th Asia–Pacific Conference on Shock and Impact Loads on Structures, Singapore, 2001; 361–368.
Landriault D. Backfill in underground mining. In Underground Mining Methods Engineering Fundamentals and International Case Studies. SME, 2001; 601–614.
Le Roux K. In situ properties and liquefaction potential of cemented paste backfill. Ph.D. Thesis. University of Toronto, Toronto, Canada, 2004.
Lee WY. Numerical modeling of blast induced liquefaction. PhD thesis. Brigham Young University, Provo, USA, 2006.
Lu G, Fall M. A coupled chemo–viscoplastic cap model for simulating the behaviour of hydrating cemented tailings backfill under blast loading. International Journal for Numerical and Analytical Methods in Geomechanics 2016;40:1123–1149.
Lu G, Fall M. Modelling blast wave propagation in a subsurface geotechnical structure made of an evolutive porous material. Mechanics of Materials 2017;108: 21–39.
Merkle DH, Dass WC. Fundamental Properties of Soils for Complex Dynamic Loadings. Final Report ADA164206, US Air Force Office of Scientific Research. Washington, DC. 1985.
Motamedi MH, Foster CD. An improved implicit numerical integration of a non-associated, three-invariant cap plasticity model with mixed isotropic–kinematic hardening for geomaterials. International Journal for Numerical and Analytical Methods in Geomechanics 2015; 39, 1853–1883.
Murray YD, Lewis BA. Numerical simulation of damage in concrete. Report DNA–TR–94–190, Defense Nuclear Agency. Alexandria, 1995.
Murray YD. Users manual for LS–DYNA concrete material model 159. Report FHWA–HRT–05–062, Federal Highway Administration. McLean, 2007.
Nelson I, Baron ML, Sandler I. Mathematical models for geological materials for wave–propagation studies. Report DASA2672, Defense Nuclease Agency. Washington, DC. 1971.
Naylor DJ. Stresses in nearly incompressible materials by finite elements with application to the calculation of excess pore pressures. International Journal for Numerical Methods in Engineering 1974; 8(3), 443–460.
Pathirage KS. Critical assessment of the CANLEX blast experiment to facilitate a development of an in-situ liquefaction methodology using explosives. Master Thesis. University of British Columbia, Vancouver, Canada, 2000.
Perzyna P. Fundamental problems in viscoplasticity. Advances in Applied Mechanics 1966; 9:243–377.
Prapaharan S, Chameau JL, Holtz RD. Effect of strain rate on undrained strength derived from pressuremeter tests. Geotechnique 1989; 39(4):615–624.
Puebla H, Byrne PM, Phillips R. Analysis of CANLEX liquefaction embankments: prototype and centrifuge models. Canadian Geotechnical Journal 1997; 34: 641–657.
Robertson PK, Wride CE, List BR, Atukorala U, Biggar KW, Byrne PM, et al. The Canadian Liquefaction Experiment: an overview. Canadian Geotechnical Journal 2000;37:499–504.
Saebimoghaddam A. Liquefaction of early age cemented paste backfill. Ph.D Thesis. University of Toronto, Toronto, Canada, 2009.
Sainoki A, Mitri HS. Dynamic modelling of fault slip induced by stress waves due to stope

production blasts. Rock Mechanics and Rock Engineering 2016;49:165–181.
Sandler IS, DiMaggio FL, Baladi GY. Generalized cap model for geological materials. Journal of the Geotechnical Engineering Division 1976; 102:683–699.
Schwer LE, Murray YD. A three–invariant smooth cap model with mixed hardening. International Journal for Numerical and Analytical Methods in Geomechanics 1994; 18:657–688.
Schwer LE. Viscoplastic augmentation of the smooth cap model. Nuclear Engineering and Design 1994; 150:215–223.
Shahsavari M, Moghaddam R, Grabinsky M. Liquefaction screening assessment for as-placed cemented paste backfill. 67th Canadian Geotechnical Conference, Regina, SK, Canada, 2014.
Sheahan TC, Ladd CC, Germaine JT. Rate–dependent undrained shear behaviour of saturated clay. Journal of Geotechnical Engineering, ASCE 1996; 122(2):99–108.
Simo JC, Kennedy JG, Govindjee S. Non–smooth multisurface plasticity and viscoplasticity. Loading/unloading conditions and numerical algorithms. International Journal for Numerical Methods in Engineering 1988; 26:2161–2185.
Simo JC, Wu JW, Pister KS, Taylor RL. Assessment of cap model: Consistency return algorithms and rate–dependent extension. Journal of Engineering Mechanics, ASCE 1986; 114(2):191–218.
Sivakugan N, Rankine RM, Rankine KJ, Rankine KS. Geotechnical considerations in mine backfilling in Australia. Journal of Cleaner Production 2006; 14(12): 1168–1175.
Theory Reference for the Mechanical APDL and Mechanical Applications, ANSYS Release 12.0, ANSYS Inc., Canonsburg, Pennsylvania, 2009.
Tong X, Tuan CY. Viscoplastic cap model for soils under high strain rate loading. Journal of Geotechnical and Geoenvironmental Engineering, ASCE 2007; 133(2):206–214.
Tu Z, Lu Y. Evaluation of typical concrete material models used in hydrocodes for high dynamic response simulations. International Journal of Impact Engineering 2009; 36(1): 132–146.
van Gool BS. Effects of blasting on the stability of paste fill stopes at Cannington Mine. Ph.D. Thesis. James Cook University, Townville, Australia, 2007.
Veyera GE, Charlie WA, Hubert ME. One-dimensional shock-induced pore pressure response in saturated carbonate sand. Geotechnical Testing Journal 2002; 25(3): 277–288.
Veyera GE, Charlie WA. Laboratory study of compressional liquefaction. Journal of Geotechnical Engineering 1990; 116: 790–804.
Wang Z, Hao H, Lu Y. A three–phase soil model for simulating stress wave propagation due to blast loading. International Journal for Numerical and Analytical Methods in Geomechanics 2004a; 28:33–56.
Wang Z, Lu Y, Bai C. Numerical analysis of blast–induced liquefaction of soil. Computers and Geotechnics 2008; 5:196–209.
Wang Z, Lu Y, Bai C. Numerical simulation of explosion–induced soil liquefaction and its effect on surface structures. Finite Elements in Analysis and Design 2011; 47(9):1079–1090.
Wang Z, Lu Y, Hao H. Numerical investigation of effects of water saturation on blast wave propagation in soil mass. Journal of Engineering Mechcanics, ASCE 2004b; 130(5):551–561.
Wang Z, Lu Y. Numerical analysis on dynamic deformation mechanism of soils under blast loading. Soil Dynamics and Earthquake Engineering 2003; 23:705–714.
Whitman RV. The response of soils to dynamic loading. Final Report AD708625, US Army

Engineer Waterways Experiment Station. Vicksburg, 1970.
Xu TH, Zhang LM. Numerical implementation of a bounding surface plasticity model for sand under high strain–rate loadings in LS–DYNA. Computers and Geotechnics 2015; 66:203–218.
Yamamuro JA, Lade PV. Effects of strain rate on instability of granular soils. Geotechnical Testing Journal 1993; 16(3), 304–313.
Yankelevsky DZ, Feldgun VR, Karinski YS. Underground explosion of a cylindrical charge near a buried wall. International Journal of Impact Engineering 2008; 35(8):905–919.
Yilmaz E. Investigating the hydrogeotechnical and microstructural properties of cemented paste backfill using the CUAPS apparatus. PhD Thesis, Université du Québec in Abitibi–Temiscamingue, 2009.

Chapter 5.
Practical Engineering Application of the Developed Multiphysics Models

5.1 Introduction

As discussed in Chapter 2, the blast operations in underground mining could pose significant risk to the stability of a backfill system in the field, including the backfill structure itself as well as its retaining structure. Thus, a reliable assessment of the response of field cemented tailings backfill (CTB) mass under mine blasting is essential to ensure mine safety and profitability. Therefore, in this chapter, the developed fundamental multiphysics models for CTB in Chapter 4 will be utilized to numerically investigate critical geotechnical responses of field CTB masses subjected to blast load. Practical engineering issues that are relevant for both understanding and designing CTB structures in such dynamic condition will be examined, which include the blast wave propagation in hydrating fill mass (Section 5.2), as well as blast-induced liquefaction susceptibility (Section 5.3) and stress redistribution (Section 5.4) of early-age fill mass. The different blast responses of field backfills are studied and evaluated in terms of their varied backfilling condition (including varied cement content, initial backfill temperature, curing time, backfilling rate, and drainage condition), stope geometry (including varied stope size and distance between barricade and stope) as well as blast operation (including varied proximity of detonation and number of blasts). The results and findings of these studies would provide useful insight for balancing the influence of different design parameters on the stability as well economy of backfill systems, thus contribute to the optimal backfill design.

5.2 Technical Paper 5: Modelling blast wave propagation in a subsurface geotechnical structure made of an evolutive porous material

Published in *Mechanics of Materials* 108, 2017, 21-39.

Gongda Lu, Mamadou Fall

Abstract:

In this study, a coupled thermo-hydro-mechanical-chemical (THMC)-viscoplastic cap model is employed to investigate the characteristics of blast wave propagation in backfill mass that is undergoing cementation under different curing conditions. The THMC model for cemented backfill (CB) is adopted to evaluate its behaviour and the changes in the material properties during the curing process, with rigorous evaluation of the coupled THMC factors. The THMC model is then coupled with a modified viscoplastic cap model to capture the nonlinear and rate-dependent behaviours of CB under blast loading. All of the material properties of CB required for the modified viscoplastic cap model are obtained from the THMC model. To validate the model, experiments carried out in high columns and impact testing on hydrating cemented backfill, as well as blast wave propagation experiments on soil and cemented backfill are adopted and simulated. A good agreement is found between the experimental and simulated results. Finally, by applying the coupled THMC-viscoplastic cap model, the effects of curing time, cement content, stope (mine cavity) size, initial backfill temperature, and filling rate on blast wave propagation in backfill mass are investigated. The obtained results provide new insight into blast wave propagation in fill mass under field curing conditions.

KEY WORDS: Geotechnical materials; Paste backfill; Tailings; Blast; THMC; Constitutive model; Concrete

5.2.1 Introduction

Cemented (tailings) backfill (CB) is a granular man-made soil that undergoes cementation. CB consists of a mixture of dewatered mine tailings (fine aggregates), binder additives (e.g. Portland cement, fly ash, slag, etc.), and water. It is extensively used to fill underground mined out voids (stopes), since it can provide a safe subsurface environment for mine workers, enable the disposal of mine waste in a more eco-friendly way, and at the same time, enhance ore recovery (Grice, 1998; Klein and Simon, 2006; Ghirian and Fall, 2014; Doherty, 2015). Despite that most research works have focused on the quasi-static mechanical behaviour of CB (Kesimal et al., 2005; Klein and Simon, 2006; Yilmaz et al., 2009; Helinski et al. 2010; Abdul-Hussain and Fall, 2012; Ghirian and Fall, 2013; Walske 2014; etc.), an understanding of blast wave propagation in backfilled stopes is also important, because production blasting is now routinely used in modern mining operations.

CB starts to change once it is placed in the field, and the changes are not only due to the chemical (C) process of cement hydration, but also thermal (T), hydraulic (H), and mechanical (M) processes as well as their mutual interactions (Ghirian and Fall, 2013, 2014). When subjected to mine blasting after a period of curing, the CB will experience large deformation and high strain rates, which is beyond the scope of conventional soil mechanics or soil dynamics. Therefore, the complexity of coupled THMC processes affect the material properties, and also, the characterization of nonlinear transient problems of blast loading is difficult, which means that current studies on blast wave propagation in hydrating CB structures are extremely limited. For example, empirical scaling laws have been proposed for the attenuation of peak particle acceleration and velocity in field CB mass (Aref, 1988; Mohanty et al., 1995; Le Roux, 2004; van Gool, 2007). Since the material properties of CB are constantly changing, on the one hand, the regression results in previous studies are only applicable to the backfilled stopes tested, and thus it becomes problematic when they are extended to different cases. On the other hand, it is not rational to use those empirical equations with field blast tests for CB in all curing conditions. van Gool (2007) and Emad et al. (2014) simulated blast wave propagation in CB structures with numerical models. However, the time-dependent backfill properties have not been considered, and the Mohr–Coulomb yield criterion is adopted, but its inadequacy for high pressure loading conditions (such as blasting) has been well acknowledged (Bloom, 2006). Furthermore, they

have not incorporated the nonlinear volume-pressure relationship and the effects of a high strain rate.

Recently, a THMC model has been developed by Cui and Fall (2015) to capture the changes of CB properties with time under the coupled influence of the environment and intrinsic ingredients of the backfill. Meanwhile, a chemo-viscoplastic cap model is also developed by Lu and Fall (2016) to rationally describe the blast response of CB, which includes an equation of state (EOS) to account for the effects of high pressure, a realistic failure model to delineate the yield behaviour, as well as a strength model to incorporate the effects of a high strain rate. Those two models were then integrated, which resulted in a coupled THMC-viscoplastic cap model (Lu et al., 2016), and all of the material properties required to simulate the blast response of CB are inputted from the THMC model into viscoplastic cap model with rigorous consideration for the multiphysics interactions. Thus, the transient behaviour of hydrating CB under blast loading can be evaluated with any curing time of concern. Therefore, the coupled THMC-viscoplastic cap model will be adopted in this study to investigate the characteristics of blast wave propagation in cemented tailings backfill structures that are undergoing cementation.

The remainder of the paper is organized as follows: the consideration and formulation of the coupled THMC-viscoplastic cap model for simulating the blast response of hydrating CB is presented in Section 5.2.2. Then, typical examples of validation of the model against laboratory and field experiments are provided in Section 5.2.3. Subsequently, in Section 5.2.4, the model is employed to simulate blast wave propagation in subsurface CB structures in various curing conditions, and the results are discussed. Finally, concluding remarks are presented in Section 5.2.5.

5.2.2 Formulation of coupled THMC-viscoplastic cap model for cemented backfill

5.2.2.1 Modelling approach

The coupled THMC model developed by Cui and Fall (2015) that determines the changes in cemented tailings backfill is adopted in this study, which has been proven to properly account for the interactions among multiple physical processes. The modified viscoplastic cap model developed by Lu and Fall (2016) is also adopted in this study as the constitutive law to characterize the behaviour of CB under blast loading. This model has been proven effective for

geomaterials under high pressure, and is also capable of capturing the strain rate effect (Katona, 1984; Simo et al., 1986; Tong and Tuan, 2007; An et al., 2011; Aráoz and Luccioni, 2015; etc.).

By integrating the two models, all of the material properties required in the modified viscoplastic cap model of CB at the curing time of interest are obtained from the THMC model. The coupling strategy and updated parameters are conceptually illustrated in Figure 5.1 and elucidated in the subsections below. Details of the multiphysics factors and their interactions can be found in Cui and Fall (2015). Finally, the developed coupled THMC-viscoplastic cap model is implemented into a commercial software package, COMSOL Multiphysics (COMSOL AB, Stockholm, Sweden), for finite element simulation.

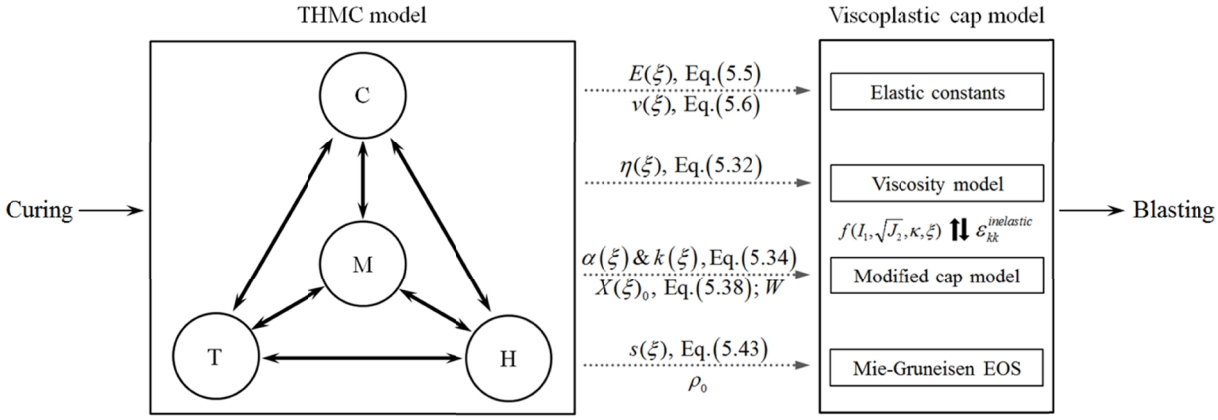

Figure 5.1 Interaction of multiphysics factors and updated parameters in coupled THMC-viscoplastic cap model

5.2.2.2 Formulation of coupled THMC model for cemented backfill

5.2.2.2.1 Binder hydration model

To quantify the progress of binder hydration in CB, Cui and Fall (2016) and Wu et al. (2012, 2013) used a binder hydration model (chemical model) developed by Schindler (2004) and Schindler and Folliard (2005) for cementitious materials. This model is also adopted in this study and written as:

$$x\left(t_e\right)=x_u\cdot\exp\left[-\left(\frac{t}{t_e}\right)^b\right] \tag{5.1}$$

with

$$\begin{cases} x_u = \dfrac{1.031 \cdot w/c}{0.194 + w/c} + 0.5 \cdot X_{FA} + 0.30 \cdot X_{slag} \\ t_e = \sum_0^t \exp\left[-\dfrac{E_a}{R_a}\left(\dfrac{1}{T_c} - \dfrac{1}{T_r} \right) \right] \cdot \Delta t \end{cases}$$

and

$$E_a(T) = \begin{cases} 33500 + 1470(20 - T_c) & T < 20^{\circ}C \\ 33500 & T \geq 20^{\circ}C \end{cases}$$

where x denotes the degree of binder hydration, and x_u the ultimate degree of hydration; t represents the hydration time parameter (hours), t_e denotes the equivalent age of CB at the reference temperature T_r, b is the hydration shape parameter, T_c is the temperature of the CB, w/c is the water/cement ratio, X_{FA} and X_{slag} refer to the fractions of the corresponding compounds with respect to the total binder content in mass, E_a is the activation energy (J/mol), and R_a is the natural gas constant (8.314 J/mol/K). The solid skeleton is assumed to be chemically inert, and in this study, the only chemical process that can occur is the hydration of the binder additives.

It should be noted that the heat exchange between CB and curing environment (surrounding rock) starts in the form of heat conduction once it is placed in the field, and this process will cause the variation of temperature distribution within CB. Consequently, due to the effect of temperature on rate of binder hydration (Equation 5.1), CB in the field will exhibit heterogeneous properties throughout the space (Nasir and Fall, 2010). Therefore, the effect of heterogeneity induced by the thermal interaction between CB and curing environment should be considered to realistically characterize the blast response of and wave propagation in subsurface CB structures.

5.2.2.2.2 Model of mechanical equilibrium

For the representative elementary volume (REV) of a three-phase system, the momentum conservation of CB can be written as:

$$\nabla \cdot \left(\frac{\partial \boldsymbol{\sigma}}{\partial t} \right) + \frac{\partial \left[(1-f) r_s + f S r_w + f (1-S) r_a \right]}{\partial t} \mathbf{g} = 0 \tag{5.2}$$

where f is the porosity, r_i denotes the density, subscript i refers to an individual phase (air, water or solid) , S is the degree of saturation of water, and $\boldsymbol{\sigma}$ is the total stress tensor which is expressed based on the effective stress principle as:

$$\boldsymbol{\sigma} = \boldsymbol{\sigma}' - aP\boldsymbol{\delta}_{\mathbf{ij}} \tag{5.3}$$

The Biot's coefficient a accounts for the compressibility of the solid particles, and is defined as:

$$a = 1 - K_b / K_s \tag{5.4}$$

where K_b and K_s are the bulk modulus of the porous skeleton and solid grains, respectively. Due to the binder hydration process, K_b will change with time, and can be estimated by using (Cui and Fall, 2016):

$$\frac{E(x)}{E_u} = \left(\frac{x - x_0}{x_u - x_0} \right)^A \tag{5.5}$$

$$n(x) = 0.5\exp(B_1 x) + B_2 x^{B_3} \exp(B_4 x^{B_5}) \tag{5.6}$$

with

$$K_b = \frac{E}{3(1-2v)} \tag{5.7}$$

where $E(x)$ is the Young's modulus at a given degree of hydration x ; E_u refers to the ultimate Young's modulus; x_0 denotes the reference degree of hydration below which no significant growth in elastic constants occurs; and A is a material constant. B_1, B_2, B_3, B_4 and B_5 are the fitting parameters to capture the variation in the Poisson's ratio v.

By separating the effects of pore gas and pore water pressure (P_a and P_w), the effective stress principle can be extended to unsaturated conditions, and the average pore pressure P can be expressed as (Chen et al., 2009):

$$P = SP_w + (1-S)P_a \tag{5.8}$$

The effective stress is then obtained as:

$$\boldsymbol{\sigma}' = \mathbf{D}^e \boldsymbol{\varepsilon}_\mathbf{e} = \mathbf{D}^e \left(\boldsymbol{\varepsilon} - \boldsymbol{\varepsilon}_\mathbf{p} - \boldsymbol{\varepsilon}_\mathbf{T} - \boldsymbol{\varepsilon}_\mathbf{c} \right) \tag{5.9}$$

where $\mathbf{D}^e$ is a fourth-order tangent elastic modulus tensor, and $\boldsymbol{\varepsilon}$ is the total strain tensor that consists of elastic, $\boldsymbol{\varepsilon}_e$, plastic, $\boldsymbol{\varepsilon}_p$, thermal, $\boldsymbol{\varepsilon}_T$, and chemical, $\boldsymbol{\varepsilon}_c$ components under the

principle of superposition. The components $\boldsymbol{\varepsilon}_p$, $\boldsymbol{\varepsilon}_T$, $\boldsymbol{\varepsilon}_c$ can be determined based on the plastic model, coefficient of thermal expansion a_T, and coefficient of chemical shrinkage b_{ch} for CB, respectively, which are elucidated in Cui and Fall (2015, 2016).

5.2.2.2.3 Fluid flow model

In this study, solid, water, and dry air in CB are treated as three independent overlapping continua within the context of the theory of mixtures. Water is the liquid phase, while dry air is the gaseous phase and also considered as the ideal gas. They migrate into the interconnected voids of solids and fill the space. Then, the mass conservation in a CB system can be characterized as (Cui and Fall, 2015):

$$fS\frac{\partial r_w}{\partial t}+fr_w\frac{\partial S}{\partial t}+Sr_w\left[\frac{\partial e_v}{\partial t}+\frac{(1-f)}{r_s}\frac{\partial r_s}{\partial t}\right]-fS\dot{m}_{hydr}\left(\frac{r_w}{r_s}S-1\right)=-\nabla\cdot\left(fSr_w\mathbf{v}^{rw}\right) \tag{5.10}$$

$$f(1-S)\frac{\partial r_a}{\partial t}-fr_a\frac{\partial S}{\partial t}+(1-S)r_a\left[\frac{(1-f)}{r_s}\frac{\partial r_s}{\partial t}+\frac{\partial e_v}{\partial t}-\frac{fS}{r_s}\dot{m}_{hydr}\right]=-\nabla\cdot f(1-S)r_a\mathbf{v}^{ra} \tag{5.11}$$

where e_v is the total volumetric strain, and $\mathbf{v}_s$ and $\mathbf{v}^{ri}$ are the phase velocity with respect to the Eulerian coordinate system, and the relative apparent velocity of fluids to a porous medium, respectively.

$\dot{m}_{hydr}$ denotes the rate of moisture consumption by the binder hydration process, and can be estimated by using (Cui and Fall, 2015):

$$\begin{aligned}\dot{m}_{hydr}=&\,2m_{hc-initial}\left(0.187x_{C_3S}+0.158x_{C_2S}+0.665x_{C_3A}+0.2130x_{C_4AF}\right)\\&\times\left\{\left(\frac{t}{t_e}\right)^b\left(\frac{b}{t_e}\right)x(t_e)\exp\left[\frac{E_a}{R_a}\left(\frac{1}{273+T_r}-\frac{1}{273+T}\right)\right]\right\}\end{aligned} \tag{5.12}$$

where $m_{hc-initial}$ is the mass of the cement used in the recipe, and x_i is the fraction of the corresponding compound with respect to the total cement content in mass.

The term $\mathbf{v}^{ri}$ can be characterized with Darcy's law, which is defined as:

$$\mathbf{v}^{ri}=-\mathbf{k}\frac{k_{ri}}{m_i}\nabla(P_i-r_ig) \tag{5.13}$$

where $\mathbf{k}$ is the intrinsic permeability tensor of the medium, the intrinsic permeability $k_0=Km_i/r_ig$, K refers to the saturated hydraulic conductivity, m_i denotes the fluid dynamic

viscosity, k_{ri} is the relative permeability of each fluid phase, and P_i is the pore fluid pressure. Based on Ghirian and Fall (2013), K can be written in terms of x as:

$$K = K_T \exp\left(C_1 x^{C_2}\right) \tag{5.14}$$

where K_T is the saturated hydraulic conductivity of the tailings used, with fitting constants C_1 =-8.173 and C_2 =4.035 (Ghirian and Fall, 2013).

The relative permeability k_{ri} can be evaluated by the well-known model of van Genuchten (1980):

$$\begin{cases} k_{rw}\left(S_{eff}\right) = \sqrt{S_{eff}}\left[1-\left(1-S_{eff}^{1/m}\right)^m\right]^2 \\ k_{ra}\left(S_{eff}\right) = \sqrt{1-S_{eff}}\left(1-S_{eff}^{1/m}\right)^{2m} \end{cases} \tag{5.15}$$

with

$$S_{eff} = \frac{1}{\left[1+\left(aP_c\right)^{\frac{1}{1-m}}\right]^m} \tag{5.16}$$

Abdul-Hussain and Fall (2011) investigated the time-dependent changes of the fitting parameters due to the hydration of CB when applying the van Genuchten (1980) model, and m and a are expressed as:

$$\begin{cases} m = f_1 x^{f_2} + f_3 \\ a = f_4 e^{f_5 x} \end{cases} \tag{5.17}$$

where the fitting constants, f_1 =0.0415, f_2 =4.231, f_3 =0.4073, f_4 =0.2103 kPa^{-1} and f_5 =-6.921 are calibrated from the measured data in Abdul-Hussain and Fall (2011) and Ghirian and Fall (2013). Then, the volumetric moisture content q can be calculated as:

$$q = q_r + S_{eff}\left(q_s - q_r\right) \tag{5.18}$$

where q_s and q_r are the saturated and residual moisture contents, respectively, and q_r is related to x with (Abdul-Hussain and Fall, 2011):

$$q_r = R_1 \cdot \exp(-R_2 \cdot x) \tag{5.19}$$

where R_1 and R_2 are dimensionless and equal to 1.314 and 7.538, respectively.

The temperature-dependence of the fluid density and dynamic viscosity can be defined by using the following expressions (Cui and Fall, 2015):

$$\begin{cases} m_w = 0.6612\left(T-229\right)^{-1.562} \\ r_w = 314.4+685.6\left\{1-\left[\left(T-273.15\right)/374.14\right]^{1/0.55}\right\}^{0.55} \\ m_a = m_0\cdot\left(T/T_0\right)^{1.5}\cdot\left[\left(T_0+c_0\right)/\left(T+c_0\right)\right] \\ r_a = \dfrac{M_a}{R_a T}P_a \end{cases} \tag{5.20}$$

where T is the absolute temperature, m_0 =1.716×10^{-5} Pa·s, T_0=273 K, c_0 = 111 K, and M_a is the molar mass of air.

5.2.2.2.4 Heat transfer model

Local thermal equilibrium is imposed on the three-phase system. Since the temperature in CB is relatively low, the phase change of water is not considered. Therefore, only two mechanisms of heat transfer in CB are considered, namely, heat conduction and convection. Under the isothermal assumption, the energy conservation for CB can be expressed as:

$$\left[\left(1-f\right)r_s C_s + fSr_w C_w + f\left(1-S\right)r_a C_a\right]\frac{\partial T}{\partial t} + Q_{cv} + Q_{cd} = Q_{hydr} \tag{5.21}$$

where C_i denotes the specific heat capacity of an individual phase, Q_{cv} and Q_{cd} the amount of convection and conduction heat transfer respectively, and Q_{hydr} is the heat released by exothermic binder hydration.

Heat convection due to the migration of water and dry air is expressed as:

$$Q_{cv} = \left(r_w C_w \mathbf{v}^{rw} + r_a C_a \mathbf{v}^{ra}\right)\cdot\nabla T \tag{5.22}$$

The heat conduction can be evaluated with Fourier's law by using:

$$Q_{cd} = -k_{eff}\nabla T \tag{5.23}$$

where the effective thermal conductivity k_{eff} of the CB is expressed as (Cui and Fall, 2015):

$$k_{eff} = k_{dry} + \sqrt{S_{eff}}\left(k_{sat} - k_{dry}\right) \tag{5.24}$$

and k_{dry} and k_{sat} denote the thermal conductivity of the CB in the saturated and dry states, respectively. k_{sat} can be evaluated by using (Ghirian and Fall, 2013):

$$k_{sat} = k_{tailings}^{1-f} k_w^f \tag{5.25}$$

where $k_{tailings}$ and k_w denote the thermal conductivity of the tailings and water, respectively. An analogous expression for k_{dry} can be expressed as (Cui and Fall, 2015):

$$k_{dry} = k_{tailings}^{1-f} k_a^f \tag{5.26}$$

where k_a is the thermal conductivity of air.

Heat production from exothermic binder hydration can be calculated with the model in Schindler and Folliard (2005), which is:

$$Q_{hydr} = H_T \left(\frac{t}{t_e} \right)^b \cdot \left(\frac{b}{t_e} \right) \cdot x\left(t_e\right) \cdot \exp\left[\frac{E_a}{R_a} \left(\frac{1}{273+T_r} - \frac{1}{273+T} \right) \right] \tag{5.27}$$

with

$$\begin{cases} H_T = \left(H_{cem} \cdot X_{cem} + 461 \cdot X_{slag} + 1800 \cdot x_{CaO/FA} \cdot X_{FA} \right) C_b \\ H_{cem} = 500 x_{C_3S} + 260 x_{C_2S} + 866 x_{C_3A} + 420 x_{C_4AF} + 624 x_{SO_3} + 1186 x_{FreeCaO} + 850 x_{MgO} \end{cases}$$

where H_T is the total heat of hydration that can be generated by the binder hydration, H_{cem} denotes the heat source from the hydration of cement, and C_b is the apparent binder density with respect to the total volume of the CB.

5.2.2.3 Formulation of viscoplastic cap model for cemented backfill under blast loading

5.2.2.3.1 Perzyna viscoplastic formulation

A Perzyna viscoplastic formulation is used to capture the rate-dependence of the material behaviour. In the Perzyna (1966) model, the total strain rate vector $\dot{\boldsymbol{\varepsilon}}$ comprises an elastic $\dot{\boldsymbol{\varepsilon}}^e$ and a viscoplastic (inelastic) component $\dot{\boldsymbol{\varepsilon}}^{vp}$:

$$\dot{\boldsymbol{\varepsilon}} = \dot{\boldsymbol{\varepsilon}}^e + \dot{\boldsymbol{\varepsilon}}^{vp} \tag{5.28}$$

The non-viscous elastic strain rate is defined as

$$\dot{\boldsymbol{\varepsilon}}^e = \mathbf{D}^{-1} \dot{\boldsymbol{\sigma}} \tag{5.29}$$

where $\dot{\boldsymbol{\sigma}}$ is the stress rate tensor, and the elements in the stiffness matrix $\mathbf{D}$ can be obtained by using Equations (5.5)-(5.7).

The viscoplastic strain rate is defined by:

$$\dot{\boldsymbol{\varepsilon}}^{vp} = h \left\langle f(f) \right\rangle \frac{\partial f}{\partial \boldsymbol{\sigma}} \tag{5.30}$$

where h is a fluidity parameter; $\langle\ \rangle$ is the Macaulay bracket defined as $\langle x \rangle = (x + |x|)/2$, f is the yield function and will be elucidated in the next subsection, and $f(f)$ is a dimensionless scaling function expressed as:

$$f(f) = \left(\frac{f}{f_0} \right)^N \tag{5.31}$$

where N is the exponent and f_0 is a constant with the same unit as f. The associated flow rule is conventionally used in the Perzyna model to capture the rate-dependent behaviour of materials under impact and blast loading, and the direction of $\dot{\varepsilon}^{vp}$ is in the outward normal direction of the yield surface f.

According to Lu and Fall (2016), N and f_0 can be assumed to be constant, while h will change as the binder hydration progresses and is expressed as:

$$h(x)(\mathrm{s}^{-1}) = 48.2 \cdot (f_c + 0.224)^{-3.51} + 0.002 \tag{5.32}$$

where f_c is the unconfined compressive strength (UCS) of CB related to the binder hydration and will be explained in the next subsection.

5.2.2.3.2 Modified viscoplastic cap model

A viscoplastic cap model is adopted in this study to capture the yield behaviour of CB. Compared to a conventional Drucker-Prager or Mohr-Coulomb criterion model, this model not only avoids the problem of incorrect prediction of strength under extremely high pressure, but is also free from unrealistic dilation. Besides, its calibration process is significantly easier than bounding surface plasticity since it contains far fewer model parameters (Lu and Fall, 2016).

Traditional cap models suffer from the numerical complexity caused by singularities, which are located at the intersection of the failure envelope with a positive slope and hardening cap with a horizontal slope. In order to address such singularities with relative simplicity, and also effectively control the volumetric dilation/compaction behaviour, a new transition approach has been proposed in Lu and Fall (2016), which expresses the failure envelope as:

$$F_1(I_1, \sqrt{J_2}, x) = \sqrt{J_2} - \frac{k(x) - [X(k,x) - L(k,x)]/R}{L(k,x)^2} I_1^2 + 2 \cdot \frac{k(x) - [X(k,x) - L(k,x)]/R}{L(k,x)} I_1 - k(x) \tag{5.33}$$

where k is the hardening parameter, $L(k,x)$ and $X(k,x)$ are the abscissa of the intersection of the cap with the failure envelope and the hydrostatic line, I_1 axis, respectively, R is the ratio of the major axis to the minor axis of the cap, and $k(x)$ is a Drucker-Prager parameter expressed as:

$$a(x)=\frac{2\sin j(x)}{\sqrt{3}\left[3+\sin j(x)\right]},\quad k(x)=\frac{6c(x)\cos j(x)}{\sqrt{3}\left[3+\sin j(x)\right]} \tag{5.34}$$

where $c(x)$ and $j(x)$ are the cohesion and internal friction angle related to the degree of binder hydration by (Cui and Fall, 2016):

$$c(x)=M_1x^{M_2},\quad j(x)=N_1x^{N_2}+N_3x \tag{5.35}$$

where M_1 and M_2, and N_1, N_2 and N_3 are constants obtained by least-squares approximation.

Then, the hardening cap can be expressed as:

$$F_2(I_1,\sqrt{J_2},k,x)=\sqrt{J_2}-\frac{1}{R}\left\{\left[X(k,x)-L(k,x)\right]^2-\left[I_1-L(k,x)\right]^2\right\}^{1/2} \tag{5.36}$$

The isotropic hardening of the cap is induced by the plastic volumetric strain, e_{kk}^p, and the hardening law can be defined by:

$$X(k,x)=-(1/D)\cdot\ln\left(1-\frac{e_{kk}^p}{W}\right)+X(x)_0 \tag{5.37}$$

where W denotes the maximum plastic volumetric strain of CB, and represents the volumetric air contents of CB, i.e. $W=f(1-S)$ (Chen and Baladi, 1985). Therefore, the maximum plastic volumetric strain will change with time with the progression of binder hydration, and can be obtained from the previous THMC model in Cui and Fall (2015). D is a constant shape parameter of the volume-pressure curve, and $X(x)_0$ is the vertex of the cap before CB is subjected to impact loading, which can be estimated by using (Lu and Fall, 2016):

$$X(x)_0(\text{MPa})=52.9\ln(0.03f_c+0.236)+75.5 \tag{5.38}$$

and the UCS of CB can be estimated with a Mohr-Coulomb criterion:

$$f_c=2c(x)\tan[45^{\circ}+\frac{j(x)}{2}] \tag{5.39}$$

Then, the intersection of the cap and failure envelope can be obtained by imposing continuity on the yield envelope:

$$k(x) = \frac{X(k,x) - R \cdot k(x)}{1 + R \cdot a(x)} \tag{5.40}$$

and

$$L(k,x) = \begin{cases} k(x) & k(x) > k(x)_0 \\ k(x)_0 & \text{otherwise} \end{cases} \tag{5.41}$$

Thus, all of the time-dependent parameters of CB in the yield envelope have been defined in terms of x . Finally, the modified cap envelope $f(I_1, \sqrt{J_2}, k, x)$ as a combination of $F_1(I_1, \sqrt{J_2}, x)$ and $F_2(I_1, \sqrt{J_2}, k, x)$ will replace the yield function f in Equations (5.30) and (5.31), and the accumulation of inelastic volumetric strain calculated by the viscous flow rule will determine the isotropic hardening of the cap envelope in the stress space.

A detailed discussion on the mechanisms of how the cap model can control dilation and capture the volumetric hysteresis in hydrostatic loading/unloading can be found in Lu and Fall (2016).

5.2.2.3.3 Nonlinear pressure-volume relationship (EOS)

Under intensive loading conditions (e.g. blasting), the volume-pressure response of a material is typically nonlinear (Henrych, 1979). Therefore, a variable bulk modulus model will be employed in this study to capture this nonlinearity of CB, and is derived from a Mie-Grüneisen equation of state (EOS) (An et al., 2011) defined as (Lu and Fall, 2016):

$$K(x) = \frac{r_0 C(x)_0^2 [1 + (1 - \frac{g_0}{2})m - \frac{a_0}{2} m^2][1 + \frac{2m[s(x) - 1]}{1 + m - s(x)m} + \frac{m(g_0 + a_0 m)}{(1+m)^2}] + r_0 C(x)_0^2 m(1 - \frac{g_0}{2} - a_0 m)}{[1 + m - s(x)m]^2} + \left[\frac{(g_0 + a_0 m)^2}{(1+m)^2} + a_0\right] E^v \tag{5.42}$$

where r_0 is the material density, which can be determined by tracking the loss of water via evaporation or drainage, and calculating the volume change of the CB in the curing process; $C(x)_0$ is the P-wave velocity of CB at an ambient pressure and temperature, and its value can be determined so that the $K(x)$ at μ=0 as obtained by Equation (5.42) equals to that provided by Equations (5.5)–(5.7); g_0 is the Grüneisen parameter, E^v is the internal energy per unit initial volume; a_0 is the first order volume correction to g_0 and often set to 0; $\mu = (V_0/V) - 1$ captures the volumetric deformation with V and V_0 as the current and initial volumes of an element; and $s(x)$

is the slope of the shock velocity vs. the particle velocity curve, which is related to the UCS by (Lu and Fall, 2016):

$$s(x)(1) = 2.06\exp(-4.38 f_c + 0.779) + 1.5 \quad (5.43)$$

Besides, to accommodate large deformations of CB under high pressure, an arbitrary Lagrangian-Eulerian (ALE) formulation is used in the proposed model for blast loading (COMSOL, 2009).

5.2.3 Model validation

5.2.3.1 Introduction

Four case studies are presented in this section to validate the coupled THMC-viscoplastic cap model. The first case study is the simulation of tests carried out on hydrating cemented paste backfill (CPB, a common type of CB) in high columns, in order to demonstrate the effectiveness of the THMC component of the coupled model to predict the properties of CPB that change with time. Then, to verify the modification of the parameters that depend on the THMC processes in the proposed viscoplastic cap model, a set of split Hopkinson pressure bar (SHPB) tests performed on hydrating CPB in laboratory are simulated. Subsequently, since not all backfills contain cement, e.g., uncemented mine tailings backfill, and CB that is still uncemented or weakly cemented at the early ages, and they are similar to soil that is made up of solid particles, water, and air without binder hydration, a laboratory explosion test on soil is simulated to demonstrate the applicability of the proposed model to blast wave propagation in uncemented backfills. Finally, the monitored peak particle velocity (PPV) data of a stope production blast in CPB are used to demonstrate the validity of the proposed model in capturing wave propagation in hydrating backfill under field conditions.

5.2.3.2 Simulation of experiments on hydrating CPB in high columns

The experiments carried out in high columns by Ghirian and Fall (2013, 2014) on CPB are adopted and numerically simulated in this section. To investigate the coupled THMC processes of CPB during curing, they performed a variety of laboratory tests on hydrating CPB in insulated-undrained high columns. The columns were filled with 3 layers of backfill which were allowed to cure for 24 h between each lift of 0.5 m in height (delayed placement), and

monitoring points were placed at the middle of each lift. More details of the experimental program can be found in Ghirian and Fall (2013, 2014).

The cylinder CPB columns were simulated by using axisymmetric elements with 1.5 cm in size, and the configuration of the model is illustrated in Figure 5.2. The delayed placement of the lifts in the backfill was simulated layer by layer. The initial values and boundary conditions for the numerical simulation are listed in Table 5.1.

Table 5.1 Input parameters, boundary conditions and initial values of simulated curing processes

	Case Study 1	Case Study 2		Case Study 4
Cement content	4.5%	7%	10%	5%
w/c ratio	7.6	5.55	3.88	5
Size of specimen	0.1 m in radius, 0.5 m in height for each of 3 layers	0.07 m in height, 0.011 m in radius		6 m in height, 8 m in radius
Insulation materials				
Category	Thermal insulating foam*	CPVC*		Rock**
Thermal conductivity (W/(m K))	0.024	0.1		3.6
Heat capacity (J/(kg K))	1400	1050		800
Density (kg/m^3)	30	1760		2000
Mechanical module				
Top surface	Free	Free		Free
Lateral sides	Roller	Roller		Roller
Bottom side	Fixed	Fixed		Fixed
Volume force	Gravity	Gravity		Gravity
Hydraulic module				
Top surface	Mass flux	No flux		No flux
Lateral sides	No flux	No flux		No flux
Bottom side	No flux	No flux		No flux
Volume force	Gravity	Gravity		Gravity
Initial value	Hydraulic head=0	Hydraulic head=0		Hydraulic head=0
Thermal module				
Top side (°C)	20.75	25		20
Lateral sides (°C)	20.75	25		20
Bottom side (°C)	20.75	25		20
Initial temperature (°C)	20.75	25		20

*: Properties adopted from Wypych (2012);
**: Properties adopted from Chen et al. (2009).

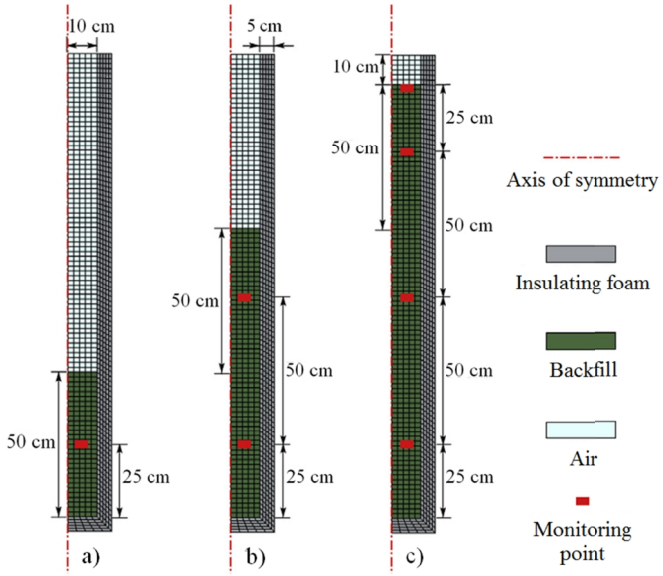

Figure 5.2 Configuration of model of high columns

a) 1st stage of backfilling; b) 2nd stage of backfilling; and c) 3rd stage of backfilling.

A comparison of the simulated temperature within the CPB column with the monitored data during the curing process is provided in Figure 5.3. As shown, there is a good agreement between the simulated and measured results, and the fluctuation of the monitored temperature is due to the change in room temperature during the course of the experiments.

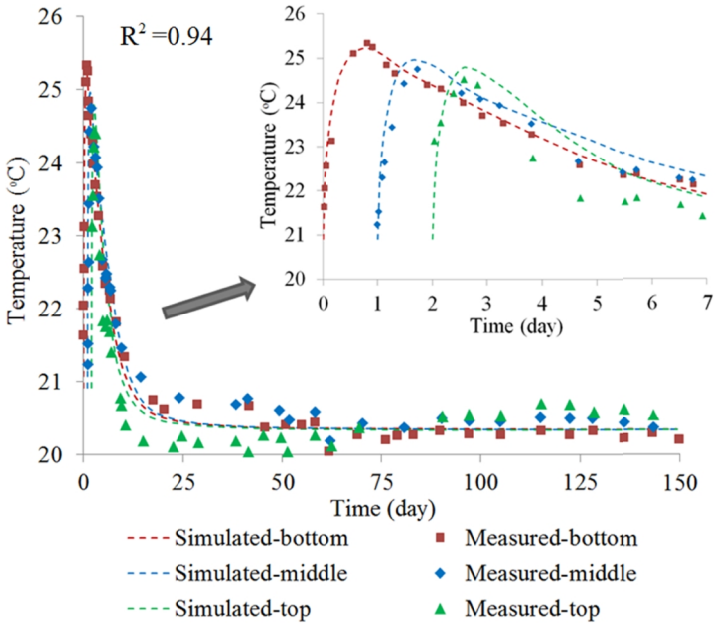

Figure 5.3 Comparison between simulated and measured temperatures at monitored points

The simulated and measured changes in the pore water pressure (PWP) in the CPB are presented in Figure 5.4. As can be observed, there is also good agreement between the simulated and experimental results, and some key phenomena have been adequately captured by the THMC model. Specifically, the negative PWP rapidly increases as cement hydration progresses and consumes the pore water. It can also be observed that the PWP of the bottom layer increases immediately after a backfill layer is poured into the upper part of the column. This phenomenon is due to the downward drainage from the fresh and saturated upper layer caused by gravity. Meanwhile, as the binder additives deplete, the PWP develops at a much slower rate, and asymptotically changes to fixed values.

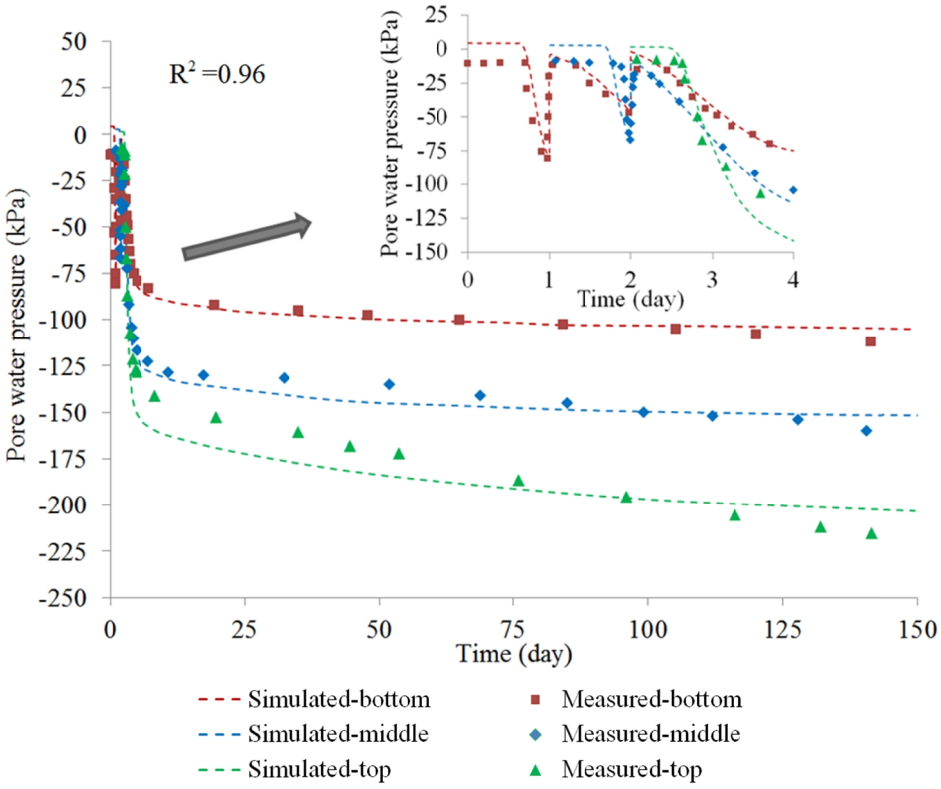

Figure 5.4 Comparison between simulated and measured PWP at monitored points

To validate the mechanical component of the THMC model, the simulated stress-strain curves of the quasi-static UCS tests on hydrating CB samples are compared with the plotted

experimental data and presented in Figure 5.5 below. The tested samples of 2.5 cm in radius and 10 cm in height were modelled with axisymmetric mesh elements with 2.5 mm in size.

As can be observed, there is good agreement between the simulated and experimental results, in that the chemical and strain softening–hardening behaviour of CB are well captured by the proposed model. More details on the mechanical performance of CB under quasi-static loading can be found in Cui and Fall (2016).

Thus, it can be concluded that the THMC model is valid and reliable in simulating the behaviours of CB in the course of binder hydration. More examples of changes in CB with testing carried out in high columns and other field case studies that validate the THMC model are available in Cui and Fall (2015).

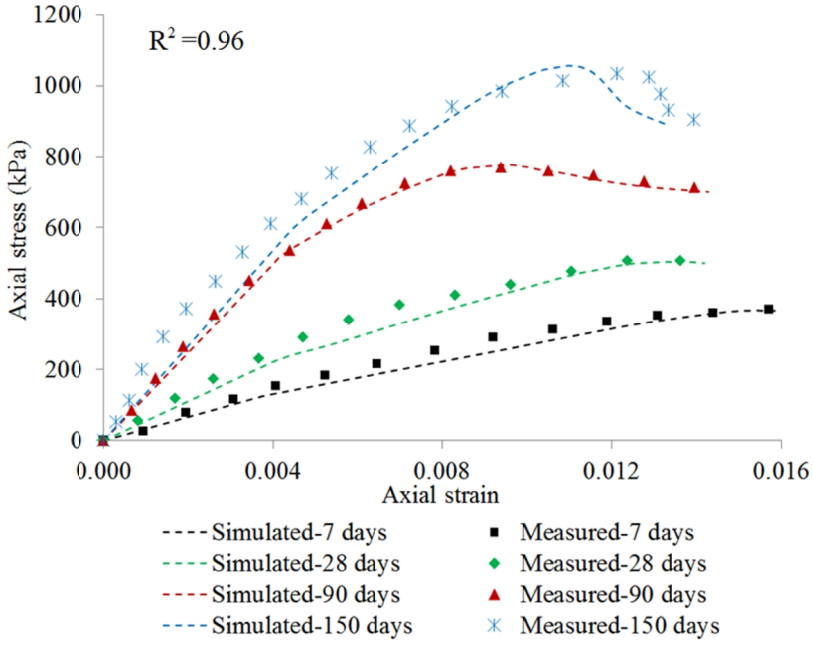

Figure 5.5 Simulated vs. measured stress-strain curves of hydrating CPB in quasi-static UCS tests

5.2.3.3 Simulation of SHPB tests on hydrating CPB

Huang (2009) examined the dynamic performance of CPB at different curing times with different cement contents by using a modified SHPB instrument, and the experimental results are adopted in this study to validate the proposed THMC-viscoplastic cap model.

The initial moisture content of the CPB was 28%, and fresh CPB was placed into PVC pipes with an internal radius of 11 mm, external radius of 12.5 mm and height of 70 mm. At specific curing times, the specimens were extracted from the CPVC pipes, and trimmed into cylinders that were 11 mm in radius and 10 mm in height. Then they were subjected to SHPB testing with a strain rate of 300 s^{-1}, 500 s^{-1}, and 750 $^{-1}$, respectively. More details of the testing can be found in Huang (2009).

Before simulating the response of the hydrating CPB under impact with the viscoplastic cap model, its material properties were determined with the THMC model beforehand. Some of the quasi-static data for the tested material with 5% cement can be found in Klein and Simon (2006), and the fitting constants in Equation (5.5) can be determined with E_u = 282.3 MPa, x_0 = 0.09, and A = 36.3 (Lu and Fall, 2016); B_1 = -0.2, B_2 = -15000, B_3 = 7, B_4 = -10.98 and B_5 = 0.7 from Equation (5.6) (Cui and Fall, 2016); $j(x)$ is assumed to be a constant and equal to 38^o, and the fitting constants in Equation (5.35) are M_1 = 0.234 MPa and M_2 = 30.3 (Lu and Fall, 2016). Other input parameters, boundary conditions and initial values used for the numerical simulation of the curing process are listed in Table 5.1.

Then, for the simulation of the SHPB tests, the time-dependent properties of CPB at the center of the specimen obtained by the THMC model were used in the viscoplastic cap model, i.e. heterogeneity due to spatially varying properties is ignored in this case, since the sample is sufficiently small. To simplify the modeling process, a typical loading history pattern in the SHPB tests on CPB (Huang, 2009; Huang et al., 2011) was used, which was also used in Lu and Fall (2016). Only a quarter of the specimens were modeled with axisymmetric elements of 0.5 mm in size. Axial velocity increments were applied at the top of the specimen while the bottom was fixed, and the sample was not laterally confined based on the experiment configuration.

Since the UCS and elastic modulus data are only available for CPB with 5% cement, empirical approaches were employed to estimate the two parameters of CPB with a cement content other than 5%. The UCS was determined by increasing that of CPB with 5% cement by the ratio of the increment in the cement content, since the strength of cementitious materials is generally proportional to the cement content (e.g., Yilmaz et al. 2004; Fall et al., 2008; Chian et al., 2011; Cihangir et al. 2012). Then, the changes in the average Young's modulus can be captured with (Fall et al., 2005):

$$E = h(f_c)^i \tag{5.44}$$

where f_c is in kPa and E is in MPa in the equation, and the fitting coefficients h = 0.0324 and i = 1.32 for the CPB considered here (Lu and Fall, 2016).

Finally, the simulated stress-strain curves of the CPB samples with 7% and 10% cement at various curing times under different loading rates are presented and compared with the available data in Figure 5.6, and the material properties obtained from the THMC model and used in the viscoplastic cap model are listed in Table 5.2. More examples on the simulation of this SHPB test can be found in Lu et al. (2016).

Table 5.2 Material properties of CPB samples used to obtain stress-strain curves

Cement content	Curing time	Strain rate (s^{-1})	r_0 (kg/m^3)	h (μsec^{-1})	N	f_0 (Pa)	K (MPa)	G(MPa)
7%	30d	500	1849.9	8×10^{-4}	2.5	2×10^{5}	54.8	49.4
7%	30 d	750	1849.9	7×10^{-4}	2.5	2×10^{5}	65.2	58.5
10%	15 d	300	1847.9	7×10^{-6}	2.5	2×10^{5}	114.7	104.1
10%	15 d	750	1847.9	9×10^{-6}	2.5	2×10^{5}	111.2	100.9
a	k(MPa)	R	D (MPa^{-1})	W	X_0(MPa)	C_0(m/s)	g_0	s
0.1966	0.0891	8	8×10^{-2}	0.125	0.7	173	1	2.04
0.1966	0.1019	8	8×10^{-2}	0.125	0.9	188	1	1.90
0.1966	0.1567	8	8×10^{-2}	0.142	5.0	250	1	1.60
0.1966	0.1529	8	8×10^{-2}	0.142	5.0	246	1	1.62

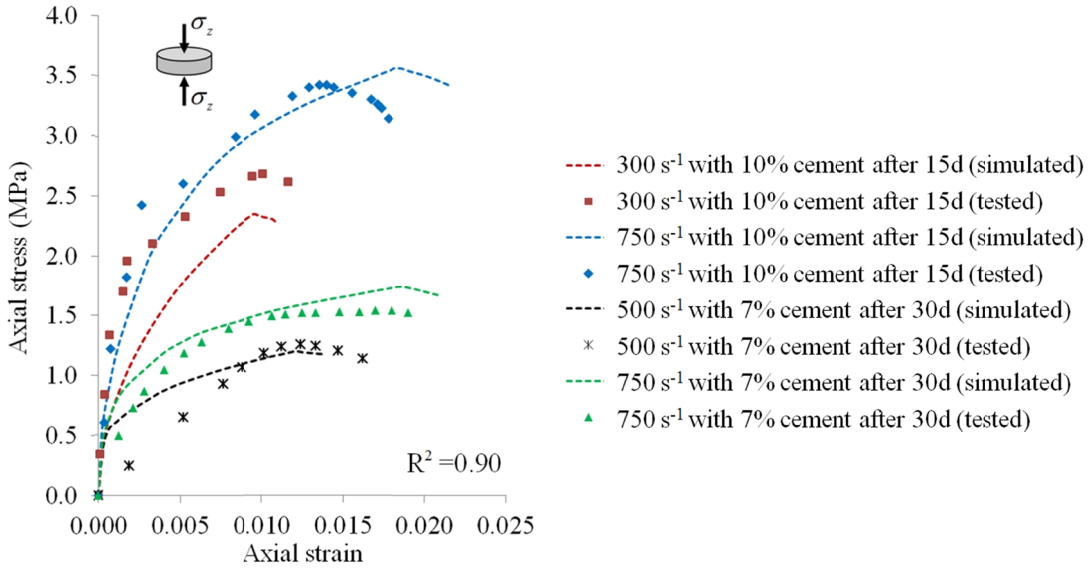

Figure 5.6 Simulated vs. measured stress-strain curves of individual CPB samples in SHPB tests

The good agreement between the simulated and experimental results shown in Figure 5.6 (coefficient of determination, R^2=0.9) indicates that the proposed model can capture well the rate-dependent behaviour of CPB under impact loading.

Therefore, as can be concluded from the previous case studies, the coupled THMC-viscoplastic cap model is competent enough to capture the transient mechanical response of hydrating CPB under blast loading.

5.2.3.4 Simulation of wave propagation in uncemented backfill

To demonstrate the capability of the model to simulate blast wave propagation in uncemented backfills (similar to the case of CB at the early ages, when there is still no cementation or the cementation is weak), explosive testing on soil documented in Bergeron et al. (1998) was adopted and numerically simulated. Their work was also applied in Tong and Tuan (2007) to validate their viscoplastic cap model.

In the explosive test, a cylindrical tank, made of a steel pipe with a thickness of 1.27 cm, internal diameter of 89.9 cm and height of 68.9 cm, was filled with sandy soil. Two C4 explosive charges, with a diameter of 6.4 cm, thickness of 2 cm, and weight of 100 grams, were placed in the center of the tank with a depth of burial (DOB) of 0 and 3 cm, respectively, while DOB= 0 cm is only used for the simulation in this study. Three carbon resistor gages were installed at different depths in the soil to measure the shock wave speed and pressure.

The problem was simulated with 2D axisymmetry. The confinement by the steel tank was simulated as a fixed boundary constraint, and the mesh size was 1 cm. As COMSOL Multiphysics has no built-in equation of state for explosives, a simplified pressure-time history of the explosives was used. It was assumed that the pressure-time history of the detonation, based on the results of Bergeron et al. (1998), is a triangular pulse and reaches its peak at 0.05 ms and drops back to zero at 0.4 ms. The peak value of the pulse was obtained from the simulated pressure-distance relationship in Tong and Tuan (2007), and the simplified pulse with a peak of 32.6 MPa that corresponds to 7 cm from the charge was applied to the proposed model as the pressure boundary condition. The material properties used are based on the work of Tong and Tuan (2007) and shown in Table 5.3. The simulated attenuation of the peak pressure and pressure-time history of the monitored point at 11.2 cm below the charge is compared with the experimental data in Figures 5.7 and 5.8.

Table 5.3 Material properties used in viscoplastic cap model for blast experiments on soil

W_e (kg)	r (kg/m^3)	h (μsec^{-1})	N	f_0 (Pa)	K (MPa)	G (MPa)	a
0.1	1636	2×10^{-4}	1	1×10^{5}	1065	63.85	0.1846
k (MPa)	R	D (MPa^{-1})	W	X_0 (MPa)	C_0 (m/s)	g_0	s
0.058	5	9.52×10^{-3}	0.2142	0.01	807	0.11	1

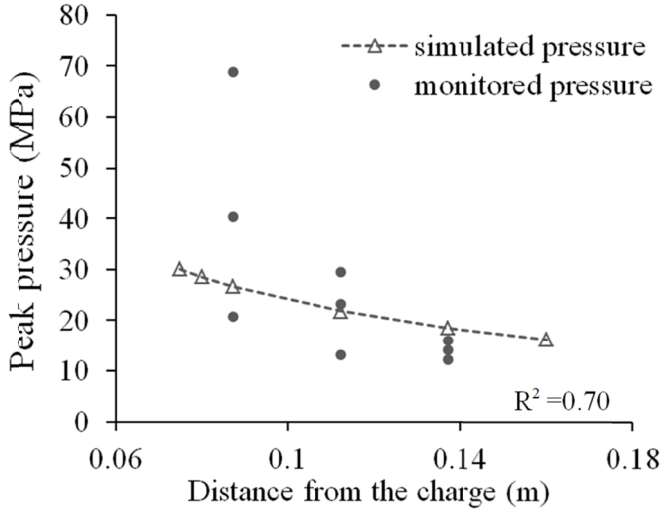

Figure 5.7 Comparison between simulated and experimental peak pressure data

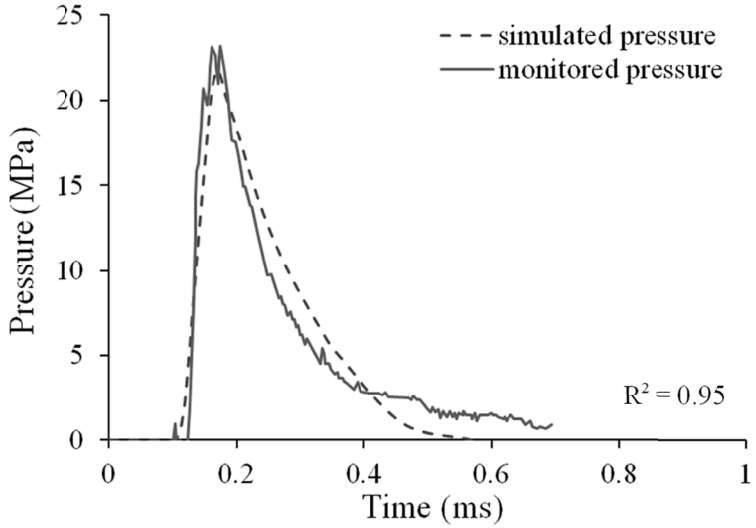

Figure 5.8 Comparison between simulated and monitored pressure-time histories of monitored point at 11.2 cm below charge

As can be observed, there is good agreement between the simulated results and the test data. Specifically, the attenuation of blast wave has been reasonably captured by the model as is shown in Figure 5.7, compared with simulation of the same test by Tong and Tuan (2007). Besides, Figure 5.8 indicates that the model is also able to represent the propagation of shock wave in the soil, and both the peak value as well as the arrival time of the wave obtained from simulation are consistent with test data.

Therefore, the proposed model is capable of evaluating the propagation and attenuation of blast waves in uncemented materials like soil and tailings.

5.2.3.5 Simulation of wave propagation in field cemented backfill mass

The monitoring of production blasts was carried out for a stope in Cannington Mine, Australia, which had been mined and backfilled with CPB. Based on the material properties provided in van Gool (2007), the backfill contained 76% solid and 4% cement, and had a quasi-static UCS of 0.69 MPa before the blast loading. The cement content (the mass of cement over the mass of total solids) was calculated to be 5% and *w/c* was 5. This field test can be simplified and modeled as the detonation of a single borehole in the middle of a CPB structure with a height of 6 m, and the configuration of the model based on the setup in van Gool (2007) is shown in Figure 5.9.

The properties of CPB were determined in the same way as outlined in Section 5.2.3.3 for the SHPB testing in Huang et al. (2011). The boundary conditions and initial values used for the simulation of the curing process with the THMC model are listed in Table 5.1. Since information on the curing time of CPB in the production blasts is not available, the UCS of the CPB was used as an indicator for the curing time. After the considered curing time, the backfill would then be subjected to blast loading and modelled with the viscoplastic cap model. However, as the structure is large in scale, the heterogeneity induced by spatially varying properties due to the heat generated by the cement hydration in the fill mass, and the thermal exchange between backfill and environment cannot be neglected. Therefore, a stored solution of the curing process was set as the initial condition for the next stage of blasting, and the CPB properties that are dependent on hydration were no longer constant in the structure. Surrounding rocks were not included in the blasting phase.

Based on a regression analysis of the PPV in the CPB during blasting (van Gool, 2007), a velocity pulse with a peak of 0.8 m/s that corresponds to a location 0.5 m away from the charge was applied as the model boundary. The profile of the pulse is the same form as that used in the simulation work by van Gool (2007) and Emad et al. (2014), and shown in Figure 5.10. The mesh elements have a maximum size of 5 cm, and a low-reflecting boundary was applied at the far end of the model to avoid the effects of wave reflection. The bottom of the CPB structure was set as a roller boundary condition and the top as a free boundary condition.

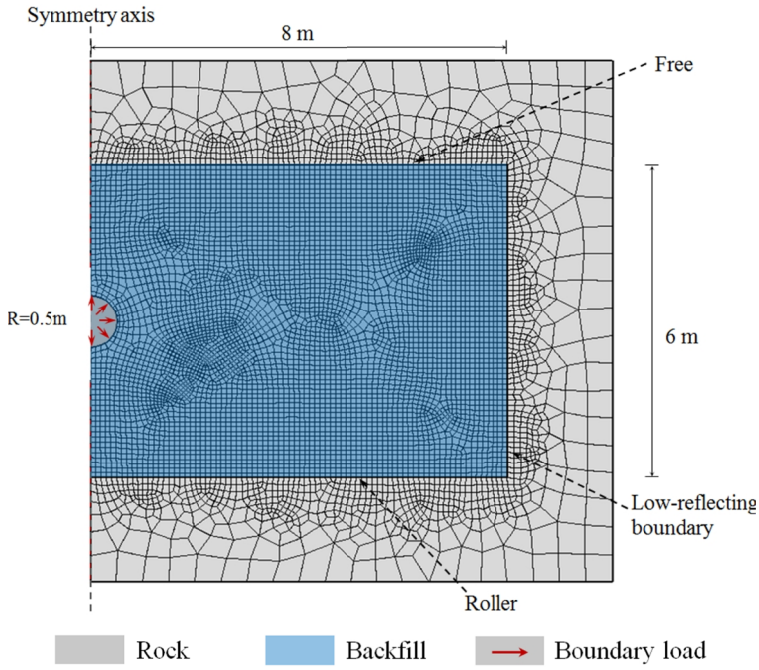

Figure 5.9 Configuration of numerical model for field blasting test

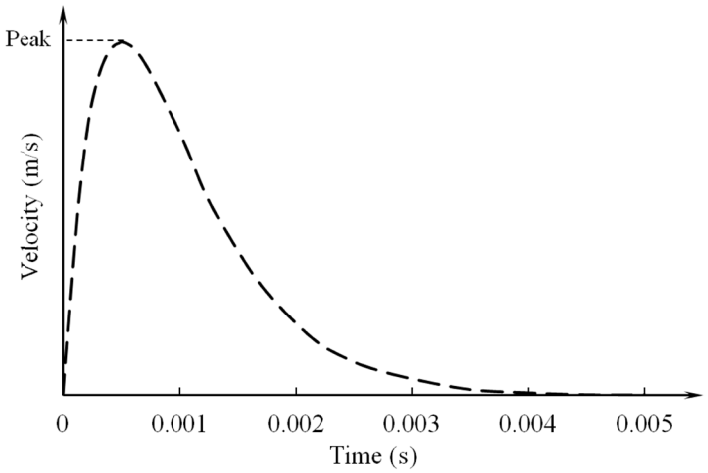

Figure 5.10 Blast pulse profile applied on the model

The simulated attenuation of the PPV in the center line of the backfill structure is compared with the monitored field data in Figure 5.11 below. As can be observed, the simulated attenuation of PPV exhibits a typical exponential pattern, and it attenuates drastically in the close range of the explosion, while the decreasing trend gradually levels off as the blast wave propagates farther away from the charge. It is shown in Figure 5.11 that both the values of simulated PPV and its trend of attenuation agree well with monitored data. Therefore, the proposed model is capable of capturing blast wave propagation in hydrating backfill structures in the field.

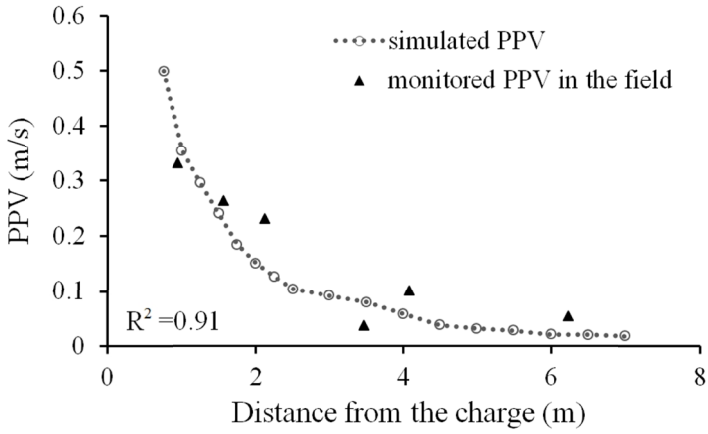

Figure 5.11 Comparison between simulated and monitored attenuation of PPV in cemented backfill in field under blast loading

5.2.4 Numerical investigation of blast wave propagation in cementing tailings backfill structures

5.2.4.1 Model configuration

After validation of the coupled THMC-viscoplastic cap model for hydrating cemented backfill, the model is employed to investigate the influence of curing conditions on the blast wave propagation in CB structures. The curing time, binder content, stope size, initial temperature and filling rate are adopted as the variant parameters in the numerical investigation, and the details of each simulation case are listed in Table 5.4, while the configuration of the model is presented in Figure 5.12.

Table 5.4 Conditions of CB structure in each simulation

Case No.	Binder content (*w/c* ratio)	Stope size (m)	Initial temperature (^{o}C)	Rate of backfilling (m/d)	Curing time subjected to blasting (d)
1	5% (7.8)	5×10	20	5	14
2	5% (7.8)	5×10	20	5	28
3	5% (7.8)	5×10	20	5	60
4	2% (19.4)	5×10	20	5	28
5	10% (3.9)	5×10	20	5	28
6	5% (7.8)	5×20	20	5	28
7	5% (7.8)	5×10	2	5	28
8	5% (7.8)	5×10	35	5	28
9	5% (7.8)	5×10	20	2.5	28
10	5% (7.8)	5×10	20	10	28

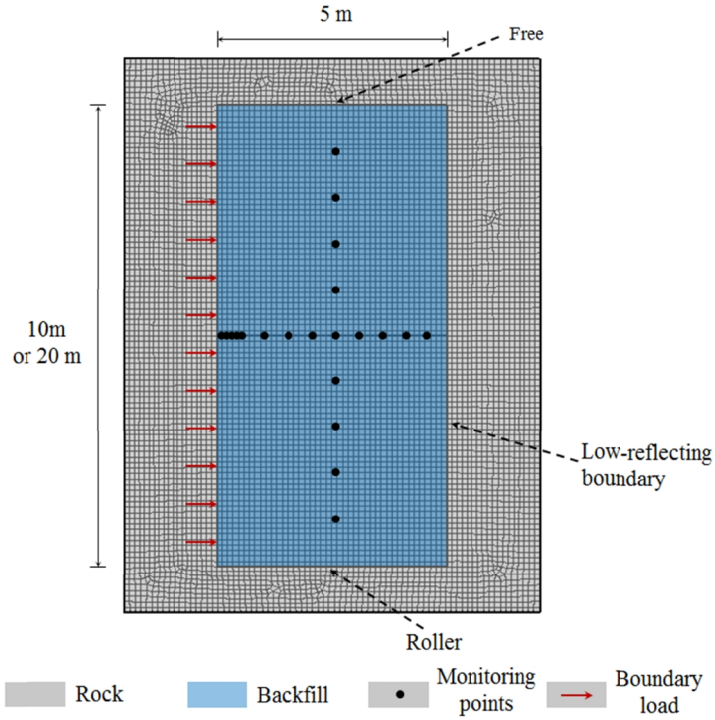

Figure 5.12 Configuration of numerical model

In the simulation of the curing processes, the same rock temperature of 20^{o}C was used for all of the cases, and the delay in the backfilling of each lift in the CB was simulated in a layer-by-layer manner, i.e., it was completed in two steps for Cases 1–5, 7 and 8, four steps for Cases 6 and 9, and one step for Case 10 (see Table 5.4). The properties of CB are determined in the same way as that described in Section 5.2.3.3. Other initial values and boundary conditions are the same as those of Table 5.1 in Section 5.2.3.5 (Case Study 4).

After the curing time of interest was reached, blast loading was applied in the model. Since the numerical model is relatively large in scale, the heterogeneity due to spatially varying properties of CB was taken into consideration. Therefore, a stored solution of each curing process was set as the initial condition for the next stage of blasting, and the material properties of CB that are dependent on cement hydration were not constant in the structure. Surrounding rocks were not included.

Boundary loading was also applied in the form of a velocity pulse at the boundary, and the peak of the pulse is 5 m/s, which corresponds to the standoff distance of 2 m of rock between the explosives and the backfill structure in van Gool (2007). Instead of using detonation in a single borehole, the pulse was applied on the left boundary of the backfill structure to represent the

detonation of explosive columns (see Figure 5.12), which are more common in production blasts (van Gool, 2007). Although delay intervals between detonations of explosives are commonly used to reduce ground vibration and enhance fragmentation, no delay sequence of detonation is used in this study for simplification purposes, and the pulse profile is the same as that provided in Figure 5.10. The mesh elements were 2.5 cm in size, and a low-reflecting boundary was applied at the far end of the model to avoid the effects of wave reflection. The bottom of the CPB structure was set as a roller boundary condition and the top was set as a free boundary condition.

To investigate the attenuation of PPV and peak pressure in the direction of wave propagation, monitoring points were placed at the mid-height of the structure (H=10 m for Case 6 and H=5 m for the others), and the interval is 0.1 m within 0.5 m of the boundary load and 0.5 m further out. Moreover, to understand the variation of PPV and peak pressure due to the heterogeneous properties of CB, monitoring points were also placed at the mid-width in the vertical direction with an interval of 2 m for Case 6 and 1 m for the others. Besides, to more easily interpret the simulated results, the PPV at the monitored points was normalized to the maximum PPV at the incident boundary, and accordingly, the peak pressure was normalized to the maximum peak pressure obtained at the incident boundary among all of the cases. The results of the numerical simulation for PPV and peak pressure in both directions are presented and discussed in the next section.

5.2.4.2 Discussion

5.2.4.2.1 Effect of curing time

The variations of the peak pressure and PPV in the CB structure with different curing times are presented in Figure 5.13. As shown in the figure, CB cured for a longer period of time shows a higher peak pressure and PPV than the early age CB at all monitored locations. This is primarily because CB has a higher degree of cement hydration as the curing time is increased, and thus more hydration products are generated (Yilmaz et al. 2015; Fall et al., 2010; Cihangir et al. 2012; Walske 2014). This reduces the pore space between the tailings particles and causes significant refinement of the microstructure of CB, which in turn, contributes to the improvement of the mechanical properties (e.g., increase in stiffness) (Klein and Simon, 2006; Yilmaz et al. 2009). This argument with respect to the improvement of the mechanical properties, particularly increase in stiffness as the curing time is increased, is supported by the results of the simulation

of the changes in the bulk modulus and its distribution in the CB structure as presented in Figure 5.14 for Cases 1 (CB structure after 14 days of curing) and 2 (CB structure after 28 days of curing).

As can be observed, the shorter curing time (or lower degree of hydration) means that the bulk modulus in Case 1 is significantly lower than that in Case 2. As well, the bulk modulus in the first layer of filling (0-5 m) is lower than that in the second layer (5-10 m) of CB structures after curing for 14 and 28 days. The distribution of the bulk modulus within the CB structure during blast loading for both cases is presented in Figure 5.15. At 5 ms after the blast impact, the pulse has propagated further in the CB structure with a longer curing time (Case 2) than in the CB structure with a shorter curing time (Case 1), since the former has higher stiffness, and thus a faster wave speed. Meanwhile, during the blast compaction, the stiffness of the material is increased due to the rearrangement of the solid particles and described with the variable bulk modulus derived from the Mie-Grüneisen EOS (Equation 5.42).

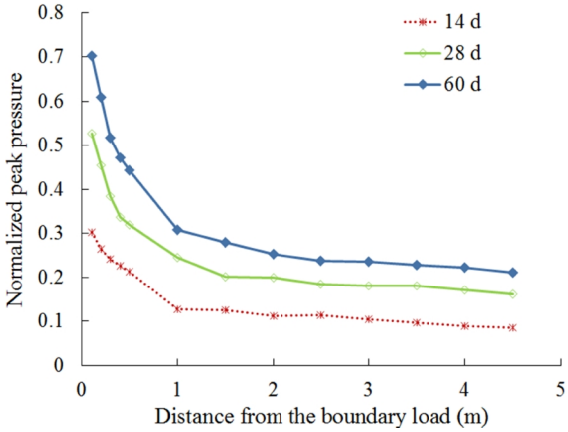

(a) Attenuation of peak pressure vs. distance in CB structure

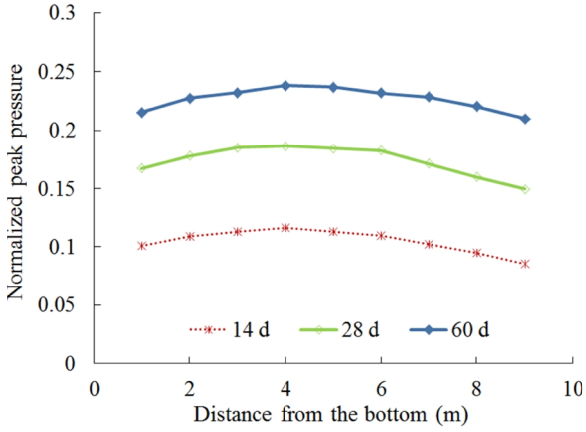

(b) Variation of peak pressure in vertical direction in CB structure

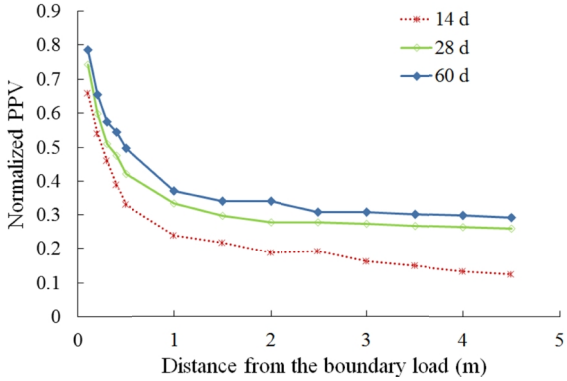

(c) Attenuation of PPV vs. distance in CB structure

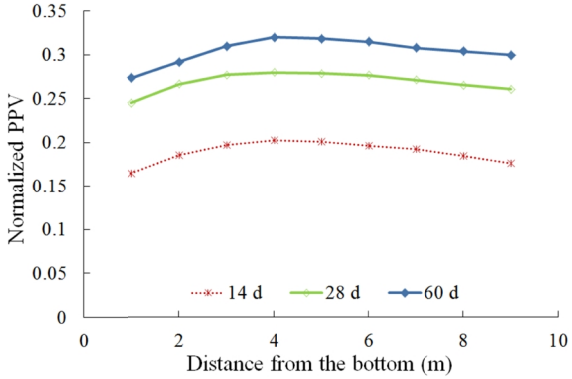

(d) Variation of PPV in vertical direction in CB structure

Figure 5.13 Variation of peak pressure and PPV in CB structure with different curing times

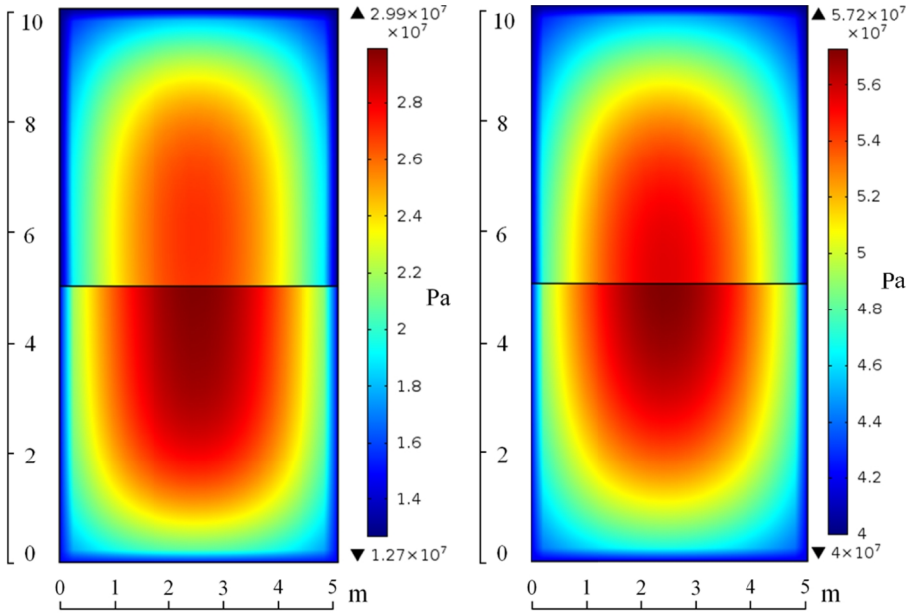

(a) (b)

Figure 5.14 Comparison of bulk modulus (Pa) of CB structures cured for (a) 14 days and (b) 28 days before blasting

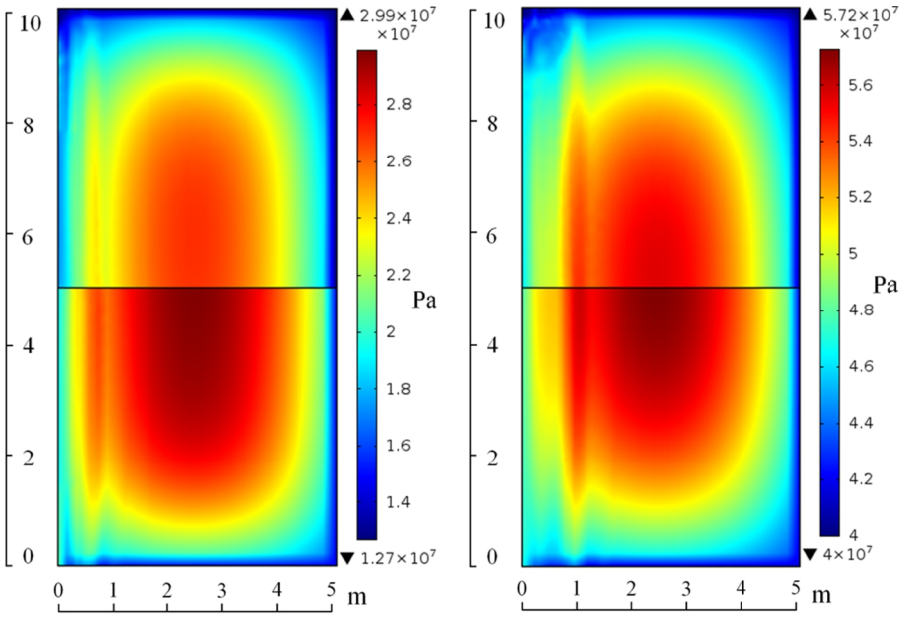

(a) (b)

Figure 5.15 Comparison of bulk modulus (Pa) of CB structures cured for (a) 14 days and (b) 28 days at 5 ms after the impact of blast pulse loading

5.2.4.2.2 Effect of cement content

The cement content is an important factor that affects the stability and cost of CB, and it is always desired in practice to maintain a balance between the two of them. The effects of cement content on the propagation of blast waves in CB are provided in Figure 5.16. As expected, a higher cement content is associated with a higher peak pressure and PPV at the same location of the CB structure when other curing conditions are the same. This is mainly because a higher cement content will lead to the generation of more hydration products (e.g., Yilmaz et al. 2015; Tariq and Yanful 2013; Walske 2014), and thus improve the mechanical properties (e.g., Klein and Simon 2006; Fall et al., 2008, 2010). As an indicator, the variation in the bulk modulus of the backfill in a CB structure with 10% cement (Case 5) is illustrated in Figure 5.17(b), which is significantly higher than that of the CB structure with 2% cement (Case 4) as shown in Figure 5.17(a).

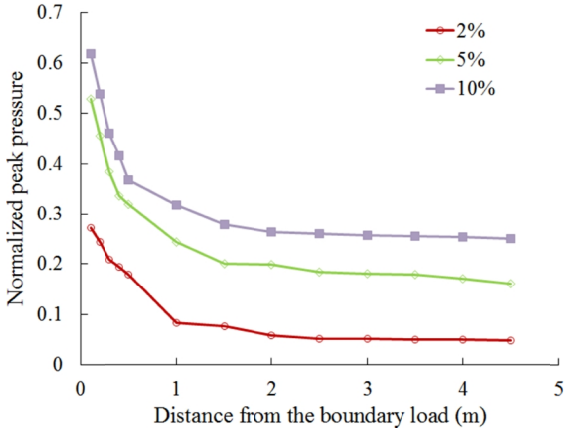

(a) Attenuation of peak pressure vs. distance in CB structure

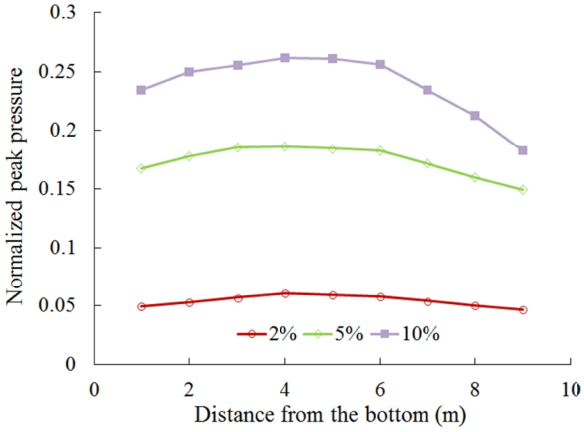

(b) Variation in peak pressure in vertical direction in CB structure

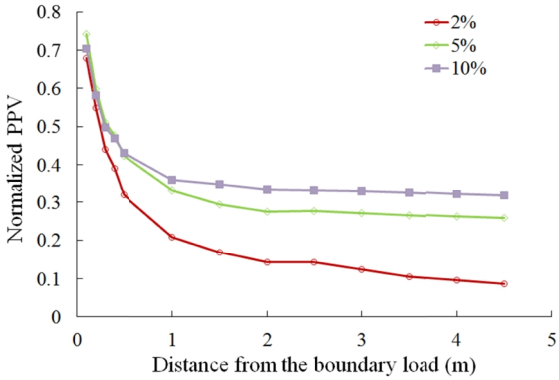

(c) Attenuation of PPV vs. distance in the CB structure

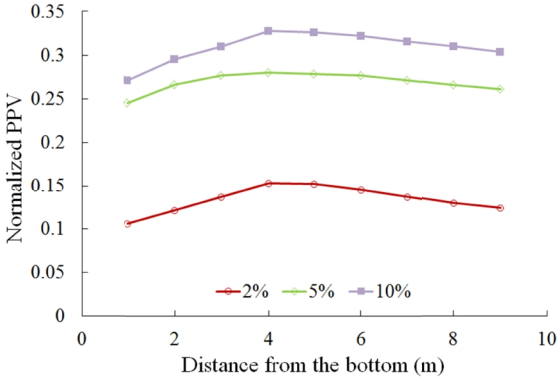

(d) Variation of PPV in vertical direction in CB structure

Figure 5.16 Variation of peak pressure and PPV in the CB structure with different cement contents

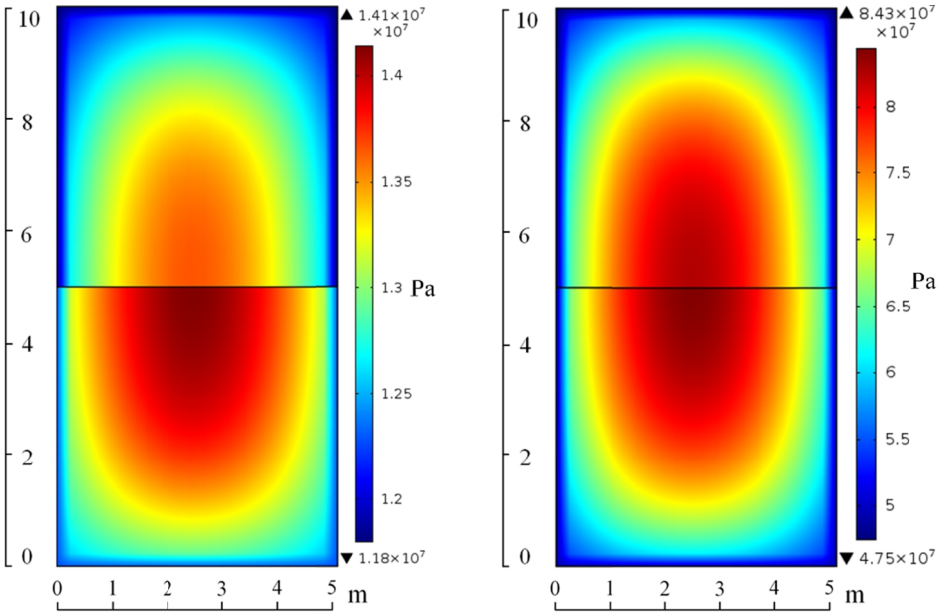

Figure 5.17 Comparison of bulk modulus (Pa) of CB structures with cement content of (a) 2% and (b) 10% before blasting

5.2.4.2.3 Effect of stope size

As CB is placed into a backfilled stope which could vary in size due to different ore body shapes and mining methods, it is important to investigate the influence of stope size on the peak pressure and PPV. The variation of the peak pressure and PPV in CB structures with different stope sizes (5 m × 10 m and 5 m × 20 m (L×H)) are presented in Figure 5.18. The CB structure with a height of 20 m (Case 6) requires 4 days to fill the stope at a rate of 5 m/d. As a result, the delay in hydration due to the delay in placement would render the values of the mechanical properties (e.g., stiffness) of the upper lifts in the CB at the early ages in Case 6 lower than those in Case 2 (5 m × 10 m) which requires only 2 days to be filled (see bulk modulus in Figure 5.19 as indicator). Thus, the peak pressure and PPV at the top of the larger stope are lower compared with the smaller stope.

Meanwhile, as can be observed from the distribution of the bulk modulus in Figure 5.19, the increase in the vertical dimensions of the structure increases the stiffness of the backfill in the core region. In fact, the observed effect of the stope size on the bulk modulus of the backfill structure is consistent with its effects on the UCS as demonstrated by Nasir and Fall (2010). This is because a larger stope means a greater volume of binder available for hydration, and more heat

will be generated which result in the precipitation of a larger amount of hydration products (Cihangir et al. 2012). Meanwhile, the increased dimensions of the structure would also reduce the effects of a colder environment by delaying the heat transfer from the backfill to the surroundings. Therefore, in the core region, heat is generated at a much faster rate than dissipated into the environment, and the accumulated heat will in turn accelerate the hydration process in accordance with the Arrhenius law (Wu et al. 2013). Consequently, in the middle of the structure with a size of 5 m×20 m or Case 6, the CB will have greater stiffness (Figure 5.19) and strength (Nasir and Fall, 2010), and its peak pressure and PPV is much higher than the stope that is 5 m×10 m in size, or Case 2. However, the differences become negligible when approaching the bottom and sides of the structure as the influence of the boundary temperature prevails.

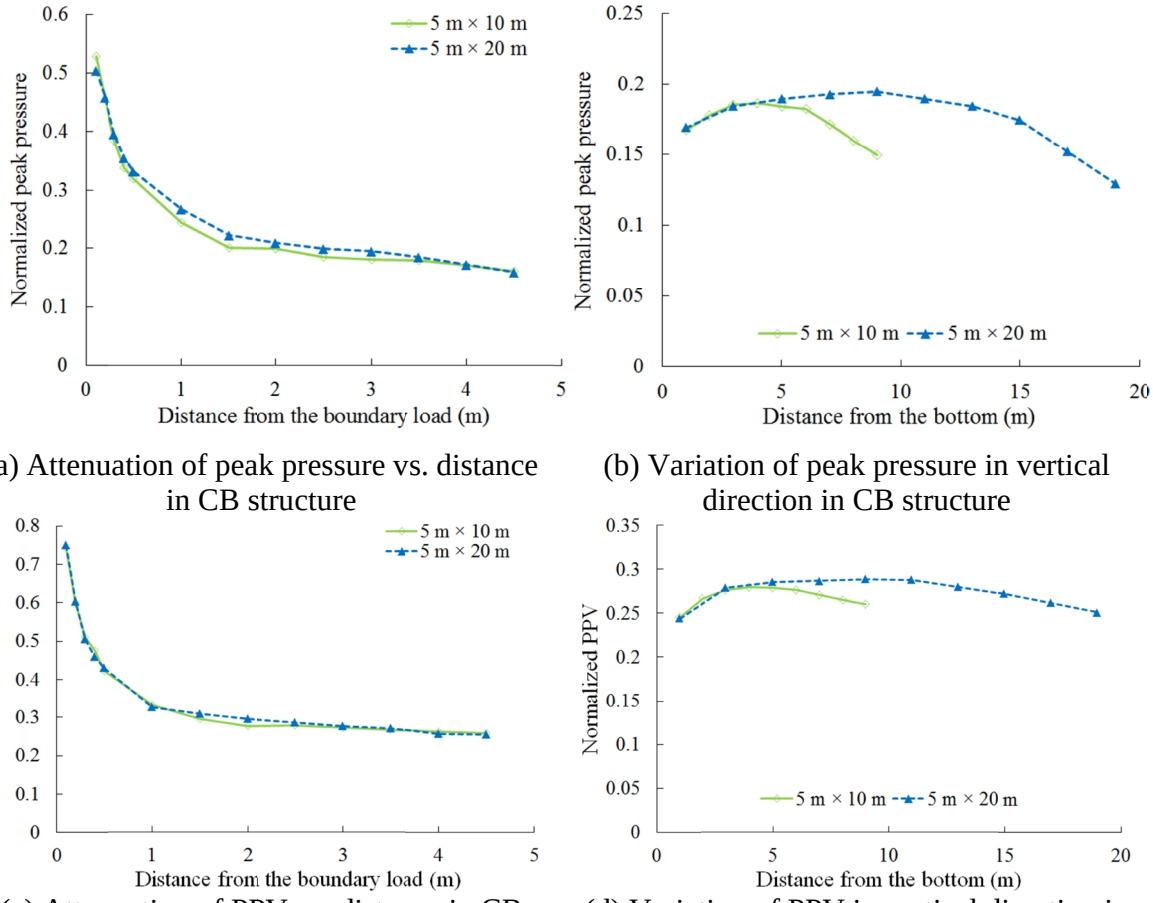

(a) Attenuation of peak pressure vs. distance in CB structure

(b) Variation of peak pressure in vertical direction in CB structure

(c) Attenuation of PPV vs. distance in CB structure

(d) Variation of PPV in vertical direction in CB structure

Figure 5.18 Variation of peak pressure and PPV in CB structure with different stope sizes

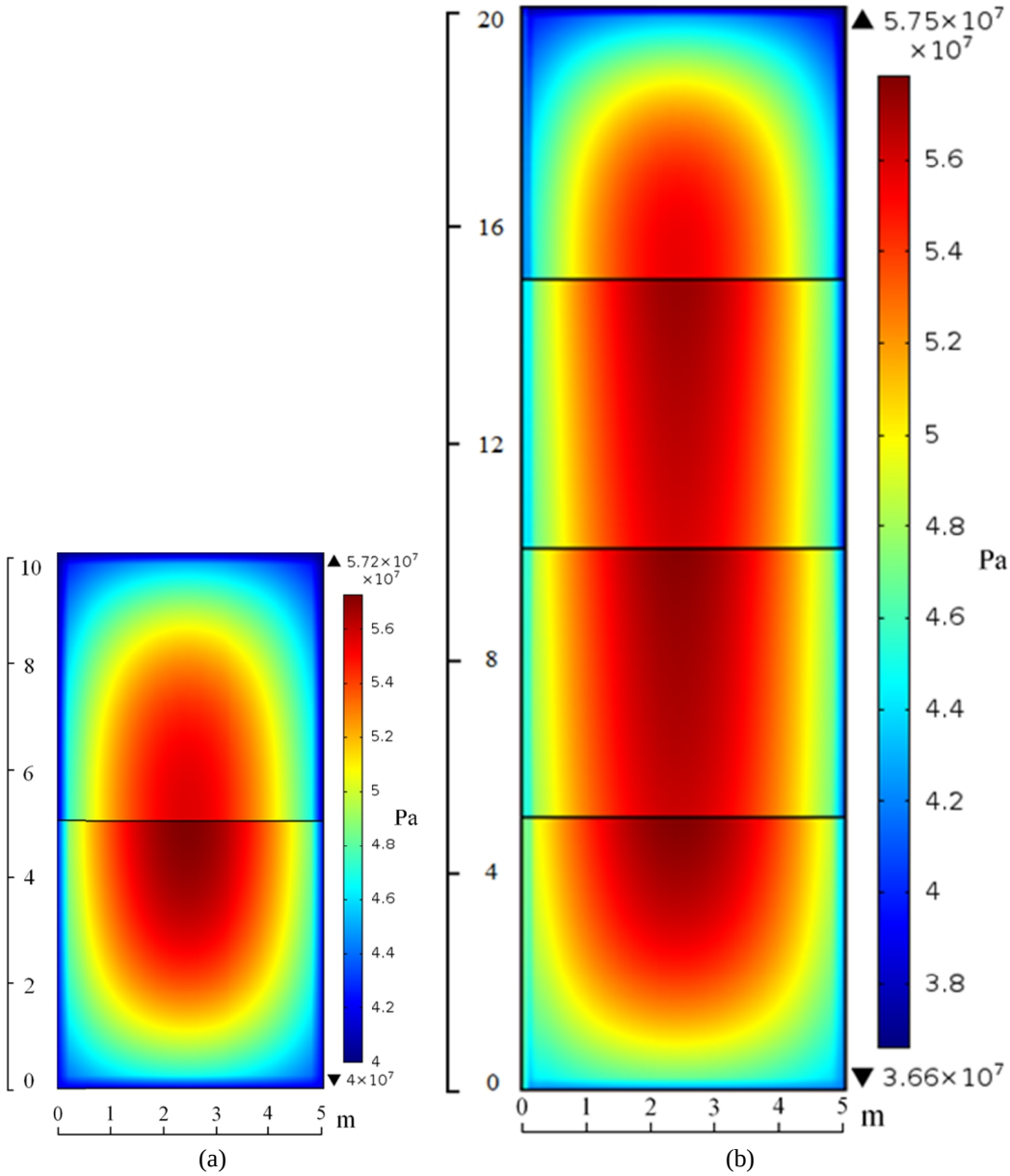

(a) (b)

Figure 5.19 Comparison of bulk modulus (Pa) of CB structures with (a) 5 m×10 m (Case 2) and (b) 5 m×20 m (Case 6) stope size before blasting

5.2.4.2.4 Effect of initial temperature

The varying initial temperatures of fresh CB (Fall et al., 2010) mean that it is necessary to investigate the effects of the initial CPB temperature on the variation of peak pressure and PPV in the CB. The variations of the peak pressure and PPV in CB structures with different initial temperatures (2^{o}C, 20 C and 35^{o}C) are presented in Figure 5.20. The figure shows that the initial

temperature of the CB material has a significant impact on the distribution and changes of peak pressure and PPV in the CB mass. It can be observed that a higher initial temperature is associated with higher peak pressure and PPV because a higher initial temperature speeds up cement hydration, thereby refining the pore structure of the CB and increasing its mechanical properties (e.g., bulk modulus). The impact of the initial temperature on the bulk modulus of backfill is graphically shown in the simulation results presented in Figure 5.21. Figures 5.21(a), 5.21(b) and 5.21(c) illustrate the distribution of the bulk modulus in CB structures with an initial temperature of 2^{o}C (Case 7), 20^{o}C (Case 2) and 35^{o}C (Case 8), respectively. From these figures, it can be observed that CB with higher initial temperatures shows higher bulk modulus values. Figures 5.20(b) and 20(d) also show that for the cases in which the initial temperature of CB is higher than or equal to the initial temperature of the surrounding rock, the highest peak pressure and PPV values are observed in the middle of the CB mass (from the bottom to the top). This is because the highest temperatures are found in the middle of these CB structures (because the middle is less affected by the thermal interactions with the surrounding rocks), as indicated in previous studies on heat development in CB structures; see Nasir and Fall (2009) and Wu et al. (2012, 2013). This higher temperature results in the improvement of the mechanical properties of CB, and thus increases the values of the peak pressure and PPV, as previously explained. This is in perfect agreement with the results of the numerical simulations of the distribution of bulk modulus in the CB structures with an initial temperature of 20^{o}C (Figure 5.21(b)) and 35^{o}C (Figure 5.21(c)), respectively. These figures show that CB structures exhibit the highest bulk modulus values in the middle.

The distribution of the bulk modulus in the backfill for Case 7 (initial temperature of 2^{o}C) is quite different from the other cases. First, the initial temperature of the CB is much lower than the temperature of the ambient rocks, which significantly inhibits the cement hydration process. Specifically, in the exterior of the structure, the backfill has a higher degree of hydration due to the relatively warmer surrounding rocks. In contrast, in the interior where heat transfer with the environment is limited, the hydration process is slow due to the low initial temperature, and the backfill is less mature and has a lower bulk modulus as illustrated in Figure 5.21(a). Therefore, according to Figures 5.20(b) and 5.20(d), the PPV and peak pressure are much lower in Case 7 and the differences with respect to Case 2 (initial temperature of 20^{o}C) and Case 8 (initial temperature of 35^{o}C) are the greatest in this core region.

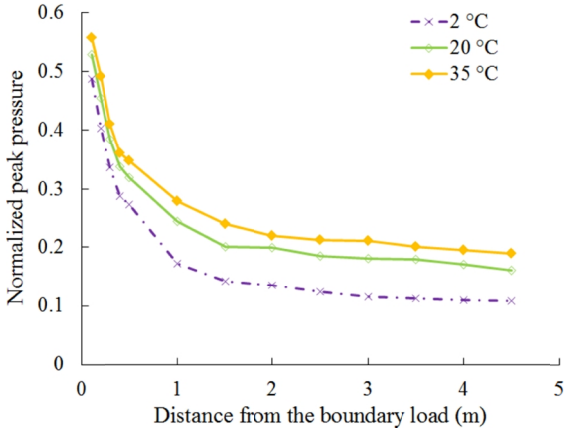

(a) Attenuation of peak pressure vs. distance in CB structure

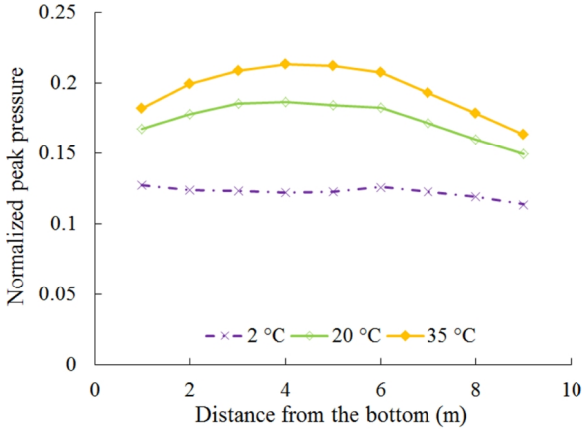

(b) Variation of peak pressure in vertical direction in CB structure

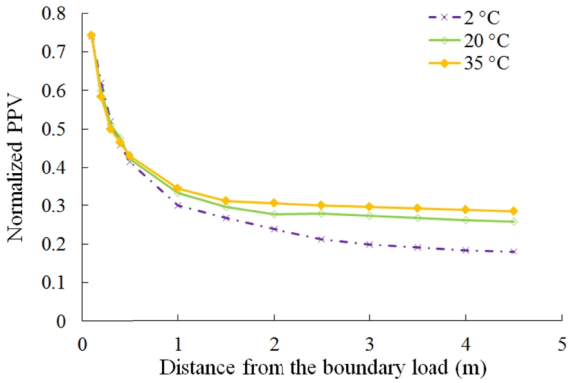

(c) Attenuation of PPV vs. distance in CB structure

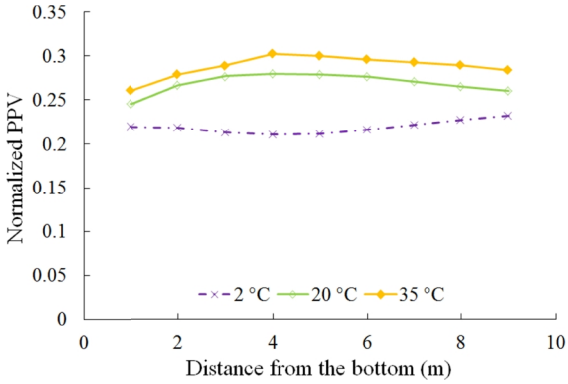

(d) Variation of PPV in vertical direction in CB structure

Figure 5.20 Variations in peak pressure and PPV in CB structure with different initial temperatures

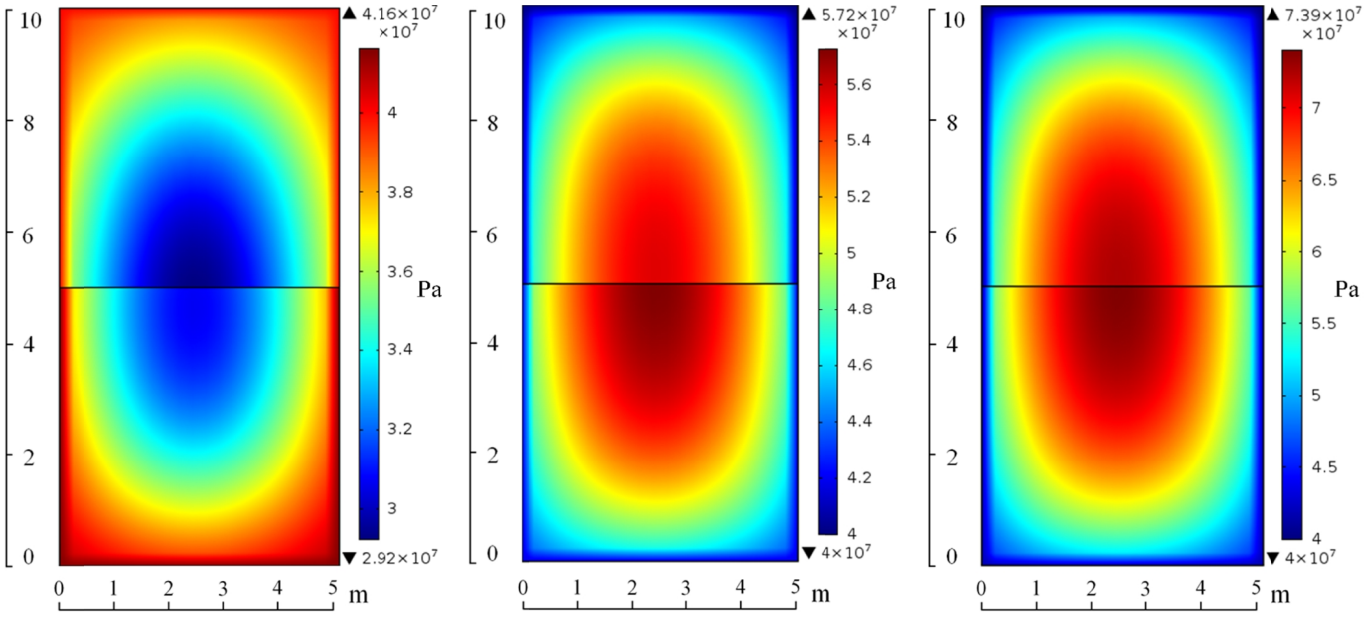

(a) (b) (c)

Figure 5.21 Comparison of bulk modulus (Pa) of CB structures with initial temperature of (a) 2^{o}C, (b) 20^{o}C , and (c) 35^{o}C before blasting

5.2.4.2.5 Effects of backfilling rate

The backfilling rate may vary from one mine to another, one stope to another and in the different stages of a mine. Therefore, simulation was conducted at various backfill rates to assess their influence on the distribution of peak pressure and PPV in the CB mass. The variations in the peak pressure and PPV in the CB structure with different filling rates (2.5 m/d, 5m/d, and 10 m/d) are presented in Figure 5.22. It can be observed that the differences in the response of the peak pressure and PPV are more pronounced closer to the top of CB structure as the layer is placed later. As expected, Case 9 (2.5 m/d) has the lowest and Case 10 (10 m/d) has the highest peak pressure and PPV in the upper part of the structure, while the differences gradually become negligible when approaching the lower parts of the structure. Figure 5.22 also demonstrates negligible differences in the peak pressure and PPV along the path of wave propagation in the mid-height of the structure. Therefore, the effects of the backfilling strategy might only be significant when the filling is delayed long enough, and this study indicates that, for the studied CB structures, the effects are limited when the delay of placement is no more than 2 days.

The variations in the bulk modulus of the CB structure in Cases 9 (2.5 m/d) and 10 (10 m/d) are shown in Figure 5.23. As can be observed, the multiple filling sequences have caused an

asymmetrical distribution of the bulk modulus in the backfill structure, and the bulk modulus of the upper lift which is delayed in placement will be lower than the lift below it. In fact, the minimum bulk modulus among Cases 2 (5 m/d), 9 (2.5 m/d) and 10 (10 m/d) is found at the top of the structure in Case 9, which corresponds to the last backfill layer (delay of 4 days after the first placement), while the maximum bulk modulus of the three cases are comparable. Therefore, the variations in the bulk modulus of the CB structures in these three cases are in agreement with those of the peak pressure and PPV as shown in Figure 5.22.

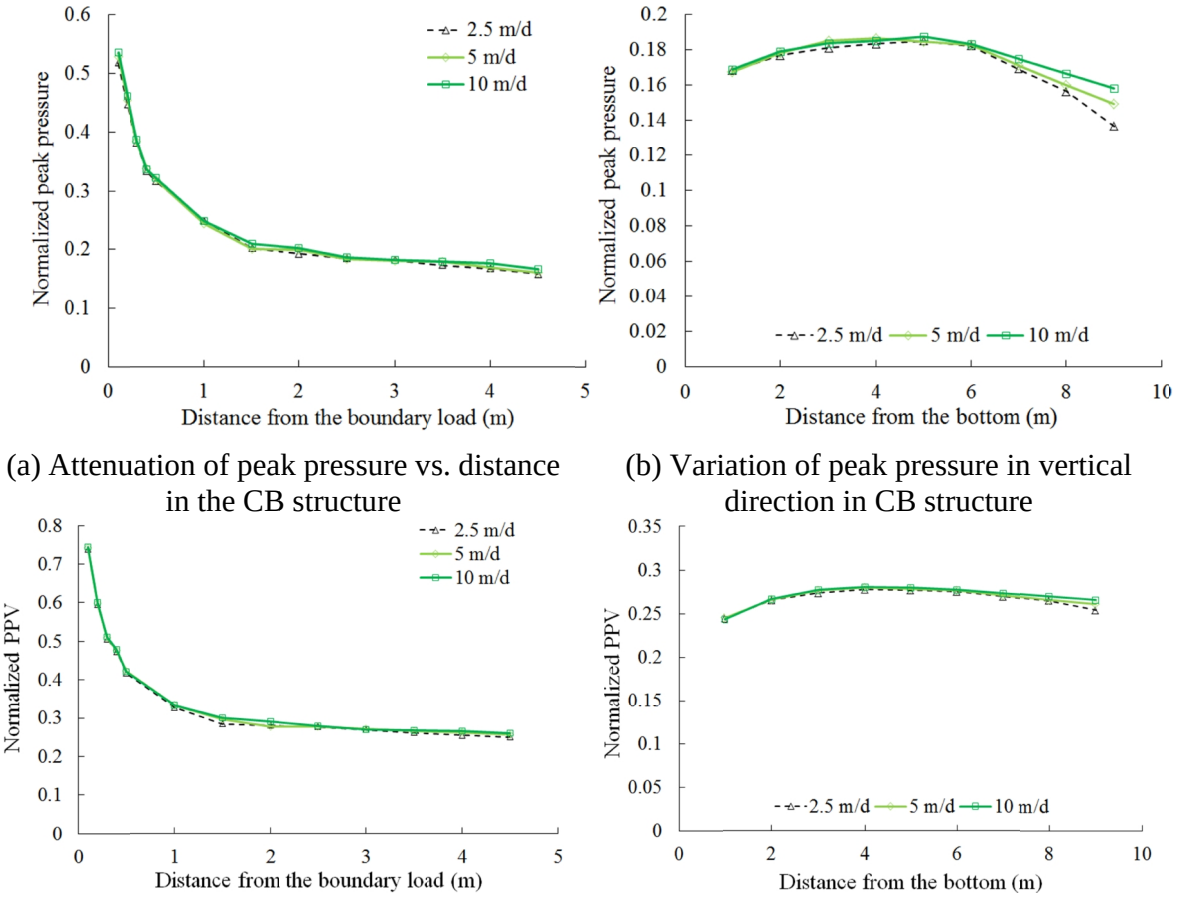

(a) Attenuation of peak pressure vs. distance in the CB structure

(b) Variation of peak pressure in vertical direction in CB structure

(c) Attenuation of PPV vs. distance in the CB structure

(d) Variation of PPV in vertical direction in CB structure

Figure 5.22 Variations of peak pressure and PPV in CB structure with different backfilling rates

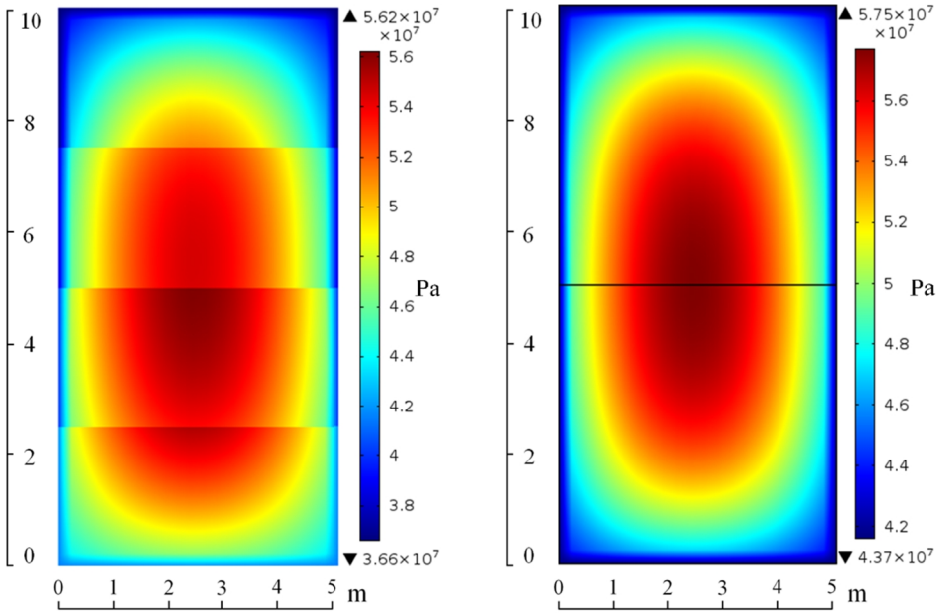

Figure 5.23 Comparison of bulk modulus (Pa) of CB structures with filling rate of (a) 2.5 m/d and (b) 10 m/d before blasting

5.2.5 Conclusions

A coupled THMC-viscoplastic cap model is proposed in this study to investigate the effects of different curing conditions and backfilling practices on blast wave propagation in cemented tailings backfill. All of the material properties required by the viscoplastic cap model to simulate the blast response of CB are provided by the THMC model with consideration for the multiphysics interactions.

The validation results indicate that the model is capable of predicting the blast response of CB reasonably well through comparisons with experimental (laboratory and field) data. Applications of the model suggest that the curing time, cement content, stope size, initial backfill temperature, and filling rate all influence blast wave propagation in CB structures. Specifically, amongst all of these factors, the curing time, cement content, and initial backfill temperature have an overall impact on the wave propagation characteristics of CB, while the effects of the stope size and filling rate appear to be localized to the core region and/or top of the backfill structure, respectively.

The results of this study provide useful information on the design of cemented backfill structures in mines that carry out production blasting, thereby helping to reduce the potential negative impacts of backfill structure failures due to blasting.

5.2.6 References

Abdul-Hussain N, Fall M. Unsaturated hydraulic properties of cemented tailings backfill that contains sodium silicate. Engineering Geology 2011; 123:288–301.

Abdul–Hussain N, Fall M. Thermo–hydro–mechanical behaviour of sodium silicate–cemented paste tailings in column experiments. Tunnelling and Underground Space Technology 2012; 29:85–93.

An J, Tuan CY, Cheeseman BA, Gazonas GA. Simulation of soil behaviour under blast loading. International Journal of Geomechanics, ASCE 2011; 11:323–334.

Aráoz G, Luccioni B. Modeling concrete like materials under sever dynamic pressures. International Journal of Impact Engineering 2015; 76:139–154.

Aref L. A study of the geotechnical characteristics and liquefaction potential of paste backfill. PhD Thesis, University of McGill, Montreal, Canada, 1998.

Bergeron D, Walker R, Coffey C. Detonation 100-gram anti-personal mine surrogate charge in sand – A test case for computer code validation. Report SR 668, Defence Research Establishment Suffield, Canada, 1998.

Bloom F. Constitutive models for wave propagation in soil. Applied Mechanics Reviews 2006; 59:146–175.

Chen WF, Baladi GY. Soil Plasticity: Theory and Implementation. Elsevier: Amsterdam, 1985.

Chen YF, Zhou CB, Jing LR. Modeling coupled THM processes of geological porous media with multiphase flow: Theory and validation against laboratory and field scale experiments. Computers and Geotechnics 2009; 36:1308–1329.

Chian SC, Nguyen ST, Phoon KK. Extended strength development model of cement-treated clay. Journal of Geotechnical and Geoenvironmental Engineering, ASCE 2011;142(2):1–7.

Cihangir F, Ercikdi B, Kesimal A, Turan A, Deveci H, 2012. Utilisation of alkali-activated blast furnace slag in paste backfill of high-sulphide mill tailings: Effect of binder type and dosage. Minerals Engineering 2012;30:33–43.

COMSOL Multiphysics User's Guide, Version 3.5a, COMSOL AB, Stockholm, Sweden, 2009.

Cui L, Fall M. A coupled thermo–hydro-mechanical–chemical model for underground cemented tailings backfill. Tunnelling and Underground Space Technology 2015; 50: 396–414.

Cui L, Fall M. An evolutive elasto–plastic model for cemented paste backfill. Computer and Geotechnics 2016; 71: 19-29.

Doherty JP. A numerical study into factors affecting stress and pore pressure in free draining mine stopes. Computers and Geotechnics 2015; 63:331–341.

Emad MZ, Mitri H, Kelly C. Effect of blast–induced vibrations on fill failure in vertical block mining with delayed backfill. Canadian Geotechnical Journal 2014; 51:975–983.

Fall M, Belem T, Benzaazoua M. The compressive and tensile properties of underground paste backfill. Proceedings of 58-th Canadian Geotechnical Conference, Saskatoon, 2005; 1–7.

Fall M, Benzaazoua M, Saa EG. Mix proportioning of underground cemented tailings backfill. Tunnelling and Underground Space Technology 2008; 23:80–90.

Fall M, Célestin JC, Pokharel M, Touré M. A contribution to understanding the effects of curing temperature on the mechanical properties of mine cemented tailings backfill. Engineering Geology 2010b;114:397–413.
Ghirian A, Fall M. Coupled thermo–hydro–mechanical–chemical behaviour of cemented paste backfill in column experiments. Part I: Physical, hydraulic and thermal processes and characteristics. Engineering Geology 2013; 164:195–207.
Ghirian A, Fall M. Coupled thermo–hydro–mechanical–chemical behaviour of cemented paste backfill in column experiments. Part II : Mechanical, chemical and microstructural processes and characteristics. Engineering Geology 2014; 170:11–23.
Grice T. Underground mining with backfill. Proceedings of the 2nd Annual Summit-Mine Tailings Disposal Systems Australian 1998, 234-239.
Helinski M, Fahey M, Fourie A. Behaviour of cemented paste backfill in two mine stopes: measurements and modeling. Journal of Geotechnical and Geoenvironmental Engineering, ASCE 2010;137(2):171–182.
Henrych J. The dynamics of explosion and its use. Elsevier, New York, USA, 1979.
Huang S, Xia K, Qiao L. Dynamic tests of cemented paste backfill: effects of strain rate, curing time, and cement content on compressive strength. Journal of Material Science 2011; 46(15):5165–5170.
Huang S. Dynamic testing of soft and ultra–soft materials. Master Thesis. University of Toronto, Toronto, Canada, 2009.
Katona MG. Evaluation of viscoplastic cap model. Journal of Geotechnical Engineering, ASCE 1984; 110(8):1106–1125.
Kesimal A, Yilmaz E, Ercikdi B, Alp I, Deveci H. Effect of properties of tailings and binder on the short– and long–term strength and stability of cemented paste backfill. Materials Letters 2005; 59(28):3703–3709.
Klein K, Simon D. Effect of specimen composition on the strength development in cemented paste backfill. Canadian Geotechnical Journal 2006; 43:310–324.
Le Roux K. In situ properties and liquefaction potential of cemented paste backfill. Ph.D. Thesis. University of Toronto, Toronto, Canada, 2004.
Lu G, Fall M, Cui L. A multiphysics–viscoplastic cap model for simulating the blast response of an evolutive soft cementitious material. Journal of Rock Mechanics and Geotechnical Engineering 2017 (Accepted for publication).
Lu G, Fall M. A coupled chemo-viscoplastic cap model for simulating the behaviour of hydrating cemented tailings backfill under blast loading. International Journal for Numerical and Analytical Methods in Geomechanics 2016;40:1123–1149.
Mohanty B, Yang R, LeBlanc M, and Kelly C. Dilution control and vibration studies at an underground mine. Proceedings of the Annual Conference on Explosives and Blasting Technique, International Society of Explosives Engineers, CONF 21//V2, pages 20, 1995.
Nasir O, Fall M. Modeling the heat development in hydrating CPB structures. Computers and Geotechnics 2009; 36(7):1207–1218.
Nasir O, Fall M. Coupling binder hydration, temperature and compressive strength development of underground cemented paste backfill at early ages. Tunnelling and Underground Space Technology 2010; 25(1):9–20.
Perzyna P. Fundamental problems in viscoplasticity. Advances in Applied Mechanics 1966; 9:243–377.

Schindler AK, Folliard KJ. Heat of hydration models for cementitious materials. ACI Material Journal 2005;102(1):24–33.
Schindler AK. Effect of temperature on hydration of cementitious materials. ACI Material Journal 2004; 101(1):72–81.
Simo JC, Wu JW, Pister KS, Taylor RL. Assessment of cap model: Consistency return algorithms and rate–dependent extension. Journal of Engineering Mechanics, ASCE 1986; 114(2):191–218.
Tariq A, Yanful EK. A review of binders used in cemented paste tailings for underground and surface disposal practices, Journal of Environmental Management 2013;131:138–149.
Tong X, Tuan CY. Viscoplastic cap model for soils under high strain rate loading. Journal of Geotechnical and Geoenvironmental Engineering, ASCE 2007; 133(2):206–214.
van Genuchten MT. A closed-form equation for predicting the hydraulic conductivity of unsaturated soils. Soil Science Society of America Journal 1980;44:892–898.
van Gool BS. Effects of blasting on the stability of paste fill stopes at Cannington Mine. Ph.D. Thesis. James Cook University, Townville, Australia, 2007.
Walske ML. An experimental study of cementing paste backfill. PhD Thesis, University of Western Australia, Perth, Australia, 2014.
Wu D, Fall M, Cai S. Coupled modeling of temperature distribution and evolution in cemented tailings backfill structures that contain mineral admixtures. Geotechnical and Geological Engineering 2012; 30(4):935–961.
Wu D, Fall M, Cai S. Numerical modelling of thermally and hydraulically coupled processes in hydrating cemented tailings backfill columns. International Journal of Mining, Reclamation and Environment 2014; 28(3):173–199.
Wypych G. Handbook of polymers. ChemTec Publishing: Toronto, 2012.
Yilmaz E, Benzaazoua M, Belem T, Bussière B. Effect of curing under pressure on compressive strength development of cemented paste backfill. Mineral Engineering 2009; 22:772–785.
Yilmaz E, Kesimal A, Ercidi B. Strength development of paste backfill simples at long term using different binders. Proceedings of 8th symposium on Minefill, Beijing, 2004; 281–285.
Yilmaz E, Belem T, Bussière B, Mbonimpa M, Benzaazoua M. Curing time effect on consolidation behaviour of cemented paste backfill containing different cement types and contents. Construction and Building Materials 2015;75:99–111.

5.3 Technical Paper 6: Simulation of blast induced liquefaction susceptibility of subsurface fill mass

(Submitted)

Gongda Lu, Mamadou Fall

Abstract:

Tailings backfill, a subsurface fill mass, is extensively utilized worldwide in underground mines to fill mined-out cavities for purposes of ground control and tailings disposal. When it is just placed, the early-age backfill that commonly contains excessive water exhibits no or marginal inter-particle bonds, and it is subjected to the risk of liquefaction induced by mine blast routines. In this study, a modified total-stress viscoplastic cap model is developed to investigate the blast-induced liquefaction susceptibility of early-age fill mass under varied practical backfilling and mining operation conditions. The developed model can well represent the strain-rate and fluid-compressibility dependence of nonlinear material behaviour under such dynamic condition, and also reasonably capture the excess pore pressure development due to irrecoverable volume compaction. The model is validated against a series of blast and impact tests on saturated natural soils (sand, silt) and tailings fill masses, and good agreement is found between the experimental and simulated results. Subsequently, the model is applied to investigate the effects of drainage condition, distance of detonation, stope size, delay of blasting, location of retaining structure, and blast sequence on the liquefaction susceptibility of early-age fill mass after mine blasting. The results obtained from the study will provide practical insight into the blast liquefaction potential of backfill mass in field conditions.

KEY WORDS: tailings; backfill; liquefaction; blast; viscoplastic cap model; mine

5.3.1 Introduction

To mitigate the risks imposed by acid mine drainage and impoundment breach associated with surface disposal of mine tailings, cemented and uncemented tailings backfills, which are subsurface fill mass, are extensively utilized in underground mines today. Moreover, by recycling tailings to subsurface mined-out voids (stopes), the fill mass could improve the stability of the rock mass and facilitate full ore recovery, while minimize potential contamination of the mine waste to the environment (Klein and Simon, 2006; Bussière, 2007; Fahey et al., 2009; Yilmaz et al., 2009; etc.).

For its transportation to underground openings, the fresh backfill is conventionally prepared with excessive water to meet desired consistency. Once placed in openings, it is then retained by structures (called barricades) constructed at the base of stopes. As a result, the fill mass placed in the stope commonly remains saturated and exhibit marginal inter-particle bonds at early ages, even it is mixed with cement. This is because the effect of cement hydration that would generate hydration products, consume water (self-desiccation), and lead to strength gain of cementitious materials is not significant at early ages. Moreover, the mixing water or tailings (particularly from hard rock mine tailings) used in the preparation of the backfill mixtures can contain a high amount of sulphate, which would strongly inhibit and significantly delay the binder hydration process (Fall and Benzaazoua, 2005). Furthermore, field measurements have also shown that saturated cemented backfills could behave in an undrained manner for a long time when fine tailings are used (Fahey et al., 2009). Therefore, the early-age fill mass that consists of granular tailings, which has grain sizes of silt to sand can be vulnerable to liquefaction. Liquefaction of backfill mass would result in additional loads on barricades and even breach of these retention structures, thus lead to severe safety consequences and loss of production (Le Roux, 2004; Pépin et al., 2012). Moreover, it has also been reported that the retention structures could even fail hours after the dynamic loading during the redistribution and dissipation of excess pore pressure (Ishihara, 1984; Ferdosi et al., 2015).

In recent years, seismically induced liquefaction of saturated tailings or tailings backfills has been extensively investigated (e.g., Wijewickreme et al., 2005; Al-Tarhouni et al., 2011; James et al., 2011; Suazo et al., 2016), and their post-liquefaction behaviour has also been studied by Pépin et al. (2012). Meanwhile, it has also been well acknowledged for decades that liquefaction of granular soils can also be induced by blast loadings (Fragaszy and Voss, 1986;

Charlie et al., 2013). However, research on the blast-induced liquefaction of tailings mass is extremely limited. In fact, it has been only examined in the CANLEX program (Al-Qasimi et al., 2005), where excess pore pressures of a tailings deposit caused by explosive detonations were investigated, while the post-liquefaction behaviour has not been studied. Therefore, as mine blasts become routinely used in mining exploitations, the risk of liquefaction of early-age fill mass induced by blast loading should also be thoroughly examined to ensure mine safety and profitability.

Considering the costs and safety concerns of field explosion experiments whose results are also commonly site-specific (e.g., Al-Qasimi et al., 2005; Charlie et al., 2013), a numerical tool for assessing the blast-induced liquefaction of fill mass would be favorable. To date, a few soil models have been developed to simulate the liquefaction caused by explosive loadings (e.g., Awad, 1990; Lee, 2006; Wang et al., 2008). However, they are subjected to various limitations, such as the use of Mohr-Coulomb type of criteria that could result in unrealistic dilation, and neglecting effects of strain rate and pore water on the material response during blast loading.

Recently, a viscoplastic cap model has been put forward by Lu and Fall (2017a) to capture liquefaction of granular porous media due to blast loads. This model can well represent the strain-rate and fluid-compressibility dependence of nonlinear material behaviour under such dynamic condition, and also reasonably capture the excess pore pressure development due to irrecoverable volume compaction. Thus, the modified viscoplastic cap model is applied in the study to investigate the blast-induced liquefaction susceptibility of early-age fill mass. Specifically, the model formulation is briefly presented at first, and it is validated against a series of blast-induced liquefaction tests on natural soils and tailings fill masses. Then, based on satisfactory validation of the model against test data, it is employed to examine the liquefaction susceptibility of early-age tailings backfill mass after blast loading in various practical engineering conditions in the mine fields, and factors affecting its risk of liquefaction is scrutinized and discussed.

5.3.2 Model formulation

5.3.2.1 Modelling approach

In the course of a blast event, there is insufficient time for relative movement of pore fluid and soil skeleton (Wang et al., 2008). Therefore, the blast response of saturated soils is undrained,

and the entrapped pore water with large stiffness will deform simultaneously with the soil skeleton at the same volumetric strain due to the volume compatibility under undrained conditions (Naylor, 1974; Griffiths, 1985; Fragaszy and Voss, 1986; Griffiths and Li, 1989; Puebla et al., 1997). According to Fragaszy and Voss (1986), liquefaction induced by blast loading is attributed to the volumetric hysteresis in the stress-strain path of soils. Specifically, since the soil skeleton is inelastic upon loading and elastic at unloading while pore water is always elastic, the irrecoverable volumetric deformation of soil after the loading cycle in the undrained condition would lead to the generation of excess pore water pressure.

To date, Lee (2006) and Wang et al. (2008) have utilized mathematical models to characterize liquefaction of soils induced by explosive loadings. However, these models employed Drucker-Prager type of yield criteria, thus they would result in unrealistic dilation (Bloom, 2006) and has been shown to underestimate pore pressure caused by blasting (Lee, 2006). To reasonably capture the irrecoverable volume compaction or hysteresis, cap models have been adopted to simulate the response of soils under blast loading, such as in Baladi and Rohani (1979), Awad (1990), Ghassemi et al. (2010) and An et al. (2011). Nevertheless, unsaturated soils have been studied in An et al. (2011), while the effects of strain rate and pore fluid compressibility on the undrained behaviour of saturated soils during the impact have not been considered in the other studies. Therefore, there is no model at present that captures the blast-induced liquefaction of soils in a rigorous scheme, and the applicability of cap models for the issue needs to be further examined despite its theoretical feasibility.

In this study, a modified viscoplastic cap model is developed to reproduce the behaviour of saturated granular soils under blast loading, and the volumetric constraints imposed by pore water is also incorporated to capture the pore pressure response in the undrained dynamic condition. The viscoplastic flow is adopted in the study, because experimental studies have revealed that both the blast response of natural soils and tailings backfills have exhibited strain-rate dependence (e.g., Yamamuro and Lade, 1993; Bolton et al., 1994; Huang et al., 2011). The model formulation is briefly presented in the following sections.

5.3.2.2 Constitutive law

A modified Perzyna type of viscoplastic cap model is developed in the study to simulate the response of saturated fill mass under blast loading. By extending the inviscid cap model to

Perzyna type of viscoplasticity (Perzyna, 1966), this type of models have been widely and successfully used for modelling the response of geomaterials (including soils, concrete and tailings backfills) under high pressure and varied strain rates (e.g., Katona 1985; Simo et al., 1986; Tong and Tuan, 2007; An et al., 2011; Aráoz and Luccioni, 2015; Lu and Fall, 2016, 2017b).

In viscoplastic models, the total strain rate vector $\dot{\boldsymbol{\varepsilon}}$ is decomposed into an elastic part $\dot{\boldsymbol{\varepsilon}}^{e}$ and a viscoplastic (inelastic) part $\dot{\boldsymbol{\varepsilon}}^{vp}$ as

$$\dot{\boldsymbol{\varepsilon}} = \dot{\boldsymbol{\varepsilon}}^{e} + \dot{\boldsymbol{\varepsilon}}^{vp} \tag{5.45}$$

The elastic strain rate is independent of viscosity, and it can be expressed as

$$\dot{\boldsymbol{\varepsilon}}^{e} = \mathbf{D}^{-1}\dot{\boldsymbol{\sigma}} \tag{5.46}$$

where $\dot{\boldsymbol{\sigma}}$ is the stress rate tensor, and **D** the elastic stiffness matrix.

The viscoplastic strain rate in Perzyna's model is generally expressed as:

$$\dot{\boldsymbol{\varepsilon}}^{vp} = h\left\langle f(f)\right\rangle \frac{\partial f}{\partial \boldsymbol{\sigma}} \tag{5.47}$$

where h is a fluidity parameter; $\langle\ \rangle$ is the Macaulay bracket; f is the yield function which is characterized by a cap envelope that will be introduced below; and $f(f)$ is a dimensionless scaling function, which is conventionally defined as (e.g., Katona, 1984; Tong and Tuan, 2007):

$$f(f) = \left(\frac{f}{f_0}\right)^{N} \tag{5.48}$$

where N and f_0 are model constants. The associated flow rule is generally employed in Perzyna type of viscoplastic models for simulating behaviours of geomaterials under dynamic loadings (e.g., Katona, 1984; Tong and Tuan, 2007), and it is also adopted in the study.

A modified smooth surface cap model is used as the yield envelope f in the study, and the shear yield envelope of this cap model is characterized by Lu and Fall (2016, 2017b):

$$F_1(I_1, \sqrt{J_2}) = \sqrt{J_2} - \frac{k - [X(k) - L(k)]/R}{L(k)^2} I_1^2 + 2 \cdot \frac{k - [X(k) - L(k)]/R}{L(k)} I_1 - k \tag{5.49}$$

where $L(k)$ and $X(k)$ is the abscissa of the joint of the elliptical cap with the shear envelope and the hydrostatic loading line (I_1 axis), respectively; R is the ratio of the major to the minor axis of the elliptical cap; and k is the Drucker-Prager criterion parameter which can be related to the Mohr-Coulomb model as:

$$a = \frac{2\sin j}{\sqrt{3}(3+\sin j)}, \qquad k = \frac{6c\cos j}{\sqrt{3}(3+\sin j)} \tag{5.50}$$

where c and j are the cohesion and internal friction angle.

Then, the hardening cap envelope is defined by following expression (Chen and Baladi, 1985):

$$F_2(I_1, \sqrt{J_2}, k) = \sqrt{J_2} - \frac{1}{R}\left\{[X(k) - L(k)]^2 - [I_1 - L(k)]^2\right\}^{1/2} \tag{5.51}$$

where the movement of $X(k)$ due to irrecoverable volume compaction (e_{kk}^{in}) can be expressed by a logarithmic hardening law as (Chen and Baladi, 1985):

$$X(k) = -(1/D)\cdot \ln\left(1 - \frac{e_{kk}^{in}}{W}\right) + X_0 \tag{5.52}$$

where e_{kk}^{in} is calculated based on Equation (5.47), constant W is the maximum inelastic volumetric strain that the material can develop, D denotes the shape parameter of the volume-pressure relation, and X_0 is the initial vertex of the cap. Then, $L(k)$ can be obtained by enforcing continuity of the entire yield envelope:

$$k = \frac{X(k) - R\cdot k}{1 + R\cdot a} \tag{5.53}$$

and

$$L(k) = \begin{cases} k & k > k_0 \\ k_0 & \text{otherwise} \end{cases} \tag{5.54}$$

where k_0 is the onset of the hardening cap. The process of irrecoverable volume compaction captured by cap models is illustrated in Figure 5.24, where e_{kk} and e_{kk}^{e} is total and elastic volumetric strain, respectively.

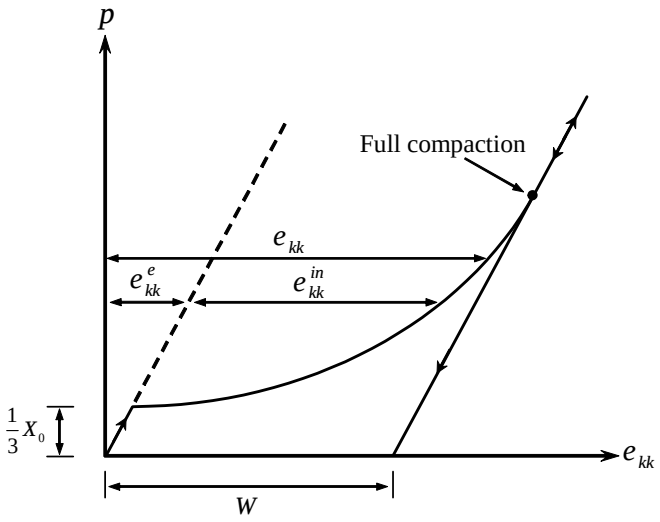

Figure 5.24 Volumetric hysteresis represented by cap models (Modified after Murray, 2007)

5.3.2.3 Undrained response

The soil skeleton and pore water will deform concurrently during the undrained blast loading. According to Naylor (1974) and Griffiths and Li (1989), the pore pressure change of saturated soils in the undrained condition can be determined as

$$dP_w = K_a de_{kk}^{f} \tag{5.55}$$

where e_{kk}^{f} is the volumetric strain of pore fluid, and it equals to volumetric strain of soil skeleton (e_{kk}) as discussed in Section 5.3.2.1; K_a is the apparent bulk modulus of the pore fluid, which can be obtained as (Naylor, 1974):

$$\frac{1}{K_a} = \frac{n}{K_w} + \frac{1-n}{K_p} \tag{5.56}$$

where n is the porosity, K_w and K_p is the bulk modulus of pore water and solid particles, respectively.

Then, the undrained behaviour of the saturated mixture can be obtained by adding the apparent pore fluid bulk modulus to the effective elastic matrix of the skeleton (Naylor, 1974; Griffiths, 1985), and it can be expressed in this study as

$$dP = dP_s + dP_w = K_s de_{kk}^{e} + K_a de_{kk} = (K_s + K_a \frac{de_{kk}}{de_{kk}^{e}}) de_{kk}^{e} = K_m de_{kk}^{e} \tag{5.57}$$

where K_s is the bulk modulus of soil skeleton. Thus, the undrained bulk modulus of the saturated mixture is obtained as K_m, and the associated Poisson's ratio in the undrained condition ν_m is also modified as (Naylor, 1974; Griffiths, 1985):

$$\nu_m = \frac{(1-2\nu)(1+\nu) + E\nu / K_a}{2(1-2\nu)(1+\nu) + E / K_a} \tag{5.58}$$

where E and ν are effective elastic constants of soil skeleton.

Meanwhile, as the volumetric behaviour of soil skeleton and pore water is nonlinear under blast loading (Henrych, 1979), the variable-bulk-modulus approach is employed in this study. The stiffness of soil skeleton and pore water can be determined by using the Mie-Grüneisen equation of state as (An et al., 2011):

$$K_i = \frac{r_{i0}C_{i0}^2[1+(1-\frac{g_{i0}}{2})m - \frac{a_{i0}}{2}m^2][1+\frac{2m(s_i-1)}{1+m-s_i m}+\frac{m(g_{i0}+a_{i0}m)}{(1+m)^2}] + r_{i0}C_{i0}^2 m(1-\frac{g_{i0}}{2}-a_{i0}m)}{(1+m-s_i m)^2} + \left[\frac{(g_{i0}+a_{i0}m)^2}{(1+m)^2}+a_{i0}\right]E_i^v \tag{5.59}$$

where i = s or w, r_{i0} is the material density; C_{i0} is the p-wave velocity of the material; s_i is the slope of the shock velocity against the particle velocity curve; g_{i0} is the Grüneisen parameter, E_i^v is the internal energy per unit initial volume; a_{i0} is the first order volume correction to g_{i0} and often set to 0; and $m = e_{kk}/(1-e_{kk})$.

5.3.3 Model Validation

5.3.3.1 Introduction

It has been well acknowledged that the grain size distribution (GSD) has a significant influence on the liquefaction susceptibility of granular soils (Ishihara, 1993). Given that tailings backfills generally have a range of GSD from sand to silt due to different sources of rocks and processing techniques, laboratory and field blast-induced liquefaction tests on various natural sand and silt are first reproduced to demonstrate the validity of the model in this GSD spectrum. Then, simulation of an explosion test in a saturated tailings mass deposit is carried out to validate the capability of the model in capturing the mechanical response and particularly liquefaction of tailings backfills under blast loading.

5.3.3.2 Case Study 1: Laboratory ramp loading on saturated sand

The ramp loading tests carried out by Fragaszy and Voss (1986) on saturated Eniwetok sand are adopted and simulated. The experiments were conducted in a triaxial cell and drainage of water during the test was precluded. The saturated sand with a height of 110 mm and a diameter of 35.6 mm was subjected to ramp loading in the form of confining pressure with an oil pump, and the initial effective stress and pore pressure was 1.03 MPa and 0.69 MPa, respectively. The ramp loading on saturated sand is simulated by using 2D symmetry in the study. The loading pattern of the test is adopted from Wang et al. (2008) for simulation of the same experiment, and the pressure is increased to its peak within 0.1 ms and it is maintained for 5 ms, then the pressure is reduced to its initial value within 0.1 ms. Two sets of experiments in Fragaszy and Voss (1986) are reproduced, and the peak pressure is 34.48 MPa (Case 1) and 20.69 MPa (Case 2), respectively. The model parameters used in the simulation are determined from experimental data in Fragaszy and Voss (1986) and those used in Wang et al. (2008), and they are listed in Tables 5.5 and 5.6. The simulated time histories of strain and pressure of a monitored point in the middle of the specimen in both cases are illustrated in Figures 5.25 to 5.26.

Table 5.5 Material properties used in the model for ramp loading tests on saturated sand

Density (kg/m^3)	h (μsec^{-1})	N	f_0 (Pa)	a	k (MPa)	R	D (MPa^{-1})	W	X_0 (MPa)
1959	4×10^{-5}	1	1×10^{6}	0.25	0	8	1×10^{-3}	0.0027	5

Table 5.6 Material properties used for undrained response of saturated sand in ramp loading tests

n	r_{s0} (kg/m^3)	r_{w0} (kg/m^3)	C_{s0} (m/s)	C_{w0} (m/s)	s_s	s_w	g_{s0}	g_{w0}	$\underline{v}$	$\underline{K_p}$ (GPa)
0.47	1490	1000	260	1460	1.64	2	0.11	0.6	0.33	54

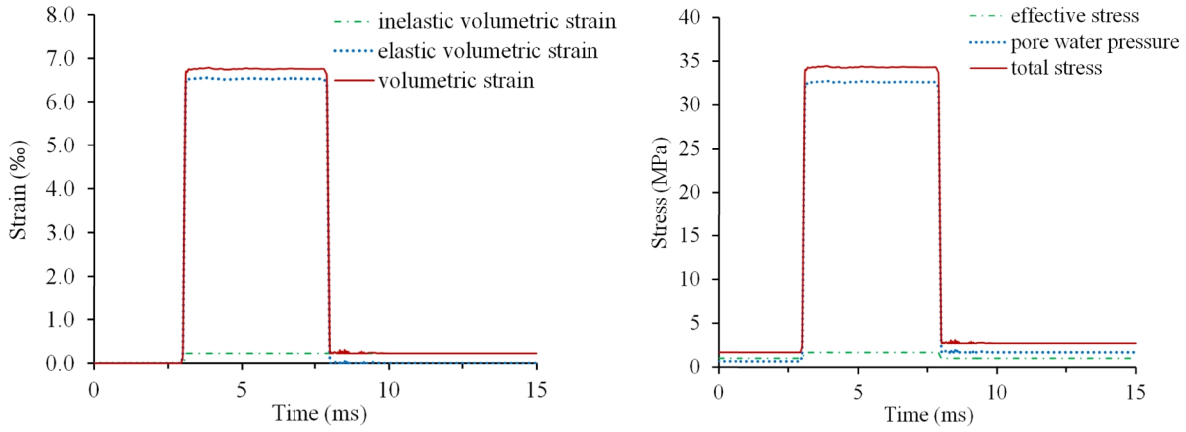

(a) (b)

Figure 5.25 Simulated loading histories of Case 1: (a) strain-time; (b) pressure-time

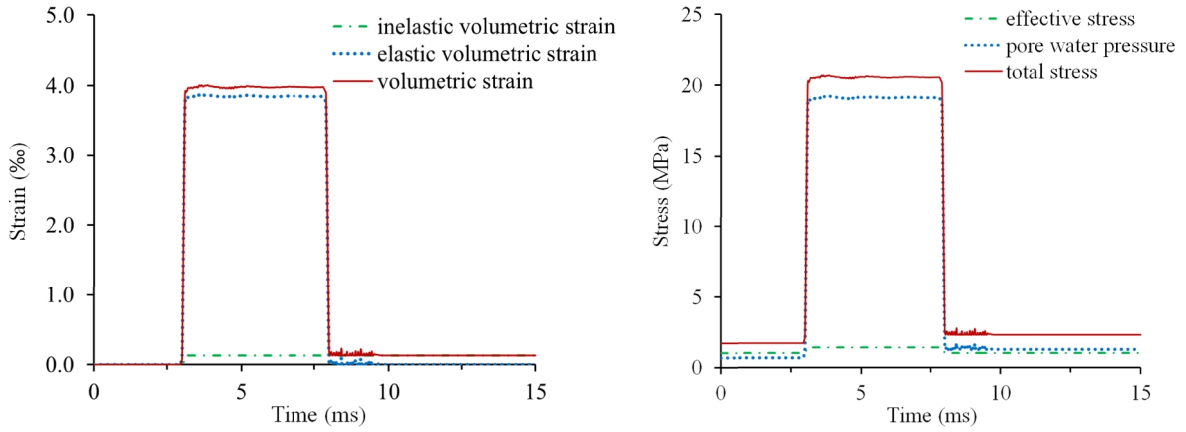

(a) (b)

Figure 5.26 Simulated loading histories of Case 2: (a) strain-time; (b) pressure-time

As can be observed from Figures 5.25 and 5.26, during initial loading, pore water has borne the majority of the external load due to its large stiffness, while the pressure in soil skeleton is insignificant by comparison. After unloading, the pore water pressure cannot return to its initial value, because the irrecoverable strain developed in the loading process (shown in Figures 5.25 (a) and 5.26(a)) has led to the generation of excess pore pressure. These processes captured by the model are in accordance with the mechanism of blast-induced liquefaction. Defining the residual excess pore pressure ratio (PPR) as the residual excess pore pressure divided by the initial effective stress, the simulated results can be summarized and compared with experimental data (Table 5.7). According to Table 5.7, good agreement is obtained between the results of

simulation and laboratory testing. Therefore, the modified viscoplastic cap model developed in the study can represent well the deformation mechanism of saturated soils under impact loading, and the pore pressure response in the undrained condition can also be reasonably captured.

Table 5.7 Comparison between simulated and experimental results for ramp loading tests on saturated sand

Test	Peak pore water pressure change (MPa)		Residual pore water pressure (MPa)		PPR	
	Tested	Simulated	Tested	Simulated	Tested	Simulated
Case 1	31.10	31.90	1.72	1.70	1	0.97
Case 2	16.38	18.40	1.30	1.29	0.59	0.58

5.3.3.3 Case Study 2: Laboratory shock loading on saturated sand and silt

A series of shock loading tests were performed on saturated Monterey sand and Bonny silt to examine the soil liquefaction by Charlie et al. (1985) and Bolton et al. (1994), and this experimental program is adopted to validate the model. During the test, soil samples with a height of 152.5 mm and a diameter of 68 mm were placed in a laterally fixed container. Then, axial shock compression was applied from the top of the sample with different amplitudes. The shock loading tests are simulated by using 2D symmetry, and the low-reflecting boundary is applied at the bottom of the model to avoid wave reflection. The shock loading pattern used in the simulation is determined from the monitored pressure time histories in the experimental tests, and it is a triangular pulse which rises to its peak and then reduces back to initial value both in half a millisecond. Two shock loading tests on sand and one test on silt in the experimental program are simulated in the study, and their peak pressures are listed in Table 5.8. The model parameters used in the simulation are obtained from experimental data in Bolton et al. (1994) and those used in Wang et al. (2008) for simulations of the tests, and they are listed in Tables 5.8 and 5.9. The simulated time histories of strain and pressure of a monitored point in the middle of the specimen are illustrated in Figures 5.27-5.29.

Table 5.8 Material properties used in the model for shock tests on saturated sand and silt

Test	Initial effective stress (MPa)	Initial pore water pressure (MPa)	Peak pressure (MPa)	Density (kg/m^3)	h (μsec^{-1})	N
Case 1 (sand)	0.172	0.35	5.04	1970	3.5×10^{-6}	1
Case 2 (sand)	0.172	0.35	7.39	1970	5.2×10^{-6}	1
Case 3 (silt)	0.172	0.35	2.66	1848	1.3×10^{-5}	1
f_0 (Pa)	a	k(MPa)	R	D (MPa^{-1})	W	X_0(MPa)
1×10^6	0.25	0	8	4×10^{-3}	0.0011	1
1×10^6	0.25	0	8	4×10^{-3}	0.0011	1
1×10^6	0.225	0	8	4×10^{-3}	0.0011	1

Table 5.9 Material properties used for undrained response of saturated sand and silt in shock tests

Test	n	r_{s0} (kg/m^3)	r_{w0} (kg/m^3)	C_{s0} (m/s)	C_{w0} (m/s)	s_s	s_w	g_{s0}	g_{w0}	$\underline{\nu}$	$\underline{K_p}$ (GPa)
Cases 1-2 (sand)	0.41	1563	1000	310	1460	1.64	2	0.11	0.6	0.33	54
Case 3 (silt)	0.48	1367	1000	221	1460	1.64	2	0.11	0.6	0.33	54

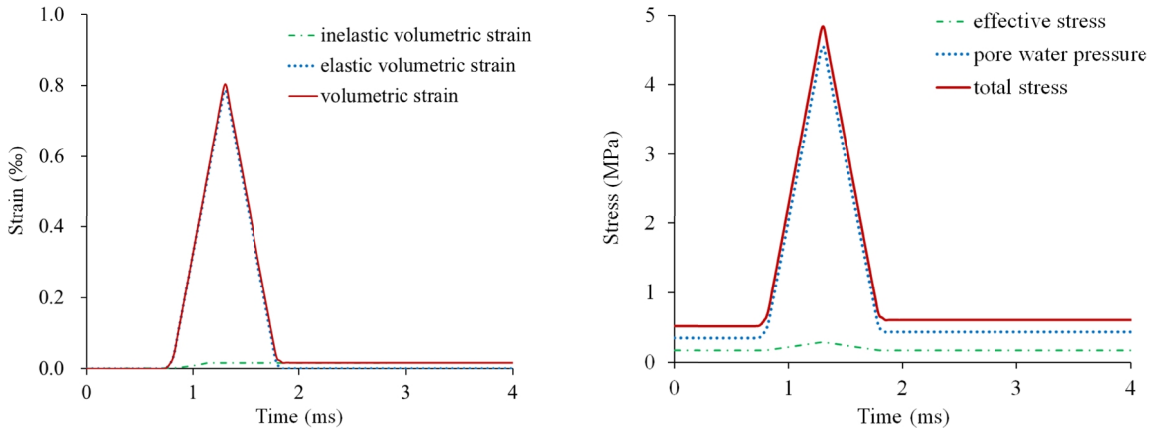

(a) (b)

Figure 5.27 Simulated loading histories of Case 1 (sand): (a) strain-time; (b) pressure-time

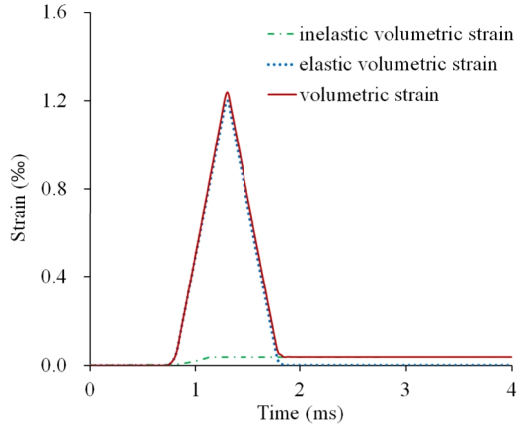

(a)

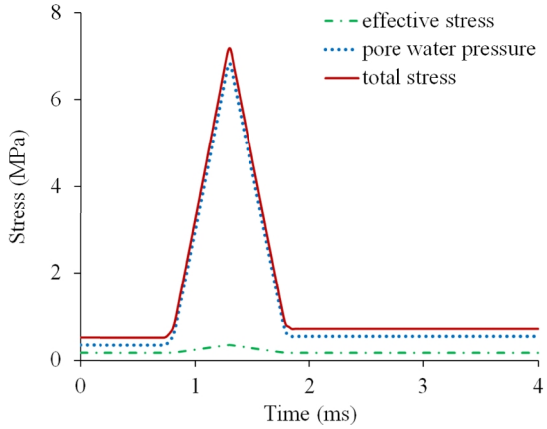

(b)

Figure 5.28 Simulated loading histories of Case 2 (sand): (a) strain-time; (b) pressure-time

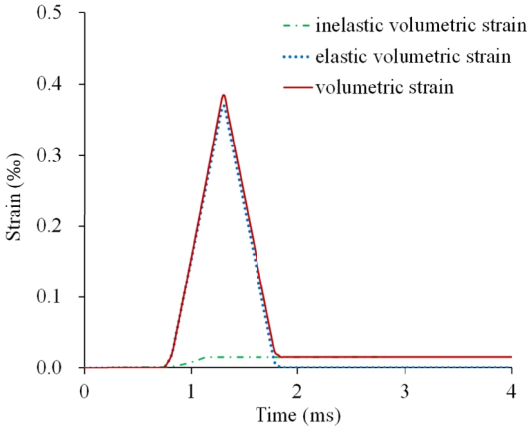

(a)

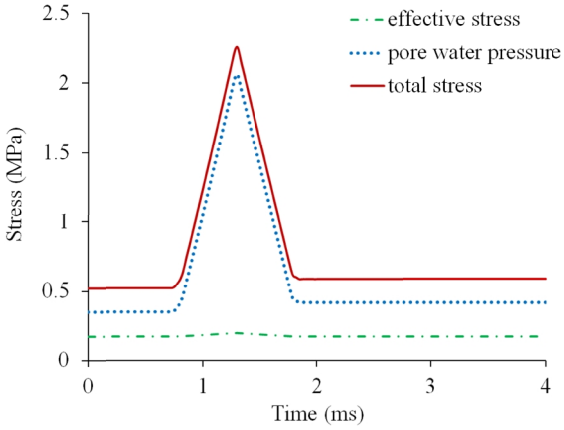

(b)

Figure 5.29 Simulated loading histories of Case 3 (silt): (a) strain-time; (b) pressure-time

According to Figures 5.27(b)-5.29(b), pore water also carries most of imposing loads compared with the soil skeleton during the shock loading tests. Besides, although the elastic strain could recover after the passage of shock wave, the pore water pressure is still above its initial value due to the irrecoverable volumetric strain developed during initial loading as indicated by Figures 5.27(a)-5.29(a). In other words, the volumetric hysteresis is responsible for the build-up of residual excess pore pressure. The simulated pore pressure response of saturated sand in the shock loading tests is compared with experimental data (Charlie et al., 1985) in Figure 5.30, while data for silt are not available. As can be concluded from Figure 5.30, there is also good agreement between simulated and test results in terms of the peak and residual values

as well as the trend of variation in pore pressure. Details of the three simulated shock loading tests are summarized in Table 5.10, and it is observed that they are also consistent with the experimental data. Therefore, the developed model is also capable of representing the deformation mechanism and pore pressure response of saturated sand and silt under shock loadings.

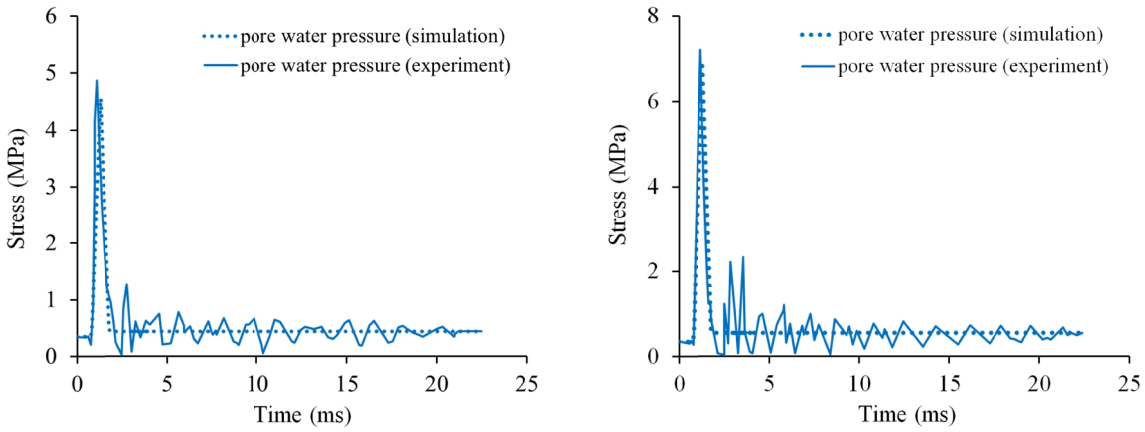

(a) (b)

Figure 5.30 Comparison between simulated and measured pore pressure response of sand in the shock tests: (a) Case 1; (b) Case 2

Table 5.10 Comparison between simulated and experimental results for shock tests on the saturated sand and silt

Test	Peak pore water pressure change (MPa)		Residual pore water pressure (kPa)		PPR	
	Tested	Simulated	Tested	Simulated	Tested	Simulated
Case 1 (sand)	4.52	4.20	436	437	0.50	0.51
Case 2 (sand)	6.87	6.50	548	547	1.15	1.14
Case 3 (silt)	2.13	1.81	415	417	0.38	0.39

5.3.3.4 Case Study 3: Liquefaction of saturated sand in field explosion test

A large scale explosion test on saturated sand reported in Bretz (1990) and is adopted and Charlie et al. (2013) reproduced in this section. The tested sand was placed in a container with 4.27 m in diameter and 1.83 m in height, and the explosive charge was detonated in water at a distance of 1.8 m above the surface of the sand. The configuration of the field test is shown in Figure 5.31.

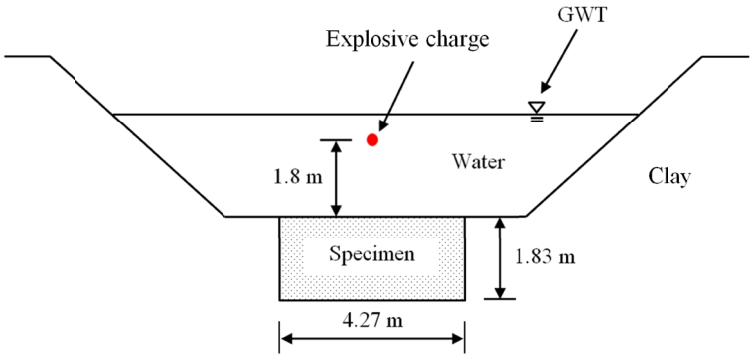

Figure 5.31 Cross section of the test site

The peak particle velocity (V_p, in m/s) of the sand caused by the spherical blast wave generated by the underwater explosion can be determined with the following expression developed for the test site (Charlie et al., 2013):

$$V_p = 12.3(R_c / Q^{1/3})^{-1.5} \tag{5.60}$$

where Q (kg) and R_c (m) are the weight of TNT charge used and the distance to the explosion, respectively. In the simulation, the time history of the incident wave that arrives at the sand surface is modelled with the following function modified from Jiang et al. (1995):

$$V(t) = V_0 t^{n_c} e^{-bt} \tag{5.61}$$

where $V_0 = V_p (b\,e / n_c)^{n_c}$ with peak velocity V_p obtained by Equation (5.60), and $V(t)$ takes this peak value at $t = n_c / b$ (Sainoki and Mitri, 2016); n_c and β are coefficients, and they are set as 1 and 6000, respectively, in this example based on the stress wave histories monitored in the field. The loading pattern represented by Equation (5.61) is illustrated in Figure 5.32. Then, the shock loading obtained by Equation (5.61) is applied on the surface of the sand with consideration for different distances to the explosion, and only the perpendicular component of the wave to the sand base is applied on the model.

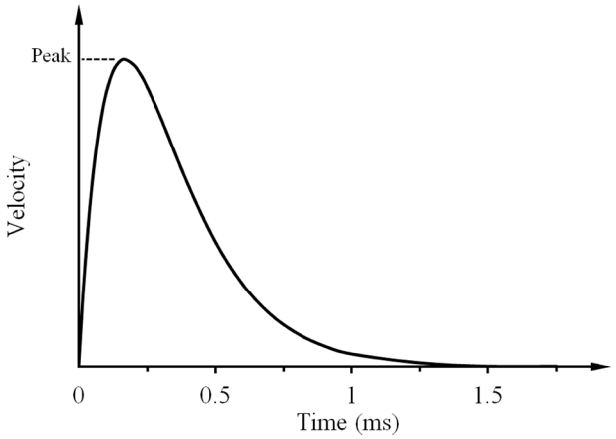

Figure 5.32 Loading pattern of the incident wave in the field explosion test

Field measurements have shown that the wave reflection at the boundaries of the container was negligible (Charlie et al., 2013). Therefore, low-reflecting boundaries are applied at the bottom and sides of the saturated sand specimen in the simulation, and the model is considered to be symmetrical. The sand properties used in the simulation are determined based on Wang et al. (2008) and Charlie et al. (2013), and they are listed in Tables 5.11 and 5.12. The weight of the explosive charge (TOVEX) used in the study is 0.76 kg, and it is equivalent to 0.68 kg of TNT (Charlie et al., 2013).

Table 5.11 Material properties used in the model for field explosion test on sand

Density (kg/m^3)	h (μsec^{-1})	N	f_0 (Pa)	a	k (MPa)	R	D (MPa^{-1})	W	X_0 (MPa)
2138	1.8×10^{-6}	1	1×10^{6}	0.25	0	8	4×10^{-4}	0.002	1

Table 5.12 Material properties used for undrained response of saturated sand in the field explosion test

n	r_{s0} (kg/m^3)	r_{w0} (kg/m^3)	C_{s0} (m/s)	C_{w0} (m/s)	s_s	s_w	g_{s0}	g_{w0}	$\underline{v}$	$\underline{K_p}$ (GPa)
0.31	1828	1000	287	1460	1.64	2	0.11	0.6	0.33	54

The simulated pore pressure histories at 0.22 m and 1.55 m beneath the sand surface on the vertical centre line of the container are compared with monitored data (Bretz, 1990) in Figure 5.33. It can be observed that the model is able to reasonably capture the propagation of shock

wave in the saturated sand, and both the peak value of pore pressure and the arrival time of the stress wave obtained from simulation agree well with test data.

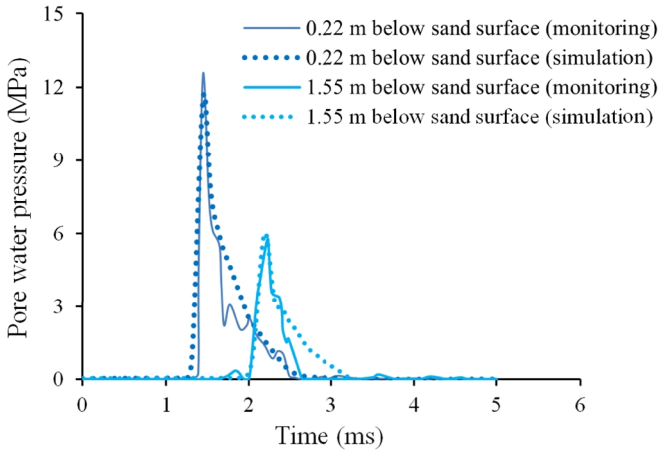

Figure 5.33 Comparison between simulated and monitored pore pressure in the field explosion test

According to residual excess pore pressure measurements at 1.7 m below the center of sand surface, the PPR for the explosion test is 0.99 at this location (Charlie et al., 2013). The simulated PPR by the model for the explosion test is illustrated in Figure 5.34 below, and it suggests that the saturated sand has been liquefied (PPR>=1) within 1.65 m from the center of sand surface in the vertical direction. Therefore, the model is also able to sufficiently characterize the blast wave propagation and the resulting liquefaction of sand in the field.

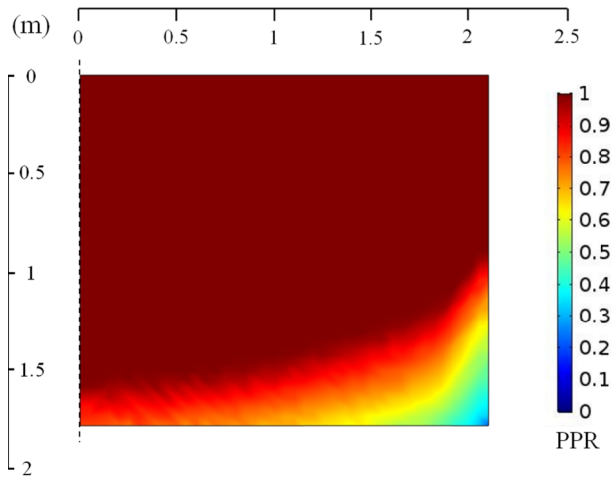

Figure 5.34 Simulated range of liquefaction after the blast loading

5.3.3.5 Case Study 4: Canadian Liquefaction Experiment (CANLEX) on tailings

The GSD of natural sand and silt used in previous validations are presented in Figure 5.35, and it can be observed that they could well represent the GSD spectrum of tailings in hydraulic backfills (HB), paste backfills (PB) and those from tailings impoundments, which are the most common types of fill mass. This implies that the present model can also be applied to capture the blast-induced liquefaction of those man-made soils. Therefore, the field explosion test performed on a saturated tailings deposit in the CANLEX program (Al-Qasimi et al., 2005) is adopted and simulated with the model, and the GSD of tailing in this program is also shown in Figure 5.35.

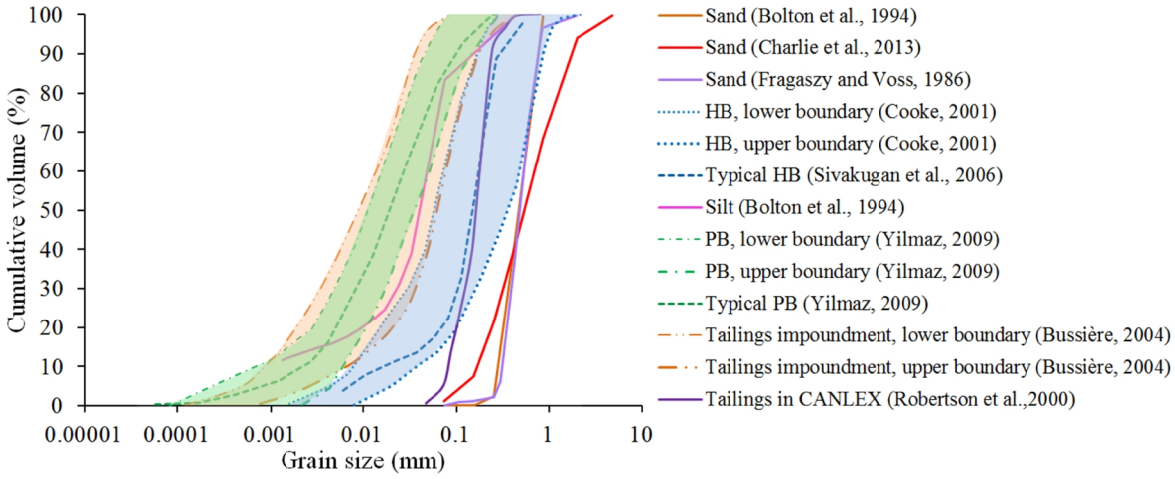

Figure 5.35 Comparison of GSDs of natural sand and silt with those of typical tailings

To examine blast-induced ground motion and pore pressure of saturated tailings, tailings were filled at the test site. The tailings deposit has a thickness of 10 m, and the groundwater is 0.5 below the ground surface (Al-Qasimi et al., 2005).

To avoid extrapolation of data obtained from the field experiments, the simulated range of the model is determined as 5.5 m to 18 m from the explosion of 1.5 kg charge, so that the comparison of site response is possible while the effect of boundary condition is negligible.

The configuration of the model is shown in Figure 5.36. The peak particle velocity of incident shock wave that arrives at the model boundary is determined by the following expression developed for the test site (Al-Qasimi et al., 2005):

$$V_p = 47.64\,[R_c / Q^{1/3}]^{-2.34} \tag{5.62}$$

The time-varying pattern of the incident wave is assumed to be the same as Case Study 3 with peak velocity obtained by Equation (5.62), and the positional relationship between locations on the model boundary and the charge is considered, while only normal component of the wave to the boundary is applied on the model.

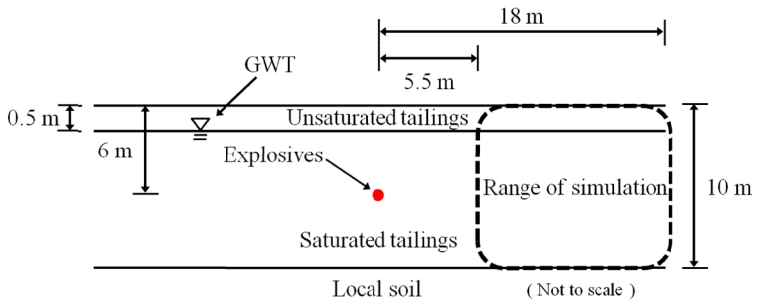

Figure 5.36 Configuration of the model for explosion in the tailings deposit

The simulation of the test is considered symmetrical. Low-reflecting boundaries are applied at the bottom and far end of the model, and a constant stress is applied on the top to represent the overburden. The material properties used in the simulation are determined from studies on the tested tailings by Puebla et al. (1997), Robertson et al. (2000) and Al-Qasimi et al. (2005), and they are listed in Tables 5.13 and 5.14.

Table 5.13 Material properties used in the model for field explosion test on tailings

Density (kg/m^3)	h (μsec^{-1})	N	f_0 (Pa)	a	k (MPa)	R	D (MPa^{-1})	W	X_0 (MPa)
1950	1.5×10^{-5}	1	1×10^{6}	0.18	0	8	1×10^{-2}	0.001	1

Table 5.14 Material properties used for undrained response of tailings in the field explosion test

n	r_{s0} (kg/m^3)	r_{w0} (kg/m^3)	C_{s0} (m/s)	C_{w0} (m/s)	s_s	s_w	g_{s0}	g_{w0}	$\underline{v}$	$\underline{K_p}$ (GPa)
0.43	1493	1000	219	1460	1.64	2	0.11	0.6	0.3	54

The comparison between the simulated attenuation of peak particle velocity (PPV) and peak pore water pressure against scaled distance with test data is presented in Figure 5.37. As can be observed, the simulated results are consistent with data obtained from the field test in both the magnitudes and trends of variation. Meanwhile, based on the empirical law for estimating the range of liquefaction developed for the test site (Al-Qasimi et al., 2005), tailings within 6.6 m from the explosion at the buried depth of the charge (6 m in this case) has been liquefied. The simulated area of liquefaction by the model after the blast is shown in Figure 5.38(a), and it indicates that the deposit is liquefied within 6.3 m from the explosion at the same depth. The simulated variation of PPR against scaled distance at this depth is presented in Figure 5.38 (b), and it also agrees reasonably well with the empirical law for the tested material. Therefore, it is confirmed that the model is also capable of capturing the wave propagation and liquefaction due to blasts in saturated tailings fill mass.

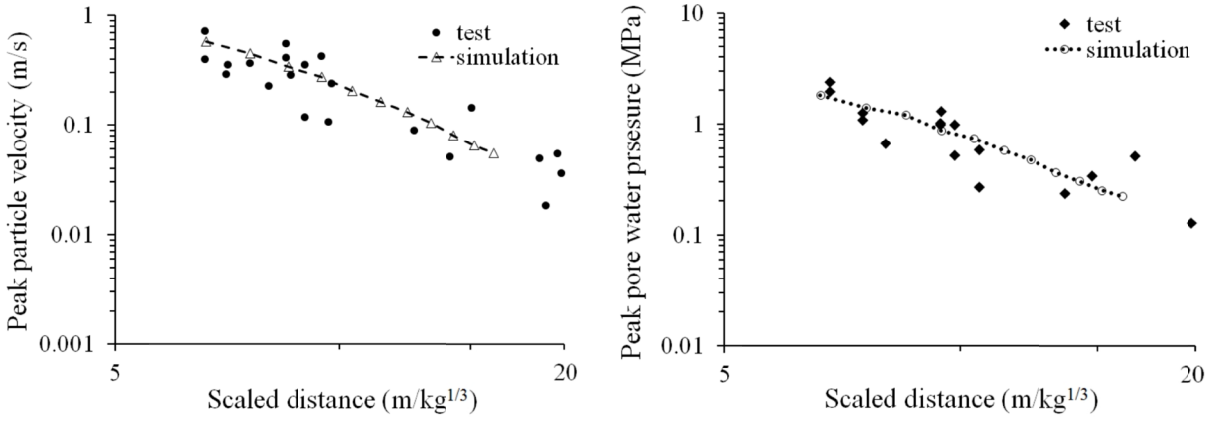

(a) (b)

Figure 5.37 Comparison between simulated and measured attenuation of blast wave: (a) attenuation of PPV; (b) attenuation of peak pore water pressure

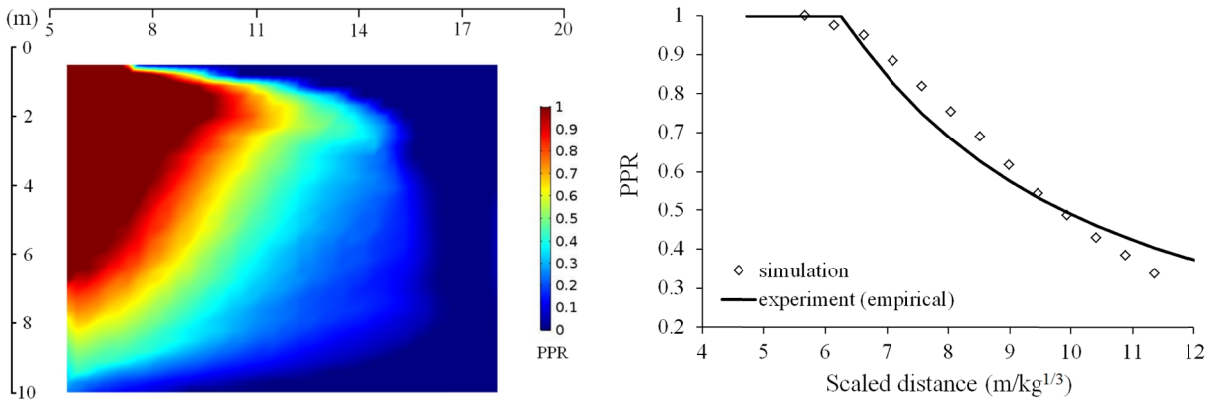

(a) (b)

Figure 5.38 Comparison between simulated and monitored liquefaction after the explosion: (a) simulated range of liquefaction; (b) attenuation of PPR

5.3.4 Analysis of liquefaction susceptibility of subsurface tailings backfill mass at early ages

5.3.4.1 Modelling configuration

After validation of the model by excellent agreement between simulated and measured material response in peak velocity and pore pressure as well as PPR, it is applied to various practical engineering applications with respect to tailings backfill in this section. Specifically, the effects of drainage condition, proximity of detonation, stope size, location of barricade and blast sequence on liquefaction susceptibility of tailings backfill mass are investigated. Detailed scenarios for these factors to be studied are listed in Table 5.15 below. The parameters used and characteristic liquefaction behaviour of tailings backfills represented by the model are the same as for the CANLEX program (Section 5.3.3.5), and they are the basis for numerical analysis of liquefaction susceptibility of the fill mass in varied conditions. A two-dimensional model is established to represent the field condition, and the configuration of the model is illustrated in Figure 5.39.

Table 5.15 Conditions of fill mass examined in the study

Case No.	Drainage condition (K_b /K_T *)	Distance between charge and stope (m)	Stope size (W×H, m)	Distance of barricade to stope (m)	Number of blasts
1	0.5	40	10×25	4	1
2	0.125	40	10×25	4	1
3	undrained	40	10×25	4	1
4	0.5	20	10×25	4	1
5	0.5	30	10×25	4	1
6	0.5	30	10×35	4	1
7	0.5	30	10×45	4	1
8	0.5	40	10×25	7	1
9	0.5	40	10×25	10	1
10	0.5	40	10×25	4	2
11	0.5	40	10×25	4	3

*: K_b and K_T represents hydraulic conductivity of the barricade and fill mass, respectively.

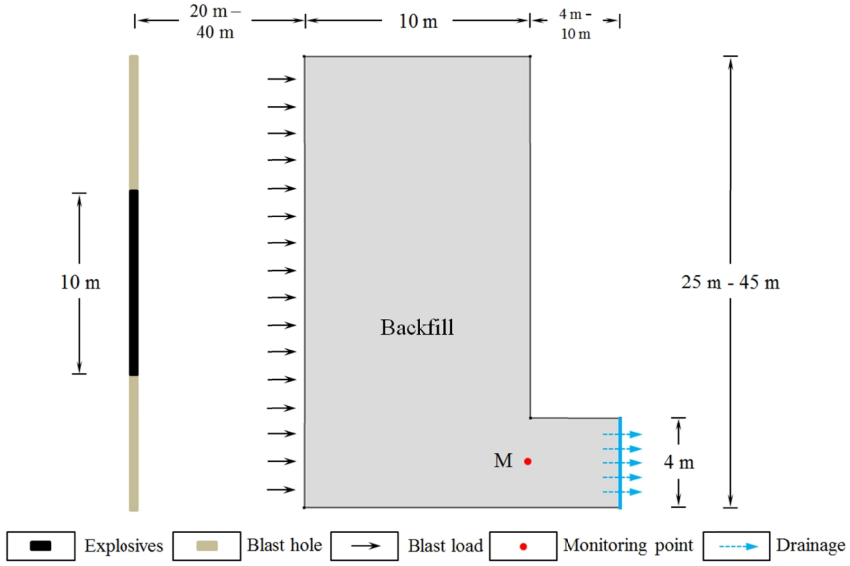

Figure 5.39 Configuration of the numerical model

Drainage of the fill mass is allowed from the barricade constructed in the access tunnel (drawpoint) at the bottom of the stope, and the rate of flow (q) through the barricade is characterized with Darcy's law as:

$$q = -\mathbf{k}\frac{k_{rw}}{m_w}\nabla\left(P_w - r_w g\right) \tag{5.63}$$

where $\mathbf{k}$ is the intrinsic permeability tensor of the medium, k_{rw} denotes the relative permeability, and m_w stands for the fluid dynamic viscosity. The intrinsic permeability of the material k_w can

be related to the hydraulic conductivity K_w by $k_w = K_w m_w / r_w g$. To evaluate the variation of k_{rw}, the following constitutive relations from the van Genuchten (1980) model is adopted:

$$\begin{cases} k_{rw} = \sqrt{S_{eff}}\left[1-\left(1-S_{eff}^{1/m}\right)^m\right]^2 \\ S_{eff} = \dfrac{1}{\left\{1+\left[a(P_a-P_w)\right]^{\frac{1}{1-m}}\right\}^m} \end{cases} \tag{5.64}$$

where P_a is assumed to be atmospheric pressure, and model constants m and a for the fill mass are 0.386 and 2.58×10^{-3} cm^{-1} based on experimental data on tailings with similar physical properties found in Aubertin et al. (1997). The hydraulic conductivity of tailings backfill (K_T) is 5×10^{-5} cm/s according to the work of Puebla et al. (1997) on the same material. The mechanical behaviour of the fill mass before and after blasting is characterized by Mohr-Coulomb model in accordance with Fahey et al. (2009) and it is coupled with the fluid flow in the process, the mechanical properties are determined from Tables 5.13-5.14.

In the numerical analysis, the initial pore pressure and effective stress distribution after continuous filling at the same rate (12.5 m/d) is obtained at first from its coupled stress-flow response, and drainage is allowed during the placement of saturated fill mass except for Case 3. Then, the shock wave is applied on the model boundary, and its time-varying pattern is same as Figure 5.32. As production blasts in mines are generally conducted in multiple lifts, an explosive column with a length of 10 m and a linear charge density of 6.22 kg/m (van Gool, 2007) is considered in the study, and its center is assumed to coincide with the mid-height of the stope. To determine the amplitude of shock wave that propagates through rock and arrives at the stope boundary, the following equation is adopted (Holmberg and Persson, 1979; Ahmed and Ansell, 2014):

$$V_p = A[R_c / (f_1 Q)^b]^{-a} \tag{5.65}$$

where constants A, a, and b are 2.94 m/s, 1.32 and 0.66, respectively, based on PPV monitoring in the rock of Cannington mine in Australia (van Gool, 2007); and f_1 is a factor that accounts for the effect of long explosive charges defined as $f_1 = [\arctan(L_c / 2R_c)] / (L_c / 2R_c)$, and L_c is the charge length. By considering the positional relationship between locations on the stope wall and the charge, normal components of shock waves with amplitudes obtained by Equation (5.65) are applied on the model boundary.

A low-reflecting boundary is applied at the far end of the model to avoid wave reflection, and the bottom of the fill mass is set as a roller, while the top is set as a free boundary. After the passage of blast wave, the pore pressure of backfill is the sum of initial pore pressure before blasting and excess pore pressure caused by the shock wave. Then, the dissipation of pore pressure in the stope due to drainage is monitored, and the variation of liquefaction susceptibility of the fill mass is evaluated in the process in terms of PPR, defined as residual excess pore pressure over initial vertical effective stress before blasting in accordance with Pépin et al. (2012) and Al-Qasimi et al. (2005). As the location of barricade varies in practice, a monitoring point (M) is set at the joint of the stope and drawpoint with 2 m above the floor. The change of pore pressure due to water consumption by cement hydration during this early age is not considered as discussed earlier. This is a conservative assumption with respect to liquefaction potential of the tailings backfill structure. The results obtained from the numerical analysis on liquefaction susceptibility of the fill mass in different backfilling and field conditions are presented and discussed in the following sections.

5.3.4.2 Effect of drainage conditions

Drainage conditions of fill mass will significantly affect the rate of pore pressure dissipation. Therefore, the influence of drainage (through barricades) on the liquefaction susceptibility of backfill mass is examined in the study. Note that the inclusion of drainage will affect both the build-up and dissipation of excess pore pressure for cyclic loading (Pépin et al., 2012). However, due to the short duration of shock wave, the blast loading process is undrained (Wang et al., 2008). Therefore, the effect of drainage refers to its influence on pore pressure dissipation before and after blast loading in the study.

The use of a plane model would represent a drawpoint extending full length of the long side (perpendicular to the plane) of the stope. Therefore, the hydraulic conductivity of barricade (K_b) for a 2D condition should be determined by reducing that of fill mass (K_T) by the ratio of side length of the stope to the drawpoint (Fahey et al., 2009; Helinski et al., 2010). This reduction ratio is set to be 2 for Case 1 (K_b=0.5K_T) while it is 8 for Case 2 (K_b=0.125K_T), i.e., the side length of barricade in Case 1 is four times of that in Case 2. The drainage of water from the barricade is precluded for Case 3, and this undrained condition of a backfill would indeed prevail in the field when it has low rate of consolidation, even when the drainage facility is constructed

(Fahey et al., 2009). The distribution of PPR for Cases 1-3 with different times of draining after passage of blast waves is illustrated in Figures 5.40-5.42. These figures show that regardless of the drainage conditions, the liquefied backfill zones (PPR>=1) are mostly limited to the upper parts of the backfill masses.

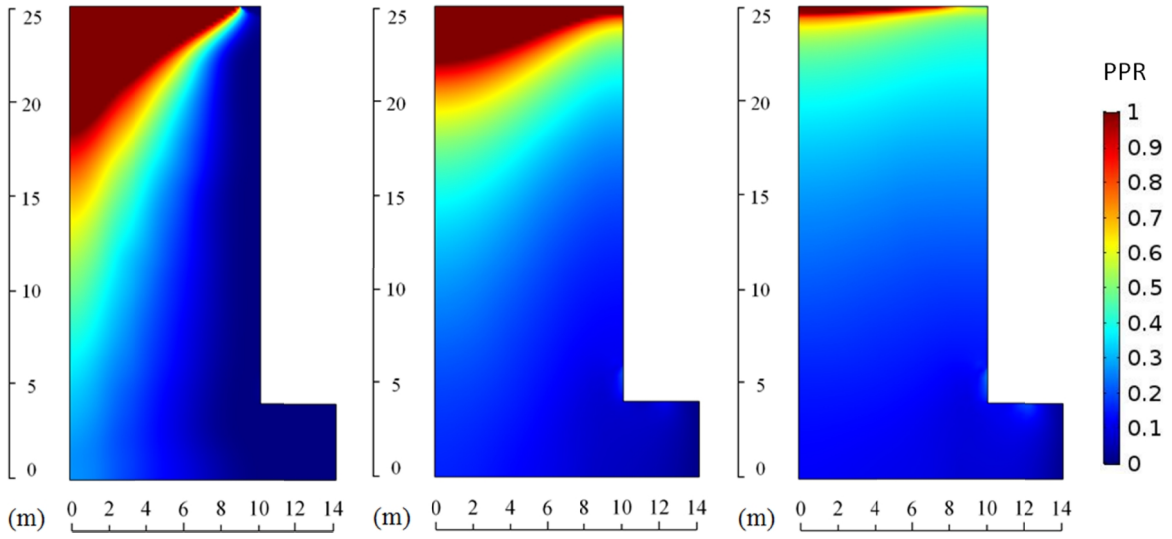

Figure 5.40 Variation of PPR for Case 1 (K_b=0.5K_T): time after blasting: (a) 0h; (b) 0.5h; (c) 1.5h

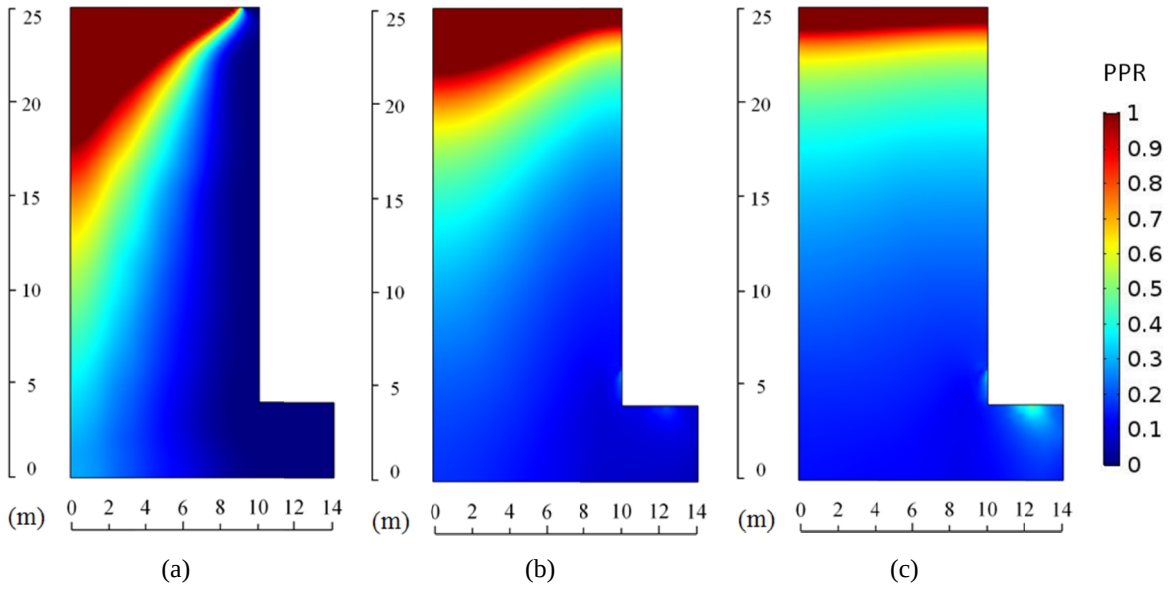

Figure 5.41 Variation of PPR for Case 2 (K_b=0.125K_T): time after blasting: (a) 0h; (b) 0.5h; (c) 1.5h

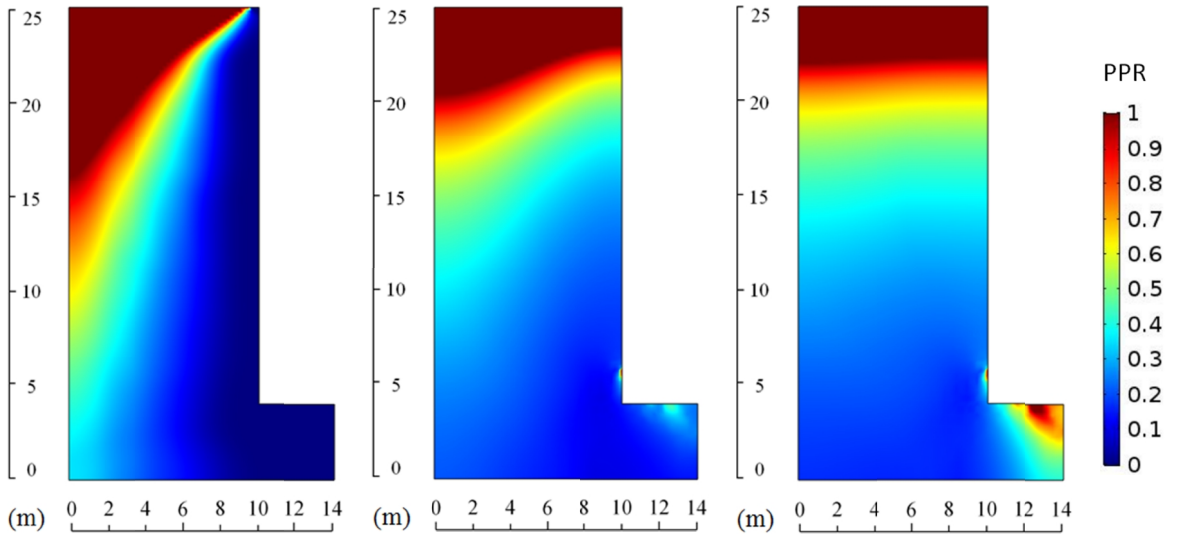

(a) (b) (c)

Figure 5.42 Variation of PPR for Case 3 (undrained condition): time after blasting: (a) 0h; (b) 0.5h; (c) 1.5h

Since the length of permeable barricade in Case 1 (K_b=0.5K_T) is 4 times of that in Case 2 (K_b=0.125K_T), higher initial effective stress can be developed for Case 1 when the filling is completed due to faster rate of drainage. Therefore, it is observed that the depth of liquefied backfill close to the loading boundary is smaller in Case 1 (6.6m) than Case 2 (7.2m) right after the passage of blast wave. Moreover, Case 1 has also exhibited smaller ranges of liquefaction at two other time grids examined, attributed to the more effective drainage of water as well, and there is almost no liquefaction in the stope at 1.5 hour after the blast. As for Case 3 (undrained conditions), with the exclusion of drainage, it has the largest liquefaction zone in the stope at all times compared with its counterparts, which is 8.9 m in depth at the loading boundary after the blast. Moreover, relatively high PPR value is also observed in access tunnel in undrained conditions.

The variation in PPR of the monitoring point M at the joint of stope and drawpoint after the blast is illustrated in Figure 5.43. It is also shown that the monitoring point in Case 1 has the lowest PPR as well as fastest pore pressure dissipation due to the enhanced drainage. Moreover, the depicted variation of PPR has reflected two mechanisms that are affecting the change of pore pressure and the associated liquefaction susceptibility of a backfilled stope. To be more specific,

the redistribution of pore pressure starts right after blast loading, and this process would continue until equilibrium is reached within the fill mass in the absence of drainage (Case 3). However, if a permeable barricade is used, the PPR at the monitoring point would increase at first due to redistribution of pore pressure, then, the effect of drainage would subsequently prevail and the PPR starts to decrease. Furthermore, with more effective drainage as is in Case 1 (four times faster than Case 2), the increase of PPR becomes less significant and it can reduce to zero more rapidly.

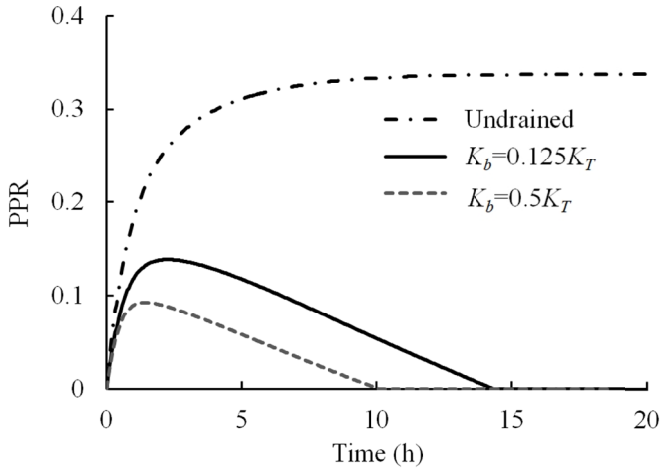

Figure 5.43 Variation of PPR at monitoring point for Cases 1-3 (Case 1: K_b=0.5K_T; Case 2: K_b=0.125K_T; Case 3: undrained)

The discussed variation of liquefaction susceptibility in Figure 5.43 can also be observed from Figures 5.40-5.42. As shown in Figure 5.42 (undrained, Case 3), the depth of liquefied backfill gradually decreases with time near the loading boundary, while it would increase on the other side of the stope due to the redistribution of pore pressure. This is because the excess pore pressure has accumulated near the loading boundary right after the blast, and it would dissipate towards the opposite end of the stope until equilibrium is obtained. With the inclusion of drainage (Figures 5.40-5.41), the pore pressure will dissipate along with its redistribution, and the range of liquefied backfill would decrease from the bottom upwards.

The simulation results presented above indicate that the drainage condition (through barricades) of backfill mass has a tremendous influence on its liquefaction resistance after mine blasts. More effective drainage by means, such as extending the side length of the drawpoint (thus the barricade) would lead to less range of liquefaction as well as faster dissipation of excess

pore pressure generated by dynamic loadings. Thus, the actual drainage condition of fill mass should be verified in the field in order not to underestimate the pore pressure distribution in the stope after dynamic loadings.

5.3.4.3 Effect of proximity of detonation

As underground mining divides the orebody into separate stopes, production blasts may be operated at different distances (D_c) from a given backfilled stope. Therefore, the effect of proximity of fill mass to explosive charge is examined, and the simulated variation of PPR at the monitoring point M after the blast for a stope located at 20 m (Case 4), 30 m (Case 5) and 40 m (Case 1) horizontal distances from the charge is presented Figure 5.44.

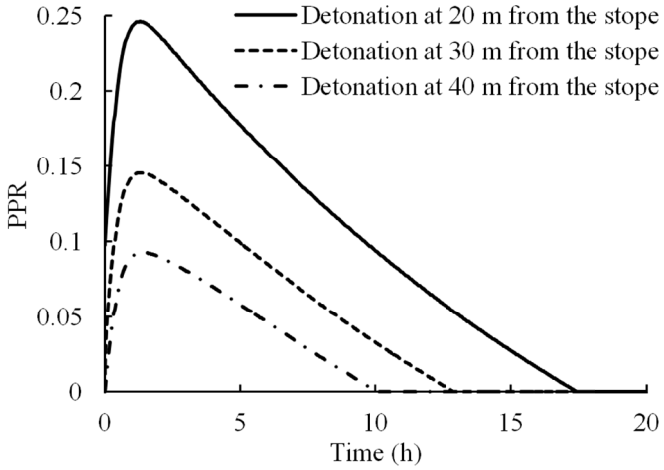

Figure 5.44 Variation of PPR at the monitoring point M for a stope located at 20 m (Case 4), 30 m (Case 5) and 40 m (Case 1) from the detonation

It can be observed that both the initial and peak PPR of the point would increase as the blast is conducted closer to the stope. This is because the PPV would increase sharply with decreased distance to the detonation (van Gool, 2007), and the increased intensity of vibration could in turn result in higher liquefaction potential due to the correlation between PPV and PPR (Al-Qasimi et al., 2005). Moreover, the higher excess pore pressure caused by more intensive loading in Case 4 (D_c=20m) has resulted in a longer time for PPR to vanish at the point, despite it would have a faster rate of draining. From these results, it can be concluded that mine blasting operation in the vicinity of freshly backfilled stopes is disadvantageous with respect to

liquefaction resistance of backfill mass, and it will not only result in higher liquefaction potential of the backfill mass, but also longer time for excess pore pressure to vanish. Therefore, securing the detonations outside of a certain range from early-age fill mass is suitable for keeping the liquefaction potential of the backfill mass at low level.

5.3.4.4 Effect of stope size

The size of stope varies in the field due to the irregularity of ore bodies as well as strategies used in mine planning. Stope size will influence the pore pressure and effective stress distribution within a fill mass, and thus affect its liquefaction susceptibility. The effect of stope size is examined in the study, and the simulated distribution of PPR for a stope with 25m (Case 5), 35m (Case 6) and 45m (Case 7) in height (H), respectively, with different times of drainage after blasting is presented in Figures 5.45-5.47.

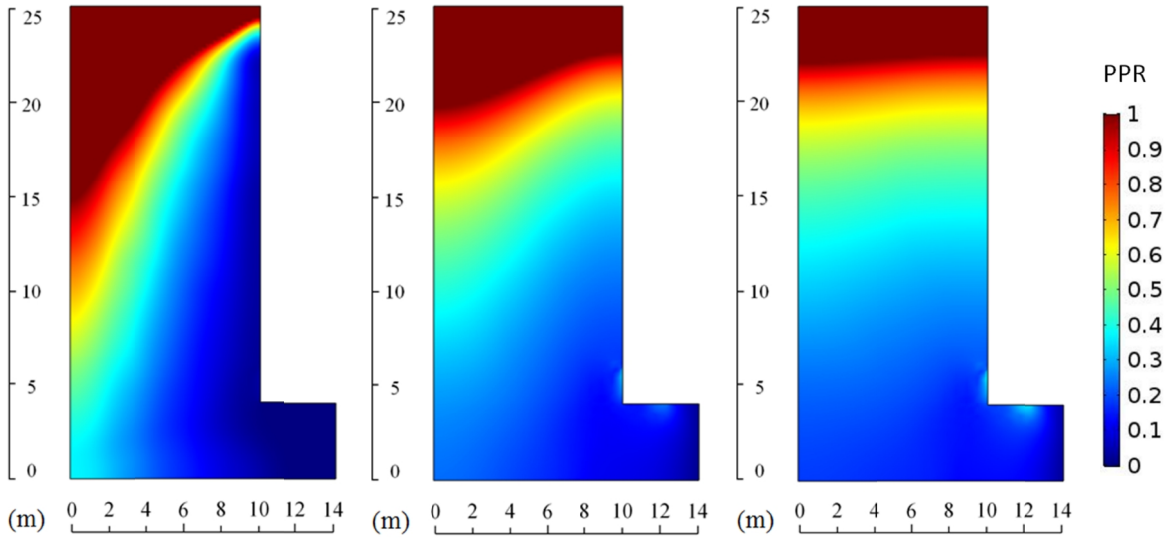

(a) (b) (c)

Figure 5.45 Variation of PPR for Case 5 (H=25m): time after blasting: (a) 0h; (b) 0.5h; (c) 1.5h

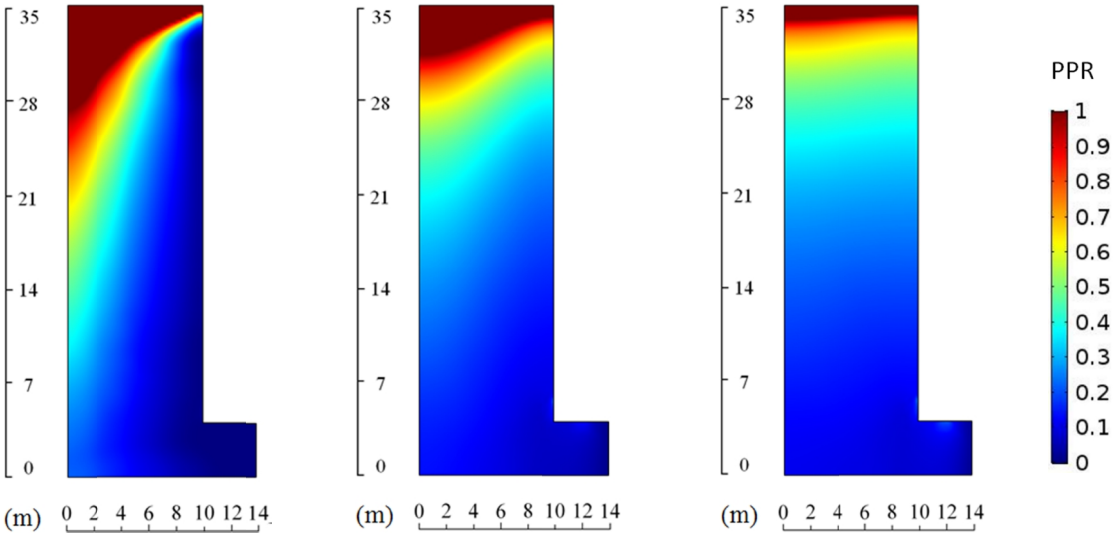

(a) (b) (c)

Figure 5.46 Variation of PPR for Case 6 (H=35m): time after blasting: (a) 0h; (b) 0.5h; (c) 1.5h

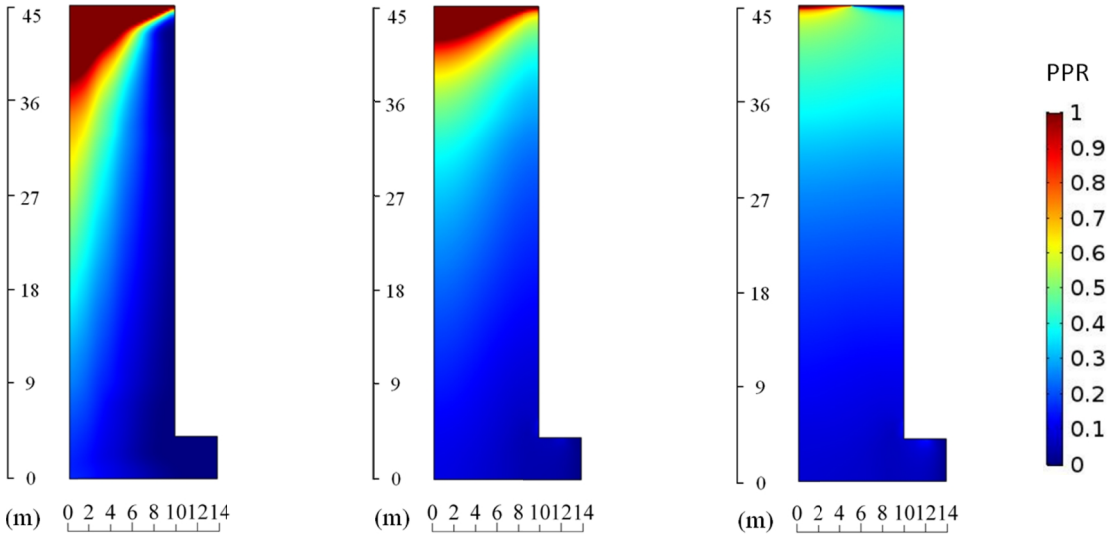

(a) (b) (c)

Figure 5.47 Variation of PPR for Case 7 (H=45m): time after blasting: (a) 0h; (b) 0.5h; (c) 1.5h

It is observed that the initial depth of liquefaction at the loading boundary after blasting is decreased as the height of the backfill mass increases. This is because a higher backfilled stope would imply larger pore pressure exerting on the barricade, thus lead to more rapid drainage of water (Equation 5.63), and higher effective stress can be developed at the same depth. Besides, with the same length and location of the charge, a larger stope height would require a longer

distance for the blast wave to travel and reach the top of the stope, thus the PPV at the upper part of the stope would consequently decrease (Equation 5.65). As a result, the range of liquefied zones within the backfill mass is always smaller in higher backfilled stopes at all times examined.

The variation of PPR at monitoring point for Cases 5-7 is illustrated in Figure 5.48. It can be seen that the peak PPR of the point would decrease with height of the stope. However, for higher stopes, more energy is absorbed in the fill mass due to increased surface (boundary) subjected to blast loading. Therefore, more excess pore pressure needs to be dissipated for a higher backfilled stope through the barricade of the same size in this condition. Consequently, although water can be drained in a faster rate for a stope with larger height, PPR of point M would in fact reduce more slowly and drop to zero after a longer period for a higher stope due to the excessive supply of excess pore pressure, while its peak PPR value is smaller.

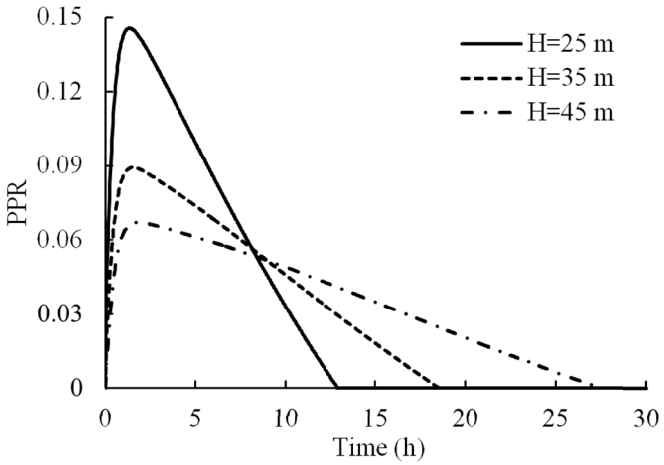

Figure 5.48 Variation of PPR at monitoring point for Cases 5 (H = 25m), 6 (H = 35m) and 7 (H = 45m)

Therefore, an increase in the height of a stope can diminish the range of blast-induced liquefaction. Besides, despite a longer time is required to dissipate the excess pore pressure in higher stopes due to increased boundary area subjected to blasting, the entire process can be indeed operated at lower risk of liquefaction. However, a higher backfilled stope would also increase the horizontal stress acting on the barricade due to self-weight of the fill mass, and thus reduce the stability of the retaining structure. Thus, the horizontal stress on the barricade induced

by the fill mass should also be considered, so that the liquefaction susceptibility of the backfill is minimized while the stability of the retaining structure can be ensured.

5.3.4.5 Effect of location of the barricade

The location of barricade in the access tunnel varies in the field due to different mine planning, and it will affect the drainage of fill mass. Therefore, Cases 1, 8 and 9 with a barricade located at a distance (D_b) of 4m, 7m and 10m away from the joint of stope and drawpoint, respectively, are examined in the study.

The variation of PPR distribution for Cases 1 (D_b=4m), 8 (D_b=7m) and 9 (D_b=10m) is depicted in Figures 5.40, 5.49 and 5.50. It can be noticed that the initial depth of liquefaction after the blast at the loading boundary decreases as the aforementioned distance increases. This is because the increase in the length of flow path to the drainage point would decrease the efficiency of pore pressure dissipation in the stope, thus result in a lower initial effective stress after the filling is completed. The extended flow path is also responsible for slightly larger depth of liquefaction at 0.5h and 1.5h after the blast in Case 9.

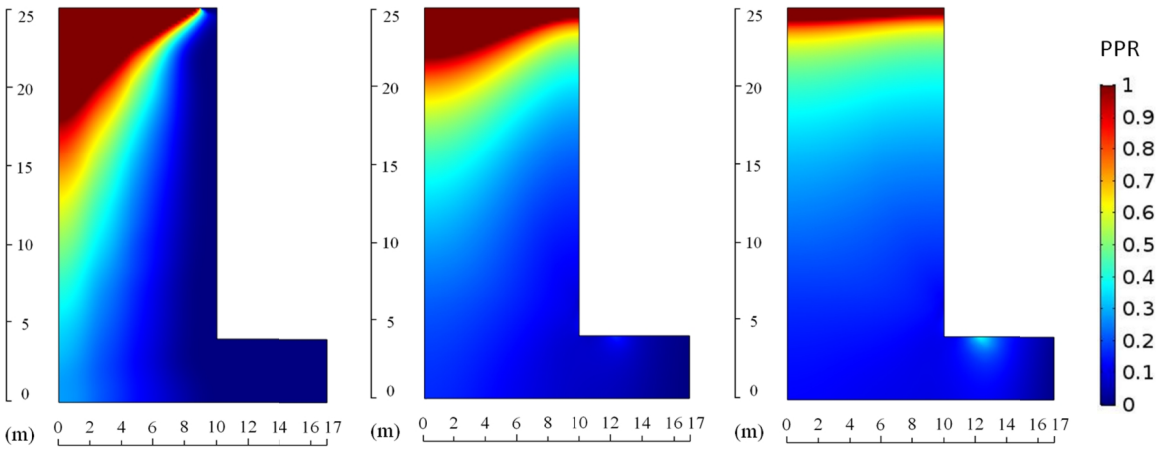

(a) (b) (c)

Figure 5.49 Variation of PPR for Case 8 (D_b=7m): time after blasting: (a) 0h; (b) 0.5h; (c) 1.5h

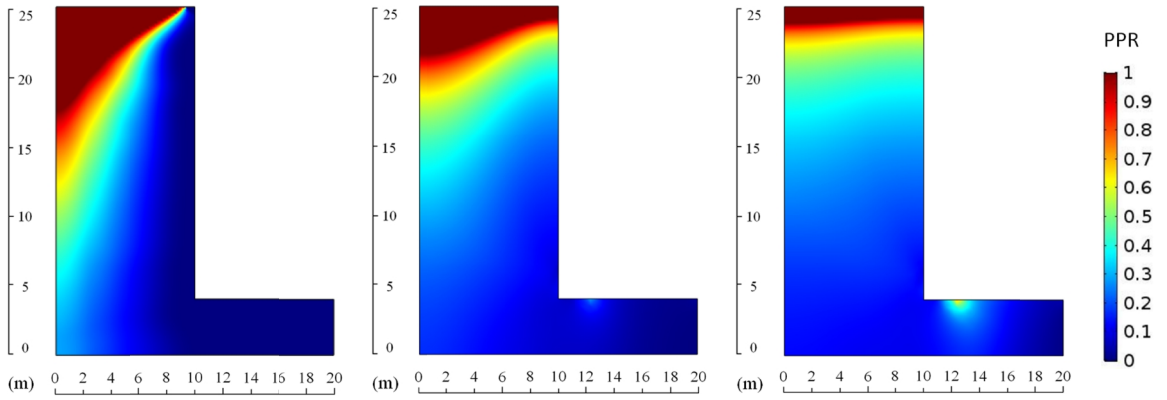

Figure 5.50 Variation of PPR for Case 9 (D_b=10m): time after blasting: (a) 0h; (b) 0.5h; (c) 1.5h

The influence of extended flow path is more clearly demonstrated by the PPR variation at the monitored point M as shown in Figure 5.51. As can be observed, when the barricade is located closer to the stope, more efficient drainage of fill mass can be facilitated and it is associated with lower peak PPR after blast loading. Meanwhile, the excess pore pressure can also be dissipated much more rapidly at the point when the barricade is closer to the stope.

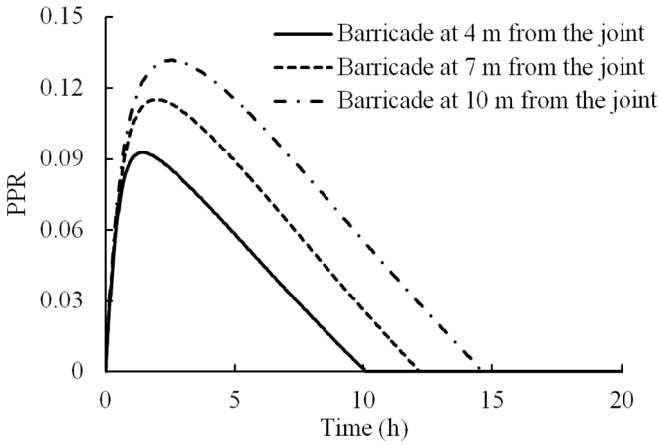

Figure 5.51 Variation of PPR at monitoring point for Cases 1 (D_b=4m), 8 (D_b=7m) and 9 (D_b=10m)

However, as blast wave propagates, its amplitude gradually attenuates and the generated excess pore pressure would decrease with distance to the charge (Al-Qasimi et al., 2005; Charlie et al., 2013). In other words, a barricade constructed closer to the stope is subjected to higher

peak stress and excess pore pressure induced by the blast wave. Therefore, although shortening the flow path can mitigate the liquefaction susceptibility of fill mass by reducing the PPR as well as time required to dissipate excess pore pressure, it may be indeed at the cost of decreasing the stability of the retaining structure. To determine the optimal location of the retaining structure, more studies on its interaction with dynamic loads are required.

5.3.4.6 Effect of blast sequences

Multiple explosive columns are conventional used for extraction of separated remnant ore pillars in mines, and thus the fill mass is subjected to multiple blast sequences. The effect of blast loading sequences is examined in the study. Specifically, one, two and three blasts (Case 1, 10 and 11, respectively) with the same peak pressure and time-varying pattern are applied on the model with 2.5 ms delay between each impact.

The distribution of PPR for Cases 1 (1 blast sequence), 10 (2 blast sequences) and 11 (3 blast sequences) after 1.5 hour of drainage time is presented in Figure 5.52. It is shown that the range of liquefaction increases significantly with additional blast impacts in the stope after the blast. With the same initial condition, the differences are solely attributed to the extra excess pore pressure induced by more number of blasts. In fact, field tests have also shown that multiple blasts could cause liquefaction at lower cumulative PPV than single detonation, and the PPV required for liquefaction decreases with increasing number of detonations (Al-Qasimi et al., 2005, Bretz, 1990). However, Figure 5.52 shows that the liquefied zones are limited to the upper part of the studied backfill mass as evidenced by the results presented in Figure 5.53. This figure illustrates the comparison of the variation of PPR at the monitoring point M for Cases 1, 10 and 11. It can be observed that regardless of the number of loading sequences the PPR value is smaller than 1, which suggests that no liquefaction has occurred at this point. It is also observed that the peak PPR increases with the number of impacts. Besides, it takes the longest time for PPR of the point in Case 11 (3 blasts) to vanish due to the excessive supply of excess pore pressure.

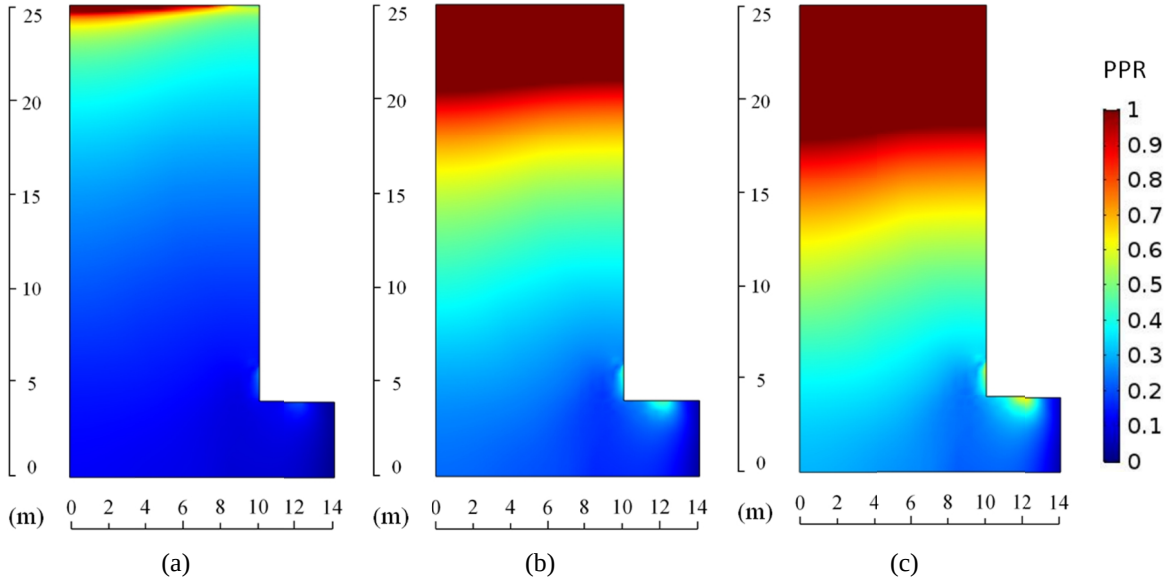

Figure 5.52 Distribution of PPR at 1.5h after blasting: (a) Case 1 (1 blast); (b) Case 10 (2 blasts); and (c) Case 11 (3 blasts)

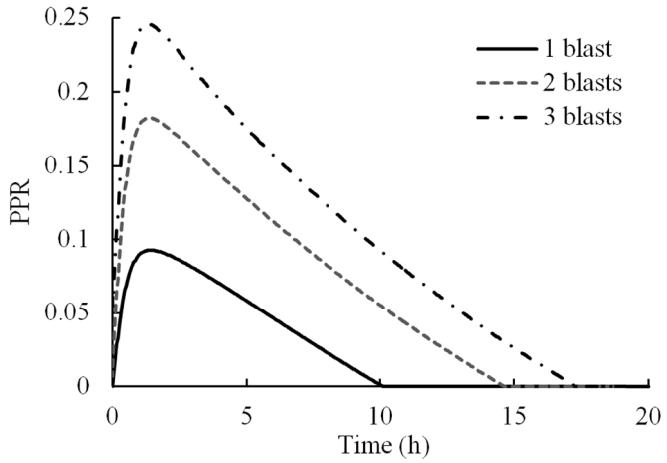

Figure 5.53 Variation of PPR at monitoring point for Cases 1 (1 blast sequence), 10 (2 blast sequences) and 11 (3 blast sequences)

From the results presented above, it can be concluded that consecutive blasts can not only increase the liquefaction potential of backfill mass, but also lead to much longer time for the excess pore pressure to be dissipated, which is unfavorable for the fill mass stability. Therefore, sufficient delay between each blast would be preferable for reducing the risk of liquefaction in backfilled stopes at early ages.

5.3.5 Conclusions

A modified total-stress viscoplastic cap model is developed and utilized in this study to investigate the effects of different backfilling and field conditions on the blast-induced liquefaction susceptibility of early-age fill mass in the field. The results of model validation against laboratory and field blast tests indicate that the model can capture the mechanical response and excess pore pressure development of granular soils such as tailings backfills under blast loading reasonably well.

The model application on field backfill mass indicates that, in most of the studied cases, the zones affected by blast induced liquefaction are limited to the upper parts of the backfill mass. The results also suggest that drainage condition, proximity of detonation, stope size, location of barricade and blast sequence all influence its liquefaction susceptibility upon blasting. Specifically, enhanced drainage and avoidance of nearby and consecutive detonations would significantly reduce the risk of liquefaction of fill mass. However, the stope size, as well as the barricade location is affected by other practical factors such as mine productivity and stability of retaining structures, and a cost-effective backfilling practice should balance over all these influencing factors. Therefore, although the results of this study provide useful insight into the blast-induced liquefaction susceptibility of fill mass in varied practical conditions, more research work is required to facilitate the optimal backfill design in the dynamic (blast) loading conditions.

5.3.6 References

Ahmed L, Ansell A. Vibration vulnerability of shotcrete on tunnel walls during construction blasting. Tunnelling and Underground Space Technology 2014;42:105–111.

Al-Qasimi EMA, Charlie WA, Woeller DJ. Canadian liquefaction experiment (CANLEX): Blast–induced ground motion and pore pressure experiments. Geotechnical Testing Journal 2005, 28(1): 1–13.

Al-Tarhouni M, Simms P, Sivathayalan S. Cyclic behaviour of reconstituted and desiccated–rewet thickened gold tailings in simple shear. Canadian Geotechnical Journal 2011;48:1044–60.

An J, Tuan CY, Cheeseman BA, Gazonas GA. Simulation of soil behaviour under blast loading. International Journal of Geomechanics, ASCE 2011; 11:323–334.

Aráoz G, Luccioni B. Modeling concrete like materials under sever dynamic pressures. International Journal of Impact Engineering 2015; 76:139–154.

Aubertin M, Ricard JF, Chapuis RP. A predictive model for the water retention curve: application to tailings from hard–rock mines. Canadian Geotechnical Journal 1998;35:55–69.
Awad AA. A numerical model for blast–induced liquefaction using displacements–pore pressure formulations. Ph.D. Thesis. Colorado State University, Colorado, USA, 1990.
Baladi GY, Rohani B. Elastic–plastic model for saturated sand. Journal of Geotechnical Engineering Division 1979; 105(4): 465–480.
Bloom F. Constitutive models for wave propagation in soil. Applied Mechanics Reviews 2006; 59:146–175.
Bolton JM, Durnford DS, Charlie WA. One–dimensional shock and quasi–static liquefaction of silt and sand. Journal of Geotechnical Engineering, ASCE 1994; 120:1874–1888.
Bretz TE. Soil liquefaction resulting from blast–induced spherical stress waves. Final Rep. No. WL–TR–89–100, Weapons Laboratory, Air Force Systems Command, 1990.
Bussière B. Colloquium 2004: Hydrogeotechnical properties of hard rock tailings from metal mines and emerging geoenvironmental disposal approaches. Canadian Geotechnical Journal 2007; 44(9):1019–1052.
CharlieWA, Bretz TE, Schure LA, Doehring DO. Blast–induced pore pressure and liquefaction of saturated sand. Journal of Geotechnical and Geoenvironmental Engineering, ASCE 2013; 139(8):1308–1319.
Charlie WA, Veyera GE, Doehring DO, Abt SR. Blast induced liquefaction potential and transient pore water pressure response of saturated sands. Technical report. Fort Collins: Colorado State University; 1985.
Chen WF, Baladi GY. Soil Plasticity: Theory and Implementation. Elsevier: Amsterdam, 1985.
Cooke R. Design procedure for hydraulic backfill distribution systems. Journal of South African Institute of Mining and Metallurgy 2001; 101(2): 97–102.
Fahey M, Helinski M, Fourie A. Some aspects of the mechanics of arching in backfilled stopes. Canadian Geotechnical Journal 2009;46:1322–1336.
Fall M, Benzaazoua M. Modeling the effect of sulphate on strength development of paste backfill and binder mixture optimization. Cement and Concrete Research 2005; 35(2): 301–314.
Ferdosi B, James M, Aubertin M. Numerical simulations of the seismic and post–seismic behaviour of tailings. Canadian Geotechnical Journal 2015; 52: 1–8.
Fragaszy RJ, Voss ME. Undrained compression behaviour of sand. Journal of Geotechnical Engineering, ASCE 1986; 112(3): 334–347.
Ghassemi A, Pak A, Shahir H. Numerical study of the coupled hydro–mechanical effects in dynamic compaction of saturated granular soils. Computers and Geotechnics 2010; 37:10–24.
Griffiths DV, Li CO. Accurate pore pressure calculation in undrained analysis. Engineering Computation 1989; 6(4), 339–342.
Griffiths DV. The effect of pore fluid compressibility on failure loads in elasto–plastic soil. International Journal for Numerical and Analytical Methods in Geomechanics 1985; 9(3), 253–59.
Helinski M, Fahey M, Fourie A. Coupled two–dimensional finite element modelling of mine backfilling with cemented tailings. Canadian Geotechnical Journal 2010; 47: 1187–1200.
Henrych J. The dynamics of explosion and its use. Elsevier, New York, USA, 1979.

Holmberg R, Persson PA. Swedish approach to contour blasting. In: Proceedings of Fourth Conference on Explosive and Blasting Techniques, New Orleans, USA, 1979, 113–127.
Huang S, Xia K, Qiao L. Dynamic tests of cemented paste backfill: effects of strain rate, curing time, and cement content on compressive strength. Journal of Material Science 2011; 46(15):5165–5170.
Ishihara K. Liquefaction and flow failure during earthquakes. Geotechnique 1993; 43(3): 351 – 415.
Ishihara, K. Post–earthquake failure of a tailings dam due to liquefaction of the pond deposit. In Proceedings of the International Conference on Case Histories in Geotechnical Engineering, 1984, 1129–1143.
James M, Aubertin M, Wijewickreme D, Wilson GW. A laboratory investigation of the dynamic properties of tailings. Canadian Geotechnical Journal 2011;48:1587–1600.
Jiang J, Blair DP, Baird GR. Dynamic response of an elastic and viscoelastic full–space to a spherical source. International Journal for Numerical and Analytical Methods in Geomechanics 1995; 19:181–193.
Katona MG. Evaluation of viscoplastic cap model. Journal of Geotechnical Engineering, ASCE 1984; 110(8):1106–1125.
Klein K, Simon D. Effect of specimen composition on the strength development in cemented paste backfill. Canadian Geotechnical Journal 2006; 43:310–324.
Le Roux K. In situ properties and liquefaction potential of cemented paste backfill. Ph.D. Thesis. University of Toronto, Toronto, Canada, 2004.
Lee WY. Numerical modeling of blast induced liquefaction. PhD thesis. Brigham Young University, Provo, USA, 2006.
Lu G, Fall M. A coupled chemo–viscoplastic cap model for simulating the behaviour of hydrating cemented tailings backfill under blast loading. International Journal for Numerical and Analytical Methods in Geomechanics 2016;40:1123–1149.
Lu G, Fall M, Cui L. A multiphysics–viscoplastic cap model for simulating the blast response of an evolutive soft cementitious material. Journal of Rock Mechanics and Geotechnical Engineering 2017a (Accepted for publication).
Lu G, Fall M. Modelling blast wave propagation in a subsurface geotechnical structure made of an evolutive porous material. Mechanics of Materials 2017b;108: 21–39.
Murray YD. Users manual for LS–DYNA concrete material model 159. Report FHWA–HRT–05–062, Federal Highway Administration. McLean, 2007.
Naylor DJ. Stresses in nearly incompressible materials by finite elements with application to the calculation of excess pore pressures. International Journal for Numerical Methods in Engineering 1974; 8(3), 443–460.
Pépin N, Aubertin M, James M. Seismic table investigation of the effect of inclusions on the cyclic behaviour of tailings. Canadian Geotechnical Journal 2012;49:416–426.
Perzyna P. Fundamental problems in viscoplasticity. Advances in Applied Mechanics 1966; 9:243–377.
Puebla H, Byrne PM, Phillips R. Analysis of CANLEX liquefaction embankments: prototype and centrifuge models. Canadian Geotechnical Journal 1997; 34: 641–657.
Robertson PK, Wride CE, List BR, Atukorala U, Biggar KW, Byrne PM, et al. The Canadian Liquefaction Experiment: an overview. Canadian Geotechnical Journal 2000;37:499–504.
Sainoki A, Mitri HS. Dynamic modelling of fault slip induced by stress waves due to stope production blasts. Rock Mechanics and Rock Engineering 2016;49:165–181.

Simo JC, Wu JW, Pister KS, Taylor RL. Assessment of cap model: Consistency return algorithms and rate–dependent extension. Journal of Engineering Mechanics, ASCE 1986; 114(2):191–218.

Sivakugan N, Rankine RM, Rankine KJ, Rankine KS. Geotechnical considerations in mine backfilling in Australia. Journal of Cleaner Production 2006; 14(12): 1168–1175.

Suazo G, Fourie A, Doherty J, Hasan A. Effects of confining stress, density and initial static shear stress on the cyclic shear response of fine–grained unclassified tailings. Géotechnique 2016;66:401–412.

Tong X, Tuan CY. Viscoplastic cap model for soils under high strain rate loading. Journal of Geotechnical and Geoenvironmental Engineering, ASCE 2007; 133(2):206–214.

van Genuchten MT. A closed–form equation for predicting the hydraulic conductivity of unsaturated soils. Soil Science Society of America Journal 1980;44:892–898.

van Gool BS. Effects of blasting on the stability of paste fill stopes at Cannington Mine. Ph.D. Thesis. James Cook University, Townville, Australia, 2007.

Wang Z, Lu Y, Bai C. Numerical analysis of blast–induced liquefaction of soil. Computers and Geotechnics 2008; 5:196–209.

Wijewickreme D, Sanin M V, Greenaway GR. Cyclic shear response of fine–grained mine tailings. Canadian Geotechnical Journal 2005;42:1408–1421.

Yamamuro JA, Lade PV. Effects of strain rate on instability of granular soils. Geotechnical Testing Journal 1993; 16(3), 304–313.

Yilmaz E, Benzaazoua M, Belem T, Bussière B. Effect of curing under pressure on compressive strength development of cemented paste backfill. Mineral Engineering 2009; 22:772–785.

Yilmaz E. Investigating the hydrogeotechnical and microstructural properties of cemented paste backfill using the CUAPS apparatus. PhD Thesis, Université du Québec in Abitibi–Temiscamingue, 2009.

5.4 Technical Paper 7: Modelling post-blasting stress and pore pressure distribution in hydrating fill mass at early age

(Submitted)

Gongda Lu, Mamadou Fall

Abstract

Cemented paste backfill (CPB) is a widely used porous medium to fill mined-out cavities in the subsurface due to its superior environmental and operational benefits. The stability of a retaining structure (barricade) is a crucial design factor in backfill operations as CPB is under pressure imposed by material conditions at the early ages. Although field monitoring has demonstrated the impacts of mine blast operations on the backfill pressure that acts on the retaining structure, current studies on stress distribution in backfilled stopes have not considered the effect of such dynamic loadings. Therefore, to analyze the redistribution of stress in backfill due to mine blasts, a total-stress viscoplastic cap model is used in this study to assess the dynamic response and generation of excess pore pressure of early-age backfill during blast loading. Then, a multiphysics model for CPB is utilized to assess the variations in the stress state after the blast impact in backfilled stopes during the binder hydration process of the material. The two adopted models are then validated against a series of laboratory and field experiments. Then, they are integrated and applied to investigate the effect of drainage condition, stope size, barricade location, proximity of detonation, blast sequence, initial backfill temperature and cement content on the redistribution of stress after blast loading in backfilled stopes. The insights obtained from the results of the study will increase understanding of the stability of retaining structures for backfills in the practical engineering conditions of mine fields.

KEY WORDS**:** cemented paste backfill, tailings, THMC, blasting, viscoplastic cap model, stress, pore pressure

5.4.1 Introduction

The creation of cavities (stopes) in underground mining often necessitates the use of backfilling to improve the stability of the local rock mass and enhance ore recovery. To date, cemented paste backfill (CPB) has emerged as one the most extensively utilized material worldwide for this purpose. CPB is an evolutive porous medium or man-made soil that consists of dewatered mine tailings (fine aggregates), binder agents (e.g. cement, slag and fly ash), and water. It is mixed in backfill plants, and then delivered by pumping or through gravity in pipe networks to fill mined-out voids in the subsurface (Klein and Simon, 2006; Fahey et al., 2009).

CPB is commonly prepared with a large amount of water to provide the required consistency that would facilitate its transport. Then, it is retained by containment barricades that are built in the stope drawpoints. However, the stability of the retaining structures under horizontal stress imposed by early-age fill mass is a major concern in backfill design (Thompson et al., 2012). A number of barricade failures due to excessive backfill loads have been reported to date (see for e.g., Yumlu and Guresci, 2007; Helinski et al., 2010). In this regard, a number of analytical and numerical studies have been conducted to analyze the stress distribution in backfilled stopes (e.g. Fahey et al., 2009; Helinski et al., 2010). In spite of the insights obtained, these studies have only addressed quasi-static conditions. However, access and production blastings have been integrated in current underground mining as part of the routine, and the excess pore pressure of early-age backfill generated by dynamic loading increases the stress that is exerted onto the barricade. The extra load which is attributed to mine blasts has not yet been considered in current backfill design or analyses. In fact, sudden increases in backfill pressure that act on retaining structures due to adjacent blasting operations have been recently monitored and confirmed in the field (e.g. Thompson et al., 2009; 2012). Meanwhile, it is also reported that the retention structures for backfills could fail even hours after dynamic loading during excess pore pressure dissipation (Ishihara, 1984; Ferdosi et al., 2015). Therefore, ignoring the stress and pore pressure redistribution in backfilled stopes due to mine blasting could result in inappropriate backfill designs or optimistic analyses, and thus increase the risk of barricade failure that could result in safety consequences and ore dilution.

In order to analyze blast-induced stress redistribution in early-age backfill, two types of material behaviours need to be characterized. First, the blast response and generation of excess pore pressure of the saturated backfill during dynamic loadings must be captured in a numerical

model. Secondly, the variations in stress, pore pressure and material properties after impact during the course of binder hydration need to be determined.

To date, there are only a few numerical tools available that capture the generation of excess pore pressure in saturated porous media due to blast loading (e.g. Awad, 1990; Lee, 2006; Wang et al., 2008). However, they have different types of limitations, such as using an open yield surface in the stress space that could result in unrealistic dilation, and neglecting the effects of pore water and strain rate on the dynamic response of the material. Therefore, a total-stress viscoplastic cap model (Lu and Fall, 2017a) is adopted in this study. This model takes into consideration the strain-rate and pore-fluid dependence of material behaviour, and can also reasonably capture the irrecoverable compaction that is associated with the generation of excess pore pressure.

Due to the hydration of the binder in the CPB as well as its interaction with the curing environment, the properties of CPB and stress distribution in backfilled stopes constantly change with time under the influence of coupled thermal (T), hydraulic (H), mechanical (M) and chemical (C, binder hydration) processes. Due to the complex interactions of the THMC factors, very few models are currently available to fully characterize CPB behaviour under quasi-static condition. For example, coupled HMC models for the hydration process of CPB have been developed by Helinski et al. (2007, 2010) and Doherty (2015). However, only the multiphysics model in Cui and Fall (2015) incorporates all of the THMC processes during the hydration of CPB, and thus their model is applied in this study.

In the remainder of this paper, the formulation of the total-stress viscoplastic cap (Lu and Fall, 2017a) and THMC (Cui and Fall, 2015) models which are applied in this study are briefly outlined, and then validated against a series of laboratory and field experiments. Then, these two models are applied to investigate the redistribution of stress and pore pressure in backfilled stopes after blast loading under various practical engineering conditions, and the influence of other factors, including the stope geometry, blast operation, and intrinsic properties of backfill, is examined and discussed.

5.4.2 Model formulation

5.4.2.1 Modelling approach

To analyze the variations of the blast-induced stress and pore pressure in CPB, the THMC model in Cui and Fall (2015) is applied in this study, which has been shown to realistically capture the changes in CPB behaviour during its interaction with the curing environment. The total-stress viscoplastic cap model (Lu and Fall, 2017a) is used as the constitutive law to assess the excess pore pressure (Δu) generated by blast loadings in the backfill. This model has already been validated with various granular materials. It should be noted that the effect of blasting is examined here at the early ages of the backfill, under the assumption that the material is still saturated and therefore the total-stress model is applicable. After blasting, the excess pore pressure generated by the dynamic loading is inputted into the THMC model, and the variation of the stresses in the stope caused by the impacts of blasting during the curing of CPB is analyzed. A schematic diagram of the modelling processes and factors considered is provided as Figure 5.54 below.

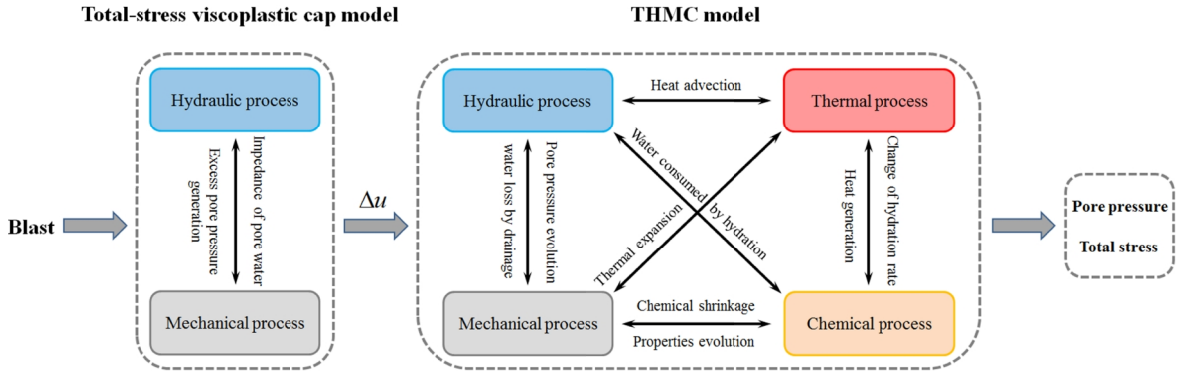

Figure 5.54 Schematic diagram of modelling processes

5.4.2.2 Formulation of coupled THMC model for cemented paste backfill

5.4.2.2.1 Binder hydration model

To determine the progression of binder hydration in CPB, a hydration model (chemical model) developed by Schindler (2004) for cementitious materials is adopted in this study, which defines the degree of binder hydration x as

$$x\left(t_e\right)=x_u\cdot\exp\left[-\left(\frac{t}{t_e}\right)^b\right] \tag{5.66}$$

with

$$\begin{cases} x_u = \dfrac{1.031 \cdot w/c}{0.194 + w/c} + 0.5 \cdot X_{FA} + 0.30 \cdot X_{slag} \\ t_e = \sum_0^t \exp\left[-\dfrac{E_a}{R_a}\left(\dfrac{1}{T} - \dfrac{1}{T_r} \right) \right] \cdot \Delta t \\ E_a(T) = \begin{cases} 33500 + 1470(20 - T) & T < 20^{\circ}C \\ 33500 & T \geq 20^{\circ}C \end{cases} \end{cases}$$

where x_u is the ultimate degree of hydration; t and b denote the hydration time and shape parameters, t_e represents the equivalent age of CPB at the reference temperature T_r, w/c is the water-to-cement ratio, X_{FA} and X_{slag} refer to the fractions of the corresponding compounds, E_a is the activation energy, R_a is a natural gas constant, and T is the temperature of the CPB.

5.4.2.2.2 Mechanical equilibrium model

For a representative elementary volume of a three-phase CPB system, the momentum conservation can be expressed as:

$$\nabla \cdot \left(\frac{\partial \boldsymbol{\sigma}}{\partial t} \right) + \frac{\partial \left[(1-f) r_s + f S r_w + f (1-S) r_a \right]}{\partial t} \mathbf{g} = 0 \tag{5.67}$$

where f is the porosity, r_i denotes the density, subscript i refers to an individual phase (air, water or solid), and S is the degree of saturation (water). $\boldsymbol{\sigma}$ is a total stress tensor and related to the effective stress as $\boldsymbol{\sigma} = \boldsymbol{\sigma}' - a_B P \boldsymbol{\delta}_{\mathbf{ij}}$. The Biot's coefficient a_B is used to account for the compressibility of the solid particles which is defined as $a_B = 1 - K_s / K_p$, and K_s and K_p are the bulk modulus of the porous skeleton and solid particles, respectively. The average pore pressure P is defined as $P = SP_w + (1-S)P_a$, where P_a and P_w are the pore gas and pore water pressures.

During the hydration of the binder, K_s will change with time, and can be estimated by using the following expressions (Cui and Fall, 2016; Lu et al., 2017):

$$\frac{E(x)}{E_u} = \left(\frac{x - x_0}{x_u - x_0} \right)^A \tag{5.68}$$

$$v(x) = B_1 x \wedge (B_2) + B_3 \tag{5.69}$$

where $E(x)$ is the elastic modulus of the CPB at a given degree of hydration, E_u =282.3 MPa and refers to its ultimate value, x_0 is 0.09 which denotes the reference degree of hydration

below which the stiffness gain is insignificant, and A is a material constant and equals to 36.3. The parameters B_1 =-0.226, B_2 =6, and B_3 =0.3 which are fitting constants to capture the variations in the Poisson's ratio $n(x)$ of the porous skeleton. Finally, K_s can be obtained as $K_s = E(x)/3[1-2v(x)]$,

The effective stress $\boldsymbol{\sigma}'$ in CPB can be obtained as:

$$\boldsymbol{\sigma}' = \mathbf{D}\boldsymbol{\varepsilon}_e = \mathbf{D}\left(\boldsymbol{\varepsilon} - \boldsymbol{\varepsilon}_p - \boldsymbol{\varepsilon}_T - \boldsymbol{\varepsilon}_c\right) \tag{5.70}$$

where $\mathbf{D}$ is the elastic stiffness matrix, and $\boldsymbol{\varepsilon}$ is the total strain tensor which consists of elastic ($\boldsymbol{\varepsilon}_e$), plastic ($\boldsymbol{\varepsilon}_p$), thermal ($\boldsymbol{\varepsilon}_T$), and chemical ($\boldsymbol{\varepsilon}_c$) strains. Determination of these strain components during the curing process of CPB are elucidated in Cui and Fall (2015, 2016).

5.4.2.2.3 Fluid flow model

The solid, water, and air in CPB are assumed to be three independent overlapping continua, so that fluid can move within the interconnected voids of the solid. Then, the mass conservation of a CPB system can be characterized as:

$$fS\frac{\partial r_w}{\partial t} + fr_w\frac{\partial S}{\partial t} + Sr_w\left[\frac{\partial e_v}{\partial t} + \frac{(1-f)}{r_s}\frac{\partial r_s}{\partial t}\right] - fS\dot{m}_{hydr}\left(\frac{r_w}{r_s}S - 1\right) = -\nabla\cdot\left(fSr_w\mathbf{v}^{rw}\right) \tag{5.71}$$

$$f(1-S)\frac{\partial r_a}{\partial t} - fr_a\frac{\partial S}{\partial t} + (1-S)r_a\left[\frac{(1-f)}{r_s}\frac{\partial r_s}{\partial t} + \frac{\partial e_v}{\partial t} - \frac{fS}{r_s}\dot{m}_{hydr}\right] = -\nabla\cdot f(1-S)r_a\mathbf{v}^{ra} \tag{5.72}$$

where e_v is the total volumetric strain, and $\mathbf{v}_s$ and $\mathbf{v}^{ri}$ denote the solid velocity with respect to the Eulerian coordinate, and the relative apparent velocity of fluids, respectively. $\dot{m}_{hydr}$ is the rate of water consumption due to binder hydration, and can be defined as (Cui and Fall, 2015):

$$\begin{aligned}\dot{m}_{hydr} = {} & 2m_{hc-initial}\left(0.187x_{C_3S} + 0.158x_{C_2S} + 0.665x_{C_3A} + 0.2130x_{C_4AF}\right) \\ & \times\left\{\left(\frac{t}{t_e}\right)^b\left(\frac{b}{t_e}\right)x(t_e)\exp\left[\frac{E_a}{R_a}\left(\frac{1}{273+T_r} - \frac{1}{273+T}\right)\right]\right\}\end{aligned} \tag{5.73}$$

where $m_{hc-initial}$ is the mass of the cement in the backfill system, and x_i is the fraction of the corresponding compound.

The fluid flow $\mathbf{v}^{ri}$ can be defined by using Darcy's law as:

$$\mathbf{v}^{ri} = -\mathbf{k}\frac{k_{ri}}{m_i}\nabla\left(P_i - r_i g\right) \tag{5.74}$$

where **k** is the intrinsic permeability tensor of the medium, the intrinsic permeability $k_0 = K m_i / r_i g$, K refers to the saturated hydraulic conductivity of the CPB, m_i is the fluid dynamic viscosity, and k_{ri} represents the relative permeability. The value of K would decrease as binder hydration progresses, and can be determined in terms of x as:

$$K = K_T \exp\left(C_1 x^{C_2}\right) \tag{5.75}$$

where K_T is the saturated hydraulic conductivity of the tailings used, and fitting constants C_1=-8.173 and C_2=4.035 (Cui and Fall, 2015).

The relative permeability k_{ri} can be obtained through the model in van Genuchten (1980):

$$\begin{cases} k_{rw}\left(S_{eff}\right) = \sqrt{S_{eff}}\left[1-\left(1-S_{eff}^{1/m}\right)^m\right]^2 \\ k_{ra}\left(S_{eff}\right) = \sqrt{1-S_{eff}}\left(1-S_{eff}^{1/m}\right)^{2m} \end{cases} \tag{5.76}$$

with

$$S_{eff} = \frac{1}{\left[1+\left(aP_c\right)^{\frac{1}{1-m}}\right]^m} \tag{5.77}$$

where the changes with time of the fitting parameters due to the hydration of the CPB can be detemined with (Cui and Fall, 2015):

$$\begin{cases} m = f_1 x^{f_2} + f_3 \\ a = f_4 e^{f_5 x} \end{cases} \tag{5.78}$$

where f_1 =0.0415, f_2 =4.231, f_3 =0.4073, f_4 =0.2103 kPa^{-1} and f_5 =-6.921 are the fitting constants determined based on experimental data.

Finally, the temperature-dependence of the fluid properties can be defined by using the following expressions (Cui and Fall, 2015):

$$\begin{cases} m_w = 0.6612\left(T-229\right)^{-1.562} \\ r_w = 314.4 + 685.6\left\{1-\left[\left(T-273.15\right)/374.14\right]^{1/0.55}\right\}^{0.55} \\ m_a = m_0 \cdot \left(T/T_0\right)^{1.5} \cdot \left[\left(T_0+c_0\right)/\left(T+c_0\right)\right] \\ r_a = \dfrac{M_a}{R_a T} P_a \end{cases} \tag{5.79}$$

where m_0 =1.716×10^{-5} Pa·s, T_0=273 K, c_0 = 111 K, and M_a is the molar mass of air.

5.4.2.2.4 Heat transfer model

A local thermal equilibrium is imposed on the three-phase CPB system. The law of conservation energy for CPB can be expressed as:

$$\left[(1-f)\, r_s C_s + f S\, r_w C_w + f\,(1-S)\, r_a C_a\right]\frac{\partial T}{\partial t} + Q_{cv} + Q_{cd} = Q_{hydr} \tag{5.80}$$

where C_i is the specific heat capacity, and the convection of heat due to fluid movement (Q_{cv}) can be determined as:

$$Q_{cv} = \left(r_w C_w \mathbf{v}^{rw} + r_a C_a \mathbf{v}^{ra}\right)\cdot \nabla T \tag{5.81}$$

The heat conduction (Q_{cd}) can be evaluated by using Fourier's law as:

$$Q_{cd} = -k_{eff}\nabla T \tag{5.82}$$

where k_{eff} is the effective thermal conductivity of CPB which can be defined as (Cui and Fall, 2015):

$$k_{eff} = k_{dry} + \sqrt{S_{eff}}\left(k_{sat} - k_{dry}\right) \tag{5.83}$$

with

$$k_{sat} = k_{tailings}^{1-f} k_w^f, \qquad k_{dry} = k_{tailings}^{1-f} k_a^f \tag{5.84}$$

where $k_{tailings}$, k_w and k_a denote the thermal conductivity of the tailings, water and air, respectively.

Finally, the heat released from exothermic binder hydration (Q_{hydr}) can be determined by using (Schindler and Folliard, 2005):

$$Q_{hydr} = H_T\left(\frac{t}{t_e}\right)^b \cdot \left(\frac{b}{t_e}\right)\cdot x\left(t_e\right)\cdot \exp\left[\frac{E_a}{R_a}\left(\frac{1}{273+T_r} - \frac{1}{273+T}\right)\right] \tag{5.85}$$

with

$$\begin{cases} H_T = \left(H_{cem}\cdot X_{cem} + 461\cdot X_{slag} + 1800\cdot x_{CaO/FA}\cdot X_{FA}\right)C_b \\ H_{cem} = 500x_{C_3S} + 260x_{C_2S} + 866x_{C_3A} + 420x_{C_4AF} + 624x_{SO_3} + 1186x_{FreeCaO} + 850x_{MgO} \end{cases}$$

where H_T and H_{cem} denote the amount of heat generated by the hydration of all binders and cement, respectively, and C_b denotes the apparent binder density.

5.4.2.3 Formulation of total-stress viscoplastic cap model

5.4.2.3.1 Introduction

Due to insufficient time for relative movement between the pore fluid and skeleton to occur during blast loading, and that the dynamic response of saturated granular media is undrained, interstitial water with high stiffness will be compressed simultaneously with the skeleton at the same magnitude because of volume compatibility (Naylor, 1974; Griffiths, 1985; Puebla et al., 1997). Consequently, the irrecoverable volumetric deformation of the material (hysteresis) after a blast load cycle would lead to the generation of excess pore water pressure (Fragaszy and Voss, 1986). To account for this phenomenon, a total-stress viscoplastic cap model (Lu and Fall, 2017a) is adopted in this study to simulate the response of saturated CPB under blast loading. This model incorporates the impedance of pore water flow under the undrained condition, and can also realistically simulate the irrecoverable volume compaction that is associated with liquefaction. The formulation of the total-stress model is briefly discussed in this section.

5.4.2.3.2 Constitutive law

A modified viscoplastic cap model based on the Perzyna model is adopted in this study to characterize the response of CPB under blast loading, and has been widely and successfully applied to capture the behaviour of various types of geomaterials (including soils, concrete and tailings backfill) under high pressure and a wide spectrum of strain rates (e.g., Katona, 1984; Tong and Tuan, 2007; Lu and Fall, 2016, 2017b).

The total strain rate vector $\dot{\boldsymbol{\varepsilon}}$ in viscoplastic models is conventionally decomposed into an elastic part $\dot{\boldsymbol{\varepsilon}}^{e}$ and a viscoplastic component $\dot{\boldsymbol{\varepsilon}}^{vp}$ as:

$$\dot{\boldsymbol{\varepsilon}} = \dot{\boldsymbol{\varepsilon}}^{e} + \dot{\boldsymbol{\varepsilon}}^{vp} \tag{5.86}$$

The elastic strain rate is related to stress rate tensor $\dot{\boldsymbol{\sigma}}$ as

$$\dot{\boldsymbol{\varepsilon}}^{e} = \mathbf{D}^{-1}\dot{\boldsymbol{\sigma}} \tag{5.87}$$

The viscoplastic strain rate in the Perzyna model is generally defined as:

$$\dot{\boldsymbol{\varepsilon}}^{vp} = h\left\langle f(f)\right\rangle \frac{\partial f}{\partial \boldsymbol{\sigma}} \tag{5.88}$$

where h is a fluidity parameter; $\langle\ \rangle$ is a Macaulay bracket; f is the yield criterion which is defined by the cap envelope provided below; and $f(f)$ is a dimensionless scaling function defined as (Katona, 1984; Tong and Tuan, 2007):

$$f(f)=\left(\frac{f}{f_0}\right)^N \tag{5.89}$$

where N and f_0 are model constants.

The smooth surface cap model proposed in Lu and Fall (2016, 2017b) is used as the yield envelope f, and the shear yield envelope of the model is characterized by

$$F_1(I_1,\sqrt{J_2})=\sqrt{J_2}-\frac{k-[X(k)-L(k)]/R}{L(k)^2}I_1^2+2\cdot\frac{k-[X(k)-L(k)]/R}{L(k)}I_1-k \tag{5.90}$$

where $L(k)$ and $X(k)$ is the abscissa of the intersection of the cap with the shear envelope and the I_1 axis, respectively; R is the ratio of the major to the minor axis of the elliptical cap; and k is a the Drucker-Prager parameter defined by:

$$a=\frac{2\sin j}{\sqrt{3}(3+\sin j)},\qquad k=\frac{6c\cos j}{\sqrt{3}(3+\sin j)} \tag{5.91}$$

where c and j are the cohesion and internal friction angle, respectively.

The elliptical cap envelope is defined by the following expression in Chen and Baladi (1985):

$$F_2(I_1,\sqrt{J_2},k)=\sqrt{J_2}-\frac{1}{R}\left\{[X(k)-L(k)]^2-[I_1-L(k)]^2\right\}^{1/2} \tag{5.92}$$

where the translation of point $X(k)$ due to irrecoverable volumetric strain (e_v^{in}) can be characterized by using an isotropic hardening law as:

$$X(k)=-(1/D)\cdot\ln\left(1-\frac{e_v^{in}}{W}\right)+X_0 \tag{5.93}$$

where W is the maximum amount of inelastic volumetric strain, D denotes the shape parameter of the volume-pressure relationship, and X_0 is the initial vertex of the cap. Subsequently, $L(k)$ can be obtained by imposing a continuity condition on the entire envelope:

$$k=\frac{X(k)-R\cdot k}{1+R\cdot a} \tag{5.94}$$

and

$$L(k)=\begin{cases}k & k>k_0\\ k_0 & \text{otherwise}\end{cases} \tag{5.95}$$

where k_0 is the onset of the hardening cap.

5.4.2.3.3 Undrained response

Since the soil skeleton and pore water will be compressed simultaneously during undrained blast loading at the same magnitude, the changes in the pore pressure of the saturated mixture can be determined by using (Naylor, 1974; Puebla et al., 1997):

$$dP_w = K_a de_v \tag{5.96}$$

where K_a is the apparent bulk modulus of the pore fluid, which can be obtained by using (Naylor, 1974):

$$\frac{1}{K_a} = \frac{n}{K_w} + \frac{1-n}{K_p} \tag{5.97}$$

where K_w is the bulk modulus of the pore water. Subsequently, the undrained response of the saturated mixture can be determined by combining the pore fluid stiffness with the effective elastic matrix of the skeleton (Naylor, 1974; Griffiths, 1985), which can be expressed in this study as:

$$dP = dP_s + dP_w = K_s de_v^e + K_a de_v = (K_s + K_a \frac{de_v}{de_v^e}) de_v^e = K_m de_v^e \tag{5.98}$$

where e_v^e is the elastic volumetric strain, and K_m is the undrained bulk modulus of the saturated mixture. Meanwhile, the associated Poisson's ratio v_m also needs to be modified for an undrained condition as (Naylor, 1974; Griffiths, 1985):

$$v_m = \frac{(1-2v)(1+v) + Ev / K_a}{2(1-2v)(1+v) + E / K_a} \tag{5.99}$$

where E and v are effective elastic constants of the soil skeleton.

Finally, to account for the nonlinear volume-pressure relationship between the soil skeleton and pore water under high pressure, their bulk moduli are determined with the Mie-Grüneisen equation of state as follows (An et al., 2011):

$$K_i = \frac{r_i C_{i0}^2 [1 + (1 - \frac{g_{i0}}{2}) m - \frac{a_{i0}}{2} m^2][1 + \frac{2m(s_i - 1)}{1 + m - s_i m} + \frac{m(g_{i0} + a_{i0} m)}{(1+m)^2}] + r_i C_{i0}^2 m (1 - \frac{g_{i0}}{2} - a_{i0} m)}{(1 + m - s_i m)^2} + \left[\frac{(g_{i0} + a_{i0} m)^2}{(1+m)^2} + a_{i0} \right] E_i^v \tag{5.100}$$

where C_{i0} is the p-wave velocity; s_i is the slope of the shock velocity against the particle velocity curve; g_{i0} is a Grüneisen parameter, E_i^v is the internal energy per unit initial volume; a_{i0} is the first order volume correction to g_{i0}; and $m = e_v/(1-e_v)$.

5.4.3 Model validation

5.4.3.1 Case Study 1: High column experiments on hydrating CPB

Ghirian and Fall (2013, 2014) conducted experiments with high columns to investigate the coupled THMC behaviours of CPB during the curing process, and the test results are adopted here as the first case study to validate the THMC model for hydrating backfill. The CPB was placed in columns with a diameter of 20 cm, and three filling sequences were carried out. Each time, a lift of 50 cm in height was added with a one-day delay between each lift, and then the column was dismantled after 3 days. Extensive measurements and testing were performed and samples were taken at different locations of the columns during the curing of the CPB. The input parameters, boundary conditions and initial values used for simulation of the curing process with the THMC model are listed in Table 5.16.

Table 5.16 Input parameters, boundary conditions and initial values for curing of CPB

	Case Study 1	Case Study 4
Cement content (%)	4.5	6.5
w/c	7.6	3.54
Insulation material	Foam	Rock
Thermal conductivity (W/(m·K))	0.024	3.6
Heat capacity (J/(kg·K))	1400	800
Density (kg/m^3)	30	2000
Mechanical boundary	Roller, except free at top	Roller, except free at top
Hydraulic boundary	No flow	No flow, except drainage at barricade
Thermal boundary (°C)	20.5	20
Initial temperature (°C)	20.5	20

The cylinder columns of CPB were modelled by using symmetry elements, and the delay in the placement of each lift of the CPB was simulated layer by layer. A comparison between the simulated and measured temperature at 25 cm (bottom), 75 cm (middle) and 125 cm (top) from the bottom of the CPB column during the curing process is presented in Figure 5.55. The figure shows that the backfill temperature is increased due to exothermic hydration at the early ages, and would decrease due to room temperature (approximately 20.5°C). It can be observed that the

simulated variation in temperature is in good agreement with the measured values in terms of both the peak temperatures and trend of changes in temperature.

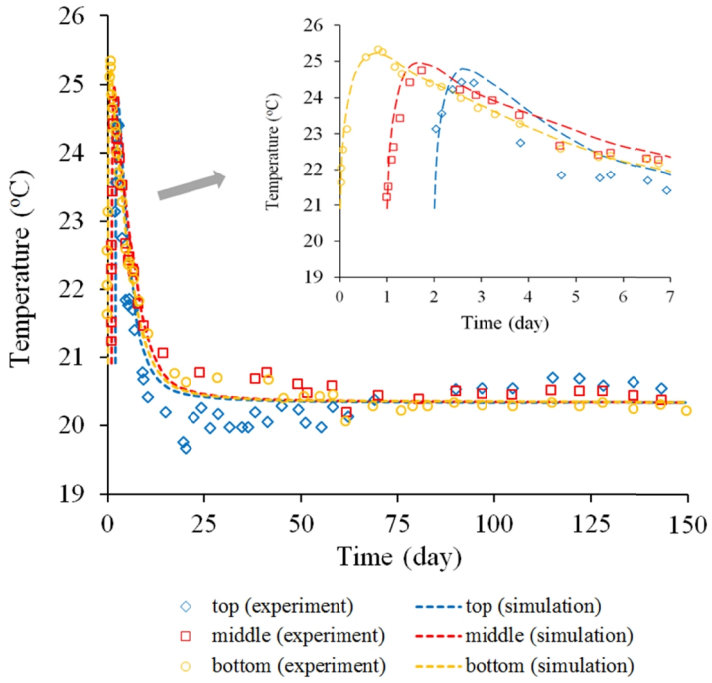

Figure 5.55 Comparison between simulated and measured temperatures in CPB column

The simulated and measured variation of the pore pressure at different locations of the column is compared in Figure 5.56. The figure also shows that there is good agreement between the model prediction and experimental results of the pore pressure as hydration progresses. It is evident that there is an immediate increase in the pore pressure in the lower lifts due to the downward drainage from the placement of fresh and saturated upper lifts, which has also been reasonably captured by the THMC model.

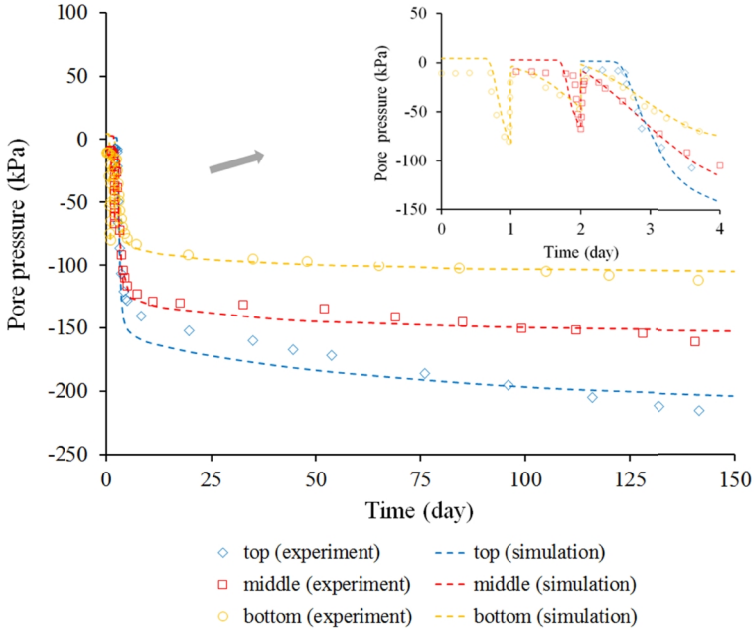

Figure 5.56 Comparison between simulated and measured pore pressure in CPB column

To verify the model capability of characterizing the changes in the mechanical behaviour of CPB in a curing process, the stress-strain curves of quasi-static uniaxial compression tests are simulated with the THMC model and compared with the experimental data, see Figure 5.57. As can be observed, the chemical and strain softening–hardening behaviours of CPB have been reasonably captured by the model, and the simulated response of CPB is in good agreement with that of the column experiments.

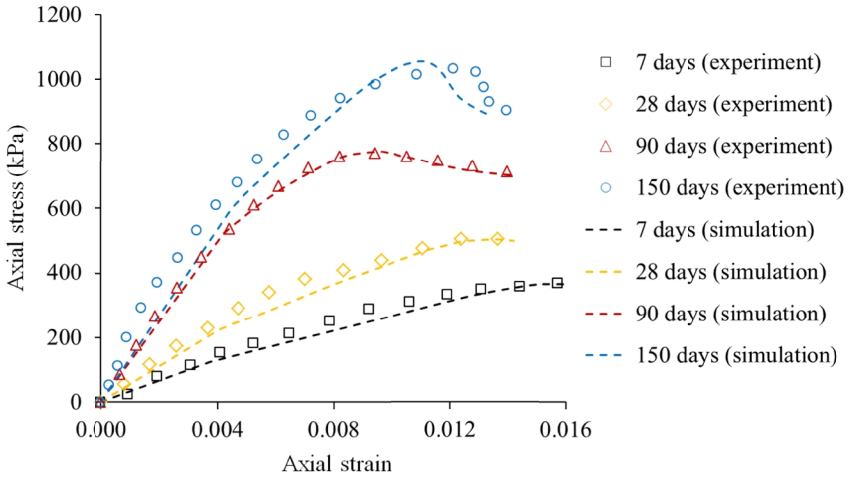

Figure 5.57 Comparison between simulated and measured stress-strain relations of CPB

It can be thus concluded that the THMC model applied in this study is reliable enough to capture the thermal, hydraulic as well as mechanical processes of CPB during its curing period. More case studies that are applied to validate the predictive capability of the THMC model can be found in Cui and Fall (2015).

5.4.3.2 Case Study 2: Laboratory shock loading tests on saturated sand and silt

As the second case study, laboratory tests of soil liquefaction under shock loading carried out on saturated Monterey sand and Bonny silt (Charlie et al., 1985; Bolton et al., 1994) were applied to validate the total-stress viscoplastic model. The tested soils have a grain size distribution (GSD) that well represents the GSD spectrum of typical tailings backfill (Lu and Fall, 2017a).

Soil samples with a height of 152.5 mm and diameter of 68 mm were laterally fixed in a container during the testing, and dynamic axial compression was then applied onto the top of the sample. The shockwaves were modelled as triangular pulses that peak and then reduced back to their initial value both in half a millisecond based on the experimental data. The model parameters used in the total-stress viscoplastic model were obtained from experimental data in Bolton et al. (1994) and those adopted in Wang et al. (2008) for simulations of the same tests, and are provided in Tables 5.17 and 5.18. The simulated variations in volumetric strain and pressure with time at a monitored point in the middle of the tested specimens are presented in Figures 5.58 to 5.60.

Table 5.17 Material properties used in model of shock tests on sand and silt

Test	Initial effective stress (MPa)	Initial pore water pressure (MPa)	Peak pressure (MPa)	Density (kg/m^3)	h (μsec^{-1})	N
Case 1 (sand)	0.172	0.35	5.04	1970	3.5×10^{-6}	1
Case 2 (sand)	0.172	0.35	7.39	1970	5.2×10^{-6}	1
Case 3 (silt)	0.172	0.35	2.66	1848	1.3×10^{-5}	1
f_0 (Pa)	a	k(MPa)	R	D (MPa^{-1})	W	X_0(MPa)
1×10^6	0.25	0	8	4×10^{-3}	0.0011	1
1×10^6	0.25	0	8	4×10^{-3}	0.0011	1
1×10^6	0.225	0	8	4×10^{-3}	0.0011	1

Table 5.18 Material properties used for undrained response of sand and silt in shock tests

Test	n	r_{s0} (kg/m^3)	r_{w0} (kg/m^3)	C_{s0} (m/s)	C_{w0} (m/s)	s_s	s_w	g_{s0}	g_{w0}	$\underline{\nu}$	$\underline{K_p}$ (GPa)
Cases 1-2 (sand)	0.41	1563	1000	310	1460	1.64	2	0.11	0.6	0.33	54
Case 3 (silt)	0.48	1367	1000	221	1460	1.64	2	0.11	0.6	0.33	54

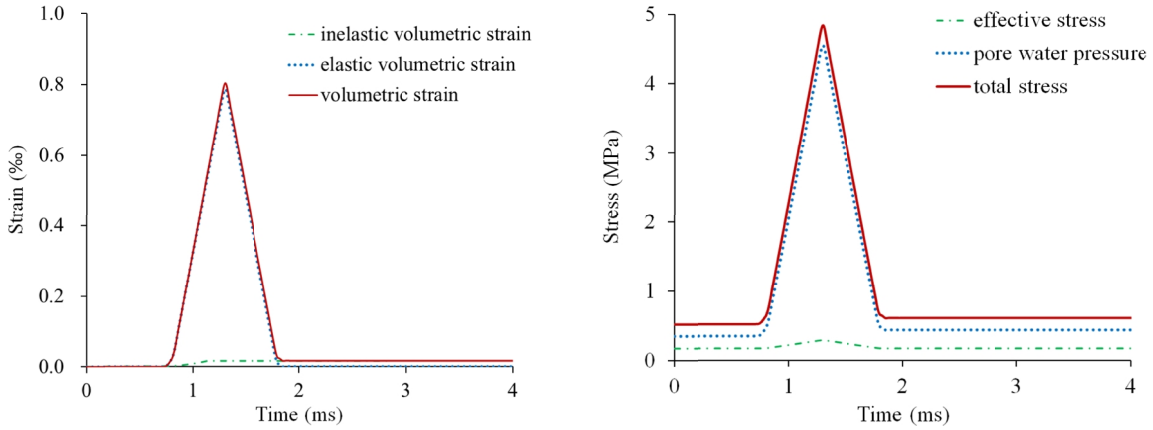

(a) (b)

Figure 5.58 Simulated loading histories of Case 1 (sand): (a) strain-time; (b) pressure-time

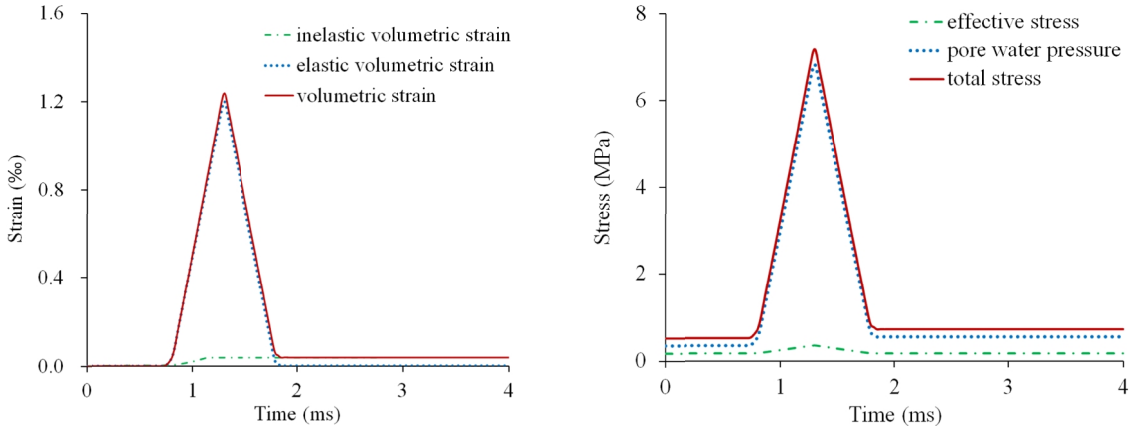

(a) (b)

Figure 5.59 Simulated loading histories of Case 2 (sand): (a) strain-time; (b) pressure-time

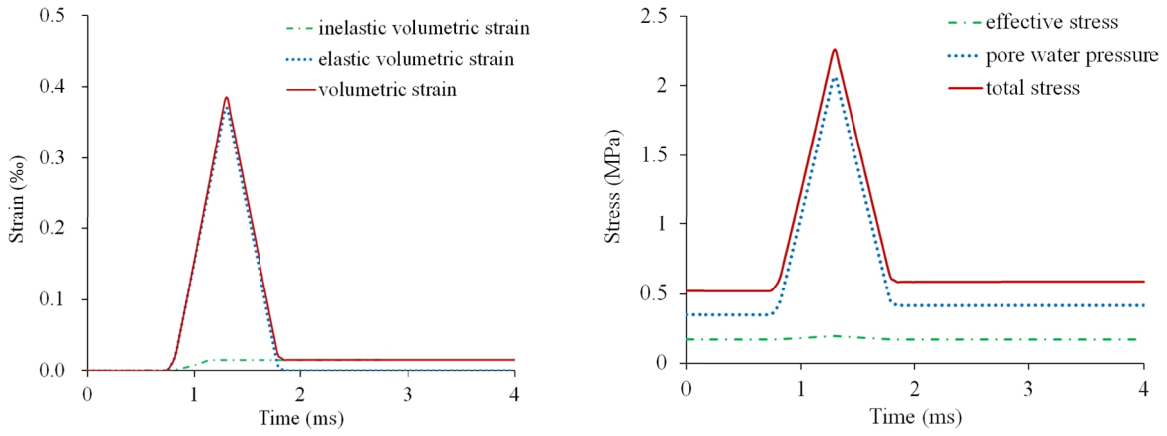

(a) (b)

Figure 5.60 Simulated loading histories of Case 3 (silt): (a) strain-time; (b) pressure-time

As can be observed from Figures 5.58(b)-5.60(b), during initial loading, the pore water supports most of the external load due to the large impedance of its flow under the undrained condition, while the stress carried by the soil skeleton is insignificant by contrast. Then, even though the elastic strain can be recovered after unloading, the pore water pressure still remains above its initial value. This is because the irrecoverable volumetric strain developed during initial loading (shown in Figures 5.58(a)-5.60(a)) has resulted in the generation of residual excess pore pressure. These processes captured by the model are consistent with the mechanism of blast-induced liquefaction in saturated porous media (Fragaszy and Voss, 1986).

The simulated pore pressure response of saturated sand in the shock loading experiments was compared with the test data in Charlie et al. (1985), see Figure 5.61. However, the test data for silt were not available. Figure 5.61 shows a good agreement between the simulated and test results in terms of the peak and residual values of pore pressure. A comparison between the simulated and experimental results for the shock tests on sand and silt is provided in Table 5.19, where the residual pore pressure ratio (PPR) is defined as the residual excess pore pressure divided by the initial effective stress. It can also be observed from Table 5.19 that the simulated results agree with the experimental results. Therefore, the total-stress viscoplastic model can well simulate the mechanical process and pore pressure response of saturated porous media under shock loading.

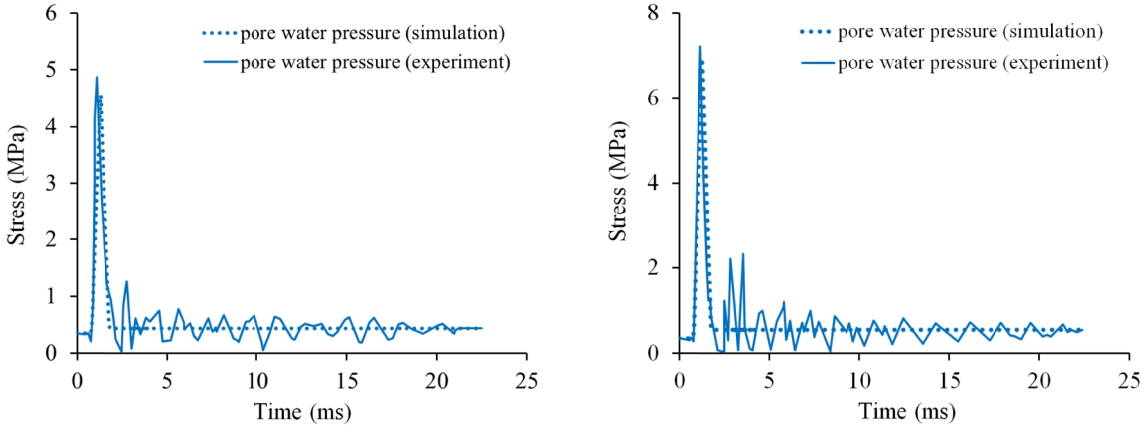

Figure 5.61 Comparison between simulated and measured pore pressure response of sand in the shock tests: (a) Case 1, (b) Case 2

Table 5.19 Comparison between simulated and experimental results for shock tests on sand and silt

Test	Peak pore pressure change (MPa)		Residual pore pressure (kPa)		PPR	
	Tested	Simulated	Tested	Simulated	Tested	Simulated
Case 1 (sand)	4.52	4.20	436	437	0.50	0.51
Case 2 (sand)	6.87	6.50	548	547	1.15	1.14
Case 3 (silt)	2.13	1.81	415	417	0.38	0.39

5.4.3.3 Case Study 3: Canadian Liquefaction Experiment on tailings

To improve the understanding and validate the assessment procedures for liquefaction, mine tailings were filled at a test site in Fort McMurray, Alberta, Canada. The tailings deposit was 10 m in thickness, and the groundwater was 0.5 m below the ground surface (Al-Qasimi et al., 2005). Field explosion tests that were performed in the tailings deposit during the Canadian Liquefaction Experiment (CANLEX) program were adopted as the third case study and simulated with the total-stress viscoplastic model.

Based on the experimental setup of the field test and the variations in the measurements, the simulated range of the model was between 5.5 m to 18 m from an explosion with a 1.5 kg charge. This model size will avoid extrapolation of the field data, and a comparison of the site response is possible while the effect of the boundary conditions is negligible. The configuration of the model is shown in Figure 5.62.

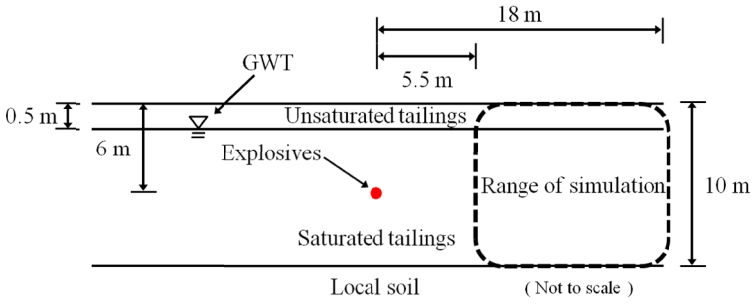

Figure 5.62 Configuration of model for explosion in tailings deposit

The peak particle velocity (V_p) of the incident blast wave that reaches the model boundary in the simulation was obtained by using the following equation developed for the test site (Al-Qasimi et al., 2005):

$$V_p = 47.64\,[R_c / Q_c^{1/3}]^{-2.34} \tag{5.101}$$

where Q_c (kg) and R_c (m) are the mass of the explosives used and the distance to the explosion, respectively. The time-varying pattern of the incident wave was determined from Jiang et al. (1995) and shown in Figure 5.63. The magnitude of the incident wave was obtained by using Equation (5.101). By considering the positional relationship between the locations along the model boundary and the explosive charge, the normal component of the incident wave was applied onto the model boundary.

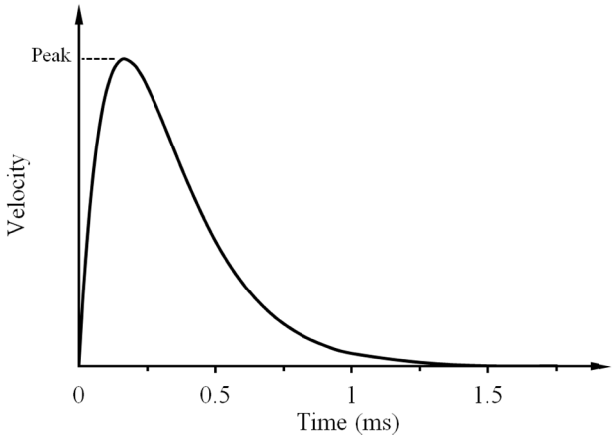

Figure 5.63 Loading pattern of incident wave in field explosion test

The field explosion test was simulated by using 2D symmetry. Low-reflecting boundary conditions were applied at the bottom and far side boundaries of the model, and a constant load was applied on the top to represent the overburden from unsaturated tailings. The parameters of the total-stress viscoplastic model used in the simulation were determined from studies on tested tailings by Puebla et al. (1997) and Al-Qasimi et al. (2005), which are listed in Tables 5.20 and 5.21.

Table 5.20 Material properties used in model for field explosion test on tailings

Density (kg/m^3)	h (μsec^{-1})	N	f_0 (Pa)	a	k (MPa)	R	D (MPa^{-1})	W	X_0 (MPa)
1950	1.5×10^{-5}	1	1×10^{6}	0.18	0	8	1×10^{-2}	0.001	1

Table 5.21 Material properties used for undrained response of tailings in field explosion test

n	r_{s0} (kg/m^3)	r_{w0} (kg/m^3)	C_{s0} (m/s)	C_{w0} (m/s)	s_s	s_w	g_{s0}	g_{w0}	$\underline{\nu}$	$\underline{K_p}$ (GPa)
0.43	1493	1000	219	1460	1.64	2	0.11	0.6	0.3	54

The simulated attenuation of the peak particle velocity (PPV) and peak pore water pressure against scaled distance is compared with the test data in Figure 5.64. It is shown that the simulated results are in agreement with those of the field measurements in terms of both the magnitude and trends of variation. Furthermore, the field tests also indicate that the tailings deposit is liquefied within 6.6 m from the explosion at the depth of burial of the charge (6 m) in the study (Al-Qasimi et al., 2005). The simulated range of the liquefaction after blasting is presented in Figure 5.65(a), which shows that the deposit is liquefied within 6.3 m from the detonation at the examined depth. The simulated attenuation of the PPR against the scaled distance at this depth is illustrated in Figure 5.65(b), in which it is shown that the simulation also agrees well with the empirical law developed for the test site. Therefore, the total-stress viscoplastic model can also well capture the blast wave propagation and resulting development of excess pore pressure in the saturated fill mass.

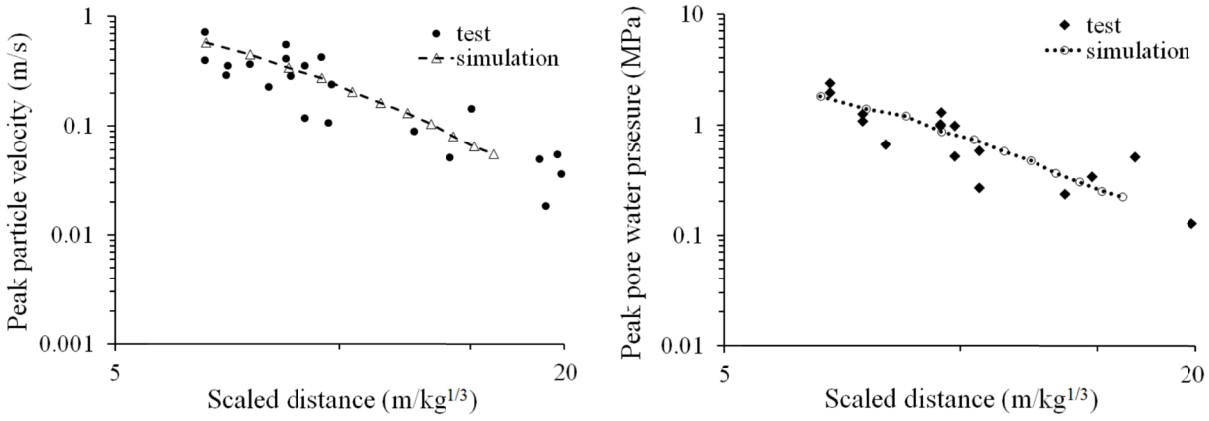

(a) (b)

Figure 5.64 Comparison between simulated and measured attenuation of blast wave: (a) PPV, (b) peak pore water pressure

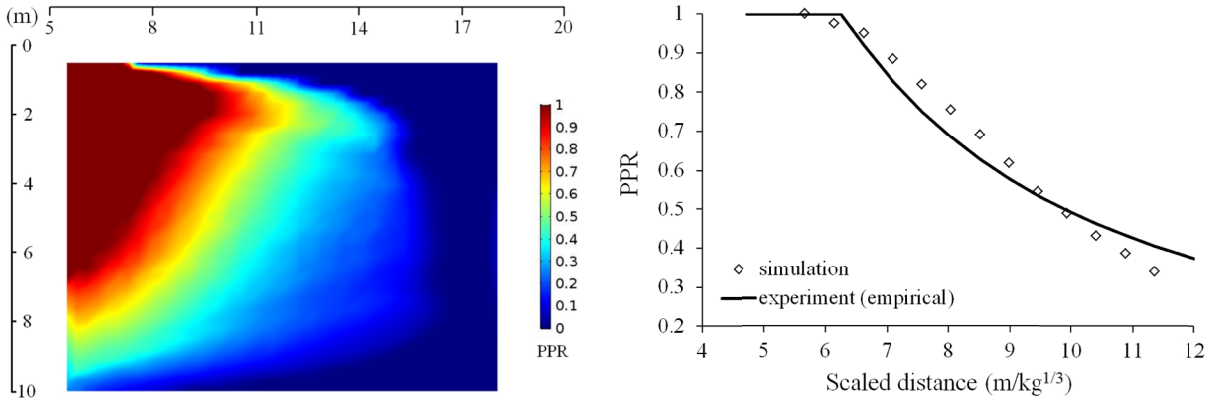

(a) (b)

Figure 5.65 Comparison between simulated and monitored liquefaction after explosion: (a) simulated range of liquefaction; (b) attenuation of PPR

5.4.3.4 Case Study 4: Mine blasts on a backfilled stope in Cayeli Mine

The earth pressure and pore pressure monitoring program in stope 715 N22 at the Cayeli Mine in Turkey (Thompson et al., 2012) was adopted as the fourth case study. The monitored stope was 15 m in height, 8.5 m in width and 14.5 m in length. The tailings backfill used in the stope had a gravimetric water content of 23% and cement content of 6.5%, and was filled at an initial rise rate of 0.3 m/h (Veenstra, 2013).

The total stress monitored at the barricade was 97 kPa at the 20th hour with a backfilled height of 6 m, and thus the filling was terminated at that time. Field monitoring indicated that the

effect of binder hydration is insignificant before the end of the pour, and hydration started at approximately the 20th hour. According to Thompson et al. (2012), the reason is probably because the binder content is relatively low, rate of filling is relatively fast, or the binder hydration might have been retarded due to the tailings chemistry.

During backfilling, two sudden increases in the total stress and pore pressure were observed from the earth pressure cells and piezometers mounted on the barricade as shown in Figure 5.66. At the same time, simultaneous displacements of the barricade were also recorded (not shown here), which are indicative of mine blast operations in the vicinity of the stope (Thompson et al., 2009). In considering that the sampling rate in long-term monitoring is generally insufficient to capture the transient stress variations during such dynamic loadings, the sudden increases in the monitored data should be interpreted as the residual values.

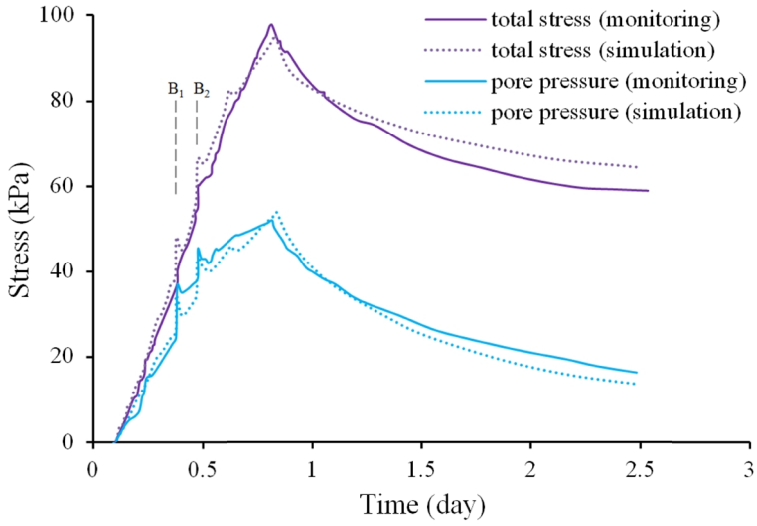

Figure 5.66 Comparison between monitored and simulated total stress and pore pressure on barricade

The model configurations for the simulation of the field test are determined from the stope measurements and presented in Figure 5.67. In the simulation, drainage during filling was allowed through the barricade that was constructed in the access tunnel (drawpoint) at the bottom of the stope, and the rate of flow was determined by Darcy's law. Based on the field data, the first impact (B_1) was applied in the model at the 9th hour (backfill height H_1= 2.7 m), and then stope filling was allowed to continue until the second impact (B_2) was applied in the model at the

11.5th hour (backfill height H_2= 3.4 m). Then, the simulated filling resumed and hydration started at the 20th hour when the first lift was completely poured.

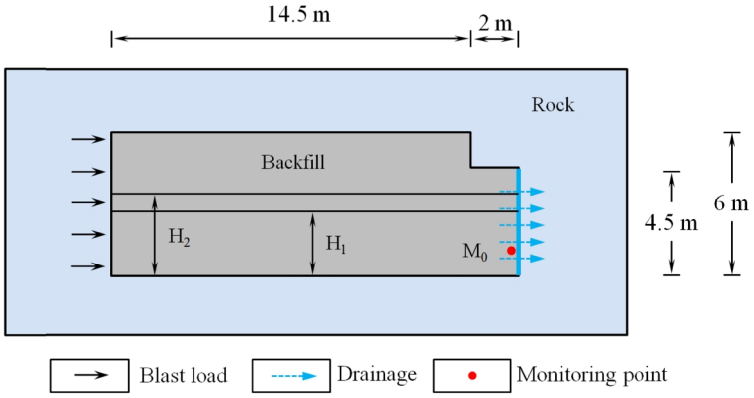

Figure 5.67 Model configuration of 715 N22 stope at Cayeli Mine

The THMC model was used to simulate the filling and curing processes of backfill, and the total-stress viscoplastic cap model was adopted to simulate the excess pore pressure induced by blast loadings. Only the surrounding rock was included in the THMC model. Details of the initial and boundary conditions of the curing environment are provided in Table 5.16. The initial density of the backfill in the Cayeli Mine is 2600 kg/m^3 and the initial hydraulic conductivity K_T is 5.7×10^{-5} cm/s (Thompson et al., 2012). Other backfill properties required for the total-stress viscoplastic cap model for blast loading were assumed to be the same as those of the tailings used in the CANLEX program in Case Study 3. The blast load was assumed to reach the backfill from the opposite side of the stope to the barricade, and applied in the model in the form of velocity impulse and its amplitude was assumed to be uniform. The time-varying pattern of the incident wave is the same as that in Figure 5.63. The magnitude of the two velocity impulses was determined by trial and error, so that the simulated total stress and pore pressure at the monitored point on the barricade (M_0) agree with the field data.

The simulated total stress and pore pressure at M_0, a monitored point of 1.1 m above the floor of the barricade are presented and compared with the field data in Figure 5.66. As can be observed in the figure, the calculated variations in total stress and pore pressure during filling and blasting agree well with the field data. Meanwhile, when the filling was completed and then the binder hydration started to be significant, the model can also well capture the changes in the

total stress and pore pressure with time. Therefore, the variations in total stress and pore pressure under the influence of mine blasting during the curing process of cemented backfill can be reasonably captured by using the THMC and the total-stress viscoplastic cap models.

5.4.4 Analysis of post-blasting stress distribution in hydrating fill mass

5.4.4.1 Model configuration

After validation of the model against both laboratory as well as field data, the model was applied to various practical engineering applications. Three factors; namely, stope geometry, blast operation, and intrinsic properties of backfill that affect the post-blasting stress and pressure distribution in the backfill mass, are examined in this study. Details of the scenarios that incorporate any combination of these factors are provided in Table 5.22. The configurations of a two-dimensional model established to represent the field conditions are shown in Figure 5.68.

Table 5.22 Details of backfilling conditions examined in this study

Case No.	Drainage condition (K_b /K^*)	Stope size (W×H, m)	Distance of barricade to stope (D_b, m)	Distance between charge and stope (D_c, m)	Number of blastings	Initial backfill temperature (T_0, ^{o}C)	Cement content (%)(w/c^{**})
1	0.5	10×25	4	30	1	20	5 (4.6)
2	0.25	10×25	4	30	1	20	5 (4.6)
3	0.125	10×25	4	30	1	20	5 (4.6)
4	0.5	10×35	4	30	1	20	5 (4.6)
5	0.5	10×45	4	30	1	20	5 (4.6)
6	0.5	10×25	7	30	1	20	5 (4.6)
7	0.5	10×25	10	30	1	20	5 (4.6)
8	0.25	10×25	4	20	1	20	5 (4.6)
9	0.25	10×25	4	40	1	20	5 (4.6)
10	0.25	10×25	4	30	2	20	5 (4.6)
11	0.25	10×25	4	30	3	20	5 (4.6)
12	0.125	10×25	4	30	1	10	5 (4.6)
13	0.125	10×25	4	30	1	30	5 (4.6)
14	0.125	10×25	4	30	1	20	2.5 (9.2)
15	0.125	10×25	4	30	1	20	7.5 (3.1)

*: K_b and K represent hydraulic conductivity of barricade and fill mass, respectively.

**: w/c denotes water-to-cement ratio.

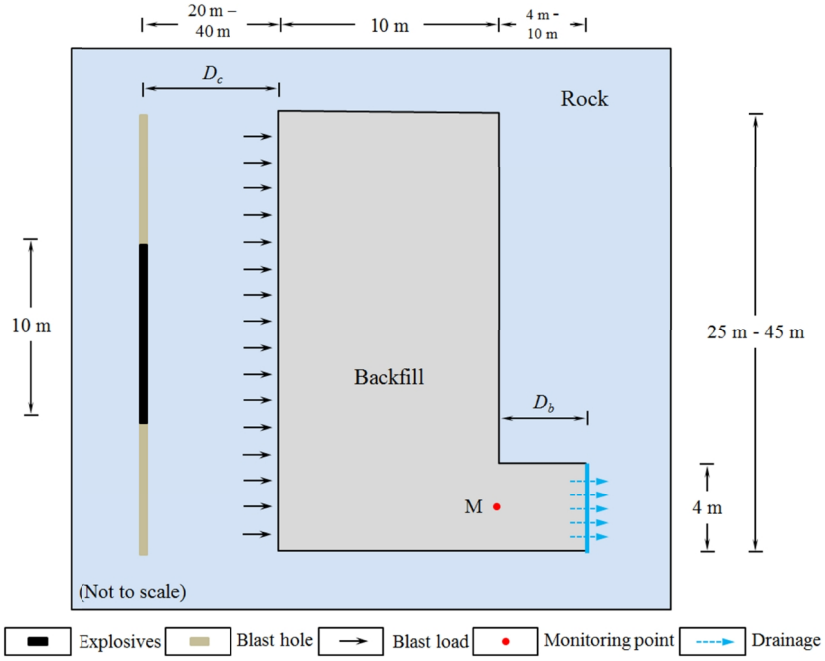

Figure 5.68 Configuration of numerical model

In the numerical analysis, first, the pore pressure and stress distribution during continuous filling at the same rate (12.5 m/d) were obtained from the THMC model for the cemented backfill. Drainage was allowed through the barricade during the placement of saturated backfill. It was also assumed that the hydration of cement in backfill only becomes significant from the 20th hour that the CPB enters the stope, per Case Study 4 of the Cayeli Mine as indicated by Thompson et al. (2012). The initial and boundary conditions of the model are the same as those in Case Study 4, except the varied values examined as indicated in Table 5.22.

Then, the blast wave was applied on the backfill mass once the backfilling was completed, and the time-varying pattern is shown in Figure 5.63. The blast response of the saturated backfill was simulated with the total-stress viscoplastic cap model, and the parameters used and characteristic behaviours of the material were the same as those in Case Study 4. Since production blasting in mines is generally operated in multiple lifts, a borehole packed with 10 m of explosives with a linear charge density of 6.22 kg/m (van Gool, 2007) is considered in this study, and its center is assumed to coincide with the mid-height of the stope. The amplitude of the blast wave that arrived at the stope boundary from the explosion in the rocks can be determined by the following expression (Ahmed and Ansell, 2014):

$$V_p = A_c [R_c / (f_c Q_c)^{b_c}]^{-a_c} \quad (5.102)$$

where constants A_c, a_c, and b_c are 2.94 m/s, 1.32 and 0.66, respectively, in accordance to the monitoring of blast-induced PPV in the rocks of the Cannington Silver and Lead Mine in Australia (van Gool, 2007); and f_c is a factor that represents the effect of the length (L_c) of the explosive charges, defined as $f_c = [\arctan(L_c / 2R_c)] / (L_c / 2R_c)$. By using the positional relationship between points on the stope wall and the explosion source, the normal components of blast waves with amplitudes determined by Equation (5.102) are applied in the model. A low-reflecting boundary is used at the far end of the stope to eliminate wave reflection, and the bottom of the backfill mass is set as a roller boundary condition, while the top is set as a free boundary. The barricade is assumed to be stable during the course of the blast loading.

After the passage of the blast waves, the excess pore pressure was generated by dynamic loading and added to the initial pore pressure of the backfill when filling was completed. Then, the dissipation of pore pressure due to both drainage through the barricade and binder hydration took place, and this process was characterized by using the THMC model for hydrating backfill. A monitoring point (M) was set at the intersection of the stope and drawpoint was 2 m above the floor. The results of the numerical analysis of post-blasting stress and pore pressure distribution in the backfill mass in various practical engineering conditions are discussed in the following sections.

5.4.4.2 Discussion

5.4.4.2.1 Effect of drainage conditions

The drainage condition of backfill mass has a significant impact on the rate of the pore pressure dissipation, thus affecting the stress distribution after dynamic loadings in a backfilled stope. Three different hydraulic conductivities of the barricade material (K_b)with respect to that of the backfill (K) are considered in this study, i.e. K_b=0.5K (Case 1), K_b=0.25K (Case 2), and K_b =0.125K (Case 3), which imply that the side length of the barricade varies by an increment of two times in each case (Fahey et al., 2009; Helinski et al., 2010).

To better understand the variations in stress of the fill mass after blast impact, the short-term redistribution of the excess pore pressure (Δu) induced by dynamic loading on the backfilled stope with time for Case 3 is illustrated in Figure 5.69. The figure shows that the accumulation of

Δu is close to the loading boundary right after the blast, and would cause a sudden increase of the total head on the loading side of the stope. Consequently, Δu is redistributed towards the opposite side of the stope where the material is less affected by dynamic loading and has a lower total head. Besides, Δu also migrates towards the bottom of the stope where the total head is lower due to more drainage as well as earlier start of binder hydration which consumes the pore water. Meanwhile, with continuous drainage and binder hydration, Δu will simultaneously dissipate along with its redistribution, and the magnitude of Δu in the stope would decrease rapidly with time. The variation of Δu in a longer time span is presented in Figure 5.70. The figure suggests that the Δu value is greater at a lower part of the stope, and can be completely dissipated after roughly 14 hours in the studied backfilled stope. This dissipation time will certainly vary with the type and composition of the backfill, drainage and initial conditions, and the field conditions.

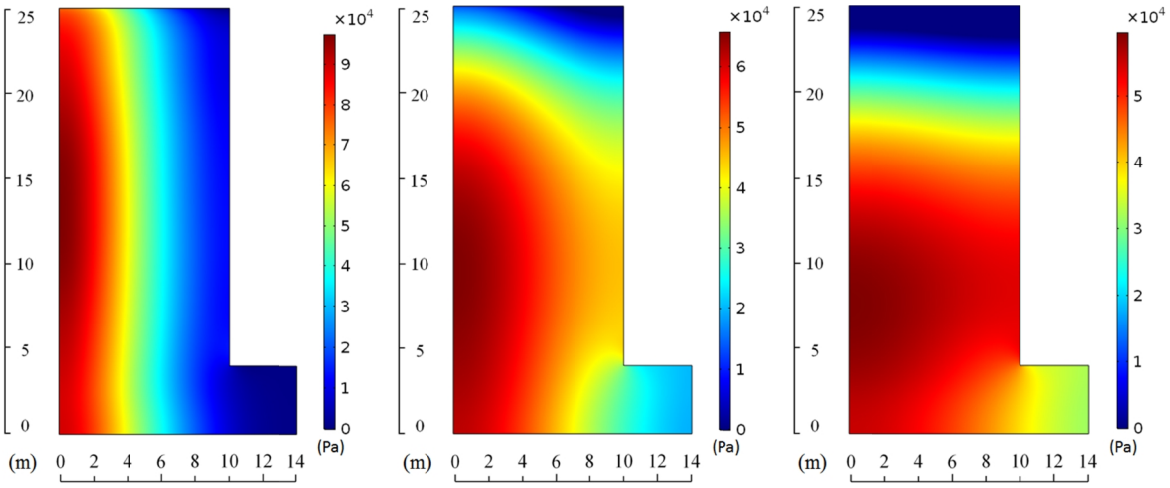

(a) (b) (c)

Figure 5.69 Variation in excess pore pressure for Case 3 (K_b=0.125 K): time after blasting: (a) 0 h; (b) 1 h; and (c) 2 h

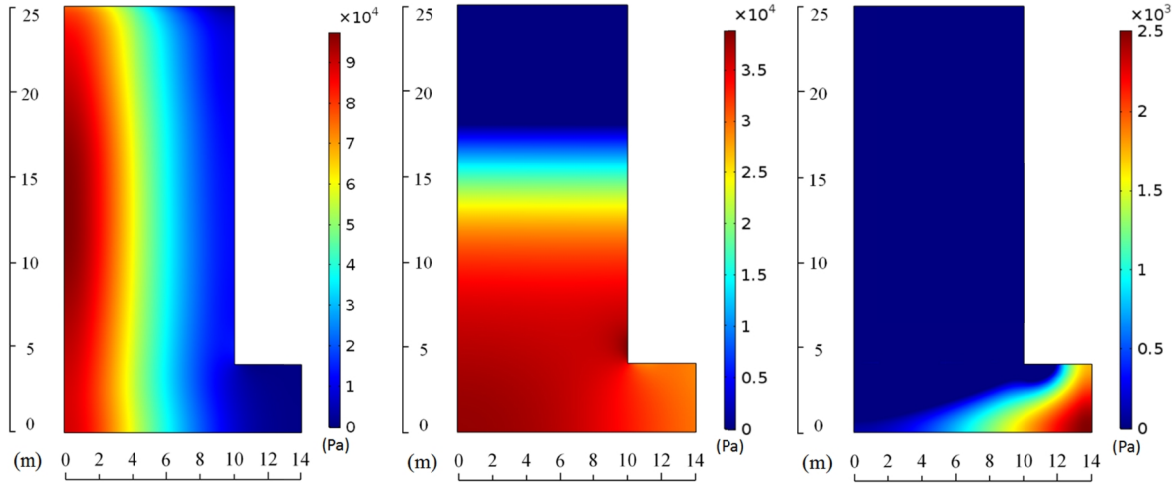

(a) (b) (c)

Figure 5.70 Variation in excess pore pressure for Case 3 (K_b=0.125 K): time after blasting: (a) 0 h; (b) 7 h; and (c) 14 h

The variations in the horizontal total stress (s_h) and pore pressure at the monitored point for Cases 1-3 are illustrated in Figure 5.71. It can be observed that Case 1, which has the fastest rate of drainage, has the lowest pore pressure when filling is completed. Then, after blasting takes place at the end of the backfilling, Δu induced by dynamic loading will redistribute within the stope and sudden increases in pore pressure can be observed. It is also shown that Case 1 has the lowest peak in pore pressure right after blasting. As well, the pore pressure dissipates more rapidly afterwards due to the enhanced drainage.

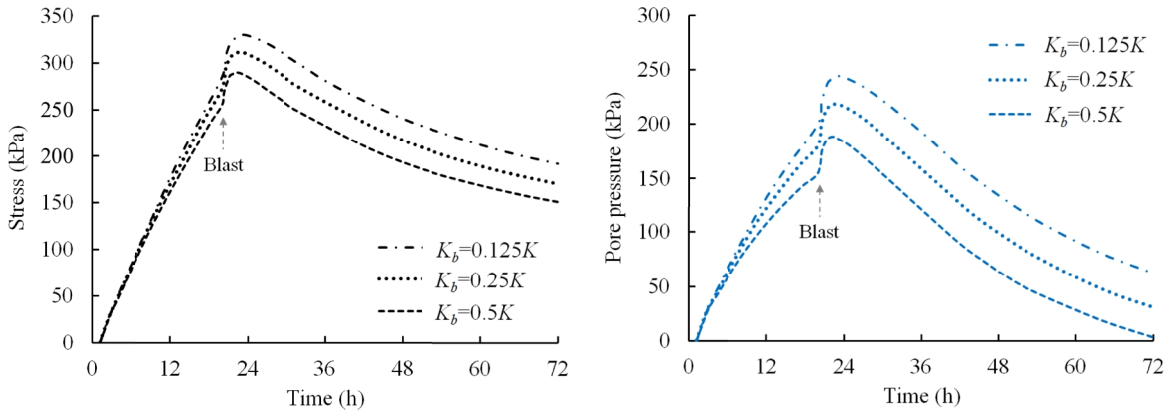

(a) (b)

Figure 5.71 Variations in stress at monitored point: (a) total horizontal stress and (b) pore pressure

Meanwhile, as water drains out through the barricade, both the pore pressure and vertical total stress are reduced due to the loss of water. Therefore, the vertical effective stress does not increase as much as the pore pressure decreases. In addition, since the ratio of the horizontal effective stress over the vertical effective stress is always less than 1 (Fahey et al., 2009), s_h will demonstrate the same trend of variation as that of pore pressure. This corresponds to the results shown in Figure 5.71; Case 1 which has the fastest rate of drainage is also associated with the lowest s_h at all times.

Therefore, the drainage condition of backfill mass will significantly influence the blast-induced stress that acts on its retaining structure. Enhancement of drainage by using different means such as extending the side length of the barricade, can be used to improve the stability of the retaining structure.

5.4.4.2.2 Effect of stope size

The size of the mine stope varies in the field due to the irregular shape of the ore body and different strategies adopted in mine planning, and will affect the stress distribution in backfill mass. Three stopes with a height of 25 m (Case 1), 35 m (Case 4) and 45 m (Case 5) are examined in this work. Although the hydration of cement starts before blasting at the end of the filling process in Cases 4 and 5 (as discussed earlier), and a longer time for filling at the same rate is required, the same characteristic blast response of the backfill is assumed in this study as a

conservative measure. The influence of the stope size on the horizontal stress and pore pressure at the monitoring point in Cases 1, 4 and 5 is shown in Figure 5.72.

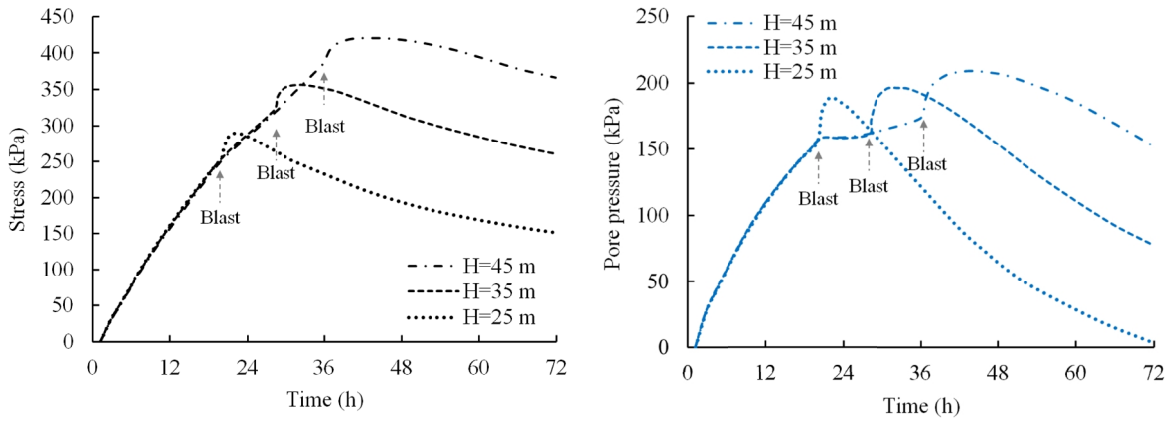

(a) (b)

Figure 5.72 Variation of stress at monitored point: (a) total horizontal stress, and (b) pore pressure

It can be observed that, as the hydration of cement starts to be significant at the 20th hour for the studied backfill, the increase in the pore pressure during the filling process in the higher stopes (Cases 4 and 5) is reduced from that time onwards. However, as the excess pore pressure caused by blasting impacts is redistributed, there is also larger pore pressure in the higher stopes. This is primarily because for higher stopes, more Δu will be generated by blasting at the same distance due to an increase in the surface (boundary) subjected to dynamic loading. In addition, more water from relatively fresh backfill can move from the top of the stope downwards under a larger position head in higher stopes. Therefore, although increased stope height would imply more pore pressure that is exerted on the barricade and thus more rapid drainage, it does indeed led to higher pore pressure and slower rate of dissipation for the backfill considered, as shown in Figure 5.72. Meanwhile, it is also shown that the total stress on the barricade significantly increases for stopes with greater heights.

The results and discussion presented above show that the stope size has a pronounced effect on blast-induced stress distribution in backfill.

5.4.4.2.3 Effect of barricade location

The location of the barricade in the mine drift varies in practice in accordance with the different types of mine planning, and may change the total stress and pore pressure distribution in backfill mass due to the variation in stope geometry. Three scenarios with a barricade located at a distance (D_b) of 4 m (Case 1), 7 m (Case 6) and 10 m (Case 7), respectively, away from the intersection of the stope and access tunnel are examined, and the variations in the horizontal stress and pore pressure at the monitored point is illustrated in Figure 5.73.

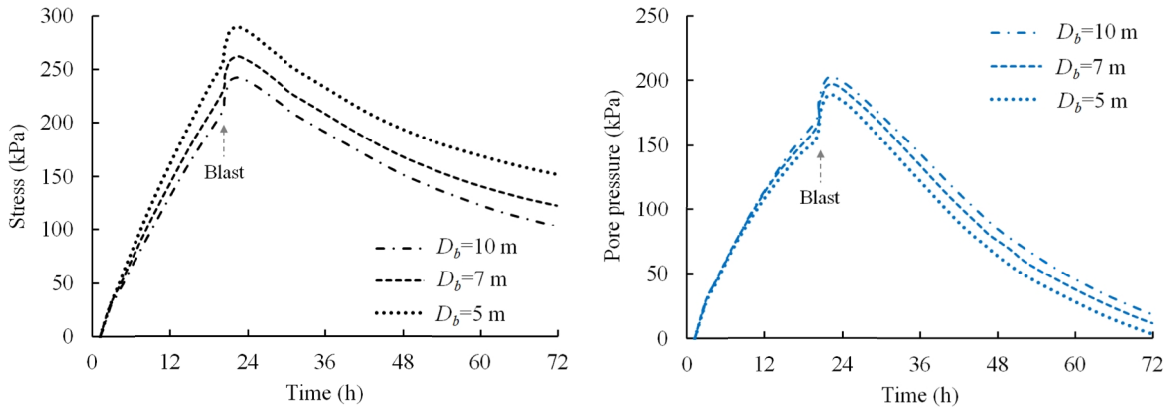

(a) (b)

Figure 5.73 Variations in stress at monitored point: (a) total horizontal stress and (b) pore pressure

As can be noticed, the pore pressure is higher at all times during filling and after blasting as the barricade is located farther from the stope. This is because extending D_b would increase the length of the flow path to the drainage point, thus reducing the efficiency of pore pressure dissipation.

However, despite that the drainage is relatively inhibited by increasing D_b, it can also reduce the s_h as shown in Figure 5.73. In fact, as D_b increases, the backfill at the stope bottom becomes less compressed and thus the horizontal strain and stress would consequently decrease.

Thus, the optimal location of a barricade in practice should be designed from both the perspective of reducing the s_h and enhancing the pore pressure dissipation.

5.4.4.2.4 Effect of proximity of detonation

Stress waves that arrive at the backfill mass may originate from mine blasting at various distances (D_c) as mining is carried out in separate stopes. The proximity of the backfill to the explosive charge has a tremendous effect on the excess pore pressure development (Al-Qasimi et al., 2005) and the stress that acts on the retaining structure.

The simulated distribution of Δu caused by blasting right after the passage of stress waves for stopes located at 20 m (Case 8), 30 m (Case 2), and 40 m (Case 9) from the detonation is depicted in Figure 5.74. As can be observed, Δu increases considerably as the explosion takes place closer to the backfilled stope.

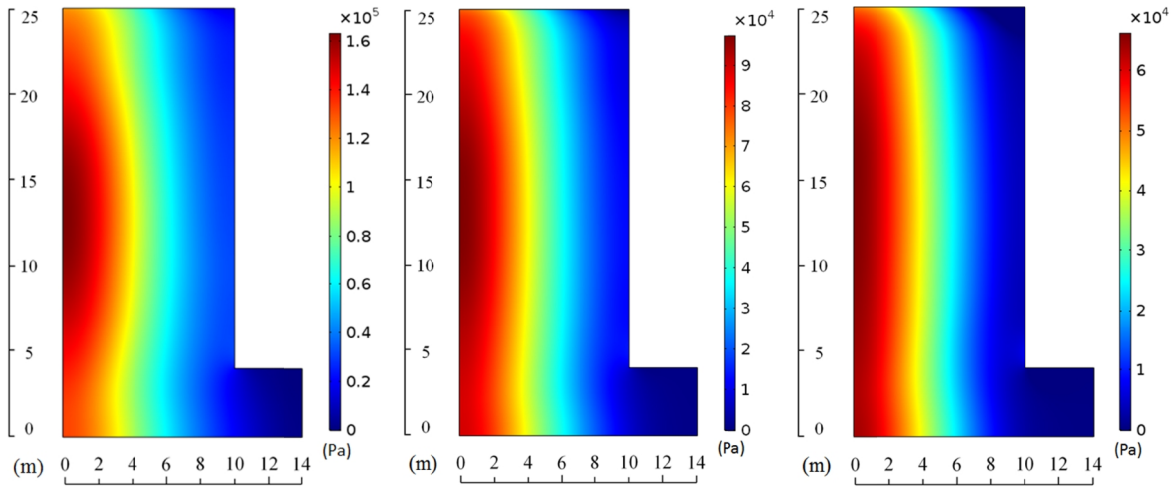

(a) (b) (c)

Figure 5.74 Excess pore pressure generated by blast loading right after passage of stress wave: (a) Case 8 (D_c=20 m); (b) Case 2 (D_c=30 m); and (c) Case 9 (D_c=40 m)

The variations in the s_h and pore pressure at the monitored point for Cases 2, 8 and 9 are plotted in Figure 5.75. The plots show that there is greater pore pressure in the stope of Case 8 which is located in closer proximity to the charge (D_c =20 m) during its redistribution and dissipation after blasting. This is primarily because greater Δu is generated by a dynamic load with higher amplitude. As previously discussed, the horizontal total stress (s_h) will also exhibit the same trend of variation as the pore pressure under the same stope geometry, i.e. when s_h is greater and detonation is carried out closer to the stope.

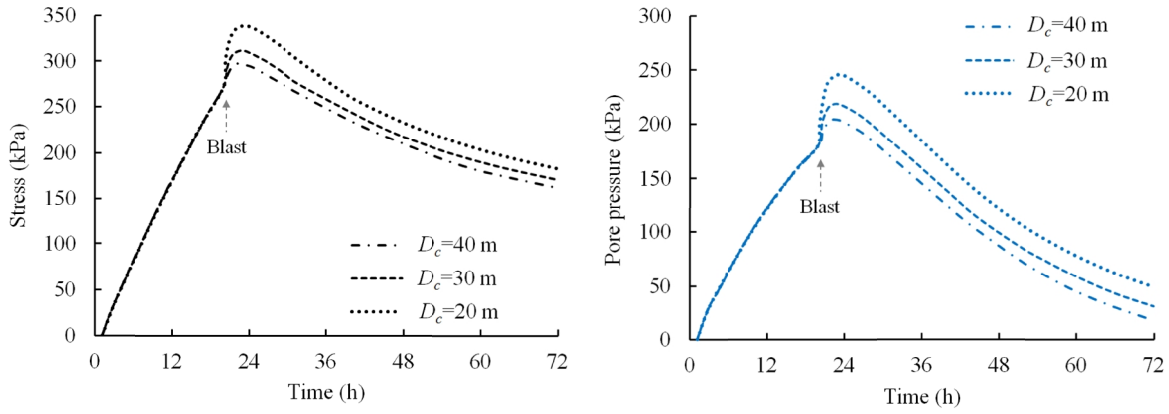

(a) (b)

Figure 5.75 Variations in stress at monitored point: (a) total horizontal stress and (b) pore pressure

It can thus be concluded that mine blasting carried out in the vicinity of freshly backfilled stopes will significantly increase the load on barricades. Therefore, maintaining a safe distance between the implementation of mine blasting and backfilled stopes will contribute to the stability of retaining structures.

5.4.4.2.5 Effect of blast sequences

Multiple explosive columns with time lags are conventionally used to blast ore pillars in mining, and thus the effect of blast loading sequences is examined in this study. One (Case 2), two (Case 10) and three (Case 11) blasts with the same magnitude and time history are applied to the model boundary with 2.5 ms of delay between each loading.

The variations in the horizontal stress and pore pressure at the monitored point are presented Figure 5.76. The figure shows that both horizontal stress and pore pressure increase with additional impacts during the redistribution and dissipation of pore pressure after blasting. This is due to increased excess pore pressure generated by consecutive dynamic loadings. Therefore, consecutive blasts will significantly increase the loads that act on a barricade and thus affect its stability. There should be sufficient delays between each detonation which would allow for the dissipation of the pore pressure so as to reduce the load on the retaining structure.

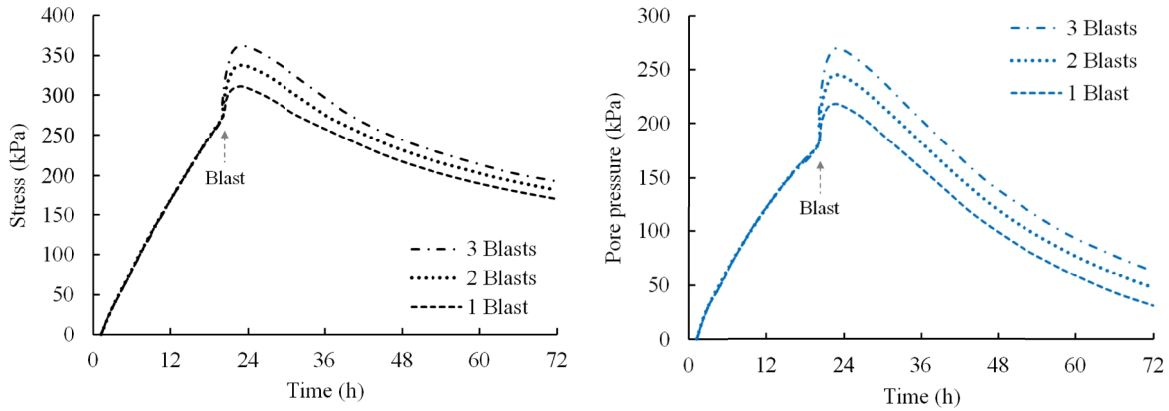

(a) (b)

Figure 5.76 Variation in stress at monitored point: (a) total horizontal stress and (b) pore pressure

5.4.4.2.6 Effect of initial backfill temperature

The initial temperature of backfill (T_0) varies in the field mainly due to the different temperature of the mix components and geographical location of the backfill plant. The effects of three different T_0 are investigated in this study, i.e. T_0 =10°C (Case 12), T_0 =20°C (Case 3), and T_0 =30°C (Case 13), and the variations in the total stress and pore pressure at the monitored point are presented in Figure 5.77.

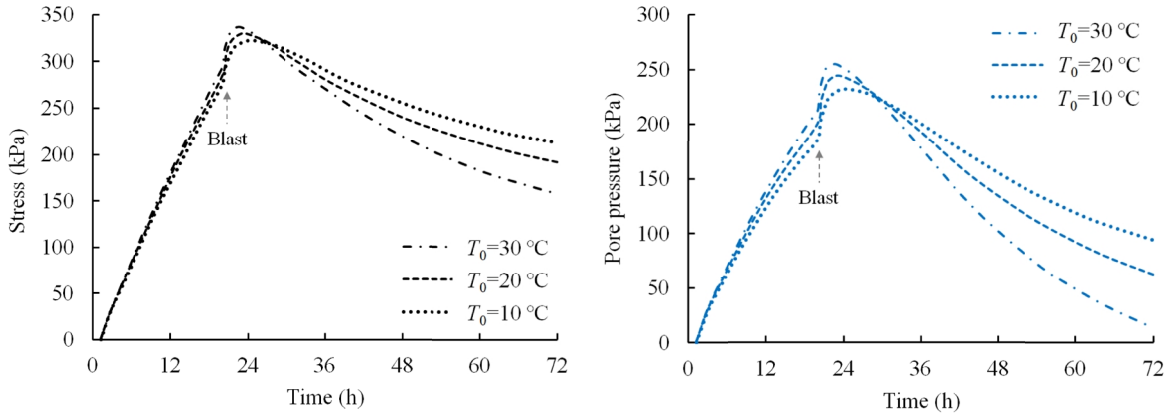

(a) (b)

Figure 5.77 Variations in stress at monitored point: (a) total horizontal stress and (b) pore pressure

It can be observed that the case with a higher T_0 results in greater pore pressure at the end of filling and initial stage of hydration, while there is lower pore pressure at a more advanced age for the backfill considered in this study. This phenomenon is attributed to the coupled effect of temperature on both the fluid flow velocity and rate of binder hydration. Specifically, temperature increases will considerably increase the flow of water due to the sensitivity of its dynamic viscosity to temperature (Equation (5.74)). For example, the dynamic viscosity of water would decrease from 1.308 $\times 10^{-3}$ to 7.978 $\times 10^{-4}$ Pa·s when the temperature increases from 10°C to 30°C (Equation (5.79)), while the resulting reduction of density is from 999.7 to 995.6 kg/m^3 (Equation (5.79)) which is less pronounced. Therefore, before the effect of cement hydration becomes significant, the supply of water from freshly placed backfill can move more rapidly downwards and thus increase the pore pressure at the stope bottom in Case 13 with a higher initial temperature, despite that the rate of drainage is also faster as shown in Figure 5.78. In fact, similar counterintuitive conclusions have been found in Helinski et al. (2007), in which greater backfill permeability has indeed resulted in greater pore pressure at the stope bottom during filling.

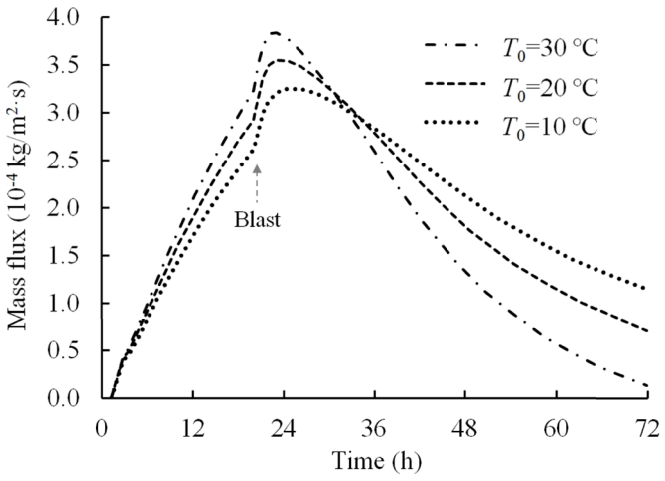

Figure 5.78 Rate of drainage at the center of barricade surface

Meanwhile, the temperature increase also increases the rate of hydration (Equation (5.66)), and this would, first of all, result in more rapid water consumption and pore pressure reduction, although the rate of drainage is also relatively slower. In addition, increased exothermic hydration can also generate more heat and thus further increase the rate of hydration as well as

reduce the water viscosity and speed up the water flow. However, increased exothermic hydration could also reduce the fluid velocity and thus the rate of drainage by decreasing the hydraulic conductivity (Equation (5.75)) due to the faster precipitation of hydration products in the flow conducting channels (pores). The effects of these coupled mechanisms on the rate of drainage of a barricade are illustrated in Figure 5.78. As can be observed, the drainage is still relatively faster in Case 13 with a higher T_0 in the first few hours of hydration. Then, due to the rapid dissipation of pore pressure and reduction in fluid conducting capability, the rate of drainage would decrease even more so at the advanced ages.

However, despite the complex mechanisms that facilitate and inhibit the dissipation of pore pressure at the same time, the monitored pore pressure at stope bottom shows an overall decreasing trend as T_0 increases when the backfill considered in this study reaches a more advanced age. Meanwhile, s_h also shows a similar trend of variation as that of the pore pressure with changes in T_0.

5.4.4.2.7 Effect of cement content

The amount of cement used in backfill preparation varies in practice to meet the criteria for strength at a reasonable cost. This is a crucial design parameter as the use of binder can be 75% of the total cost of backfill operations (Grice, 1998). Three different backfill recipes in terms of cement content are studied, i.e. 2.5% (52.8 kg/m^3, Case 14), 5% (105.7 kg/m^3, Case 3), and 7.5% (158.5 kg/m^3, Case 15), and the simulated variations of the total stress and pore pressure at the monitored point are presented in Figure 5.79.

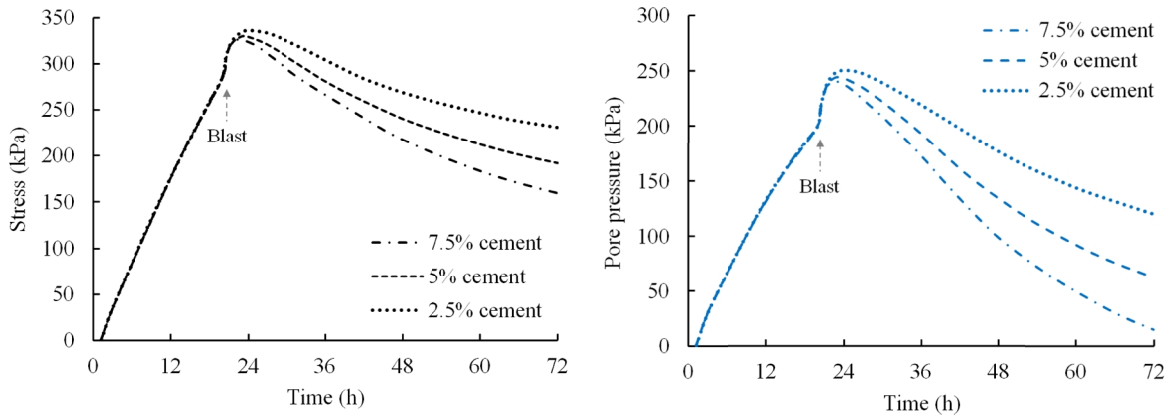

(a) (b)

Figure 5.79 Variations in stress at monitored point: (a) total horizontal stress and (b) pore pressure

As can be observed, the use of more binder results in lower pore pressure during its redistribution and dissipation after blasting, and this becomes more pronounced as the backfill reaches a more advanced age. This is because increased cement content in backfill can cause more water consumption and pore pressure reduction by hydration, although it would also reduce the efficiency of drainage. Besides, it could generate more heat which further contributes to hydration as well as increase the water flow, while the hydraulic conductivity and rate of drainage would also be reduced more rapidly. The coupled effects of hydration on the rate of drainage through a barricade are illustrated in Figure 5.80, which shows that Case 14 which uses less binder has indeed better efficiency of draining. Similar to the previously discussed effect of temperature, the monitored loads presented in Figure 5.79 still demonstrate an overall decreasing trend as the cement content is increased, despite its complex effect on pore pressure dissipation.

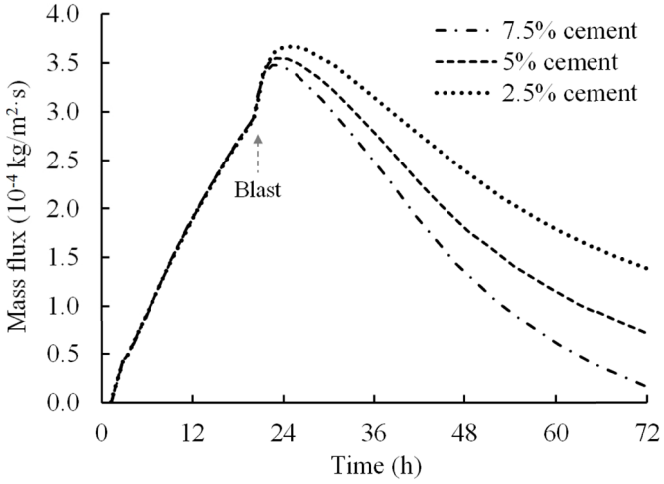

Figure 5.80 Rate of drainage at the center of barricade surface

From the results presented above, it can be concluded that increased cement content in backfill can significantly reduce the blast-induced loads that act on the retaining structure with time. Its benefit of load reduction may decrease as the drainage is relatively inhibited. Therefore, an optimal calculation of the cement content is necessary not only to ensure the backfill strength and control the operation cost, but also reduce the stress on the barricade while taking better advantage of its drainage capability.

5.4.5 Conclusions

To analyze the redistribution of stress and pore pressure in backfilled stopes after mine blasting, a total-stress viscoplastic cap model and a THMC model for CPB are integrated and applied. The results of the model validation show good agreement between the simulation and experimental data.

The results of the model application for various practical engineering conditions suggest that stope geometry, blast operation, and the intrinsic properties of backfill all have significant influence on the post-blasting stress and pore pressure redistribution in backfilled stopes due to different mechanisms. Notably, enhanced backfill drainage, and avoiding consecutive detonations in close proximity to the backfill can effectively reduce the stress that acts on the retaining structure. Meanwhile, this study has also highlighted the importance of an optimal backfill design due to the complex effects of other parameters on the stability and cost of backfill

systems. Specifically, reducing the blast-induced stress by reducing the stope height or extending the drawpoint outwards can be achieved by compromising the liquefaction resistance or drainage efficiency of the fill mass. Besides, while increasing the initial backfill temperature can contribute to significantly greater stress reduction at a more advanced age, the retaining structure may indeed be subjected to higher stress from the material at the early ages if there is a delay in the cement hydration. Finally, the increase of cement in a backfill recipe can also lead to more rapid stress reduction. However, this would cost more and reduce the effect of the drainage facility at the same time. Therefore, all of these influencing factors should be balanced with respect to the stability of the backfill and retaining structure as well as the operation cost in a rational backfill design.

5.4.6 References

Ahmed L, Ansell A. Vibration vulnerability of shotcrete on tunnel walls during construction blasting. Tunnelling and Underground Space Technology 2014;42:105–111.

Al-Qasimi EMA, Charlie WA, Woeller DJ. Canadian liquefaction experiment (CANLEX): Blast-induced ground motion and pore pressure experiments. Geotechnical Testing Journal 2005; 28(1): 1–13.

An J, Tuan CY, Cheeseman BA, Gazonas GA. Simulation of soil behaviour under blast loading. International Journal of Geomechanics, ASCE 2011; 11:323–334.

Awad AA. A numerical model for blast–induced liquefaction using displacements–pore pressure formulations. Ph.D. Thesis. Colorado State University, Colorado, USA, 1990.

Bolton JM, Durnford DS, Charlie WA. One–dimensional shock and quasi–static liquefaction of silt and sand. Journal of Geotechnical Engineering, ASCE 1994; 120:1874–1888.

Charlie WA, Veyera GE, Doehring DO, Abt SR. Blast induced liquefaction potential and transient pore water pressure response of saturated sands. Technical report. Fort Collins: Colorado State University; 1985.

Chen WF, Baladi GY. Soil Plasticity: Theory and Implementation. Elsevier: Amsterdam, 1985.

Cui L, Fall M. A coupled thermo–hydro-mechanical–chemical model for underground cemented tailings backfill. Tunnelling and Underground Space Technology 2015; 50: 396–414.

Cui L, Fall M. An evolutive elasto–plastic model for cemented paste backfill. Computer and Geotechnics 2016; 71: 19-29.

Doherty JP. A numerical study into factors affecting stress and pore pressure in free draining mine stopes. Computers and Geotechnics 2015; 63: 331–341.

Fahey M, Helinski M, Fourie A. Some aspects of the mechanics of arching in backfilled stopes. Can Geotech J 2009;46(11):1322–36.

Ferdosi B, James M, Aubertin M. Numerical simulations of the seismic and post-seismic behaviour of tailings. Canadian Geotechnical Journal 2015; 52: 1-8.

Fragaszy RJ, Voss ME. Undrained compression behaviour of sand. Journal of Geotechnical Engineering, ASCE 1986; 112(3): 334–347.

Ghirian A, Fall M. Coupled thermo–hydro–mechanical–chemical behaviour of cemented paste backfill in column experiments. Part I: Physical, hydraulic and thermal processes and characteristics. Engineering Geology 2013; 164:195–207.
Ghirian A, Fall M. Coupled thermo–hydro–mechanical–chemical behaviour of cemented paste backfill in column experiments. Part II : Mechanical, chemical and microstructural processes and characteristics. Engineering Geology 2014; 170:11–23.
Grice T. Underground mining with backfill. Proceedings of the 2nd Annual Summit-Mine Tailings Disposal Systems Australian 1998, 234-239.
Griffiths DV. The effect of pore fluid compressibility on failure loads in elasto-plastic soil. International Journal for Numerical and Analytical Methods in Geomechanics 1985; 9(3), 253–259.
Helinski M, Fahey M, Fourie A. Numerical modeling of cemented mine backfill deposition. Journal of Geotechnical and Geoenvironmental Engineering 2007; 133(10): 1308–1319.
Helinski M, Fahey M, Fourie A. Coupled two-dimensional finite element modelling of mine backfilling with cemented tailings. Canadian Geotechnical Journal 2010; 47: 1187–1200.
Ishihara, K. Post-earthquake failure of a tailings dam due to liquefaction of the pond deposit. In Proceedings of the International Conference on Case Histories in Geotechnical Engineering, 1984, 1129–1143.
Jiang J, Blair DP, Baird GR. Dynamic response of an elastic and viscoelastic full-space to a spherical source. International Journal for Numerical and Analytical Methods in Geomechanics 1995; 19:181-193.
Katona MG. Evaluation of viscoplastic cap model. Journal of Geotechnical Engineering, ASCE 1984; 110(8):1106–1125.
Klein K, Simon D. Effect of specimen composition on the strength development in cemented paste backfill. Canadian Geotechnical Journal 2006; 43:310–324.
Lee WY. Numerical modeling of blast induced liquefaction. PhD thesis. Brigham Young University, 2006.
Lu G, Fall M. A coupled chemo-viscoplastic cap model for simulating the behaviour of hydrating cemented tailings backfill under blast loading. International Journal for Numerical and Analytical Methods in Geomechanics 2016; 40:1123–1149.
Lu G, Fall M. Simulation of blast induced liquefaction susceptibility of subsurface fill mass. 2017a. (Submitted).
Lu G, Fall M. Modelling blast wave propagation in a subsurface geotechnical structure made of an evolutive porous material. Mechanics of Materials 2017b; 108:21–39.
Lu G, Fall M, Yang Z. An evolutive bounding surface plasticity model for early-age cemented tailings backfill under cyclic loading. 2017. (Submitted).
Naylor DJ. Stresses in nearly incompressible materials by finite elements with application to the calculation of excess pore pressures. International Journal for Numerical and Analytical Methods in Geomechanics 1974; 8(3): 443–460.
Puebla H, Byrne PM, Phillips R. Analysis of CANLEX liquefaction embankments: prototype and centrifuge models. Canadian Geotechnical Journal 1997;34:641–657.
Schindler AK, Folliard KJ. Heat of hydration models for cementitious materials. ACI Material Journal 2005;102(1):24–33.
Schindler AK. Effect of temperature on hydration of cementitious materials. ACI Material Journal 2004; 101(1):72–81.

Thompson BD, Grabinsky MW, Counter DB, Bawden WF. In-situ measurements of cemented paste backfill in longhole stopes. In ROCKENG09: Proceedings of the 3rd CANUS Rock Mechanics Symposium, Toronto, May 2009.

Thompson BD, Bawden WF, Grabinsky MW. In situ measurements of cemented paste backfill at the Cayeli Mine. Canadian Geotechnical Journal 2012;49: 755–772.

Tong X, Tuan CY. Viscoplastic cap model for soils under high strain rate loading. Journal of Geotechnical and Geoenvironmental Engineering, ASCE 2007; 133(2):206–214.

van Genuchten MT. A closed-form equation for predicting the hydraulic conductivity of unsaturated soils. Soil Science Society of America Journal 1980;44:892–898.

van Gool BS. Effects of blasting on the stability of paste fill stopes at Cannington Mine. Ph.D. Thesis. James Cook University, Townville, Australia, 2007.

Veenstra RL. A design procedure for determining the in situ stresses of early age cemented paste backfill. Ph.D. Thesis. University of Toronto, Toronto, Canada, 2013.

Wang Z, Lu Y, Bai C. Numerical analysis of blast–induced liquefaction of soil. Computers and Geotechnics 2008; 5:196–209.

Yumlu M, Guresci M. Paste backfill bulkhead monitoring–a case study from Inmet's Cayeli mine, Turkey. In Proceedings of the 9th International Symposium in Mining with Backfill, Montréal, Quebec, 2007.

Chapter 6.
Results Synthesis and Discussion

6.1 Introduction

The blast response of cemented tailing backfill (CTB) is significantly affected by the multiphysics processes to which the material has been subjected, prior to dynamic loading. Fundamental models were developed and validated in Chapter 4 of this study, to incorporate and characterize the effect of THMC factors on the blast response of CTB during its curing process. These models were then applied in Chapter 5 to investigate the effects of various practical backfilling conditions and design strategies on the field behaviour of hydrating fill mass under blast loading. The features and applicability of the fundamental models developed in this study are summarized in this chapter. Additionally, the study findings are synthesized in this chapter, to facilitate a better understanding of the blast response of CTB during the multiphysics processes of curing, and of how to derive a more rational backfill design.

6.2 Features and applicability of developed models for blast response of CTB

6.2.1 Coupled chemo-viscoplastic cap model

The coupled chemo–viscoplastic cap model incorporates the effect of binder hydration on the mechanical response of CTB under blast loading. Specifically, with respect to the blast response, the modified viscoplastic cap model developed in this study considers the typical rate-dependence, irrecoverable compaction, strain hardening, full compaction, and nonlinear hydrostatic behaviours of porous media upon blast load application. These characteristic phenomena among porous media have also recently been observed and identified in the blast response of CTB. As for the effect of chemical processes, the model adopts a binder hydration model to quantify the evolution of those CTB properties required by the viscoplastic cap model during its curing process. Therefore, the coupled chemo–viscoplastic cap model can be used to evaluate the blast response of and blast wave propagation in CTB when only the effect of binder hydration on the material evolution is considered predominant.

6.2.2 Multiphysics-viscoplastic cap model

In addition to the effect of binder hydration (chemical; C), the dynamic response of CTB is also subject to the significant influence of thermal (T), hydraulic (H), and mechanical (M) factors inherent in the curing process. Therefore, the coupled chemo–viscoplastic cap model is modified by incorporating all the THMC processes inherent in the curing stage with a multiphysics model for CTB, resulting in a new multiphysics–viscoplastic cap model. The evolution of CTB properties as required by the viscoplastic cap model is captured by the multiphysics model for the CTB curing process. Consequently, the blast response of CTB, as captured by the model, is fully coupled with the multiphysics processes that the material experienced prior to dynamic loading. Thus, the multiphysics–viscoplastic cap model can be used as an integrated tool in assessing the blast response of and blast wave propagation in CTB that features ongoing binder hydration, under various backfilling and curing conditions.

6.2.3 Total-stress viscoplastic cap model

The total-stress viscoplastic cap model is developed by incorporating the impedance of pore water in saturated granular media during the course of undrained blast loading, based on the prototype viscoplastic cap model developed in the study. Use of the total-stress formulation, in addition to the previously listed capabilities of the viscoplastic cap model, allows for the rational assessment of excess pore pressure generation due to irrecoverable compaction upon blasting. Therefore, the total-stress viscoplastic cap developed in this study can be used to evaluate the blast-induced liquefaction susceptibility of early-age CTB, which is typically saturated and has marginal cementation.

6.3 Effect of multiphysics processes on the blast response of CTB

The following multiphysics processes during the curing stage of CTB are considered in the developed fundamental models of the dynamic behaviours of CTB. The detailed influence of these processes on the blast response of CTB is elucidated in the following subsections.

6.3.1 Effect of thermal processes

The thermal processes affect the blast response of CTB, mainly in an indirect manner (i.e., through the other fields). For early-age CTB, an increase in backfill temperature would accelerate binder hydration and fluid flow (by reducing viscosity) and thus promote pore pressure dissipation. This would generally lead to a reduced risk of dynamic liquefaction. In contrast, for more mature CTB, a higher backfill temperature would lead to faster hydration and thus result in more strength gain; this would in turn result in a stiffer dynamic response by CTB. This is considered in the study through an increase in elastic constants, friction angle, cohesion, and parameter $X(x)_0$, as well as a reduction in $h(x)$. Besides, it can also contribute to more rapid water consumption (via hydration) and water loss (via evaporation), and the water content has been shown to have a significant impact on the mechanisms of blast response of porous materials; this will be discussed in Section 6.3.2. Finally, thermal strain would modify both heat exchange and fluid flow processes, through the porosity-dependent properties of CTB; this would in turn further influence its dynamic response.

6.3.2 Effect of hydraulic processes

The hydraulic processes control the mechanisms of the blast response of CTB at different curing ages. Early-age CTB in a saturated condition is subject to blast-induced liquefaction, and hydraulic processes such as self-desiccation and drainage could significantly alleviate the risk of dynamic liquefaction. For mature CTB, however, the amount of water presence under the influence of these hydraulic processes will strongly affect the deformation mechanism and pressure attenuation of CTB in the course of blast loading. Specifically, at low saturation levels, the water present in the pores is insufficient in modifying stress transmission, and the stress waves would still predominantly propagate through the skeleton. This is considered in the study through parameter $s(x)$, as discussed in Section 4.2.3.2.3. Besides, the stress waves would also attenuate more drastically under this condition through the irrecoverable closure of large empty voids. This is considered in the study through parameter $W = f(1-S)$, as discussed in Section 5.2.2.3.2. At higher saturation levels, on the other hand, both pore water and skeleton deformations are important, and so stress waves can propagate significantly faster and attenuation would also decrease. This is considered in the study through both $W = f(1-S)$ and $s(x)$.

6.3.3 Effect of mechanical processes

The mechanical processes that take place during the curing of CTB also influence its behaviour under blast loading, in an indirect way. The deformation of CTB due to thermal expansion, chemical shrinkage, and external stresses in the curing process can result in changes in the porosity of the material. Variations in the void size of CTB would affect the thermal and hydraulic processes of the material through heat conduction and convection, as well as the flow of fluids; this in turn imposes an indirect impact on its blast response, as previously discussed.

6.3.4 Effect of chemical processes

The chemical processes that take place during the curing of CTB strongly affect its blast response, due to their direct impacts in all other fields. For early-age CTB, binder hydration will dissipate the excess pore pressure generated by dynamic loading, which in turn reduces the potential for dynamic liquefaction. In addition, binder hydration is also exothermic, and so it can accelerate fluid flow and generally enhance drainage; this would further reduce the risk of liquefaction. For more mature CTB, binder hydration would also consume pore water and change the rate of fluid flow; it would thus modify its mechanical behaviour under blast loading (through water content), as previously discussed. Meanwhile, binder hydration would result in strength development in CTB, and thus improve its dynamic performance.

6.4 Effect of backfilling conditions and design strategies on the blast response of hydrating fill mass

Using the fundamental multiphysics models developed and validated in Chapter 4, three aspects of those factors that may affect the blast response of hydrating fill mass in the field are investigated in Chapter 5. These include backfilling conditions, stope geometry, and blast operations. The findings from these multiphysics simulations are synthesized in this section, and their implications for field backfill design are also discussed. The favourable (+) and negative (-) impacts of various backfilling conditions and design strategies on the stability of backfill systems are schematically illustrated in Figures 6.1 and 6.2.

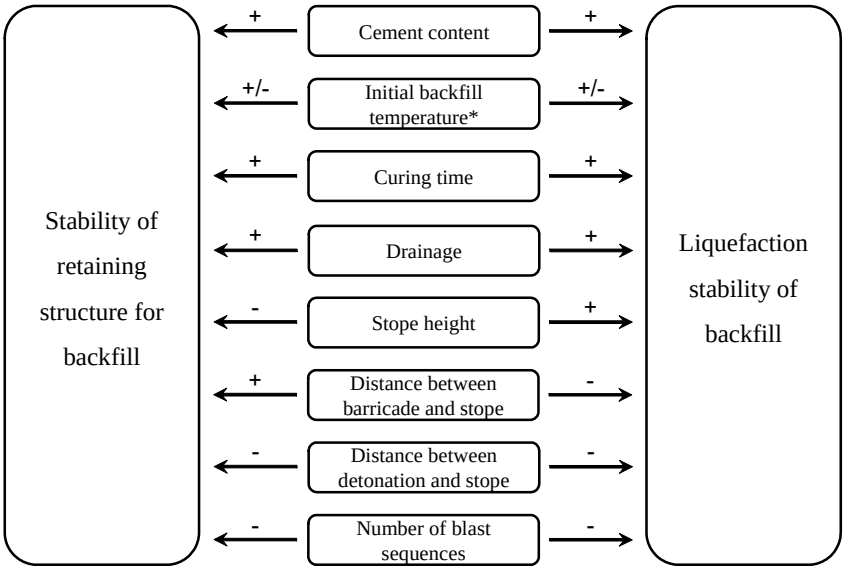

(*: Depends on different stages of backfilling)

Figure 6.1 Effect of different backfilling conditions and design strategies on early-age fill mass

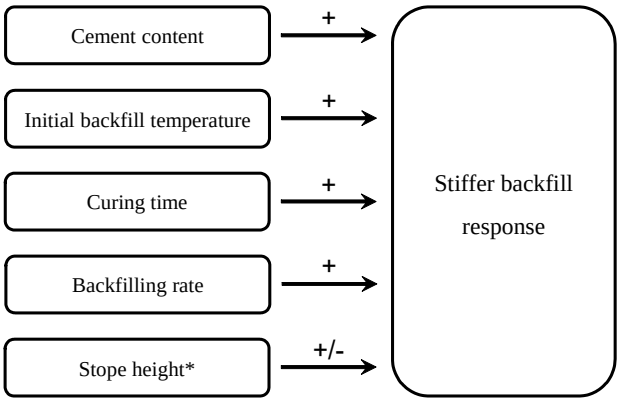

(*: Depends on relative relation between the temperature of backfill and rock)

Figure 6.2 Effect of different backfilling conditions and design strategies on mature fill mass

6.4.1 Effect of backfilling conditions

The backfilling conditions considered in this study include the intrinsic properties of backfill (i.e., cement content, initial temperature, and curing time) and the backfill operation conditions (i.e., filling strategy and drainage condition). Applications of fundamental multiphysics models suggest that all these variables affect the blast response of a field CTB mass through different mechanisms.

(1) Effect of cement content. For early-age fill mass, an increase in cement dosage in the backfill recipe can significantly accelerate excess pore pressure dissipation, mainly through more consumption of pore water via hydration. It could thus lead to lower post-blasting stress on the retaining barricade from the backfill (i.e., barricade pressure), faster dissipation of excess pore pressure, and thus faster mitigation of associated dynamic liquefaction. For more mature fill mass, an increase in cement content would cause a stiffer backfill response under blast loading, due primarily to the generation of more hydration products.

(2) Effect of initial backfill temperature. For early-age fill mass, a higher initial backfill temperature could result in accelerated hydration and thus faster excess pore pressure dissipation, which would in turn lead to lower post-blasting barricade pressure and the reduced risk of dynamic liquefaction. However, it could also increase stress and pore pressure at the stope bottom during the filling process, due to the rapid supply of water from freshly placed backfill above, as a result of increased permeability. For more mature fill mass, on the other hand, an increase in the initial temperature would lead to a stiffer blast response of the material, which can largely be attributed to faster strength gain from boosted hydration.

(3) Effect of curing time. Extending the duration of curing allows for more water drainage and pore water consumption via binder hydration, and thus facilitates greater dissipation of the excess pore pressure generated by dynamic loading. Therefore, longer curing times could reduce the post-blasting stress on the barricade, as well as the tendency towards liquefaction in early-age fill mass. In addition, a longer curing period also permits the generation of more hydration products, which would then result in a stiffer dynamic response by the material.

(4) Effect of backfilling rate. This study shows that the effect of the backfilling rate on the blast response of hydrating fill mass becomes more evident as one approaches the top of backfilled stopes, where the difference in the time of placement (or the effect of any delay) becomes more pronounced.

(5) Effect of drainage condition. The drainage condition of fill mass is crucial to its stability, as enhanced drainage is associated with more rapid (excess) pore pressure dissipation, and thus with a lower risk of blast-induced liquefaction and a faster reduction of post-blasting barricade pressure.

6.4.2 Effect of stope geometry

The stope geometry examined in this study consists of the stope size (i.e., height) and the location of the permeable barricade in the mine drift at the stope bottom. These factors affect, in different ways, the blast response of fill mass and the stability of its retaining structure.

(1) Effect of stope size. For early-age fill mass, extending the height of the stope is an effective means of mitigating liquefaction, as doing so can increase the effective stress of the fill mass at each depth. However the full dissipation of excess pore pressure requires more time, given the increased boundary area subjected to mine blasting and a greater supply of water from fresh backfill. Moreover, a larger stope height can also significantly increase the stress acting on the barricade, which is unfavourable to the stability of the backfill system. For more mature fill mass, the backfill would exhibit more distinct behaviours in the core region of a higher backfill structure, primarily because the effect of the environment (i.e., rock) temperature is less significant there.

(2) Effect of distance between barricade and stope. A barricade located closer to the stope is favourable to the drainage of the fill mass, due to there being a shorter flow path. This would cause faster dissipation of (excess) pore pressure and thus lower the risk of dynamic liquefaction. However, a shorter distance between the barricade and stope could also result in higher backfill stress acting on the retaining structure, as the fill mass would be more horizontally compressed at the stope bottom.

6.4.3 Effect of blast operations

The effects of blast operations are discussed in this study in terms of the distance between the charge and the backfilled stope, and the number of blast sequences; these effects have been found to have a significant impact on the stability of backfill systems.

(1) Effect of proximity of detonation. Conducting mine blasts closer to the stope would significantly increase the amount of excess pore pressure generated in the fill mass. This would in turn increase the risk of liquefaction and post-blasting barricade pressure.

(2) Effect of the number of blasts. Repetitive mine blasts would result in the accumulation of excess pore pressure in the fill mass, and thus also lead to a higher potential for dynamic liquefaction and a higher barricade pressure.

Chapter 7.
Conclusions and Recommendations

7.1 Conclusions

Cemented tailings backfill (CTB) is often exposed to mine blasts during the accessing and recovery of ore pillars. Due to limited understanding as well as the lack of a reliable tool for rational assessment of its behaviour under blast loading, fundamental multiphysics modelling of the blast response of CTB is carried out in this study. The following conclusions can be drawn from the study.

1. The properties as well as quasi-static and dynamic behaviours of CTB are predominately controlled by the coupled multiphysics or THMC processes during its curing stage.

2. A comprehensive literature review has been carried out on available approaches to characterizing the blast response of granular media, and advantages and limitations of different methods are compared. It also reveals the absence of a model to capture the behaviours of hydrating CTB under blast loading, and thus demonstrates the relevance and novelty of multiphysics modelling of the study.

3. A novel coupled chemo-viscoplastic cap model has been first developed to characterize the blast response of hydrating CTB. Then, this model is modified by incorporating all the THMC factors during the curing process of CTB, and it results in a new multiphysics-viscoplastic cap model for simulating the evolutive behaviours of CTB under blast loading. These series of models have considered typical rate-dependence, irrecoverable compaction, strain hardening, full compaction and nonlinear hydrostatic behaviours of porous media upon blast load application, which have also been recently observed in the dynamic response by CTB. In addition, the coupled models have also rationally incorporated the evolution of CTB properties due to THMC processes of the curing stage with a multiphysics model. Thus, the dynamic response of CTB captured by the proposed models is fully coupled with the multiphysics processes that the material has experienced prior to blast loading. The good agreement between simulation and experimental results suggests that these models can be used

as an integrated tool for assessing the blast response of and blast wave propagation in CTB with ongoing binder hydration under varied practical backfilling and curing conditions.

4. A new total-stress viscoplastic cap model has been developed to characterize the blast-induced liquefaction of early-age CTB in a saturated state. In addition to the ability to capturing aforementioned typical nonlinear behaviours of porous media when subjected to blast loading, this model has also incorporated the dependence of material behaviour on fluid impedance in such undrained dynamic condition. The developed model can reasonably capture the excess pore pressure development due to irrecoverable volume compaction in accordance with the mechanism of blast-induced liquefaction. The good agreement between simulation results and experimental data indicates the model is well capable of capturing the liquefaction of natural and man-made granular materials, including tailings backfills, due to blast loading. Thus, the model can be used to evaluate liquefaction susceptibility of saturated fill mass at early age in such dynamic conditions.

5. After validation of the developed fundamental models against experimental data, these models are applied to practical scenarios to examine the effect of backfilling conditions, stope geometry, and blast operations on the blast response of field CTB mass. As far as early-age fill mass is concerned, a longer curing period would permit more reduction in the excess pore pressure generated by dynamic loading, thus reduce the associated risk of liquefaction, and the stress acting on the retaining structure by backfill (barricade pressure) would also drop with time. Besides, the enhancement of backfill drainage, and avoidance of close and consecutive blasting can effectively decrease the excess pore pressure and the associated liquefaction potential, and the barricade pressure can also be reduced. Meanwhile, decreasing the stope height or locating the barricade farther to the stope could reduce the barricade pressure, but it would also compromise the liquefaction susceptibility of the fill mass. Moreover, despite a higher backfill temperature could lead to faster reduction of barricade pressure, excess pore pressure, and thus the risk of liquefaction, the retaining structure is indeed subjected to higher stress from the material during backfilling. Finally, spending more investments by increasing the cement dosage in the backfill recipe can more effectively reduce the barricade pressure and excess pore pressure as well the risk of dynamic liquefaction.

6. As for fill mass at a more advanced age, a longer curing time allows generation of more hydration products, while a higher initial backfill temperature would accelerate the hydration

process. Both of the two factors would result in better strength development of CTB and thus a stiffer dynamic response by the material. Meanwhile, a larger stope size alters the blast response of CTB mainly at the core region of the fill mass, by delaying the heat exchange with the curing environment. The effect of backfilling rate on dynamic behaviours of CTB is more significant at the top of the stope where the difference in the time of placement is more pronounced. Besides, the use of more binder in the backfill recipe would also result in a stiffer backfill response under blast loading.

7. The findings of the study have highlighted the importance of optimal backfill design. It has also provided useful insight for balancing the influence of different design parameters on different aspects of stability (e.g. liquefaction potential and barricade stability) and economy of backfill systems.

7.2 Recommendations for future studies

The following recommendations are made for future works.

1. The emphasis of the presented study has been placed on the blast response and blast wave propagation in cemented tailings backfill. As production and development blasts are detonated in ore body or rock mass, it is recommended for a future study to include the rock in the numerical model for analyzing the dynamic process. This type of work requires not only a reliable model for blast response of rock, but also necessitates a hydration-dependent interface model that can characterize the reflection/refraction of stress wave at the interface of rock and hydrating backfill. In particular, this effort is imperative because more energy of blast waves can be transmitted from the rock to the saturated backfill than its unsaturated counterparts due primarily to the contribution of high impedance of pore water. Therefore, the stability of early-age backfill is critical due to its high vulnerability to liquefaction, and a rational evaluation of wave transmission at the interface is crucial for a reliable assessment of liquefaction susceptibility of fill mass. In the meantime, more experimental and field monitoring efforts are required for the development of such an integrated model.

2. Unsaturated backfills are deemed liquefaction resistant in conventional practice. However, the air-filled pores of the initially unsaturated backfill could also be closed by the high pressure of blast loading, and thus it would become nominally saturated and is subjected to the risk of liquefaction. Despite the numerical tools that are available for capturing such a process, more

experimental studies should be carried out for the development of a model to characterize the blast-induced liquefaction of hydrating backfills in an unsaturated state.

3. Although a total-stress viscoplastic cap model has been developed in the study to simulate the blast-induced liquefaction of early-age tailings backfill, its change of liquefaction resistance due to material evolution during the binder hydration process has not been explicitly included. This limitation is due to the lack of experimental data for developing such a model. While applying the developed model for early-age tailings backfill would be on the safe side, it is inevitably conservative. Therefore, in order to develop a model for assessing the evolutive liquefaction characteristics of hydrating backfill, shock loading tests with integrated pore pressure measurements should carried out on the material that is still saturated and undergoing cementation.

4. The numerical analyses performed in the study have involved the transferring of data between quasi-static and dynamic models of cemented tailings backfills. For example, the backfill properties obtained from the multiphysics model are transferred to the viscoplastic model to capture the response of the material at different curing time during blast loading. Conversely, the excess pore water pressure determined from the total-stress viscoplastic model needs to be transferred to the multiphysics model for simulating the stress redistribution in the fill mass after the blast impact. This is primarily because the current study is dealing with the behaviours of tailings backfills at two distinct time scales (i.e. a magnitude of days for quasi-static curing process and a magnitude of microseconds to milliseconds for blast loading process). The data exchanges are inevitably complex and time-consuming from a modelling point of view. A unified model that can delineate the backfill behaviours in both quasi-static and dynamic conditions should be desirable to simplify the modelling procedures.

5. This study has focused on the dynamic behaviours and liquefaction of cemented tailings backfill due to blast loading. As blast wave attenuates, it gradually becomes of seismic nature at the far field of mine blasts. Moreover, the seismic waves can also originate from fault slips or rock bursts in underground mines. Therefore, characterizing the mechanical response and liquefaction of tailings backfill under cyclic loadings during multiphysics processes of its curing stage should also be an important task of future studies.

Appendix A: Mesh sensitivity analysis

Mesh sensitivity analyses have been performed before numerical simulations with four-node quadrilateral mesh elements in the study. An example of mesh sensitivity analysis for simulation of the field explosion test in saturated sand (Section 4.4.4.4) is presented below.

The axially symmetric model of 2.14 m in radius and 1.83 m in height is simulated with varying mesh sizes, and the peak pore water pressure obtained at the monitoring point 0.22 m beneath the sand surface is recorded for each case. This process is repeated again and again until relatively consistent model response is obtained. The variation of the simulated peak pore pressure at the monitoring point with the mesh size is presented in Figure A.1. It is observed that the peak pore pressure has gradually stabilized for a mesh size less than 0.01 m. Therefore, the final mesh used for simulation of the field explosion test is 0.01 m in order to get a reasonable balance between the model accuracy and solving time.

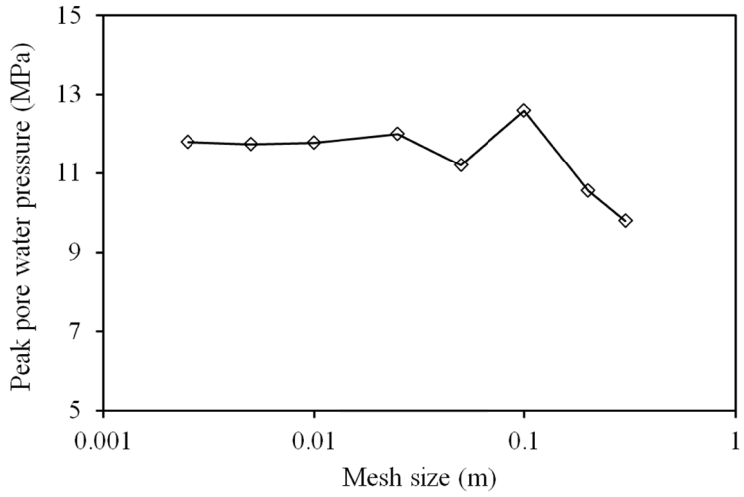

Figure A.1 Variation of simulated peak pore pressure at monitoring point with mesh size